THE UNIVERSITY OF HULL

PROPAGATION OF AERATED PYROCLASTIC DENSITY CURRENT ANALOGUES: FLOW BEHAVIOUR AND THE FORMATION OF BEDFORMS AND DEPOSITS

Being a thesis submitted for the Degree of

Doctor of Philosophy in Earth Science

in the University of Hull

by

Gregory Michael Smith MGeol (University of Leicester)

September 2020

Abstract

Pyroclastic Density Currents (PDCs) are deadly volcanic phenomena which pose an active risk to millions of people. Particularly dangerous due to their great unpredictability, despite decades of study the internal physics of PDCs are still poorly understood, especially in dense currents. Much of our understanding relies on the interpretation of PDC deposits, but there is a lack of quantitative links between internal processes and deposit characteristics. Analogue modelling of PDCs attempts to bridge this gap. Recent modelling has emphasised the importance of high gas pore pressures within dense PDCs, which allows them to behave as a fluid and so travel great distances. However, the heterogeneity of pore pressure in PDCs has not yet been replicated.

A series of flume experiments are presented using a novel apparatus to investigate heterogeneous pore pressures within granular currents, analogous to dense PDCs. Experiments show that flow behaviour is affected by variable pore pressures, which also control the morphology of the deposit, with thick wedges of sediment rapidly aggrading where the current undergoes a large drop in pore pressure.

These deposits are further investigated by using coloured particles to visualise internal surfaces. Numerous bedforms are identified, despite most conventional models suggesting that bedforms are indicative of deposition from dilute currents. Their stoss-aggrading nature results in very steeply-dipping upstream beds, which are usually interpreted as recording the transition from supercritical to subcritical flow, although in these experiments they form by topographic blocking.

Particle Image Velocimetry allows the high-resolution characterisation of the granular currents and the identification of the flow-boundary zone through analysis of velocity profiles. Velocity and shear conditions are observed to have some control on the deposit characteristics, in conjunction with other factors such as topography.

The experimental bedforms are validated by detailed comparison with field examples, which shows that they share similar geometries and scaling parameters. Therefore, interpretations made from observing the analogue currents can apply to PDCs. Greater understanding of how PDC behaviour is recorded in their deposits has important ramifications for hazard assessment.

Acknowledgements

First and foremost I wish to thank my three supervisors: Rebecca Williams, Pete Rowley, and Dan Parsons. It made all the difference knowing that I had such considerate and knowledgeable people supporting me every step of the way, and always pushing me to do my best.

This project was funded by a University of Hull PhD scholarship in the Catastrophic Flows Research Cluster. Experiments were performed in the Geohazards Lab at the University of Portsmouth (thank you to Phil Benson, Sam Capon, and Rob Walmsley for assistance with these), using equipment funded by a British Society for Geomorphology Early Career Researcher Grant held by Pete Rowley. I am grateful to the Volcanic and Magmatic Studies Group for awarding me with a bursary which allowed me to attend the European Geosciences Union 2019 meeting.

Fieldwork in Italy was successful due to the support and guidance of Guido Giordano, Matteo Trolese, and Aurora Silleni (Università Roma Tre), who also made helpful and encouraging comments on the resulting manuscript. Sample analysis at Hull was carried out with assistance from Mark Anderson and Kim Rosewell. The logistics of organising fieldwork was greatly smoothed by Sarah Ord, as well as Jo Dewey and Jo Arnett in the Energy and Environment Institute, who also helped me greatly with the administrative side of the PhD.

Chapter 3 in this thesis was published as a journal paper, which was possible due to Andrew Harris, Richard Brown and two anonymous reviewers, whose comments and suggestions significantly improved the manuscript. Likewise with Chapter 4, and I would like to thank Benjamin Andrews, Guilhem Douillet, and an anonymous reviewer whose comments substantially improved that work.

The volcanology community has been very supportive and friendly and I have had many interesting conversations and much encouragement from various people at academic events. Particular individuals who stand out include: Steve Sparks, Ben Clarke, Alistair Hodgetts, Guilhem Douillet, Brittany Brand, and Nick Pollock. I would especially like to thank the last two for the fascinating and informative field trip exploring the Mt St Helens PDC deposits they organised as part of IAVCEI 2017. I also wish to thank Mike Branney, under whom I first studied volcanology as an undergraduate at the University of Leicester.

I would like to thank my fellow postgraduates at Hull especially Bobby (thanks for all the Matlab help!), Bas, Cindy, Sergio, Cian (a great help with sample prep!), and Chloe. It was a great community to be a part of. I am also grateful to staff including Dave Bond, Eddie Dempsey, Anna Bird, Mike Rogerson, Mike Widdowson, and Liam Herringshaw, for both great discussions as well as support during demonstrating tasks and undergraduate field courses.

I feel very lucky to have some of the most supportive friends anybody could ever wish for, who have been instrumental in keeping me sane and happy over the past several years. Thank you especially: Duncan, Lisa, Davey, Matt, Charlotte, Pete, Catherine, Amelia, Atul, Cameron, Sam, Mike, Sophie, Matt, George, Catherine, Dave, Yasmin, Lianne, Brad, Beth, Liam, and Joe.

Finally, I am incredibly thankful to my parents, not in the least for keeping a roof over my head this past year. It would not have been possible without their unconditional love and support. Thank you.

Contents

List of figures

List of tables

Symbol Glossary

Symbol	Definition
D	Diffusion coefficient.
Da	Darcy number. Defined as $\mu_f/(\varphi_s\rho_s K\Upsilon)$.
F_1	Weight percentage finer than 1 mm.
F_2	Weight percentage finer than 63 µm.
Fr	Froude number. Defined as $\frac{U}{(gH)^{\frac{1}{2}}}$.
g	Gravitational acceleration.
H	Flow or bed(form) thickness.
(H-Y')/H	Height in the flow as proportion of H.
K	Hydraulic permeability.
k	von Karman's coefficient (~0.4).
L	Flow or bed(form) length.
N_B	Bagnold number. Defined as $\frac{\varphi_s\rho_s\delta^2\left(\frac{U}{H}\right)}{(1-\varphi_s)\mu}$.
N_F	Friction number. Defined as $\frac{N_B}{N_S}$
N_S	Savage number. Defined as $\frac{\rho_s\left(\frac{U}{H}\right)^2\delta^2}{(\rho_s-\rho_f)gH\tan\theta}$.
Pn_i	Rouse number. Defined as w_i/kU^*.
Re	Reynolds number. Defined as $Re = \frac{U\rho H}{\mu}$.
s.d.	Standard deviation.
t_d	Pore pressure diffusion time.
U	Velocity.
U_{max}	Maximum velocity below the free surface.
U_{mf}	Minimum fluidisation velocity.
U_{mf_st}	Static minimum fluidisation velocity.
U^+	Dimensionless velocity. Defined as U/U*.
U*	Shear velocity. Defined as $\sqrt{\frac{U\mu_f}{Y\rho_f}}$.
V	Kinematic viscosity. Defined as μ_f/ρ_f.
W*	Dimensionless width.
w_i	Settling velocity (w) of population (i).
x_i	Weight fraction (x) of population (i).
Y	Distance above flow base.
Y'	Distance below free surface.
Y^+	Dimensionless distance from flow base. Defined as $(\rho_f U^* Y)/\mu$.
ϒ	Shear rate.
δ	Particle diameter.
δ_i	Particle diameter (δ) of population (i).
δ_{32}	Sauter mean diameter.
Θ	Particle internal friction angle.
Θ_{Dyn}	Dynamic angle of repose.
Θ_{Smin}	Minimum static angle of repose.

θ_{Smax}	Maximum static angle of repose.
μ	Bulk dynamic viscosity.
μ_f	Fluid dynamic viscosity.
μm	Micrometres.
ρ	Bulk density.
ρ_f	Fluid density.
ρ_s	Particle density.
τ	Shear stress. Defined as ${U^*}^2\rho_f$
τ_{max}	Maximum shear stress below the free surface.
ϕ	Phi scale.
φ_s	Solid volume fraction.

==

Chapter 1

1. Introduction

==

1.1 Pyroclastic Density Currents

Pyroclastic Density Currents (PDCs) are ground-hugging flows of hot gas and volcanic particles which are driven by their density difference with the surrounding air (Branney & Kokelaar, 2002; Dufek, 2016), formed during volcanic eruptions. They can travel at hundreds of kilometres per hour (Druitt, 1998; Dufek, 2016; Roche & Carazzo, 2019) for tens, or in some cases, hundreds of kilometres (Cas et al., 2011; Roche et al., 2016). PDCs have caused ~60,000 deaths since 1500 CE (Brown et al., 2017), and are one of the most hazardous volcanic phenomena, with death:injury ratios as high as 230:1 (Baxter, 1990).

Figure 1.1 A PDC travelling down the north flank of Mt St Helens, WA, USA on 7th August 1980. The overriding ash cloud obscures the actual PDC from view. Photo credit: USGS.

However, despite their hazardous, unpredictable nature and the fact that hundreds of millions of people live within 100 km of a Holocene volcano (Brown et al., 2015), PDCs remain poorly understood (Cashman & Sparks, 2013) due to their complex physics and the inherent danger involved in making direct measurements. This limits our ability to validate field-derived data against observation of the actual phenomena, leading to uncertainties in parameters used for hazard assessment calculations.

PDCs can be formed in several ways, generally as a result of the collapse of a lava dome, lateral blasts, or the collapse or fountaining of an eruption column. After a PDC is formed it can be classified as being either granular fluid-based or fully dilute (Branney & Kokelaar, 2002), which are end-members of a continuum that can vary in time and space. These terms replace the older classification of pyroclastic flow and pyroclastic surge, which were previously treated as discrete phenomena (e.g. Sparks et al., 1973; Wohletz & Sheridan, 1979; Cas & Wright, 1987). The present classification is based on the mechanism of particle support and the predominance of turbulence. Granular fluid-based PDCs exhibit high particle concentrations, resulting in particle support dominated by particle interactions, and the suppression of turbulence. In fully dilute PDCs fluid turbulence is the dominant method of particle support and particle interactions are insignificant due to their very low concentration. The fact that PDCs exist between these end-members has important implications for hazard assessment. For example highly concentrated granular PDCs (or parts of PDCs) may travel large distances carrying decimetre-scale blocks due to high pore pressures (Roche et al., 2013, 2016), and are more likely to destroy buildings due to the greater dynamic pressures imparted by higher density (Cole et al., 2015). Dilute PDCs, on the other hand, are capable of surmounting topography and travelling in unexpected directions (Fisher, 1995), although high dynamic pressures have recently been identified within them as well (Breard & Lube, 2017).

It is very important, therefore, to understand the behaviours of the full spectrum of PDCs to better improve our hazard assessments.

1.2 Research approach

PDCs are i) unpredictable ii) incredibly hazardous iii) difficult to image due to the accompanying ash cloud. These challenges make gathering data on the internal dynamics of a PDC very difficult if not outright impossible. This contrasts with the collection of data in fluvial and marine systems, where established methodologies exist (e.g. Sumner et al., 2013; Sumner & Paull, 2014; Talling et al., 2015). Although much of what we know about PDCs has been deduced from the sedimentological study of their deposits (e.g. Sparks, 1976; Wilson & Walker, 1982; Branney & Kokelaar, 2002; Brown & Andrews, 2015), this approach is limited by the fact that PDCs can erode their own deposits, and that under present understanding only a small part of the PDC (the "flow-boundary zone") is responsible for the sedimentary characteristics of the deposit (e.g. Branney & Kokelaar, 2002; Brown et al., 2007; Sulpizio & Dellino, 2008; Brown & Branney, 2013; Sulpizio et al., 2014). Importantly, there is currently the lack of a quantitative link between the current, the flow-boundary zone, and the resultant deposit.

Experimental modelling is a useful way to reproduce the behaviour and deposits of PDCs under controlled conditions, albeit with very restricted and controlled variables. Flume experiments simulating dense PDCs are a relatively recent development in volcanology, compared to the much more advanced experiments in the fields of fluvial sedimentology and turbidity currents, as well as the modelling of dilute PDCs (e.g. Huppert et al., 1986; Woods & Bursik, 1994; Andrews & Manga, 2011, 2012). Due to the amount of processes occurring at a variety of scales through time and space, the variability of particle characteristics and the variability in temperature, simplifications and assumptions are necessary in order to focus on the exact parameters and processes under investigation. However, important advances in our understanding of dense PDCs can still be made using physical modelling (e.g. Lube et al., 2004; Roche et al., 2008; Girolami et al., 2010; Roche, 2012; Rowley et al., 2014; Lube et al., 2015; Delannay et al., 2017; Roche & Carazzo, 2019). Such experiments have provided greater understanding of the complex physics of granular-dominated PDCs, but interpretation of PDC deposits is still largely based on field studies and conceptual models.

1.3 Aims and motivations

The aim of this thesis is (a) to investigate the behaviour of sustained, fluidised granular currents (analogous to dense PDCs) through a series of flume experiments, (b) to experimentally generate some of the wide range of bedforms seen in PDC deposits, and (c) in turn quantify the process controls on depositional character. By forming complex deposits under quantifiable conditions of velocity, time, current thickness, and degree of fluidisation the project will achieve an improved, quantitative interpretation of PDC deposits, which will ultimately improve our understanding of the behaviour of PDCs in the interests of consistent, predictable hazard assessment.

1.4 Specific research questions

- Can heterogeneous fluidisation of granular currents be replicated in the lab and what effect does this have on flow parameters?

- What is the effect of slope angle on the behaviour of sustained, variably fluidised granular currents?

- How do conditions in variably fluidised granular currents control deposition (and vice versa)?

- Can recognisable bedforms be deposited by these currents, and are different bedforms systematically deposited under different flow conditions?

- If so, are these comparable to bedforms in PDC deposits and are the laboratory conditions realistic?

- Can the flow-boundary zone concept be experimentally quantified in fluidised granular currents? Do the currents deposit via gradual progressive aggradation?

1.5 Thesis outline and structure

Chapter 1 outlines the aims and structure of the thesis as well as the specific research questions to be addressed. A brief introduction to PDCs in general is provided and the experimental approach that has been used is described.

Chapter 2 is a literature review which describes our current understanding of PDCs, from their generation and associated hazards to the physics of their transport and the current state of the art in their physical modelling.

Chapter 3 investigates how analogue PDCs may be heterogeneously aerated using a novel flume apparatus. Flow front velocity is controlled by the degree of proximal aeration, although maximum runout distance is achieved by currents aerated along their entire propagation length. Deposit morphologies are controlled by spatial differences in aeration, forming a thick wedge where there is a large aeration drop. This chapter has been published as "Investigation of variable aeration of monodisperse mixtures: implications for pyroclastic density currents" in the *Bulletin of Volcanology* (Smith et al., 2018). The author of this thesis carried out the experimental work, led the analysis of the experimental data and drafted the manuscript. All co-authors discussed results and edited/commented on the manuscript.

Chapter 4 investigates the internal architecture of the depositional wedges formed by a large decrease in aeration. The introduction of coloured sediment allows the identification of bedforms and the measurement and calculation of internal flow parameters such as velocity, Froude Number, and Friction Number. A bedform phase diagram is produced, showing how very steep upstream-dipping beds are formed at low velocities and Froude numbers after deposition has been triggered by a large aeration drop. These findings are validated by comparison with bedforms in the Pozzolane Rosse ignimbrite, the deposit of a dense granular PDC. This chapter has been published as "A bedform phase diagram for dense granular currents" in *Nature Communications* (Smith et al., 2020). The author of this thesis carried out the experimental work, led the analysis of the experimental data and drafted the manuscript. PR, GG, MT, and AS assisted the author with fieldwork. All co-authors except SC discussed results and edited/commented on the manuscript. Characterisation of the experimental materials was led by SC.

Chapter 5 focuses on processes at the flow-boundary zone. The introduction of tracking particles into the flow allows the construction of velocity profiles and the calculation of shear velocities and bed shear stresses. The various bedforms fall into different fields for such parameters, supporting the conclusion in Chapter 4 that steep backset bedforms are deposited by a waning flow with strong frictional forces. The flow velocity profiles can broadly be separated into exponential and quasi-linear zones, with the lower exponential curve analogous to the widely accepted concept of a 'flow-boundary zone' in PDCs.

Chapter 6 compiles PDC bedform measurements taken from the literature and fieldwork at Laacher See, Germany and central Italy, and highlights some key issues in the recording/reporting of geometrical data. The experimental deposits and models from the previous chapters are compared with the real PDC bedforms showing that the experimentally created features have similar geometries to natural ones.

Chapter 7 is a synthesis of the research presented in Chapters 3-6, answering the research questions posed by this thesis. It finishes with concluding remarks, and suggestions for future research directions.

==

Chapter 2

2. Literature Review

==

Pyroclastic density currents (PDCs) are complicated phenomena which incorporate many different processes operating at various scales, and whose characteristics can change through time and space. Fundamentally, PDCs are a type of gravity current; a dense pyroclast and gas mixture flowing through the less dense atmosphere, but are much less well understood than other gravity-driven mixtures such as turbidity currents due to the highly variable nature of their parameters. PDCs can be a range of temperatures (Mastrolorenzo et al., 2001; Cole et al., 2015) and particle concentrations (Branney & Kokelaar, 2002); interstitial fluid can have little effect (Hayashi & Self, 1992), or create high pore pressures, resulting in friction-reduction and high mobility (e.g. Sparks, 1976; Wilson, 1980; Roche et al., 2002; Roche et al., 2016; Breard et al., 2018; Lube et al., 2019); they can deposit huge amounts of sediment (Barberi et al., 1978; Wilson et al., 1995), bypass (Brown & Branney, 2004a) or become erosive (Roche et al., 2013; Pollock et al., 2016), and both deposition and erosion can affect the flow dynamics. Volcanologists have spent over half a century investigating PDCs using a number of techniques; field-based, experimental, and numerical.

2.1 Pyroclastic density current generation and hazards

PDCs can be formed by a range of mechanisms, and the mode of initiation has some effect on how long-lived a PDC is, as well as its behaviour (i.e. unsteady or quasi-steady) and the resulting deposit lithofacies and composition.

Many PDCs form from the partial or complete collapse of a Vulcanian or Plinian eruption column (Druitt, 1998), where the column has failed to entrain enough air to remain buoyant, creating a highly unsteady PDC (Fig. 2.1a). Column collapses have created PDCs at Vesuvius in CE 79 (Carey & Sigurdsson, 1987), El Chichon in 1982 (Sigurdsson et al., 1987), and Pinatubo in 1991 (Scott et al., 1996). It is thought that most of the very largest PDC deposits are the deposits of column collapse PDCs (Orton, 1996; Druitt, 1998).

If the entire column becomes too dense to be sustained and collapses, or never developed to begin with, a low pyroclastic fountain may form instead, giving rise to a sustained (quasi-steady) PDC (Fig. 2.1c). A low pyroclastic fountain is sometimes referred to as a 'boil over' eruption (e.g. Clarke et al., 2002; Cas et al., 2011; Pacheco-Hoyos et al., 2018). Higher fountains, sometimes existing alongside a buoyant column, are also possible (Fig. 2.1b; Branney & Kokelaar, 2002). PDCs associated with pyroclastic fountaining have been observed at Soufrière Hills 1997-1999 (Cole et al., 2002) and Tungurahua in 2006 (Rader et al., 2015).

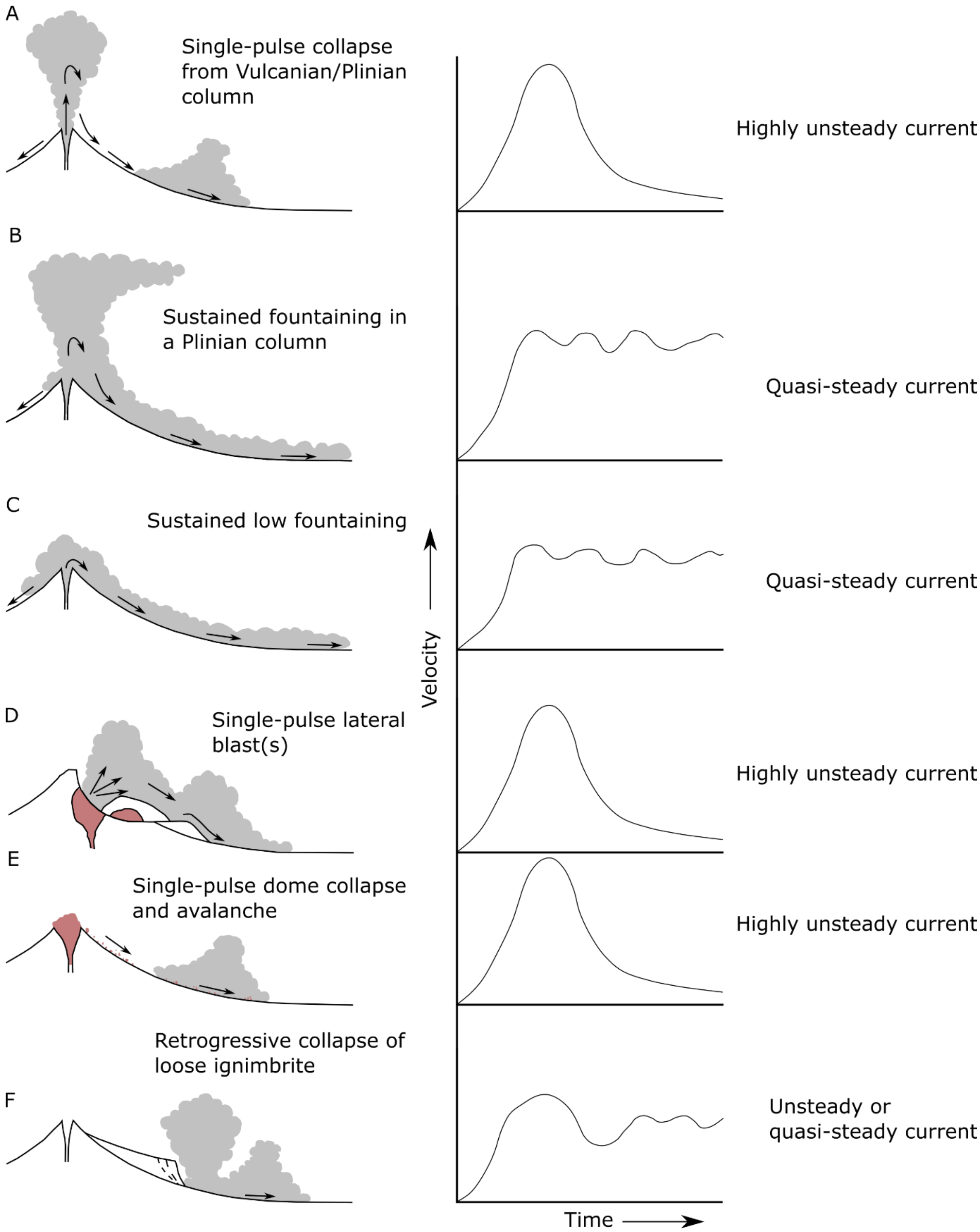

Figure 2.1 Mechanisms for the generation of PDCs, with graphical representations of degree of unsteadiness. Modified from Branney & Kokelaar (2002).

A less common way of generating PDCs is by a lateral blast, as in the initial moments of the 1980 Mt St Helens eruption or the 1956 eruption of Bezymianny (Kieffer, 1981; Crandell &

Hoblitt, 1986; Belousov et al., 2007). In both these cases the collapse of an unstable portion of the volcanic edifice instantaneously released the pressure on an intrusion of viscous magma, causing the explosive decompression of the magma in a lateral direction and forming a highly unsteady PDC (Fig. 2.1d). Lateral blasts can also occur in lava domes – the 8th May 1902 eruption of Mt. Pelée is thought to have occurred in this way (Sparks, 1983). The PDCs formed by lateral blasts are short-lived phenomena, and are generally followed by the formation of a vertical eruption column.

Most PDCs related to lava domes are generated by their gravitational collapse (Fig. 2.1e). This occurs when part of the dome becomes too steep and gravitationally unstable, causing it to collapse under its own weight, or due to instability caused by seismicity or magma movement. The hot, dense fragments have low mechanical strength (Druitt, 1998), and so develop into highly unsteady PDCs through clast comminution and entrainment of air (Branney & Kokelaar, 2002). PDCs of this type have been observed at Mt. Unzen (Yamamoto et al., 1993) and Soufrière Hills (Cole et al., 1998, 2002; Loughlin et al., 2010) amongst others.

PDCs can also be formed by the post-depositional remobilization of loose ignimbrite (Fig. 2.1f), due to the low strength of recent deposits (Branney & Kokelaar, 2002). Remobilization of deposits occurred years after the eruption of Mt Pinatubo in 1991 (Torres et al., 1996), and was inferred to occur during the eruptions of Mt St Helens in 1980 (Rowley et al., 1981). PDCs derived from remobilization material are highly mobile, possibly due to the intrusion of water into pore space (Druitt, 1998).

Steadiness refers to the variation of a parameter over time at a single reference point; a current is said to be steady if the parameter is invariable (Branney & Kokelaar, 2002; Sulpizio & Dellino, 2008). All PDCs are inherently unsteady, but the degree to which this is the case is largely related to their method of generation (Fig. 2.1). These first-order differences range from highly unsteady to quasi-steady. Transient phenomena such as lateral blasts and dome collapses form PDCs where flow is highly unsteady – parameters such as velocity, mass flux, and concentration rapidly wax and then wane (Fig. 2a, d, e). Where sustained fountaining occurs, however, flows reach a quasi-steady state where parameters fluctuate around an average over time (Fig. 2b, c). Importantly, the ability of a PDC to deposit is not controlled by steadiness: waning PDCs are able to erode and waxing PDCs are able to deposit (Branney & Kokelaar, 2002).

2.2 PDC types and concepts

Field studies of PDC deposits have led to a classification of PDCs on a spectrum based on particle concentration, where the end-members are defined as 'fully-dilute' and dense 'granular fluid-based' PDCs (Fig. 2.2; e.g. Branney & Kokelaar, 2002; Brown & Branney, 2013; Smith & Kokelaar, 2013; Breard & Lube, 2017). These end-members describe PDCs where particle collisions are a negligible and important support mechanism, respectively, and may be used in place of the older terms pyroclastic surge and pyroclastic flow, which were long considered to be separate phenomena. In the dilute regime, both particles and gas affect the behaviour of the other (two-way coupling), whereas in the dense regime particles also interact with each other, and clusters of particles compress gas to generate high pore pressures (four-way coupling, Lube et al., 2020).

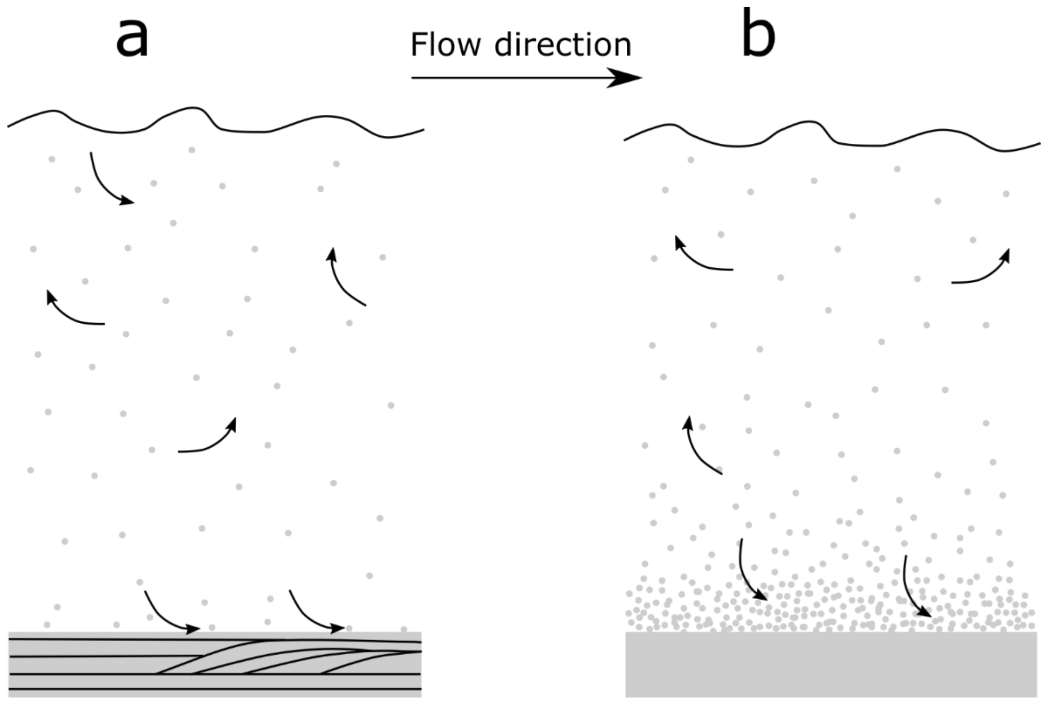

Figure 2.2 End-members of the PDC spectrum. **a** shows a dilute PDC, where particles are supported by fluid turbulence throughout the current. Deposition takes place by direct fallout or traction, creating stratified deposits. **b** shows a granular-fluid PDC, in which the bulk of mass transport is in a high concentration contact-dominated part of the current, resulting in massive deposits. A fluid-turbulence dominated layer may exist above this, but any depositing material must pass through the granular layer.

Despite this dichotomy PDCs are considered to be density stratified, regardless of absolute particle concentration (Valentine, 1987; Druitt, 1998; Branney & Kokelaar, 2002; Sulpizio et al., 2014). Valentine (2020) has shown that a high-density basal underflow can form from collapsing mixtures with as little as 1% solid volume fraction, assuming at least 50% of the particles are coarse. Recent experimental work has shown that density stratification occurs in marked jumps rather than gradually (Breard et al., 2016; Breard & Lube, 2017), agreeing with the two-layer model of Doyle et al., (2011). The density stratification within PDCs can result in spatial variations in velocity, and density-stratified PDCs have been modelled with various velocity profiles (Branney & Kokelaar, 2002), and experimental work has shown velocity profiles can change with time and location in the PDC (Breard & Lube, 2017). A schematic figure (Fig. 2.3) shows a generalised density stratified PDC with a convex velocity profile, reflecting the greater friction at the base and air resistance at the top. The smooth gradient demonstrates that momentum transfer between the different zones is efficient, despite the density difference (Breard et al., 2016).

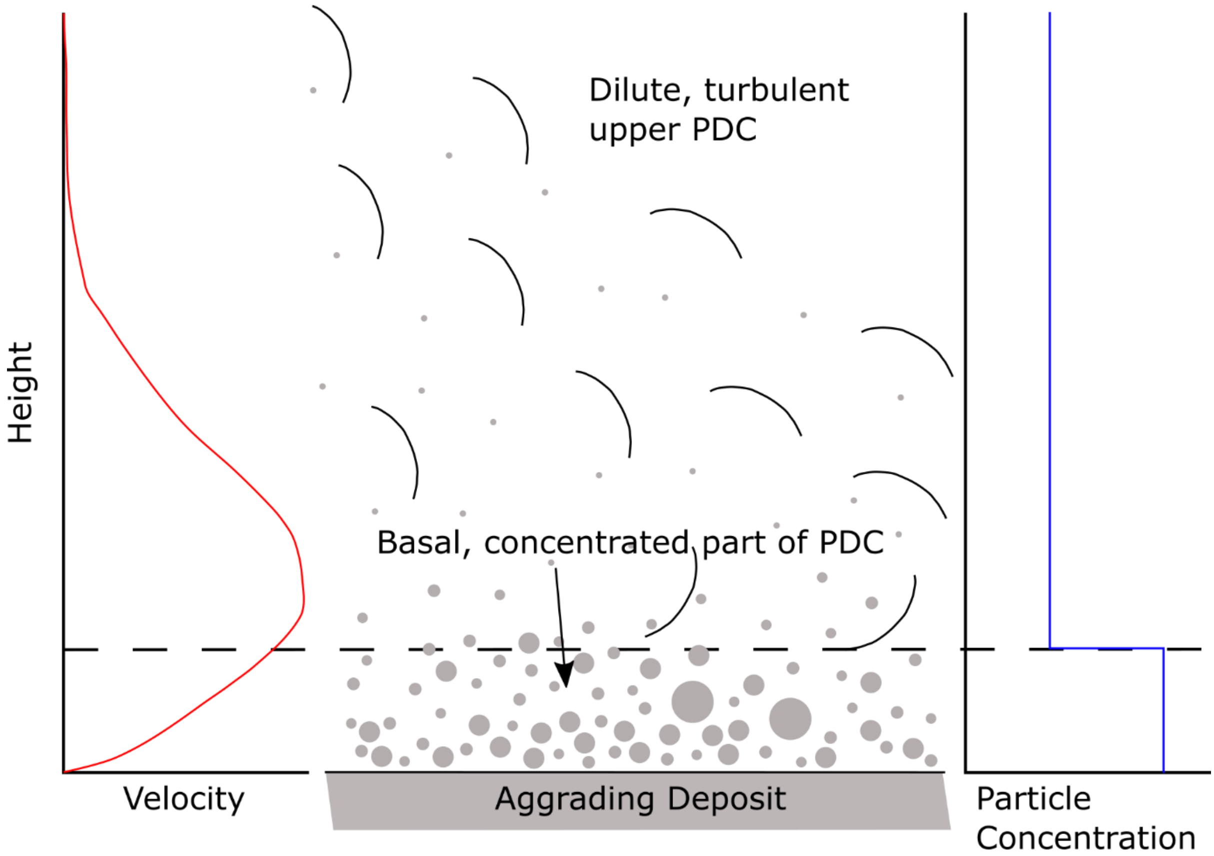

Figure 2.3 Velocity and density profiles through a granular fluid-based PDC. Modified from Sulpizio et al. (2014).

Due to this density stratification, conditions in the main body of the current may be very different to those in the basal zone. As processes such as particle support, interactions, and segregation in this zone control the characteristics of the resultant deposit, the fully-dilute/granular-fluid classification only strictly describes conditions at the base of the current. For example, a ‘granular-fluid based’ PDC may be mostly dilute, with grain interactions only dominating within the concentrated basal part of the current (Fig. 2.2b, Fig. 2.3). Therefore, transport mechanisms operating within the upper bulk of PDCs cannot be inferred from field deposits.

2.3 Particle support, interactions and segregation

As dense granular currents, granular-fluid based PDCs are part of a group that encompasses a range of natural phenomena including snow avalanches, rock avalanches, debris flows, and some turbidity currents. Furthermore, dense granular currents are found in a variety of industrial contexts, where granular material is the second most manipulated substance after water (de Gennes, 1999), such as grain storage in silos (Saleh et al., 2018), food processing (Wang et al., 2006), fluidised beds (Eames & Gilbertson, 2000; Savage & Oger, 2013), pharmaceutical processing (Prescott, 2001; Muzzio et al., 2002), pebble-bed nuclear reactors (Rycroft et al., 2006) and production of construction materials (Vidales et al., 2006). The particles within a granular current can be supported by numerous mechanisms, usually acting in combination. Which mechanisms are active largely depends on how concentrated the current is, and whether interstitial fluid is present.

2.3.1 Granular currents

The behaviour of high concentration (solid volume fraction ≥0.03, Lube et al., 2020) PDCs is complex, and explanations must be based on granular flow theory (Campbell, 1990). In a rapidly shearing mass of clasts, each particle moves quasi-randomly around the mean as a consequence of interparticle collisions. The mean square of these random velocities is known as the *granular temperature* (Ogawa, 1978; Campbell, 1990). The term was introduced as the quasi-random motion of the grains is reminiscent of the thermal motion of molecules. As the granular temperature increases, so does the dilation of the granular mass as a result of increasing dispersive pressure (Bagnold, 1954). At high granular temperatures, therefore, granular masses act less like a solid and are able to flow more easily. However, as collisions between grains are inelastic and energy is constantly being lost (Goldhirsch, 2008), granular temperature must be maintained by shearing.

Flows which are dominated by granular temperature are known as *true grainflows,* in which interstitial fluid is unimportant, and *modified grainflows,* where the interstitial fluid has some effect on flow properties and behaviour (Lowe, 1976; Iverson & Vallance, 2001). Although PDCs may include both types of granular flow, modified grainflows are prevalent because of the abundance of dusty gas as an interstitial fluid (Branney & Kokelaar, 2002).

The *Savage Number* describes the importance of momentum transfer by grain collisions to that by grain friction:

$$N_S = \frac{\rho_s\left(\frac{U}{H}\right)^2 \delta^2}{(\rho_s - \rho_f) g H tan\theta} \quad \text{(Savage \& Hutter, 1989; Iverson, 1997)} \qquad \text{(Eq. 2.1)}$$

Where ρ_s is particle density, ρ_f is fluid density, δ is particle diameter, U is flow velocity, H is flow thickness, g is acceleration due to gravity, and θ is the internal friction angle of the particles. Where $N_S > 0.1$ grain collisions are important in momentum transfer and the flow regime is said to be collisional, whereas where $N_S < 0.1$ the flow regime is frictional. Typical N_S in dense PDCs is 10^{-9}-10^{-8} (Roche, 2012), which is orders of magnitude smaller than ranges for debris flows and avalanches (Iverson & Denlinger, 2001).

Where granular temperature (and N_s) is high, grains interact predominantly in binary collisions and flow is rapid and dilute (Goldhirsch, 2003). At low granular temperatures (and N_s) a *quasi-static* regime exists where grain contacts are frictional and long-lasting, and flow is slow and dense (Nedderman, 1992). An *intermediate dense* regime, where grains interact through collisional and frictional forces and the current flows like a liquid, includes most natural and industrial granular currents (GDR MiDi, 2004; Jop et al., 2006; Forterre & Pouliquen, 2008).

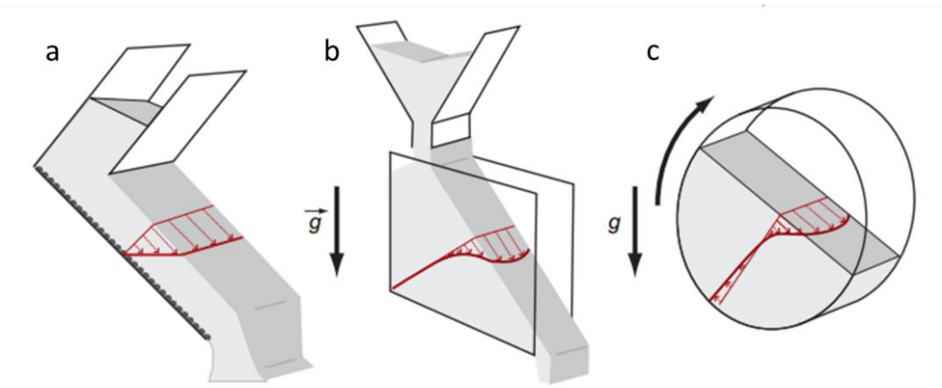

Figure 2.4 GDR MiDi (2004) free-surface experimental set ups and shear profiles. **a** Flow down inclined channel. **b** Flow down a pile. **c** Flow in a rotating drum. From Forterre and Pouliquen (2008).

Figure 2.4 illustrates some of the dense granular currents from the GDR MiDi (2004) study, showing that velocities are greatest at the free surface (top of the granular current) and decline towards the base (or centre in the case of the rotating drum). These profiles transition from a linear to exponential curve (Fig. 2.5) which can signify the transition of the current from an intermediate dense regime to a quasi-static one (Taberlet et al., 2003; GDR MiDi, 2004; Richard et al., 2008; Mangeney et al., 2010; Wang et al., 2019).

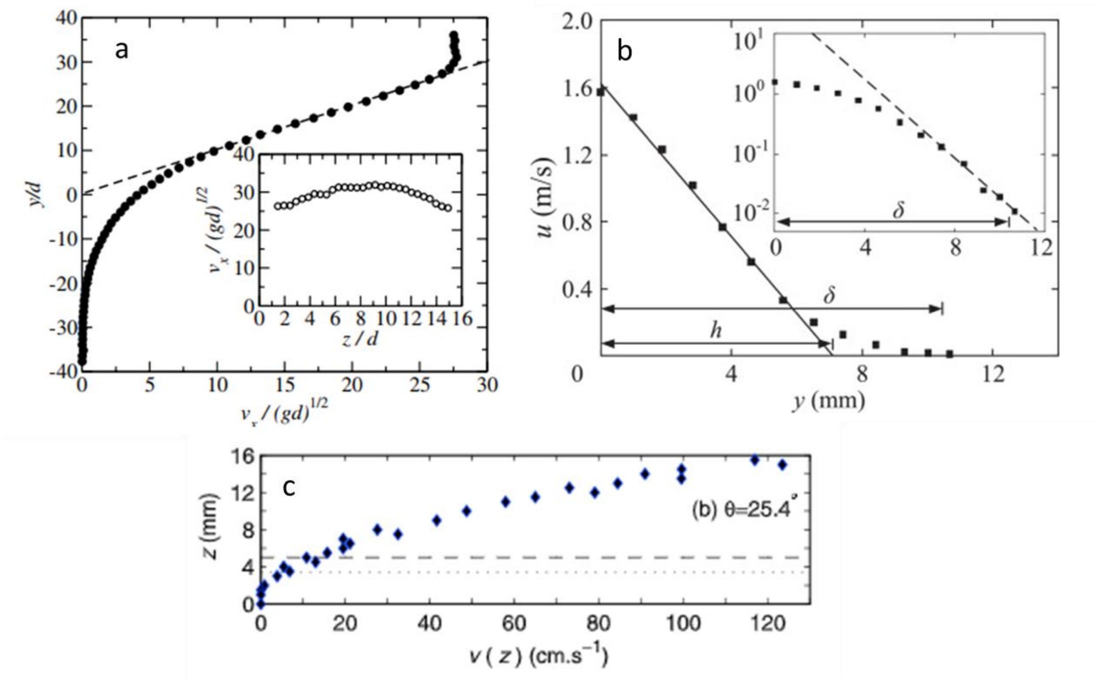

Figure 2.5 Velocity profiles for dense granular currents on inclined planes. The profiles show a linear portion smoothly transitioning to a curve which decreases exponentially to zero velocity, representing the transition from dense fluid-like flow to quasi-static. **a** Taberlet et al. (2003). **b** Wang et al. (2019). **c** Mangeney et al. (2010).

Segregation of particles by size within a dense granular current can take place due to the *kinematic sieving* and *squeeze expulsion* mechanisms. Kinematic sieving, or percolation, occurs when smaller particles fall towards the base of a flow through the voids between larger particles, so that the upper levels of a flow become enriched in coarser grains (Middleton, 1970). Savage and Lun (1988) call this process ‘the random fluctuating sieve’, and attribute it to the probability of there being a void for a small grain to fall into being greater than a void for a large grain to fall into.

It was realised, however, that there had to be a concurrent process operating in order for larger grains to be transported upwards and inverse grading to form (Savage & Lun, 1988). This is accomplished by squeeze expulsion, the process by which grains are compressed and squeezed out of their layer due to imbalanced contact forces. The combined effect of kinematic sieving and squeeze expulsion results in a net upwards movement of large particles towards the free surface (Savage & Lun, 1988).

It was initially suggested (Bagnold, 1954) that segregation in granular flows occurred because dispersive pressure forced the migration of larger grains away from zones of high shear strain, i.e. towards the upper free surface of a flow, while smaller particles would drift towards greater shear strain i.e. the bed. The role of dispersive pressure as an important mechanism of particle segregation has been challenged (Middleton, 1970; Sohn, 1997; Legros, 2002; Kleinhans, 2004). Problems with Bagnold's theory included that they were working with well-sorted particles rather than natural, poorly-sorted mixtures, and that increasing dispersive pressure should result in expansion of the flow, causing a decrease in particle concentration and thus dispersive pressure. Nevertheless, a reasonable compromise has been proposed that dispersive pressure may still assist in segregation by squeeze expulsion, or "kinematic squeezing" (Le Roux, 2003), and this has been cited by numerous volcanologists investigating PDCs (e.g. Charbonnier & Gertisser, 2011; Sarocchi et al., 2011; Sulpizio et al., 2014).

2.3.2 Fluid turbulence in granular currents

Within dilute PDCs, clasts may be transported through fluid turbulence, saltation, and traction. These mechanisms may also operate in the more dilute upper levels of granular fluid-based PDCs, alongside mechanisms such as particle interactions, fluid escape, and excess pore pressure in the more concentrated basal region (Branney & Kokelaar, 2002).

Where fluid turbulence is important in particle support, the particle population can be seen to occupy three partially overlapping levels within the PDC depending on their dominant mode of support (Middleton & Southard, 1984). These are (a) the suspension population, operating at all levels within the current and supporting clasts fully through fluid turbulence, (b) the intermittent suspension population, closer to the flow boundary and partially supporting particles through fluid turbulence, and (c) the traction population, where particles are supported by the deposit surface. Such segregation will also be present in more concentrated currents, but with the increasing importance of particle-particle interactions in the lower levels.

Whether a particle or particle population can be efficiently supported by fluid turbulence can be determined by its *particle Rouse Number*:

$$Pn_i = w_i/kU^* \qquad \text{(Valentine, 1987)} \qquad \text{(Eq. 2.2)}$$

Which is the ratio of the settling velocity (w) of a population (i) to the turbulence intensity (kU*) where k is von Karman’s coefficient (~0.4) and U* is the shear velocity. A low Pn_i corresponds to a particle population which can be efficiently supported and transported by fluid turbulence, whereas a large Pn_i (>2.5 Valentine, 1987) belongs to a population which would be unable to be fully supported by turbulence.

2.3.3 Fluidised granular currents

In highly concentrated granular currents, the interstitial fluid (dusty gas in the case of PDCs) can play an important role in particle support through fluidisation. This is the process whereby an upwards gas flux counterbalances the weight of the particles, allowing the dispersion to behave as a fluid (Kunii & Levenspiel, 1991). The importance of an interstitial fluid is described by the *Bagnold Number*, as defined by Iverson (1997):

$$N_B = \frac{\varphi_s \rho_s \delta^2 \left(\frac{U}{H}\right)}{(1-\varphi_s)\mu_f} \qquad \text{(Eq. 2.3)}$$

Where φ_s is the solid volume fraction, ρ_s is particle density, δ is particle diameter, U is flow velocity, H is flow thickness, and μ_f is the dynamic viscosity of the fluid. Where N_B <40 the flow regime is macroviscous, and the pore fluid plays an important role in momentum transfer. Where N_B is >450 the flow regime is inertial, and grain-grain interactions dominate. In pyroclastic density currents in particular, the bulk current is very unlikely to enter the macroviscous regime (Iverson & Denlinger, 2001; Bursik et al., 2005); it would have to be uniformly fine-grained to do so. Typical N_B in dense PDCs is 10^0-10^2 (Roche, 2012), considerably lower than ranges for debris flows (Iverson & Denlinger, 2001).

The *Darcy number* shows how increased fluidisation affects the dynamics of a PDC. The Darcy number is defined by Iverson (1997) as:

$$Da = \mu_f/(\varphi_s \rho_s K \Upsilon) \quad \text{(Eq. 2.4)}$$

Where μ_f is the dynamic viscosity of the fluid, Υ the shear rate, K the hydraulic permeability, φ_s the solid volume fraction, and ρ_s is particle density. It is an expression of the tendency of pore fluid pressure to dampen interparticle interactions. Fluidisation occurs when this number is greater than 1 (Dufek, 2016), and typical values in dense PDCs are 10^1-10^4 (Roche, 2012). PDCs which are rich in finer particles, and so have low permeability, are able to sustain high pore pressures for longer and thus travel further (Roche et al., 2004).

Although the high mobility of PDCs is often attributed to high dynamic pore pressures as a result of fluidisation (e.g. Sparks, 1976, 1978; Druitt et al., 2007; Girolami et al., 2008; Roche et al., 2008; Roche, 2012; Gueugneau et al., 2017; Breard et al., 2019), the polydisperse nature of PDCs means that fluidisation cannot support all the clasts; if the fluidisation velocity were high enough to suspend the larger blocks typically found in PDCs and ignimbrites then it would almost completely elutriate fine particles. PDCs, then, can only be considered to be semi-fluidised (Sparks, 1976).

The sources of gas for fluidisation can be internal or external. When invoking fluidisation, volcanologists rarely specify which source(s) generate the gas flux, although several have been proposed (see Wilson (1980) and Branney and Kokelaar (2002) for reviews).

Grain self-fluidisation (Fig. 2.6a), where gas is exsolved from juvenile particles, was the first type of fluidisation to be envisaged, but there was disagreement on whether it was able to be the primary support mechanism over the required timescales (Reynolds, 1954; McTaggart, 1960, 1962; Brown, 1962). Experiments by Sparks (1978) showed that grain self-fluidisation could substantially fluidise PDCs, although it is unlikely to be important in smaller flows.

Bulk self-fluidisation (Fig. 2.6b) occurs due to the entrainment of air beneath the front of the current, and was first suggested by McTaggart (1960). However, this mechanism did not find widespread acceptance until the 1980s, where it was invoked to explain the presence of fines-depleted facies near the base of ignimbrites (Walker et al., 1980a; Wilson, 1980; Wilson & Walker, 1982). Further work by Allen (1984) showed that bulk self-fluidisation was most effective in high-concentration currents comprised of fine ash.

One type of fluidisation that does not require either an external source of gas or one from juvenile clasts inside the current is called hindered settling, or *sedimentation fluidisation* (Fig. 2.6c; Branney & Kokelaar, 2002; Chédeville & Roche, 2018). This occurs when settling particles displace fluid upwards, and this upwards fluid flux acts to decrease the settling rate of other clasts. Experiments by Chédeville and Roche (2014, 2015) have shown that sedimenting particles can displace air from surface interstices at velocities greater than the minimum fluidisation velocity (U_{mf}) of the pyroclastic material, which suggests that sedimentation fluidisation is especially important for fine-grained PDCs flowing over rough substrates. Similarly, rapid sedimentation of mesoscale clusters can trap gas and result in a fully fluidised dense basal layer (Breard et al., 2016, 2018; Lube et al., 2020).

Decompression fluidisation (Fig. 2.6d) is suggested by Druitt and Sparks (1982) to be important in proximal PDCs formed by column collapse; fluidisation is caused by the upflow of rapidly decompressing gas, which was compressed at the base of the collapsing column.

This is consistent with the numerical modelling of collapsing columns by Valentine and Sweeney (2018). Branney and Kokelaar (2002) also suggest this process could occur during a lateral blast.

Additionally, Lube et al., (2019) have shown that basal air lubrication of PDCs can result from a shear-induced downward gas flux.

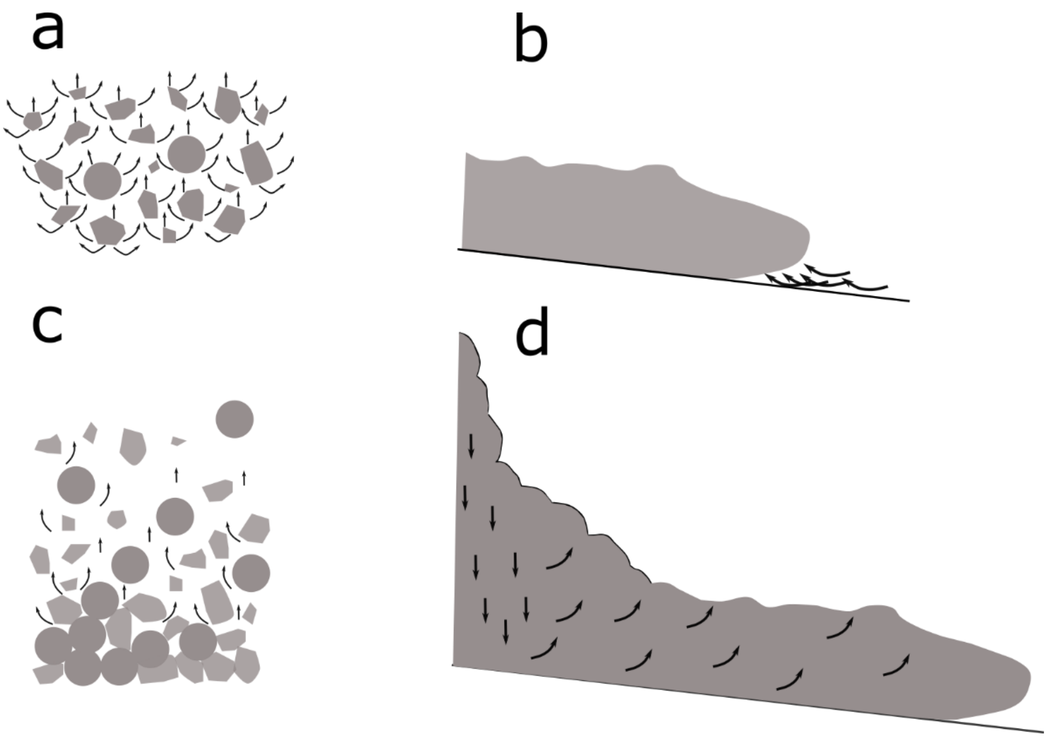

Figure 2.6 Mechanisms of fluidising a PDC. **a** Grain self-fluidisation. **b** Bulk self-fluidisation. **c** Sedimentation fluidisation/hindered settling. **d** Decompression fluidisation. Modified from Branney & Kokelaar (2002) and Druitt & Sparks 1982.

The internal kinematics of dam-break initially fluidised granular currents along horizontal channels were studied by Girolami et al. (2010) and Roche et al. (2010). Velocity profiles show increases towards the free surface (Fig. 2.7), with a slight decrease at the top of the current in the experiments of Girolami et al. (2010). This may be due to air drag which did not affect the currents of Roche et al. (2010) as they used 80 μm glass beads as opposed to a <250 μm mixture of ash.

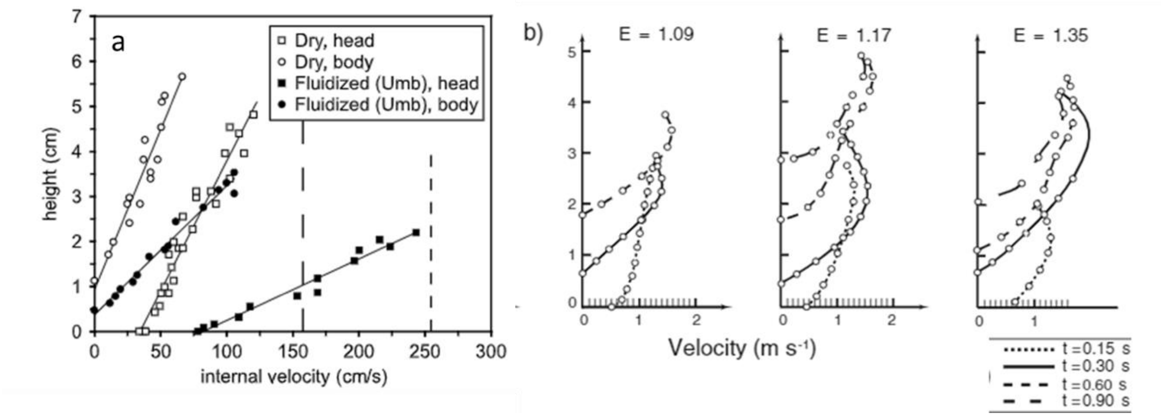

Figure 2.7 Velocity profiles for initially fluidised dense granular currents on horizontal planes. **a** Roche et al. (2010). **b** Girolami et al. (2010). E is initial expansion.

With the exception of the drag-affected region these profiles are much more linear than those seen for dry (supported mainly by particle interactions) granular currents travelling down inclined channels (Fig. 2.5). In the flow body the velocity is zero at the basal deposit and then increases upwards relatively linearly throughout the current to U_{max}.

Jessop et al. (2017) examined the velocity profiles of dense granular currents which undergo sustained fluidisation down an inclined channel. The solutions given by their numerical model differ from measurements by PIV: after U_{max} velocities decrease upwards whereas the model shows an increase to the free surface (Fig. 2.8). This is thought to be caused by the ballistic regime at the top of the current (which has fluctuating depth) being included in the bulk current by the PIV averaging process.

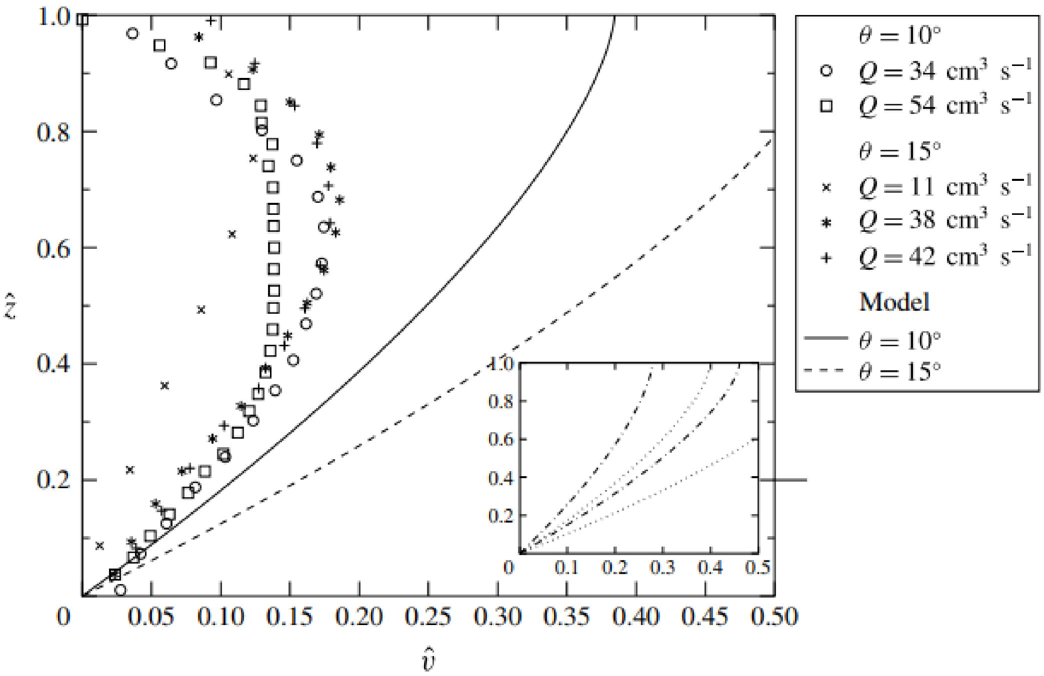

Figure 2.8 Measured and modelled velocity profiles for fluidised dense granular currents down inclined planes (Jessop et al., 2017). Q is flow rate.

The previous sections highlight that PDCs can have a variety of processes operating at any one time which affect the transportation and segregation of particles. Although this has been recognised for a long time, there is still much debate on how exactly these mechanisms are recorded in PDC deposits. A previous model of *en masse* deposition, treating dense PDCs as plug flows where position in the deposit equalled position in the current, enjoyed prominence in the 1970s and 1980s (e.g. Sparks et al., 1973; Sparks, 1976; Wright & Walker, 1981; Freundt & Schmincke, 1986), although opposition mounted over time (e.g. Branney & Kokelaar, 1992; Druitt, 1992; Fisher et al., 1993). The present widely accepted depositional model for PDCs utilises the concept of the *flow-boundary zone*.

2.3.4 The flow-boundary zone

Pyroclastic density currents are thought to form deposits via progressive aggradation, i.e. the deposit is built up over time in either a gradual or stepwise manner (Fisher, 1966; Branney & Kokelaar, 1992, 2002; Sulpizio & Dellino, 2008). The characteristics of the deposits, therefore, result from processes taking place solely in the lower part of the current and the upper deposit itself. This area is named the ‘flow-boundary zone’ by Branney and Kokelaar (2002), where the flow-boundary separates the current and the deposit.

Four end-members of flow-boundary zones are defined by Branney and Kokelaar (2002), which are intergradational into each other (Fig. 2.9). Direct fallout-dominated flow-boundary zones (Fig. 2.9a) occur when the basal region is sufficiently dilute for particle interactions to be unimportant and individual grains are able to settle. Traction-dominated flow-boundary zones (Fig. 2.9b) are also low particle concentration regions, but fluid turbulence and shearing cause the clasts to move by traction and saltation. Granular flow-dominated flow-boundary zones (Fig. 2.9c) have increased particle concentration and moderate-high shear intensity, allowing grain interactions to dominate. Finally, a fluid escape-dominated flow-boundary zone (Fig. 2.9d) also occurs as a result of high particle concentration, where sedimenting grains expel fluid upwards. According to this scheme, a dense, granular-fluid current would form massive deposits due to the suppression of turbulence inhibiting the formation of bedforms.

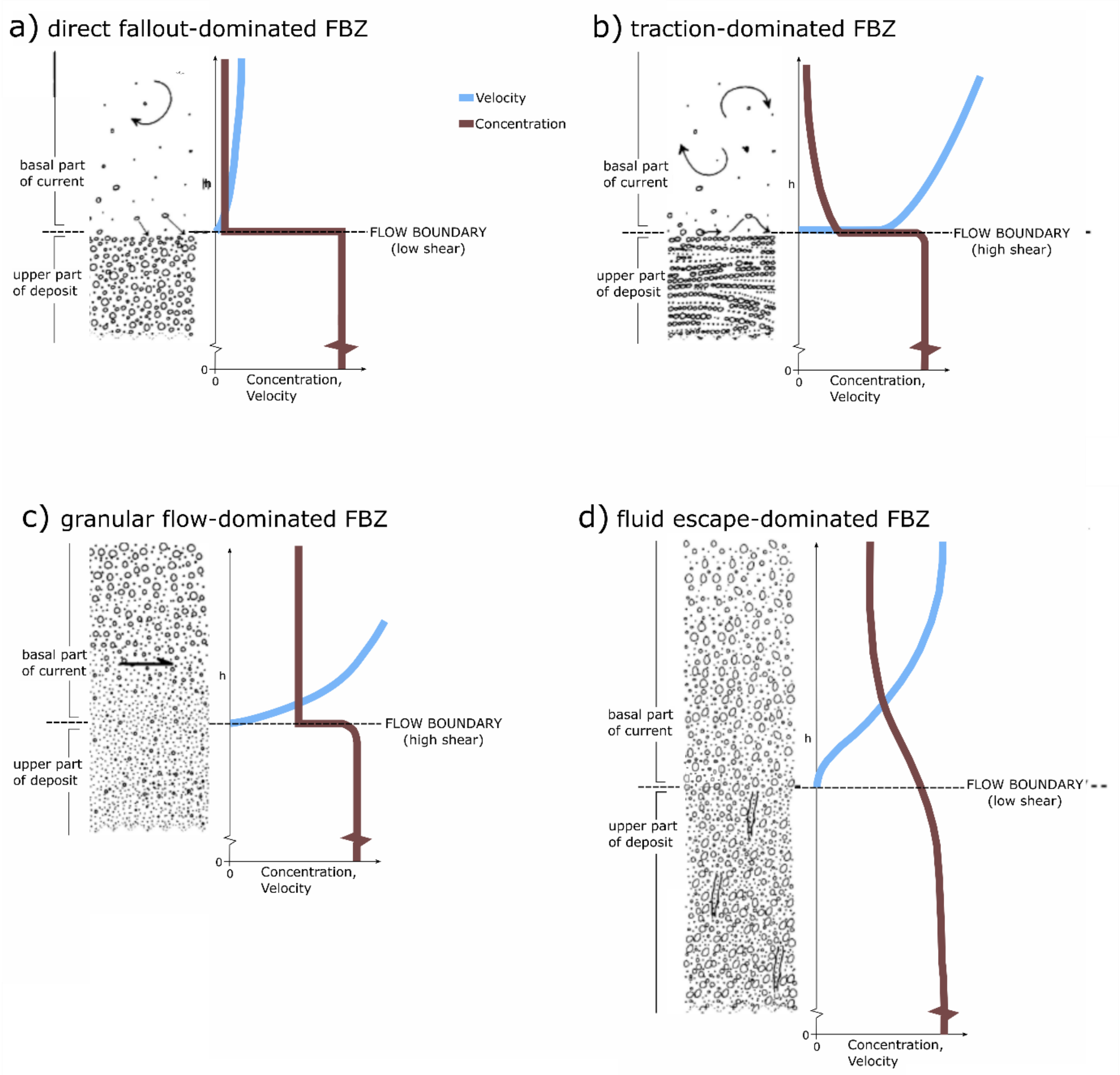

Figure 2.9 Flow-boundary zone end-members, modified from Branney and Kokelaar (2002).

The term 'flow-boundary zone' is used overwhelming in respect to PDCs (e.g. Brown & Branney, 2004b; Brown et al., 2007; Doronzo & Dellino, 2013; Sulpizio et al., 2014; Breard et al., 2015; Brown & Andrews, 2015; Scarpati et al., 2015; Hernando et al., 2019; Platzman et al., 2020), and other terms are used to describe similar zones in other geophysical gravity currents (see below). However, the flow-boundary zone scheme has not universally been accepted amongst volcanologists, as some of its assumptions are disputed. In particular some workers argue that deposition by progressive aggradation does not always take place (e.g.

Wilson & Hildreth, 2003; Lube et al., 2004; McClelland et al., 2004; Schwarzkopf et al., 2005). It is also important to remember that the flow-boundary zone classification is not based on quantitative values, and only recently have velocity and concentration profiles been taken through large-scale experimental PDCs (Breard & Lube, 2017).

'Flow-boundary zone', has, however, found some use outside of volcanology, in the description of turbidity currents (Sumner et al., 2008, 2012), hyperpycnal flows (Ponce & Carmona, 2011), and hybrid events (Southern et al., 2017). Differentiation of regimes within turbidity currents is usually based on changes in the velocity gradient (Fig. 2.10), with the area below maximum velocity (negative gradient), characterised by interactions with the bed, referred to as the 'lower shear layer' (Dorrell et al., 2019; Kelly et al., 2019) or 'inner region' (Kneller et al., 1999). However, 'inner region' is also used to refer to the basal part of the lower shear layer where the flow transitions from turbulent to viscous (Dorrell et al., 2019).

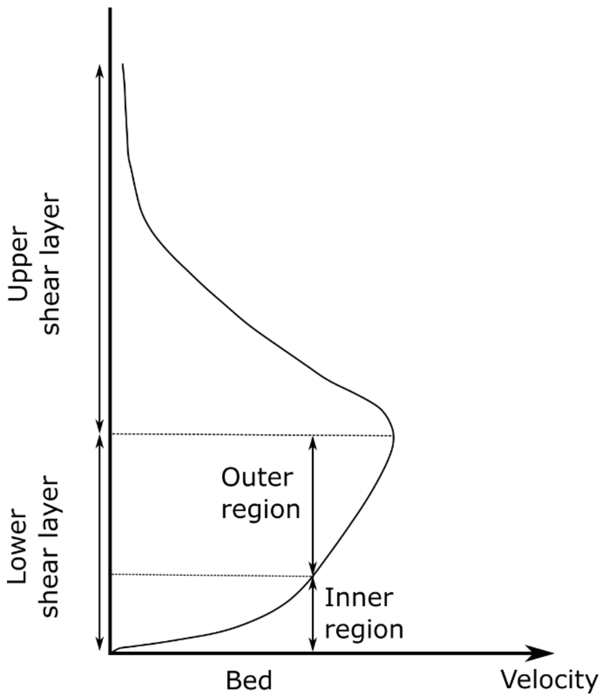

Figure 2.10 Standard model velocity profile for a seafloor gravity current. Turbulence is dampened in the inner region. Modified from Dorrell et al. (2019).

As the flow-boundary zone includes both the lower part of the current and the upper deposit, velocity profiles of particles sedimenting through the zone would be expected to show velocities decreasing to zero (assuming the deposit is static) as frictional forces increase. The flow-boundary zone, then, could be seen as analogous to the quasi-static regime (section 2.3.1), the inner region of turbidity currents, or even the viscous sublayer of clear-water flows (Southard, 2006).

2.4 The sedimentation of ignimbrites

Ignimbrites are the ash- and pumice-rich deposits of PDCs. Traditionally, the term ignimbrite has only been applied to those (usually massive) deposits which were deposited by PDCs initiated by column collapse during large-volume eruptions, i.e. the deposits of 'pyroclastic flows'. The typically well stratified deposits of 'pyroclastic surges' were recognised as separate to ignimbrites (Sparks, 1976; Wohletz & Sheridan, 1979; Druitt, 1998). However, with the recognition of pyroclastic flows and surges forming the two end-members of a spectrum, the deposits of PDCs are now regarded as intergradational (Branney & Kokelaar, 2002). What were previously known as pyroclastic surge deposits are now seen to be subordinate lithofacies in ignimbrite successions.

Ignimbrites can be divided into two types by their aspect ratios (the ratio of average thickness to the diameter of a circle encompassing the surface area of the deposit). High-aspect ratio ignimbrites are thick but do not cover a large area, being generally confined to valleys and emplaced by moderately-sized eruptions. Low-aspect ratio ignimbrites, on the other hand, are thin and widespread, and not confined by topography (Walker et al., 1980b).

Ignimbrites are can be deposited by large-volume, explosive eruptions, covering thousands of square kilometres (Whitney & Stormer, 1985) and reach thicknesses of hundreds of metres (Cas & Wright, 1987). Ignimbrites have been found hundreds of kilometres from their sources – an eruption of Taupo in New Zealand deposited the Kidnappers Ignimbrite over 190 km from source (Wilson et al., 1995), and the Peach Springs Tuff is found over 170 km from its source at Silver Creek Caldera, AZ (Roche et al., 2016). The depositional characteristics of ignimbrites can be widely variable. Lithofacies may include massive to stratified, non-graded to normal or inversely graded, compositionally zoned or not, loose to compacted, and many more (Cas & Wright, 1987; Branney & Kokelaar, 2002; Brown & Andrews, 2015). Branney and Kokelaar (2002) introduced a lithofacies scheme for ignimbrites, in order to ease their description and interpretation. Some of the more common lithofacies and sedimentary structures are summarized below.

Massive lapilli-tuff

The most common lithofacies found in ignimbrites. It is poorly sorted, and contains no stratification. It is interpreted to be deposited from a high concentration, fluid escape-dominated flow-boundary zone where turbulence is suppressed, leading to poor sorting and little shearing/tractional processes (Fig. 2.11).

Figure 2.11 a Massive lapilli-tuff in Victoria Land, Antarctica. Pencil is 8 cm (Smellie et al., 2018). **b** Massive lapilli-tuff from the Portezuelo ignimbrite, Andean southern volcanic zone (Hernando et al., 2019).

Stratified and cross-stratified tuffs and lapilli-tuffs

This lithofacies can be well to poorly sorted, and individual beds are rarely continuous over more than several tens of metres. Metre-scale bedforms are common. Where cross-stratification is present, strata are often as steep as 30-40° (Fig. 2.12a). Stratified lithofacies are thought to represent deposition from a traction-dominated flow-boundary zone (Fig. 2.12b).

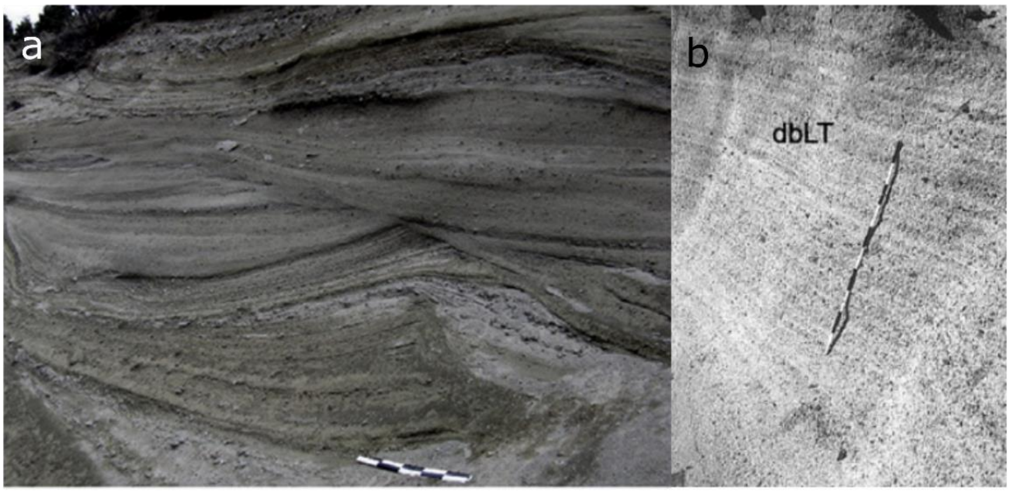

Figure 2.12 Examples of stratified tuffs, rulers are 1 m.**a** Cross-stratified ignimbrite, Gölcük volcano, Turkey (Brown & Andrews, 2015). **b** Diffuse-stratification in the Poris ignimbrite, Tenerife (Brown & Branney, 2004b).

Pumice-rich layers

These are enriched in pumice relative to lithic clasts (Fig. 2.13), and extremely variable in thickness and morphology. They are common at the margins of ignimbrites, where large pumice clasts have accumulated due to overpassing, i.e. a tendency to remain in the current due to a combination of buoyancy and kinetic sieving/squeeze expulsion (section 2.3.1; Branney & Kokelaar, 2002). They can be distinguished from pumice fall layers by the roundness of the pumice clasts; clasts in pumice fall tend to be more angular. Pumice-rich layers record the segregation of pumice from the rest of the current due to their density and/or size difference. However, pumice clasts do not always overpass and can behave similarly to lithic clasts (Brown et al., 2007).

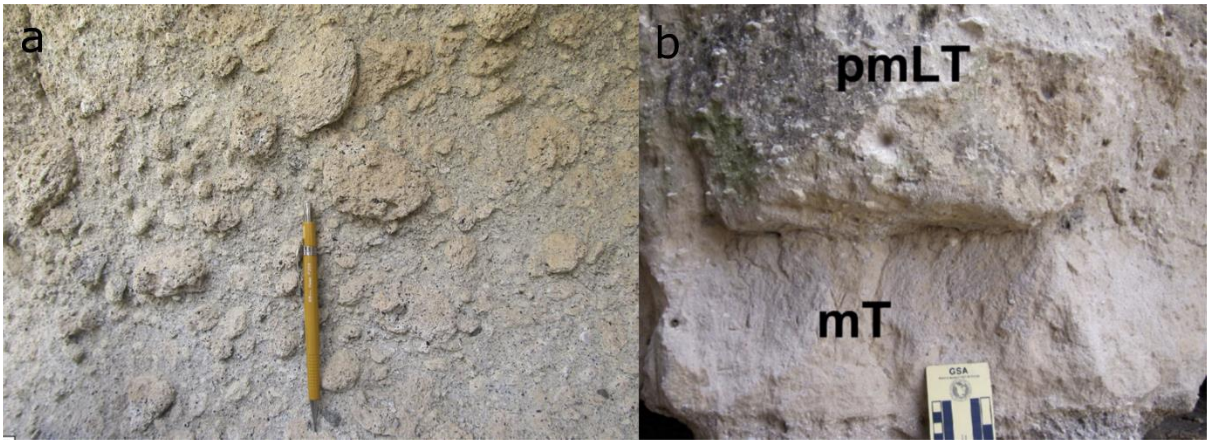

Figure 2.13 a Pumice-rich facies in an ignimbrite unit at Coranzulí caldera, Central Andes (Guzmán et al., 2020). **b** Pumice-rich facies overlaying massive tuff in the Huichapan ignimbrite, Central Mexico. Divisions on left of scale are cm (Pacheco-Hoyos et al., 2018).

2.4.1 Sedimentary structures

Vertical grading:

Ignimbrites can show multiple types of normal and inverse grading (Fig. 2.14), for example normal grading of lithics and inverse grading of pumice. Because through deposition by progressive aggradation each clast has to pass over the flow boundary, grading that develops in a PDC is not recorded as grading in the ignimbrite, as was once thought (Sparks, 1976; Wilson, 1980). Grading is the result of variations in conditions in the flow-boundary zone over time, or changes in clast supply at source (Branney & Kokelaar, 2002). Normal grading may arise due to waning current competence – i.e. being unable to transport larger clasts as far, or from a decrease in the availability of clasts at source. Inverse grading, then could be caused by waxing current competence or an increase in clast availability, or decreasing shear rates at the flow-boundary allowing the deposition of coarser clasts.

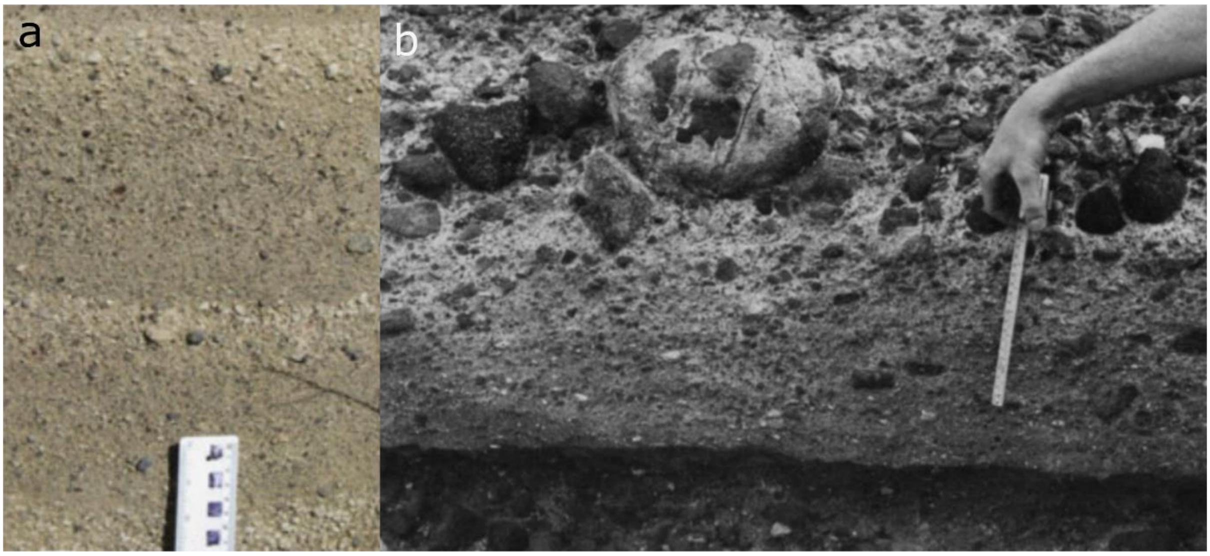

Figure 2.14 a Repeated inverse grading of pumice in the Poris ignimbrite, Tenerife (Smith & Kokelaar, 2013). **b** Inverse grading of pumice and lithics in a lithic breccia, Santorini (Druitt & Sparks, 1982).

Bedforms

A bedform is "a single geometric element, such as a ripple or a dune" (Bridge & Demicco, 2008, Fig. 2.15). Various bedforms occur in ignimbrites, especially in what were previously known as pyroclastic surge deposits (Schmincke et al., 1973; Allen, 1984; Cole, 1991; Douillet et al., 2013). The term *sand-wave* was used to describe undulating bedforms in PDC deposits for many years (e.g. Wohletz & Sheridan, 1979; Allen, 1984; Cole, 1991; Druitt, 1992) in an attempt to move away from terminology used in aqueous systems. However as pointed out by Douillet et al. (2013), bedforms are not waves, so the term *dune bedform*, or variations upon, has been adopted, and usage has become more common in the past few years (e.g. Brown & Branney, 2013; Breard et al., 2015; Brand et al., 2016; Douillet et al., 2018).

Bedforms are commonly seen as diagnostic of deposition from dilute PDCs, where tractional processes dominate in the flow-boundary zone due to the predominance of fluid turbulence as a particle support mechanism, and as such are associated with 'surge' deposits. (e.g. Walker, 1983; Valentine, 1987; Branney & Kokelaar, 2002; Brown & Andrews, 2015).

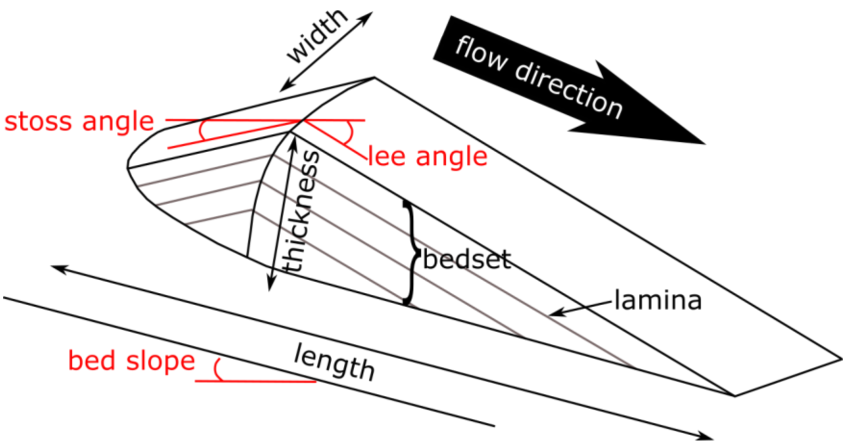

Figure 2.15 Schematic figure of an idealised bedform, with definitions of terminology used in this thesis. Modified from Douillet et al., (2013).

The first worker to examine dune structures in PDC deposits was Moore (1967), in the deposits of the 1965 phreatomagmatic eruption at Taal, Philippines. Examining base surge deposits, they noted that these structures were oriented perpendicular to the surge direction, that they were steeper on their stoss sides than on their lee sides, and that they decreased in wavelength away from the volcano. Fisher and Waters (1969) refer to the characteristics of the 'bed waves' recorded by Moore (1967) and introduce the aqueous term antidune to name them. Antidunes are sediment features formed under supercritical conditions which are in phase with surface waves (standing waves) and typically migrate upstream (Kennedy, 1963). The shared characteristics of the structures at Taal and antidunes include low amplitudes, stoss and lee sides inclined at angles lower than the angle of repose, and steeper stoss-side laminae (Fisher & Waters 1969, 1970). Waters and Fisher (1971) suggested that antidunes seen in surge deposits could also be the result of standing waves, a position taken by Crowe and Fisher (1973), Mattson and Alvarez (1973), and Schmincke et al. (1973). It was thought that these 'antidunes' not only looked like, but were formed in the same manner as their aqueous counterparts, in upper flow regime conditions. This was despite the fact that steep stoss-side structures could be formed in subcritical conditions as well (Allen, 1984), so there was little justification in adopting the aqueous interpretation.

In Allen's (1984) scheme, sand-wave bedforms can be classified as progressive, regressive, or stationary, depending on whether the successive positions of the sand-wave’s crests indicate upstream migration, downstream migration, or no movement. Progressive sand-waves were interpreted as forming from relatively dry and/or hot currents, and regressive sand-waves from relatively wet and cool currents. Cole (1991) uses the progressive etc. qualifiers in describing sand-waves (Fig. 2.16b) but challenges Allen's (1984) assertion that their morphology is a function of temperature and moisture rather than flow conditions. However, dune and antidune continued to be used widely, both in describing bedforms and in interpreting them, up until recently (e.g. Brand & White, 2007; Gençalioğlu-Kuşcu et al., 2007; Brand et al., 2009), resulting in some confusion.

Douillet et al. (2013) provide a brief review of the use of the term ‘antidune’ and why they believe it is inappropriate for the majority of PDC bedforms. They introduce the new interpretative term *regressive climbing dunes* for dune-like bedforms which show upstream crest migration due to sediment fall-out on the stoss side, and which may have been interpreted in the past as antidunes. Brand et al. (2016) adopt similar terminology, using *progressive dune bedforms* and *regressive dune bedforms* (Fig. 2.16c), but still interpret the latter as forming under supercritical flow conditions.

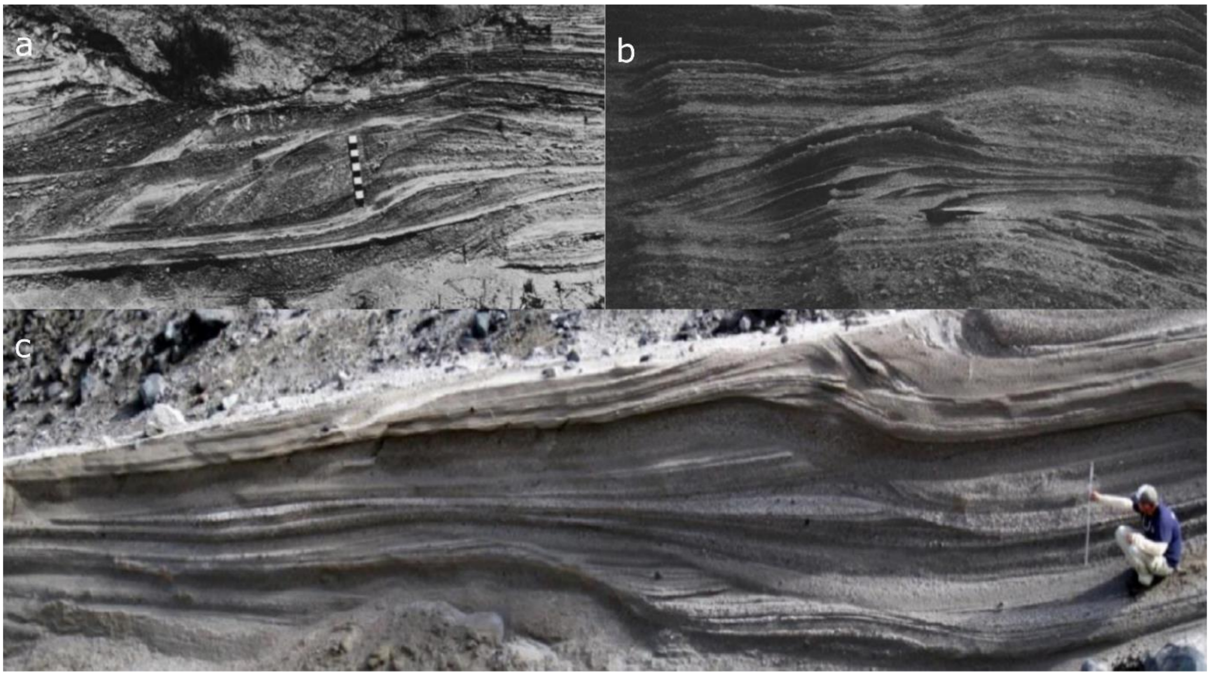

Figure 2.16 Various bedforms in PDC deposits. **a** 'Chute-and-pool' structure at Laacher See, Germany. Flow direction left to right, scale 1 m (Schmincke et al., 1973). **b** 'Type D' regressive sandwave at Sugarloaf Mountain, AZ. Flow direction left to right, trowel is 30 cm (Cole, 1991). **c** 'Regressive dune bedform' in the proximal bedded deposits of Mt St Helens, WA. Flow direction right to left, scale is 1 m (Brand et al., 2016).

Chute-and-pool like structures were first recognised in dilute PDC deposits by Schmincke et al. (1973) (Fig. 2.16a). In non-granular flows, the sudden jump from supercritical to subcritical flow can produce steeply dipping stoss-side bedding (Jopling & Richardson, 1966). As with antidunes, the term chute-and-pool is now rarely used to describe bedforms in PDCs, such features falling instead under terms such as 'regressive dune bedform'.

The wavelengths and amplitudes of dune bedforms in PDC deposits are seen to vary systematically in a deposit, and this has been linked to changes in current conditions. Wavelengths and amplitudes have been observed to decrease in distance away from the crater (e.g. Moore, 1967; Waters & Fisher, 1971; Wohletz & Sheridan, 1979; Sigurdsson et al., 1987; Brand & White, 2007). Their sizes are also affected by underlying topographic slope angle: Moore (1967) notes a decrease in wavelength on uphill slopes, and Brand et al. (2016) record a decrease in wavelength and amplitude of several metres over a slope decrease of 4°.

These observations can be attributed to the loss of velocity as the PDC travels further or decelerates on decreasing slopes; in other words, current energy is the critical factor in determining dune bedform morphology (Brand et al., 2016).

There have been recent attempts at developing quantitative understanding of the conditions under which PDC bedforms are created (Rowley et al., 2011; Pollock et al., 2019; Dellino et al., 2020). Advances in analogue modelling, in particular, are allowing the complex processes which operate in PDCs to be recorded.

2.5 Physical Modelling of PDCs

Physical experiments are an important part of understanding PDC dynamics. Observation of the propagation of PDCs in the field is impractical because of the lack of regular, safe viewing possibilities; and viewing actual depositional processes would be challenging due to the basal zone of PDCs being hidden by the overriding ash cloud. Physical modelling, however, provides a direct way to quantify a number of processes which take place in PDCs under controlled, variable conditions, as well as creating easily accessible deposits which are analogous to their natural counterparts.

2.5.1 Dilute currents

Laboratory experiments investigating the dynamics of PDCs can be subdivided into two broad categories based on the behaviour that is being replicated: dilute or dense. Dilute PDCs were first investigated with the classic lock-exchange technique used for turbidity currents, where liquids of different densities were used for both the current and the ambient fluid (e.g. Huppert & Simpson, 1980; Huppert et al., 1986; Woods & Bursik, 1994). The inclusion of particles in these currents showed that deposition decreased the density of the current and contributed to buoyancy reversal and lift-off (Sparks et al., 1993; Woods & Bursik, 1994). These types of experiment could well investigate how dilute currents responded to both entrainment of ambient fluid and sedimentation of particles but were not direct analogues of PDCs due to the small differences in density and viscosity between the experimental liquids. Other dilute PDC models have involved feeding heated talc powder into a channel via conveyor belt, where it lofts and begins to deposit (Andrews & Manga, 2011, 2012; Andrews, 2014). This configuration uses air as the ambient fluid so is a better representation of dilute PDCs, and results showed that unlike in ambient liquid, entrainment occurred laterally rather than at the flow front, and deposition was unsteady, consisting of cycles of sedimentation and erosion.

2.5.2 Dense currents

Dense granular currents have typically been modelled using a flume tank with either an attached reservoir separated by a lock-gate or a hopper suspended above one end of the tank. Using a hopper allows particles to approach free-fall, simulating PDC generation mechanisms such as column collapse. The reservoir contains particles used to simulate the PDC, which may be actual pyroclastic material (e.g. Girolami et al., 2008, 2010; Sulpizio et al., 2016; Breard & Lube, 2017; Lube et al. 2019) or analogous substitutes such as glass beads (e.g. Roche et al., 2004; Chédeville & Roche, 2014; Rowley et al., 2014; Montserrat et al., 2016). The particles may be fluidised inside the reservoir before been released into the flume, which may be variably inclined, and form a current which deposits along the channel length.

2.5.2.1 Dry granular currents

Experiments on dense granular currents without an interstitial fluid phase have used both dam-break and axisymmetric column collapse configurations (e.g. Lajeunesse et al., 2004; Lube et al., 2004, 2011; Roche et al., 2008; Farin et al., 2014), establishing scaling laws which show that runout distance and flow duration are related to the height of the initial column. Runout is also increased by increased slope angle and entrainment of the substrate (Mangeney et al., 2010; Farin et al., 2014). Currents follow a three-phase span of acceleration, quasi-steady propagation, and deceleration (Delannay et al., 2017). Velocity profiles within the propagating granular currents show that an upper layer shears over a quasi-static region which is represented by an exponential velocity profile (e.g. GDR MiDi, 2004; Lube et al., 2005; Mangeney et al., 2010). On a horizontal substrate, the free surface of the resulting deposit is inclined at close to the angle of repose (Roche et al., 2008).

2.5.2.2 Fluidised granular currents

Although clast interactions are important in dense PDCs, the fluid phase is not negligible and the large (tens of kilometres) runout distances are attributed to high, long lived gas pore pressures and the resulting fluidisation of the current (e.g. Sparks, 1976; Wilson, 1980; Roche, 2012). The gas velocity at which fluidisation occurs is known as the minimum fluidisation velocity, U_{mf}. As velocity increases above this value, expansion of the particle mass occurs until the formation of gas bubbles at the minimum bubbling velocity, U_{mb} (Roche, 2012). Fluidisation may occur naturally in PDCs several ways (see section 2.3.3). Low internal friction in PDCs does not require a continuous source of gas (Branney & Kokelaar, 2002; Roche, 2012), but this can be hard to replicate in a laboratory environment due to fast pore pressure diffusion times at a laboratory scale (Rowley et al., 2014).

Fluidisation of particles in flume experiments occurs when gas is injected vertically into the particle mass. Similar methods have been used in fluidising the particles prior to them being released into the flume. Typically, flume reservoirs are equipped with a basal porous plate that gas is injected through. In most cases air is used to fluidise the particles (e.g. Eames & Gilbertson, 2000; Roche et al., 2004; Girolami et al., 2008; Rowley et al., 2014; Montserrat et al., 2016), however Druitt et al. (2007) used nitrogen to ensure minimal humidity and prevent cohesion of ash. Chédeville and Roche (2014) show that a rough substrate can cause some degree of autofluidisation through the displacement of air in the substrate interstices, with no need for an external gas source.

In dam-break experiments Roche et al. (2008) showed that initially fluidised granular currents acted as fluids if particle diameters were small enough to slow defluidisation; the currents decelerated once pore pressure was not large enough to dampen frictional forces. Similarly to dry currents, for a given degree of fluidisation the runout distance is controlled by initial column height, and fluidised currents follow the same three-phase emplacement process, but reach greater velocities.

At laboratory scales pore pressure diffusion is relatively quick so runout distances are small when compared to natural PDCs (Roche, 2012). Experiments on defluidising mixtures have established pore pressure diffusion timescales of seconds to tens of minutes (Roche, 2012), quicker than that estimated for natural PDCs (minutes to hours, Druitt et al., 2007; Breard et al., 2019). Although fine particle dominance has often been cited as the primary factor in decreasing pore pressure diffusion times, Breard et al. (2019) show that poor sorting (as is typically seen in PDCs) is more important. Initial expansion of the mixture is also an important factor in sustaining pore pressure, as deflation results in an upwards gas flux (Girolami et al., 2008; Breard et al., 2019; Roche & Carazzo, 2019). Rowley et al., (2014) tackle the problem of rapid pore pressure diffusion by using a flume where the entire channel has a basal porous plate. Feeding an air flux through the substrate allows continuous fluidisation of the current rather than just the initial fluidisation of its source. This results in sustained, pulsating currents which through progressive aggradation form deposits thicker than themselves and which contain both progradational and retrogradational surfaces.

2.5.3 Large-scale experiments

In the last fifteen years large-scale simulations of PDCs have become more commonplace. These have the advantage of being comparable in scale to the actual phenomena, but it may be hard to separate out the large amount of processes involved. Initial large-scale experiments by Dellino et al. (2007, 2010) and Sulpizio et al. (2008a) demonstrated that various generation mechanisms (column collapse, fountaining, and an overpressured jet) could be reliably simulated and that the resultant current reproduced PDC transport mechanisms.

More recent large-scale experiments have reproduced PDCs which contain both dilute and dense regimes (e.g. Lube et al., 2015; Breard et al., 2016; Breard & Lube, 2017; Lube et al., 2019). These currents consist of a dilute, turbulent cloud which, through an intermediate zone, is coupled with a dense basal underflow. This basal zone has been found to have a reversed pore pressure gradient due to high shear, reducing friction at the base of the dense underflow (Lube et al., 2019).

2.5.4 Experimental considerations

2.5.4.1 Sidewalls

Sidewalls can affect flow properties due to friction, especially flow thickness and velocity (Jop et al., 2005). For dry granular flows, Jop et al. (2005) showed that flow thickness decreases and velocity increases with decreasing channel width. However simply widening the channel may not get rid of sidewall effects –free surface velocity actually decreases in transverse uniformity with increasing channel width. In experiments by Rowley et al. (2011) vortical features deposited by a dry granular current show different degrees of development with distance from the sidewall.

However other authors believe that sidewall effects are not important in their experiments. Girolami et al. (2008, 2010) show that fluidised granular currents slip against the sidewalls and the effect of basal stress predominates. Similarly, Mangeney et al. (2010) report quasi-linear transverse velocity profiles in dry granular currents, showing minimal sidewall friction. Montserrat et al. (2016) point out that sidewall effects should be reduced at high channel width:particle diameter ratios (dimensionless width, W*). The highest W* examined by Jop et al. (2005) was 570, and the W* in the experiments of Rowley et al. (2011) was 600.

Meanwhile, W* in other analogue PDC experiments has been greater. Roche et al. (2010), Rowley et al. (2014), and Montserrat et al. (2016) had a W* 1333, using a mean particle size of 75 µm and 0.1 m wide flumes. Experiments on fluidised 45-90 µm particles in a 0.08 m wide flume give a W* range of 888-1777 (Roche, 2012). None of these authors reported definite sidewall effects, but this may have also been due to the lubrication effect of high gas pore pressure allowing the current to slip against the walls (Gilbertson et al., 2008).

2.5.4.2 Particle Selection

Experiments can use either synthetic particles or natural ones sampled from PDC deposits. An advantage of using pyroclastic materials is that they possess the same physical characteristics (density, shape) as particles composing natural PDCs, so giving greater confidence when scaling results up to nature (Dellino et al., 2007). However they are by nature poorly sorted and preventing cohesion of fine particles may require extra procedures such as heating, stirring, and removing fines by elutriation (Girolami et al., 2008). Scaling issues will remain, however, in lab-scale experiments, e.g. particle diameter to flow thickness ratios will be greater than in nature. Synthetic particles, on the other hand, are easier to acquire in specific diameters or size distributions, and are readily available in varying densities and colours, allowing more targeted experiments. Furthermore the use of synthetic particles of known shape, density etc. which are easily acquired makes comparisons between the experiments of different authors much simpler. Glass beads are commonly used as they are well-sorted and cohesionless, although other types of particles have been utilised, such as industrial cracking catalysts (Girolami et al., 2015).

Geldart (1973), proposed a classification of fluidised particles based on the effect grain size has on fluidisation behaviour. Group C particles are incredibly fine (<20 µm at particle and gas densities of 2.5 and 1 g/cm^3 respectively) and dominated by cohesion forces. Group A particles are fine (typically 20-150 µm at the above conditions) and undergo homogenous expansion at U_{mf}. Group B and D particles are coarser and undergo heterogeneous expansion and bubble formation at U_{mf} (Roche et al., 2004).

Druitt et al. (2007) showed that ash-rich PDC samples possess Group A properties – negligible cohesion and uniform expansion. In addition, Roche et al. (2004, 2006) showed that initially fluidised flows of Group B and D particles rapidly return to a non-fluidised state, re-establishing grain contacts and non-negligible internal friction. Therefore, studies attempting to simulate fluidised PDCs tend to use particles that belong to Geldart's (1973) Group A in order for homogenous fluidisation to be achieved during experiments.

2.5.4.3 Slope Angle and Topography

PDCs propagate on a range of slopes, from ~30° on the high flanks of volcanoes to subhorizontal (Lube et al., 2007; Chédeville & Roche, 2015; Roche et al., 2016), and breaks in slope are known to effect PDC dynamics and promote deposition (Sulpizio & Dellino, 2008). Farin et al. (2014) found that accepted scaling laws for the runout distance of dry granular currents ceased to be valid after the slope passed a critical angle (between 10 and 16°). Chédeville and Roche (2015) demonstrate that autofluidisation by a rough substrate can occur on slope angles up to at least 30°, which results in an increase of runout distance with slope angle until 10-12°, where the effect is reduced. More complex topographies have also been examined – hydraulic jumps in dilute currents were caused by breaks in slope (Woods & Bursik, 1994). Sulpizio et al. (2016) showed that for dry granular currents, greater breaks in slope decrease velocity and runout distance. Slope analysis has not, however, been looked at for sustained, fluidised granular currents.

Barriers to flow may have different effects depending on the current type. Dilute, warm mixtures of talc powder and air could surmount barriers less than 1.5 times their height, and the barriers caused flow and buoyancy reversals within the current (Andrews & Manga, 2011). Doronzo and Dellino (2011) showed that the impact of a turbulent PDC with a building causes turbulence heterogeneities which result in preferential deposition of coarse particles at the building front. For dry granular currents, experiments by Faug (2015) demonstrated that barriers could produce an upstream-propagating granular bore or a downstream-propagating jet depending on the height of the barrier and the Froude Number of the current.

2.5.4.4 Scaling

Scaling is a common problem when attempting to apply interpretations derived from analogue models to actual natural phenomena. As mentioned in section 2.5.3 some authors minimise scaling issues through carrying out large-scale experiments, but these can be impractical in many cases. In lab-scale experiments especially, then, it is therefore vital to ensure that parameters such as particle diameter and density are appropriate and that the analogues are meaningful. Scaling issues for this work are dealt with separately in each chapter and discussed in the synthesis (section 7.1.1).

2.6 Numerical Modelling

Numerical modelling depends on physical models or fieldwork to provide realistic initial parameters, but then has the advantages of simple scaling to nature and ease of changing variables. Numerical modelling of PDCs is also used in hazard assessment. Although most hazard maps are reliant solely on previous deposits numerical simulations are an important contribution (Calder et al., 2015). Most numerical models of PDCs fall into three categories; the first two correspond to the dilute and concentrated end-members (section 2.2), and the third uses a multiphase approach.

2.6.1 Dilute box-model

This approach assumes a dilute, turbulent current which is well mixed. Work by Bursik and Woods (1996) and Dade and Huppert (1996) applied box-models to several ignimbrite-forming eruptions including Taupo (232 CE) and closely reproduced parameters such as deposit thickness and mass flux. Bursik and Woods (1996) demonstrated that the runout distance of dilute PDCs is controlled by mass flux and the degree of sedimentation and air entrainment. However, these models do not recognise density stratification and therefore are only applicable to very dilute PDCs where there is no great concentration gradient (Dufek et al., 2015).

2.6.2 Depth-averaged dense flow models

Modelling dense PDCs and other granular currents has often used the depth-averaging technique, although a variety of rheologies can be chosen. Depth-averaging is much more appropriate in dense PDCs than dilute because the vertical density variations are much less. Savage and Hutter's (1989) pioneering work showed that the flow of granular currents down a slope could be described by Coulomb friction, an approach which has also been adopted for PDCs (e.g. Kelfoun et al., 2009; Charbonnier & Gertisser, 2012; Faccanoni & Mangeney, 2013). However, Coulomb friction models often need to use smaller basal friction angles than expected (Kelfoun et al., 2009; Charbonnier & Gertisser, 2012; Dufek, 2016). Despite Hayashi and Self (1992) concluding that there was no need to invoke a friction-reduction mechanism specific to PDCs, it is likely that this is caused by processes such as fluidisation, commonly invoked in explaining PDC mobility (section 2.3.3). Indeed, a depth-averaged Coulomb friction model modified to account for high pore pressures has given good results (Gueugneau et al., 2017). However, although the use of Coulomb friction models is widespread, plastic models have reproduced behaviour not replicable by friction models –

Kelfoun (2011) and Gueugneau et al. (2019) show that using a plastic rheology better reproduces PDC deposit architecture, particularly on steeper slopes.

2.6.3 Multiphase models

The most complex numerical models involve solving different equations for different phases, and capture the variety of interactions between the gas and particle phases as well as the complexity of the internal structure of PDCs. These models were first applied to PDCs by Valentine and Wohletz (1989), whose simulated PDCs showed good comparisons with existing analogue models of gravity currents. Multiphase simulations have been used to model the interaction of PDCs with buildings (Doronzo & Dellino, 2011), as well as reproducing the dynamics of the Mt St Helens lateral blast (Esposti Ongaro et al., 2012) and examining the formation of PDCs by column collapse (Valentine & Sweeney, 2018). Multiphase models use huge amounts of computational power, and are considered non-optimal for probabilistic hazard assessment (Lube et al., 2020).

2.7 Summary

Despite a great many advances PDCs are still poorly understood compared to many other geophysical mass flows. In the past two decades the role of high gas pore pressure in dense PDCs has been investigated in analogue experiments, but in most cases fluidisation of the current has been very short-lived due to rapid pore pressure diffusion. The flow-boundary zone concept is widely applied by physical volcanologists in the interpretation of PDC deposits, but is overlooked in experimental work. Indeed, although experiments are now replicating many of the processes inferred to operate inside PDCs, there is very little work on how flow dynamics are recorded in experimental deposits, particularly at a lab scale. It has been shown that deposits with complex internal surfaces can be formed by sustained fluidisation of granular currents, but as PDCs are intrinsically heterogeneous can this be replicated by variably fluidised currents? If so, it is also critically important to determine that the experimental sedimentary structures are valid analogues of actual PDC bedforms. The subsequent chapters present the results of experiments built around the research questions given in section 1.4 with the aim of providing a quantifiable link between PDC flow behaviour and deposit characteristics.

==

Chapter 3

3. Investigation of variable aeration of monodisperse mixtures: implications for Pyroclastic Density Currents

==

The high mobility of dense pyroclastic density currents (PDCs) is commonly attributed to high gas pore pressures. However, the influence of spatial and temporal variations in pore pressure within PDCs has yet to be investigated. Theory suggests that variability in the fluidisation and aeration of a current will have a significant control on PDC flow and deposition. In this study, the effect of spatially heterogeneous gas pore pressures in experimental PDCs was investigated. Sustained, unsteady granular currents were released into a flume channel where the injection of gas through the channel base was controlled to create spatial variations in aeration. Maximum current front velocity results from high degrees of aeration proximal to the source, rather than lower sustained aeration along the whole flume channel. However, moderate aeration (i.e. ~0.5 minimum static fluidisation velocity (U_{mf_st})) sustained throughout the propagation length of a current results in greater runout distances than currents which are closer to fluidisation (i.e. 0.9 U_{mf_st}) near to source, then de-aerating distally. Additionally, although all aerated currents are sensitive to channel base slope angle, the runout distance of those currents where aeration is sustained throughout their lengths increase by up to 54% with an increase of slope from 2° to 4°. Deposit morphologies are primarily controlled by the spatial differences in aeration; where there is large decrease in aeration the current forms a thick depositional wedge. Sustained gas-aerated granular currents are observed to be spontaneously unsteady, with internal sediment waves travelling at different velocities.

3.1 Introduction

Pyroclastic Density Currents (PDCs) are hazardous flows of hot, density driven mixtures of gas and volcanic particles generated during explosive volcanic eruptions, or from the collapse of lava domes (e.g. Yamamoto et al., 1993; Branney & Kokelaar, 2002; Cas et al., 2011). They are capable of depositing large ignimbrite sheets, which can exhibit a variety of sedimentary structures and grading patterns (e.g. Rowley, 1985; Wilson, 1985; Fierstein & Hildreth, 1992; Branney & Kokelaar, 2002; Brown & Branney, 2004a; Sarocchi et al., 2011; Douillet et al., 2013; Brand et al., 2016). As evidenced by the occurrence of these deposits far from sources, PDCs can achieve long runout distances on slopes shallower than the angle of rest of granular materials, even at low volumes (e.g. Druitt et al., 2002; Cas et al., 2011; Roche et al., 2016). Explanations for these long runout distances vary according to whether the current in question is envisaged as dilute or dense (cf. Dade & Huppert, 1996; Wilson, 1997). PDC transport encompasses a spectrum whose end-members can be defined as either fully dilute or granular-fluid currents (Walker, 1983; Druitt, 1992; Branney & Kokelaar, 2002; Burgissier & Bergantz, 2002; Breard & Lube, 2017). In the first type, clast interactions are negligible, and support and transport of the pyroclasts is dominated by fluid turbulence at all levels in the current (Andrews & Manga, 2011, 2012). In contrast, in highly concentrated granular-fluid based currents, particle interactions are important and turbulence is dampened (e.g. Savage & Hutter, 1989; Iverson, 1997; Branney & Kokelaar, 2002). Here, the differential motion between the interstitial gas and solid particles is able to generate pore fluid pressure due to the relatively low permeability of the gas-particle mixture (Druitt et al., 2007; Montserrat et al., 2012; Roche, 2012). An intermediate regime has also recently been defined, characterised by mesoscale turbulence clusters (Breard et al., 2016), which couple the dilute and dense regions of a PDC.

Where dense PDCs are concerned, their high mobility is commonly attributed to the influence of fluidisation of the current’s particles caused by high, long-lived gas pore pressures (Sparks, 1976; Wilson, 1980; Druitt et al., 2007; Roche, 2012; Gueugneau et al., 2017; Breard et al., 2018). These high gas pore pressures fundamentally result from relative motion between settling particles and ascending fluid, and can be produced through various processes including (i) bulk self-fluidisation (McTaggart, 1960; Wilson & Walker, 1982); (ii) grain self-fluidisation (Fenner, 1923; Brown, 1962; Sparks, 1978); (iii) sedimentation fluidisation/hindered settling (Druitt, 1995; Chédeville & Roche, 2014); and (iv) decompression fluidisation (Druitt & Sparks, 1982); see Wilson (1980) and Branney and Kokelaar (2002) for reviews.

As gas pore pressures within a gas-particle mixture increase, inter-particle stresses are reduced as the particles become fluidised (Gibilaro et al., 2007; Roche et al., 2010). Fluidisation of a granular material is defined as the condition where a vertical drag force exerted by a gas flux is strong enough to support the weight of the particles, resulting in apparent friction reduction and fluid-like behaviour (Druitt et al., 2007; Gilbertson et al., 2008). The gas velocity at which this occurs is known as the minimum fluidisation velocity (U_{mf}). Where there is a gas flux through a sediment which is less than U_{mf}, then that sediment is partially-fluidised and is often termed aerated.

The gas pore pressure decreases over time during flow, once there is little or no relative gas-particle motion, according to:

$$\mathrm{t}_d \propto \mathrm{H}^2/D \qquad \text{(Eq. 3.1)}$$

where H is the bed height and D is the diffusion coefficient of the gas (Roche 2012). PDCs are dominated by finer-grained particles, which confer a greater surface area than coarse particles, conveying low mixture permeability (Druitt et al., 2007; Roche, 2012). PDCs are therefore thought to sustain high pore pressures for longer, resulting in greater mobility than their unfluidized ‘dry’ granular counterparts (i.e. rockfalls).

The detailed fluid dynamics and processes involved with pore pressure in PDCs are elusive due to the significant challenge of obtaining measurements. Moreover, the observation of depositional processes is challenging as the basal parts of PDCs are hidden by an overriding ash cloud. Scaled, physical modelling can provide a direct way to simulate and quantify the behaviour of several processes which take place in PDCs under controlled, variable conditions, as well as creating easily accessible analogous deposits.

Dam break-type experimental current aimed at representing simplified, uniformly permeable, dense PDCs have attempted to model fluidisation processes by fluidising particles before release into a flume (Roche et al., 2002; Roche et al., 2004). These demonstrate that fluidisation has an important effect on runout distance. However, rapid pore pressure diffusion results in shorter runout distances and thinner deposits than might be expected in full scale currents (e.g. Roche et al., 2004; Girolami et al., 2008; Roche et al., 2010; Roche 2012; Montserrat et al., 2016). This is because while the material permeability in both natural and experimental currents is similar (with experimental currents being somewhat fines depleted in comparison to natural PDCs), experimental currents are much thinner than their natural counterparts, resulting in more rapid loss of pore pressure. Experiments have demonstrated that the degree of fluidisation is also important in contributing to substrate entrainment and the resulting transport capacity of fluidised currents (Roche et al., 2013). Early work on the sustained fluidisation of granular currents by injection of air at the base of the current (Eames and Gilbertson, 2000) was not focused on replicating the behaviour of PDCs in particular, but did demonstrate that this was a valid method of preventing rapid pore pressure diffusion in granular currents. Rowley et al. (2014) reproduced the long-lived high gas pore pressures of sustained PDCs using an experimental flume which fed a gas flux through a porous basal plate to simulate long pore pressure diffusion timescales in natural, thicker currents. This resulted in much greater runout distances than unaerated or initially fluidised currents. However, these experiments were unable to explore defluidisation due to the constant uniform gas supply along the flume length.

Natural PDCs are unlikely to be homogenously aerated (Gueugneau et al., 2017) and are inherently heterogeneous due to factors such as source unsteadiness and segregation of particles (Branney & Kokelaar, 2002), which can cause spatial variability in factors controlling U_{mf}, such as bulk density. Hence, different pore pressure generation mechanisms may be operating in different areas of the PDC at once. For example, fluidisation due to the exsolution of volatiles from juvenile clasts (Sparks, 1978; Wilson, 1980) could be dominant in one part of the PDC and fluidisation from hindered settling of depositing particles (Druitt, 1995; Girolami et al., 2008) or autofluidisation from particles settling into substrate interstices (Chédeville & Roche, 2014) dominant in another. It is important, then, to understand the impacts of variable fluidisation on such currents.

Here we present experiments using a flume tank which we set up to investigate the effect of spatially variable aeration on a sustained granular current at different slope angles. The flume allows the simulation of various pore pressures and states of aeration in the same current down the channel. This allows the currents to stabilise and propagate for a controlled distance before de-aeration occurs. We report how this spatially variable aeration, as well as the channel slope angle, affects the current runout distance, frontal velocity, and characteristics of the subsequent deposit. It should be noted that our work attempts to simulate the fact that PDCs are fluidised/aerated to some degree for long periods of time, rather than attempting to replicate a particular mechanism of fluidisation.

3.2 Methods

The experimental flume is shown in Fig. 3.1. A hopper supplies the particles to a 0.15 m wide, 3.0 m long channel through a horizontal lock gate 0.64 m above the channel base. The base of the flume sits above three 1.0 m long chambers, each with an independently controlled compressed air supply, which feeds into the flume through a porous plate. The flume channel can be tilted up to 10 degrees from horizontal.

The air-supply plumbing allows a gas flux to be fed through the base of the flume, producing sustained aeration of the current. In such thin (<30 mm), rapidly degassing laboratory currents this enables us to simulate the long-lived high gas pore pressures that characterize thicker PDCs (Rowley et al., 2014). An important aspect of this flume is that the gas flux for each of the three chambers may be controlled individually, allowing the simulation of spatially variable magnitudes of pore pressures.

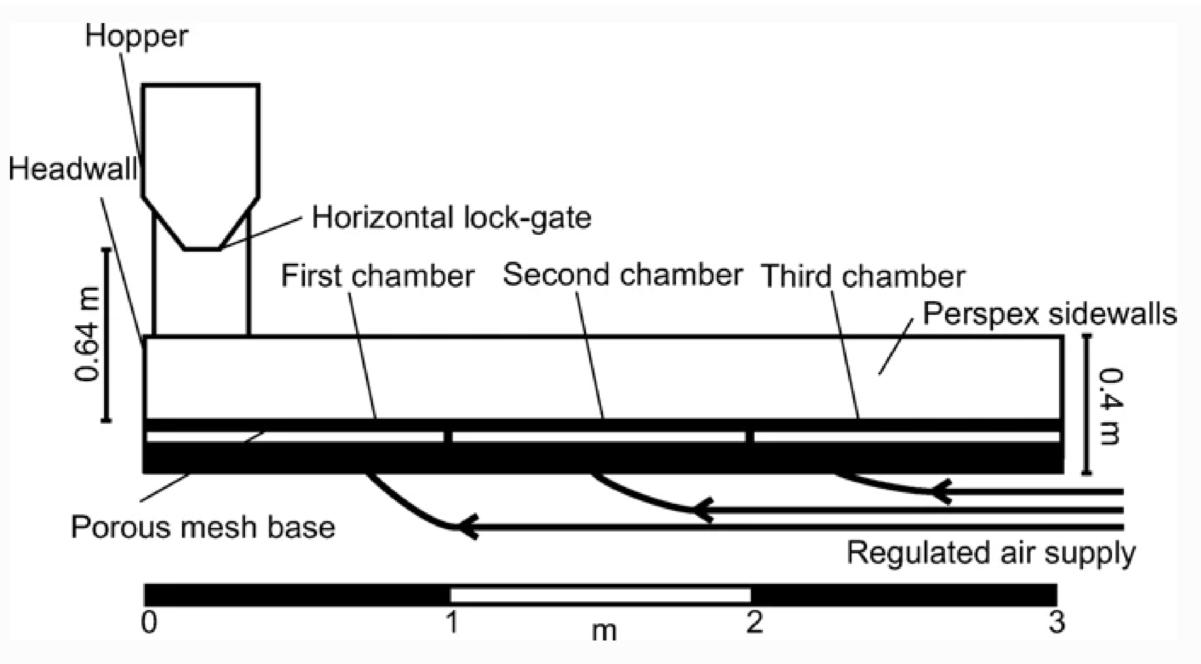

Figure 3.1 A longitudinal section view of the experimental flume.

The experiments were performed using spherical soda lime ballotini with grain sizes of 45-90 μm (average δ_{32} = 63.4 μm calculated from six samples across the material batch, see Supplementary Table A.1 in Appendix A for grain size information), similar to the type of particles used in previous experimental granular currents (e.g. Roche et al., 2004; Rowley et al., 2014; Montserrat et al., 2016). δ_{32}, or the Sauter mean diameter, can be expressed as

$$\delta_{32} = \frac{1}{\Sigma \frac{x_i}{\delta_i}} \qquad \text{(Eq. 3.2)}$$

where x_i is the weight fraction of particles of size δ_i. In line with Breard et al. (2018), δ_{32} was given here because it exerts some control on current permeability (Li & Ma, 2011).

These grain sizes assign the ballotini to Group A of Geldart (1973), which are those materials which expand homogenously above U_{mf} until bubbles form. As PDCs contain dominantly Group A particles, this allows dynamic similarity between the natural and experimental currents (Roche, 2012). Ballotini grains have a stated solid density of 2500 kg/m^3 and a repose angle measured by shear box to be 26°.

The experiments were recorded using high-speed video at 200 frames per second. This video recorded a side-wall area of the channel across the first and second chambers, allowing the calculation of variations in the current front velocity. Velocities were calculated at 0.1 m intervals, from high-speed video which recorded the currents across a section of the flume from 0.8 to 1.7 m. All runout measurements are given as a distance from the headwall of the flume.

The variables experimentally controlled, and thus investigated, in these experiments are: (i) the gas flux supplied through the base in each of the three sections of the channel, and (ii) the slope angle of the channel. The slope angles examined were 2° and 4°. A range of gas supply velocities were used to vary the aeration state of the particles, all of which were below U_{mf} as complete fluidisation would result in non-deposition. Static piles of particles used in these experiments achieve static minimum fluidisation (U_{mf_st}) with a vertical gas velocity of 0.83 cm/s. This is comparable to Roche (2012), who used the same 45-90 μm glass ballotini. Because our fluidisation state was measured in a static pile, we explicitly use U_{mf_st} rather than

U_{mf} in order to denote the origin of this value in these experiments. In a moving (i.e. shearing) current U_{mf} will be higher than U_{mf_st} because dilatancy would be anticipated, and therefore an increase in porosity should be observed.

Aeration states were varied from 0 cm/s (non-aerated) through various levels of aeration to a maximum of 0.77 cm/s. Table 3.1 shows the gas velocities used as a proportion of U_{mf_st} across the experimental set. The mass of particles comprising the currents (the "charge") was kept constant, at 10 kg for each run.

Table 3.1 Conversion of gas velocities used in the experiments into proportions of U_{mf_st} (0.83 cm/s).

Proportion of U_{mf_st}	Gas velocity (cm/s)
1.00	0.83
0.93	0.77
0.66	0.55
0.53	0.44
0.46	0.38
0.4	0.33

3.3 Results

3.3.1 Runout distance and current front velocity

Runout distance is markedly affected by variations in the aeration states. For a given slope angle, if the aeration states are the same in all three chambers, then increasing the gas flux causes runout distances to increase. The measurable limit for runout distance in these experiments is 3 m (i.e. when the current exits the flume) (Fig. 3.2). In this work, when describing the aeration state of the flume as a whole, the gas velocities of each chamber are listed as proportions of U_{mf_st}, in increasing distance from the headwall. For example, an aeration state of 0.93-0.93-0 means that the first two chambers are aerated at 0.93 U_{mf_st} and the third chamber is unaerated.

Where aeration state is decreased along the length of the flume, greater runout distances are still correlated with greater aeration states. At a high aeration state in the first chamber behaviour of the current is dependent on the aeration state in the second chamber. For example, Fig. 3.2 demonstrates how 0.93-0.93-0 U_{mf_st} currents have greater runout distances than 0.93-0.66-0 U_{mf_st} currents which in turn have greater runout distances than 0.93-0-0 U_{mf_st} currents. At a lower aeration state in the first chamber the runout distance seems to be dependent on the aeration state in the third chamber. For example, in Fig. 3.2 0.66-0.53-0.4 U_{mf_st} currents have greater runout distances than 0.66-0.66-0 U_{mf_st} currents and 0.53-0.4-0.4 U_{mf_st} currents have greater runout distances than 0.53-0.53-0 U_{mf_st} currents.

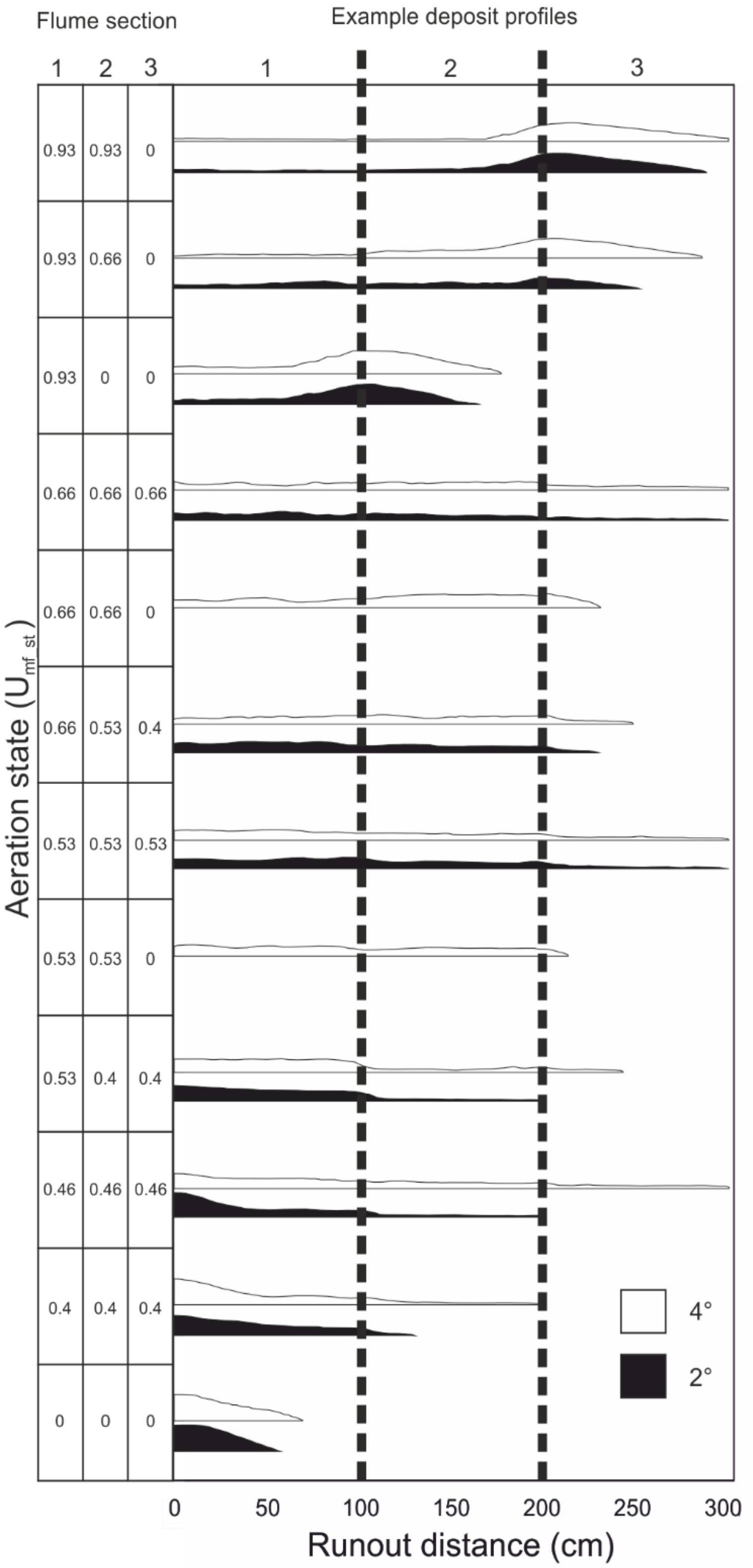

Figure 3.2 Runout distances for various aeration states on different slope angles. Results are shown as profiles of the actual deposits formed. Aeration states of the three chambers are given on the y-axis. Dividing lines show the transition points between the three chambers. Flume length is 300 cm. Vertical scale = horizontal scale.

The current front velocity is also dependent on the aeration state. Current front velocity does not exceed 1.5 m/s (Fig. 3.3). This is considerably less than the calculated free fall velocity $(2gh)^{1/2}$ = 3.5 m/s, where g is gravitational acceleration and h is the 0.64 m drop height, however by the interval at which velocity is measured the currents have travelled 0.8 m and will also have lost energy upon impingement. Generally, regardless of the aeration state in the first or second chamber, the current front velocity decreases over the measured interval (Fig. 3.3). Higher aeration states, however, sustain higher current front velocities across greater distances. Also, where the aeration state decreases from the first chamber into the second, the current front velocity is not always immediately affected, and may even temporarily increase (Fig. 3.3). Overall, the highest current front velocities across the whole 0.9 m interval are always found in the 0.93-0.93-0 U_{mf_st} aeration state.

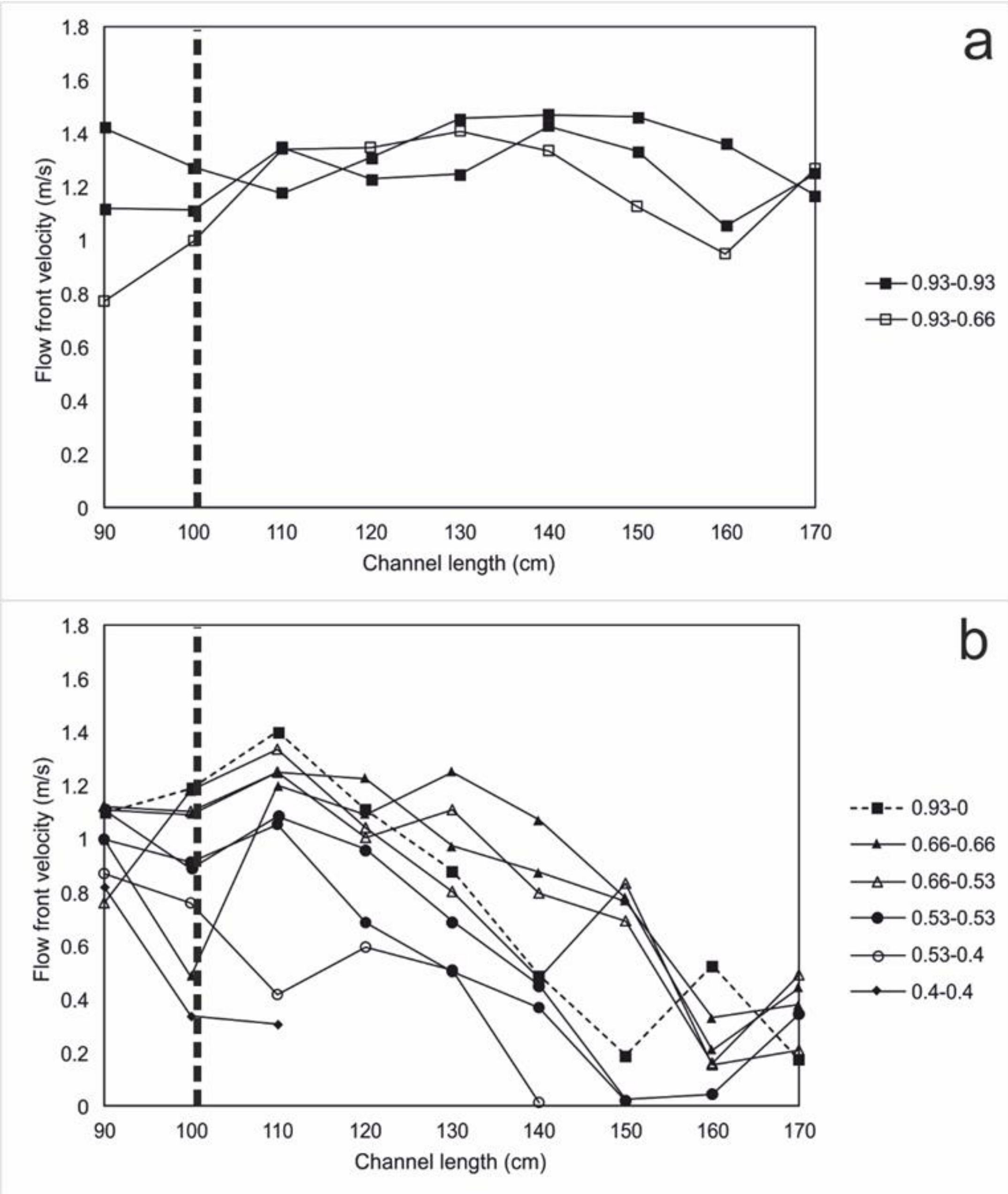

Figure 3.3 Plots showing front velocity as each current propagates past the distance intervals 0.8-1.7 m, on a 4° channel slope. Note that where a profile stops on the x-axis this does not necessarily mean the current has halted; in some cases it represents where the current front has become too thin to accurately track. Dividing line shows the transition between the first and second chambers along the flume. The aeration states (in U_{mf_st}) of a current in the first two chambers are given in the legend. **a** plots for currents which experience a high and uniform, or near-uniform, gas supply from chamber 1 into chamber 2, whereas **b** plots results for currents which experience a low and uniform gas supply, or a lower gas supply into chamber 2 than chamber 1, which encourages de-aeration.

3.3.2 Slope angle and runout distance

For a given aeration state, increasing the slope angle acts to increase the runout distance of the current (Fig. 3.2). However, the magnitude of the increase is dependent on the overall aeration state of the current; large increases in runout distance from increased slope angle only occur where the current is uniformly aerated or there is a small decrease in gas flux between chambers. For example, as slope increases from 2 to 4° 0.4-0.4-0.4 U_{mf_st}, 0.46-0.46-0.46 U_{mf_st}, and 0.53-0.4-0.4 U_{mf_st} currents see increases in runout distances from 1.3 m to 2 m (54%), 2 to 3+ m (≥50%), and 2 m to 2.43 m (22%) respectively. Whether this is also the case for higher and uniformly aerated states (0.53-0.53-0.53 U_{mf_st} and 0.66-0.66-0.66 U_{mf_st}) is not clear as here both slope angles resulted in maximum current runout (i.e. 3+ m).

The effect of increasing slope angle on increasing runout distance is subdued when currents are allowed to de-aerate more quickly. For example, currents of 0.93-0.66-0 U_{mf_st} conditions only experience a runout increase from 2.53 m to 2.86 m (13%) as slope increases from 2 to 4°, while 0.93-0-0 U_{mf_st} conditions undergo increases of 2.88 m to 3+ m (≥6%). Slope angle is thus a secondary control on runout distance compared to aeration state. Only in one condition (-0.4-0.4-0.4 U_{mf_st}) does increasing the slope from 2 to 4° increase the runout distance by more than 50% (1.3 m to 2 m), whereas on a 2° slope, increasing aeration from zero to just 0.4-0.4-0.4 U_{mf_st} results in a 120% increase in runout distance (0.59 m to 1.3 m). Increasing this to the maximum aeration state used, 0.93-0.93-0 U_{mf_st}, gives a further increase in runout distance of 122% (1.3 m to 2.88 m).

3.3.3 Current behaviour and deposition

Regardless of aeration state, all of the experimental currents appear unsteady. This is manifested in the transport of the particles as a series of pulses. Pulses are not always laterally continuous down current, where slower, thinner pulses at the current front are overtaken by faster, thicker pulses. This can partly be seen in the waxing and waning of the velocity profiles in Fig. 3.3; some of the fluctuations in current front velocity are caused by a faster current pulse reaching the front of the current (Fig. 3.4). However, in most cases overtaking of the flow front by a pulse happens outside the area of the high-speed camera, and appears to be triggered by the current front slowing as it transitions into a less aerated chamber.

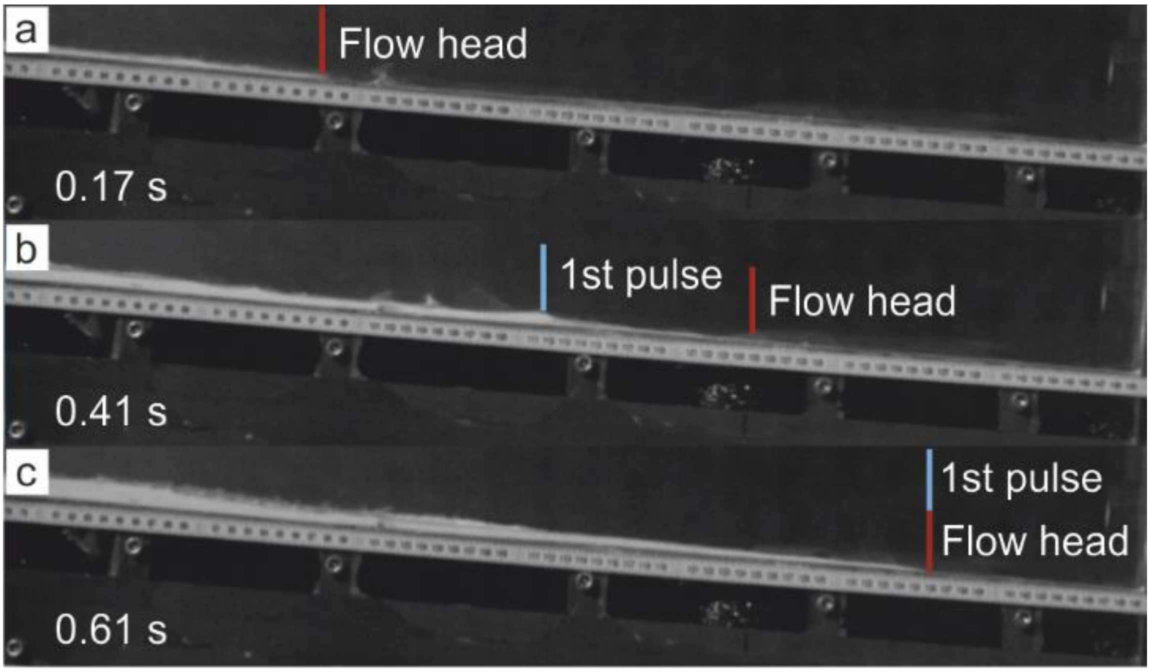

Figure 3.4 High-speed video frames of an experimental current on a 4° slope under 0.93-0-0 U_{mf_st} conditions (**Fig. 3.2**). Numbers on left are time in seconds since the current front entered the frame. **a** The front of the current enters the frame. **b** The current front continues to run out as the first pulse catches and begins to override it. **c** The current front is completely overtaken by the first pulse. A video of this experiment is presented in Online Resource A.1 (Appendix A).

There appears to be five different groups of deposit morphology types generated by the various combinations of aeration states and slope angles (Table 3.2):

- *Large aeration decrease* - In cases where the current front passes into an unaerated chamber from a chamber that is aerated at 0.93 U_{mf_st}, the resulting deposit is mostly confined to the unaerated chamber and has a wedge shape, with its thickest point being at the transition between the highly aerated and completely unaerated chambers. Such behaviour is also seen in the aeration state 0.93-0.66-0 U_{mf_st}, and most clearly on a 4° slope.

- *Uniform aeration* - Where all three chambers are aerated at 0.53 U_{mf_st} or more, the current reaches the end of the flume. Except for currents passing through all chambers at 0.66 U_{mf_st}, the currents forming these deposits experience stalling of the current front, which then progresses at a much slower velocity while local thickening along the body of the current results in deposition upstream. The section of the deposit in the third chamber is usually noticeably thinner than in the first two chambers, which tends to be of an even thickness. Such deposits are also formed by 0.46-0.46-0.46 U_{mf_st} currents on a 4° slope.
- *Moderate – low aeration decrease* - Where the gas fluxes in the first two chambers are at 0.66 U_{mf_st} or 0.53 U_{mf_st}, but there is no (or low) flux in the third, the deposits formed are of approximately even thicknesses, with their leading edges inside the third chamber. This group also includes deposits formed under 0.93-0.66-0 U_{mf_st} conditions on a 2° slope.
- *Low uniform aeration* - Where the second and third chambers are aerated at 0.46 U_{mf_st} or less, and the first chamber is at no more than 0.53 U_{mf_st}, deposits with a centre of mass located inside the first chamber form. Beyond this the deposit thicknesses decreases rapidly.
- *Unaerated* - Under no aeration whatsoever, deposits form flat-topped wedges. These show angles steeper than the wedges in other groups.

Table 3.2 Groups of deposit types and the aeration states and slope angles which form them.

Deposit population	**Flow conditions**	**Aeration State (*U_{mf_st}*)**	**Example profile**
Thick downstream wedge	Large aeration decrease	0.93-0.93-0 0.93-0-0 0.93-0.66-0 (4°)	
Even thickness but thin in third chamber	Uniform aeration	0.66-0.66-0.66 0.53-0.53-0.53 0.46-0.46-0.46 (4°)	
Even thickness	Moderate – low aeration decrease	0.93-0.66-0 (2°) 0.66-0.66-0 0.53-0.53-0 0.66-0.53-0.4	
Centre of mass inside first chamber	Low uniform aeration	0.53-0.4-0.4 0.4-0.4-0.4 0.46-0.46-0.46 (2°)	
Flat-topped wedge	Unaerated	0-0-0	

3.4 Discussion

3.4.1 Runout distance

Once the current is fluidised or aerated it is able to travel further than dry granular currents, as seen in previous experiments (e.g. Roche et al., 2004; Girolami et al., 2008; Roche, 2012; Chédeville & Roche, 2014; Rowley et al., 2014; Montserrat et al., 2016). This is because the increased pore pressures reduce frictional forces between the particles in the current, thus increasing mobility. However, here we find that the relationship between aeration state and runout distance is not a simple correlation between higher gas fluxes and greater runout distances. A current with high initial aeration rates followed by a rapid decline does not travel as far as a current that is moderately aerated across a greater distance. For example, a current run with 0.93-0-0 U_{mf_st} conditions does not travel as far as runs with conditions set at 0.66-0.66-0.66 U_{mf_st} or 0.53-0.53-0.53 U_{mf_st} (Fig. 3.2).

A highly aerated current may continue for some distance after passing into an unaerated chamber. Where only the first two chambers are aerated, this distance is dependent on the magnitude of the aeration state of the first chamber. For example, a current under 0.93-0.66-0 U_{mf_st} conditions travels up to 24% further than one under 0.66-0.66-0 U_{mf_st} conditions, but a current under 0.93-0.93-0 U_{mf_st} conditions only travels up to 14% further than one under 0.93-0.66-0 U_{mf_st} conditions. However, a current that is moderately aerated for its entire passage can travel at least as far as those which are initially highly aerated. This is a result of the high pore pressures being sustained across a greater portion of the current, simulating the long-lived high pore pressures of much thicker natural PDCs. Where a current passes into an unaerated chamber, the pore pressure diffusion time is dependent on the current thickness, current permeability, and the present pore pressure magnitude. As many current fronts are of similar thickness when they pass into an unaerated chamber, de-aeration seems to be controlled largely by the aeration state of the chambers prior to the unaerated one. A current with a lower aeration state will reach a completely de-aerated state and halt sooner than a current with a higher aeration state. This has implications for both runout distance and deposit characteristics.

3.4.2 Velocity

Higher initial gas velocities sustain higher current front velocities for greater distances, as seen in Figure 3.3, where the 0.93-0.93-0 U_{mf_st} and 0.93-0.66-0 U_{mf_st} current velocity profiles sustain current front velocities of >1 m/s across the measured interval, in contrast to the other aeration states, where current front velocities rapidly fall below 1 m/s. High gas fluxes sustain high pore pressures, decreasing frictional forces between particles, reducing deceleration relative to less aerated currents. As the rate of pore pressure diffusion becomes greater than the supply of new gas to the current it undergoes an increase in internal frictional forces and a consequent decrease in velocity.

When a current crosses into a chamber with a lower aeration state, this results in the lowering of its current front velocity (Fig. 3.3), although this change does not immediately take place and the current front may even accelerate as it crosses the boundary (as seen in many profiles in Fig. 3.3). The only currents which immediately decelerate in all cases are those where the aeration state of both chambers is 0.53 U_{mf_st} or less. The temporary acceleration seen in the other currents mostly occurs over a distance of ~10 cm. Over this distance, these currents have sufficient momentum that the decreasing gas velocity and consequent increase in internal frictional forces does not immediately take effect. This is in line with our knowledge of pore pressure diffusion in PDCs—mostly composed of fine ash. In such cases the pore pressure does not instantly diffuse due to the low permeability of the material (Druitt et al., 2007). In our experimental currents, passing into a lower or non-aerated chamber does not cause the current to immediately lose pore pressure (Fig. 3.3), but the magnitude of the difference in gas velocities between the chambers does influence the depositional behaviour of the current.

3.4.3 The influence of slope angle

The effects of slope angle on both dam-break type initially fluidised (Chédeville & Roche, 2015) and dry granular currents (Farin et al., 2014) are relatively well known. However, the influence of varying slope angle for currents possessing sustained pore pressures is largely unquantified. Although only two (2° and 4°) slope angles were examined, there is a clear effect on both current runout distance and current front velocity. Runout distance may be increased by up to 50% and higher current front velocities are sustained for greater distances on a steeper slope. The influence of small changes of slope on PDC dynamics is important because in nature low slope angles can be associated with PDC runout distances >100 km (Valentine et al., 1989; Wilson et al., 1995).

The effect of slope angle on runout distance is most apparent when aeration is sustained over the whole current. Where the current front comes to a halt in an unaerated chamber, the runout distance increases no more than 13% on a 4° slope compared to a 2° slope. However, the overall effect of slope angle on the runout distance of sustained, moderate-to-highly aerated currents is difficult to quantify using our flume as such runs commonly move out of the flume.

3.4.4 Propagation and deposit formation

These experimental currents travel as a series of pulses generated by inherent unsteadiness developed during current propagation. Froude numbers ($Fr = \frac{U}{(gH)^{\frac{1}{2}}}$ where U is current front or pulse velocity) were determined for a number of current fronts and pulses by plotting the current front or pulse velocity as a function of $(gH)^{\frac{1}{2}}$ (Fig. 3.5). The slope of line of best fit gives Fr = 7, which fits with anticipated supercritical flow conditions (Gray et al., 2003). This is higher that the Fr of 2.58 obtained by Roche et al. (2004), likely due to the higher energy initiation and sustained nature of our currents compared to the depletive, dam-break currents of Roche et al. (2004).

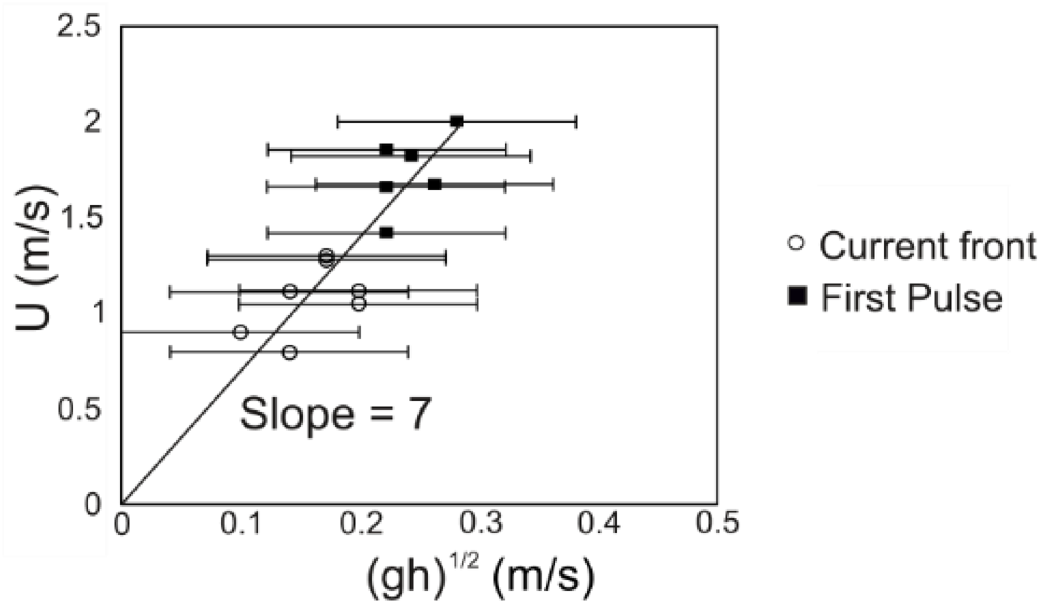

Figure 3.5 Froude number for the fronts and first pulses of selected experimental currents. Uncertainties in velocity are smaller than the size of the symbols. Uncertainties in current height are relatively large due to the thinness of the current fronts relative to video resolution.

The currents form a range of depositional structures depending on the flow dynamics and can deposit, through aggradation, much thicker deposits than the currents themselves. Our observations that the currents are both unsteady and can consist of a series of pulses suggests that deposition is occurring by stepwise aggradation (Branney & Kokelaar, 1992; Sulpizio and Dellino, 2008). The deposits produced in the experiments form five different groups; from which the following three important observations can be made: First, where the current front moves from an aerated chamber into an unaerated one, the shape and thickness of the deposit appears to depend on the magnitude of the drop in aeration state. Where the drop is high (0.93 U_{mf_st} and 0.66 U_{mf_st} to unaerated), a thick (~ x 10 current thickness) wedge forms downstream, thickening mainly through retrogradational deposition as the high aeration states of the first two chambers quickly deliver the current body into the growing wedge. Second, sustained flow can build a deposit of relatively even thickness behind a stalling current front as inferred by Williams et al. (2014). Third, flat-topped wedges form where currents are dry and runout distance is therefore affected only by channel slope angle. Overall, these observations suggest that a decrease in aeration state may be an important control on deposit formation, character, and distribution. These experiments provide a first attempt to directly control de-aeration in dense granular PDC analogues, and greatly simplify the system, providing three relatively uniformly aerated segments of flow. This is in contrast to the high degree of spatial and temporal variation that might be envisaged in PDCs, and the more gradual degassing a natural current will experience. We stress that the de-aeration rates observed in these experiments are faster than we would anticipate in natural PDCs; the sustained gas pore pressure provided here is applied so as to overcome the very rapid pore pressure diffusion timescales found in laboratory flows (Druitt et al., 2007; Rowley et al., 2014). This is due to the similarity of their bulk grainsize to the ash found in PDCs, but much thinner flow thicknesses and hence more rapid pore pressure diffusion. Nevertheless, the decreases in aeration observed in some of our experimental flows have relevance for PDCs which may experience, for example, a loss of fines or undergo temperature drops, thinning, and/or the entrainment of coarser material, all of which would act to de-aerate the current (e.g. Bareschino et al., 2007; Druitt et al., 2007; Gueugneau et al., 2017).

3.4.5 Implications for future work

We have demonstrated that variable aeration states in conjunction with slope angle can affect the shape and location of an experimental current's deposit. It seems logical to assume that these different types of deposit aggrade differently and so have different internal architectures, which may be analogous to features seen in ignimbrites. However, the internal architectures of these experimental deposits are hidden due to the uniform colour and grain size of the particles used. In future work, the use of dyed particles or particles of a different size would help identify the internal features of these deposits.

3.5 Conclusions

These experiments examined granular currents emplaced along inclined slopes which possessed long-lived pore pressures under two conditions: (1) pore pressures which decreased down-current, and (2) pore pressures which were uniform throughout the current. The flume configuration allowed the simulation of different aeration states within the currents, in order to simulate the dynamics and heterogeneous nature of pore pressure in pyroclastic density currents. We examined the effects of varying combinations of aeration states, as well as the effect of slope angle on flow field dynamics and deposit characteristics.

It is clear that, in a general sense, higher gas fluxes (i.e. higher pore pressures) in the flume chambers result in greater runout distances. However, moderate (0.53 U_{mf_st} – 0.66 U_{mf_st}) sustained gas fluxes produce at least equal runouts to high (0.93 U_{mf_st}) initial fluxes that are subsequently declined. Similarly, high fluxes sustain higher current front velocities for greater distances, and currents may travel for 0.1 m – 0.2 m after experiencing a decrease in gas flux supplied to their base before undergoing the consequent decrease in current front velocity.

Slope angle variation between 2° and 4° has a measurable impact on current runout distance, resulting in increases of between 0.11 m and 1 m (i.e. 7% - > 50%), with greater increases occurring when low (0.4 U_{mf_st} – 0.46 U_{mf_st}) levels of aeration are sustained for the whole runout distance of the current. A higher slope angle also sustains higher current front velocities for greater distances.

The experimental currents travel as a series of supercritical pulses ($Fr = 7$) which come to a relatively rapid halt, supporting the model of stepwise aggradation for dense basal currents (e.g. Schwarzkopf et al., 2005; Sulpizio & Dellino, 2008; Charbonnier & Gertisser, 2011;

Macorps et al., 2018). Our findings also demonstrate intricate links between the overall current dynamics and the deposit morphology characteristics, with thicker, more confined deposits aggrading rapidly where the current transitions from a high aeration state to lower aeration states. Such behaviour may be seen in natural PDCs subject to processes which result in de-aeration, such as temperature drops and/or loss of fines.

==

Chapter 4

4. A bedform phase diagram for dense granular currents

==

Pyroclastic density currents are a life-threatening volcanic hazard. Our understanding and hazard assessments of these flows rely on interpretations of their deposits. The occurrence of stratified layers, cross-stratification, and bedforms in these deposits has been assumed as indicative of dilute, turbulent, supercritical flows causing traction-dominated deposition. Here we show, through analogue experiments, that a variety of bedforms can be produced by denser, aerated, granular currents, including backset bedforms that are formed in waning flows by an upstream-propagating granular bore. We are able to, for the first time, define phase fields for the formation of bedforms in PDC deposits. We examine how our findings impact the understanding of bedform features in outcrop, using the example of the Pozzolane Rosse ignimbrite of the Colli Albani volcano, Italy, and thus highlight that interpretations of the formative mechanisms of these features observed in the field must be reconsidered.

4.1 Introduction

Particulate density currents are the largest mass transporters of sediment on the Earth's surface. Deep-sea turbidity currents deposit the largest sediment accumulations on Earth (Bouma et al., 1985), density currents emplace ejecta blankets around bolide impact craters (Siegert et al., 2017) and pyroclastic density currents (PDCs) can transport thousands of cubic kilometres of volcanic material during a single event (Self, 2006). These flows also pose a major geohazard, with deep-sea turbidity currents threatening seafloor infrastructure and PDCs being responsible for over 90,000 deaths since 1600 CE (Tanguy et al., 1998; Auker et al., 2013). Understanding the behaviour of these particle-laden, fast-moving currents is fundamental to decreasing the risks they pose to society.

The dynamics and depositional processes of PDCs are difficult to analyse due to their destructiveness, and the concealment of the internal dynamics by an accompanying ash cloud. Understanding of PDC behaviour therefore, is primarily based on interpretation of the geological record preserved in sedimentary deposits (Sparks, 1976; Wilson, 1985; Cas & Wright, 1987; Branney & Kokelaar, 2002; Pollock et al., 2019), complemented by analogue and numerical modelling (Valentine, 1987; Dobran et al., 1993; Roche, 2012; Dufek, 2016).

The presence and morphology of sedimentary structures, such as bedforms, in a deposit can be interpreted to tell us about the internal behaviour of the density current that formed them (Bouma, 1962; Jopling & Richardson, 1966; Normark et al., 1980; Allen, 1982; Alexander et al., 2001). Various types of cross-stratified bedforms occur in PDC strata and are assumed to be formed by dilute, high-velocity (surge) PDCs (Schmincke et al., 1973; Wohletz & Sheridan, 1979; Allen, 1982; Walker, 1984; Cas & Wright, 1987; Cole, 1991; Douillet et al., 2013), where tractional processes dominate in the flow-boundary zone due to the predominance of fluid turbulence as a particle support mechanism (Walker, 1983; Valentine, 1987; Branney & Kokelaar, 2002; Dellino et al., 2008). Denser, granular fluid-based PDCs are usually thought to be responsible for the creation of massive deposits, lacking in sedimentary structures (Sparks, 1976; Fisher et al., 1983; Branney & Kokelaar, 2002; Cas et al., 2011).

Bedform-related sedimentary structures in PDC deposits include backset features (i.e. upstream-dipping beds) formed by stoss-side aggradation, similar to chute-and-pool structures and antidunes found in fluvial systems (Fig. 4.1a & 4.1f and Fig. 4.1b & 4.1d), which are generally thought to be formed under supercritical flow conditions (Middleton, 1965; Jopling & Richardson, 1966; Alexander et al., 2001; Cartigny et al., 2014). Early work on such structures in PDC deposits interpreted them similarly as the result of supercritical flows (Fisher & Waters, 1969, 1970; Waters & Fisher, 1971; Crowe & Fisher, 1973). These backset bedforms have commonly been referred to as regressive, for example by Allen (1982) who interpreted them as sandwaves deposited by wet and cool pyroclastic surges. Since then regressive has been commonly used to describe stoss-aggrading features in PDC deposits, although linking this to flow conditions, rather than temperature and moisture content (Cole, 1991; Druitt, 1992; Cole & Scarpati, 1993; Gençalioğlu-Kuşcu et al., 2007). However, there have been attempts to introduce new terminology which does not hold the genetic connotations of antidune, chute-and-pool, or sandwave. For example, Brown and Branney (2004a) use the term regressive bed form for a giant set of sigmoidal, upstream dipping lenses. Douillet et al. (2013) introduce the term regressive climbing dunes for bedforms which show upstream crest migration (Fig. 4.1c). Brand et al. (2016) adopt similar terminology, using regressive dune bedforms (Fig. 4.1e). In this paper we avoid using such terms, in the interests of being purely descriptive, opting instead to use backset bedforms to refer to stoss-aggrading features which have both asymmetrical (much steeper stoss sides; Fig. 4.1g) or roughly symmetrical lee and stoss slopes (Fig. 4.1h).

Analogue modelling of dense PDCs has advanced considerably over recent years including work focusing on the influence of pore pressure (Roche et al., 2004; Girolami et al., 2010; Montserrat et al., 2012; Roche, 2012; Chédeville & Roche, 2014; Rowley et al., 2014; Gueugneau et al., 2017). High gas pore pressure created by various mechanisms within PDCs (Sparks, 1976; Wilson, 1980; Giordano, 1998; Branney & Kokelaar, 2002; Druitt et al., 2007) has been shown to be responsible for their unusually high mobility (Hayashi & Self, 1992; Calder et al., 1999; Lube et al., 2019), but only recently has physical modelling reflected the sustained and variable nature of such pore pressures with distance from source (Rowley et al., 2014; Smith et al., 2018).

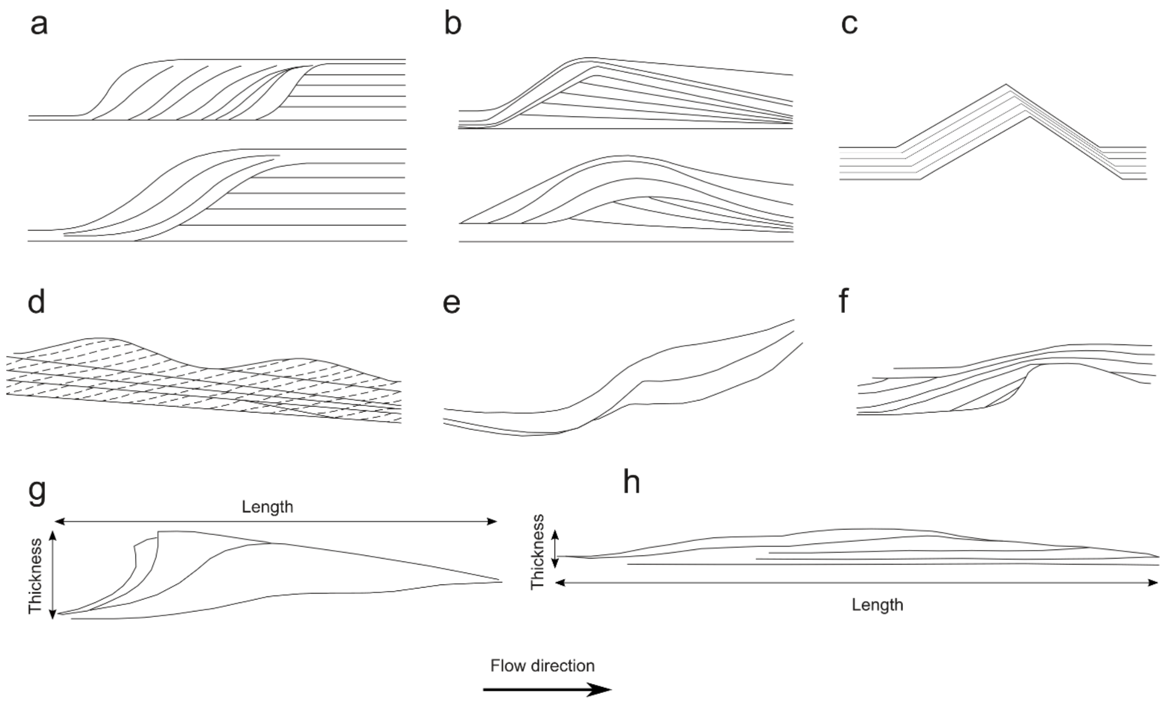

Figure 4.1 Sketches of backset bedforms in PDC and fluvial deposits. **a** Chute-and-pool structures in dilute PDC deposits at Laacher See (Schmincke et al., 1973). **b** Antidunes in dilute PDC deposits at Laacher See (Schmincke et al., 1973). **c** Regressive dune bedform (Douillet et al., 2013). **d** Stable antidunes (Cartigny et al., 2014). **e** Regressive bedform from the Proximal Bedded Deposits at Mt St Helens (Brand et al., 2016). **f** Fluvial chute-and-pool structure (Fielding, 2006). **g** Steep backset bedform as described in this paper, showing length and thickness definitions. **h** Shallow backset bedform as described in this paper.

Here we examine the conditions which promote the growth of bedforms in aerated dense granular flows, as analogues for PDCs and their deposits. This work describes laboratory experiments in which we use partially fluidised (aerated) fine-grained particles in a 3 m long flume (see Methods). These experiments are able to simulate many behaviours of PDCs (Roche, 2012; Chédeville & Roche, 2014; Rowley et al., 2014; Smith et al., 2018). As the deposit aggrades from the quasi-steady currents, the growth of bedforms is recorded using a high-speed camera. We study how backset bedform features form within the dense granular currents. Deposition is triggered in the experiments as the sustained aerated flow passes into a section of the flume with a reduced or absent basal gas flux, resulting in rapid deaeration and a consequent increase in frictional forces between particles. This is not intended to represent a specific natural process but rather simulate the rapid deaeration hypothesised to occur in natural PDCs as a result of various processes such as loss of fines, temperature drops, thinning, and/or the entrainment of coarser material (Bareschino et al., 2007; Druitt et al., 2007; Gueugneau et al., 2017). The initial deaeration would be accelerated by the slowing current (decreasing shear rates), and increasing inter-particle frictional forces. We are able to, for the first time, define phase fields for the formation of types of bedforms in PDC deposits using current velocity, current thickness, Froude number, and Friction number. We examine how our interpretations impact on the understanding of similar features in outcrop, using the example of the Pozzolane Rosse ignimbrite of the Colli Albani volcano, Italy.

4.2 Results

4.2.1 Bedform morphology

A range of bedforms were observed growing under a variety of flow conditions within the suite of experimental runs (see Methods). We categorise these bedforms into three types (Fig. 4.2): planar/very shallow backset (<2°) bedsets, backset bedforms with shallow stoss sides less than the dynamic angle of repose ($< \Theta_{Dyn}$), and backset bedforms with steep ($>\Theta_{Dyn}$) stoss sides. Planar bedsets, shallow backset bedforms and steep backset bedforms are present in each deposit except one (Fig. 4.2e), which does not show steep backset bedforms. Both steep and shallow backset bedforms comprise a bedset of multiple (3-4) stoss-side lamina dipping at varying angles, converging into a single corresponding lee-side lamina (Table 4.1). No progressive (prograding) bedforms were observed in any of the experimental runs because our experiments are run with waning, not waxing currents.

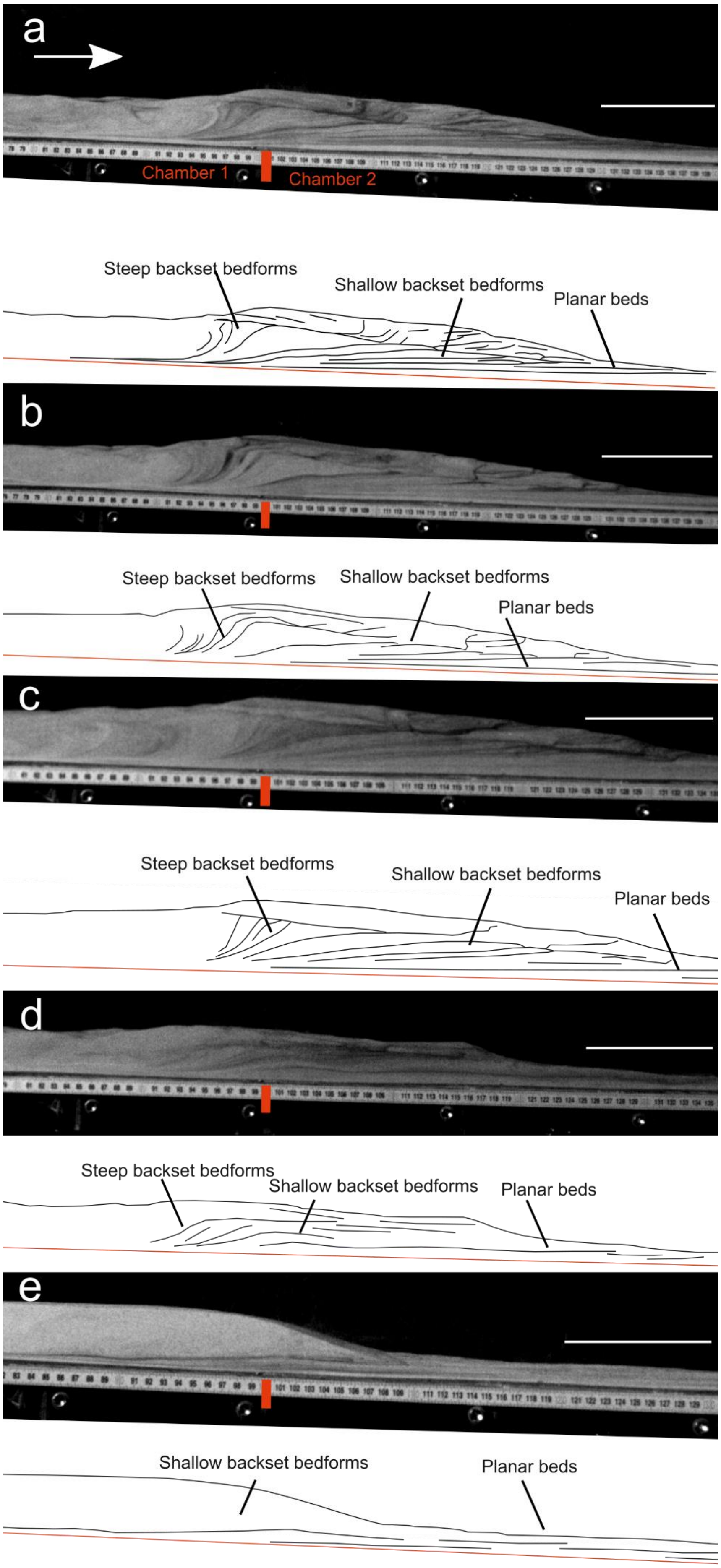
a
Chamber 1
Chamber 2
Steep backset bedforms
Shallow backset bedforms
Planar beds
b
Steep backset bedforms
Shallow backset bedforms
Planar beds
c
Steep backset bedforms
Shallow backset bedforms
Planar beds
d
Steep backset bedforms
Shallow backset bedforms
Planar beds
e
Shallow backset bedforms
Planar beds

Figure 4.2 Deposits from five separate experimental runs. Scale bar = 10 mm. **a**, **b**, **c** show backset bedforms deposited by currents passing above a chamber aerated at 0.93 U_{mf_st} to one unaerated. **d** shows backset bedforms deposited by a current passing above a chamber aerated at 0.93 U_{mf_st} to one aerated at 0.66 U_{mf_st}. **e** shows backset bedforms deposited by a current passing above a chamber aerated at 0.66 U_{mf_st} to one aerated at 0.53 U_{mf_st}.

Table 4.1 Dimensions and angles of our experimental backset bedforms.

Bedform	Lengths (m)	Thickness (m)	Stoss angles (°)	Lee angles (°)
Steep backset (Fig. 4.1g)	0.18-0.4	0.35-0.4	20 - overturned	<10
Shallow backset (Fig. 4.1h)	0.18-0.21	0.003-0.01	<10	<10

4.2.2 Bedform deposition

The experiments began when the particles were released into the flume via trapdoor and impinged on the basal porous mesh, forming an aerated current. The leading edges of the currents were travelling at ~2 ms^{-1} as they passed into the lesser/un-aerated second chamber of the flume (Fig. 4.3a, see Supplementary Movie B.1). The sustained currents rapidly deaerate as they pass over the second chamber of the flume, promoting deposition. Small spontaneously-generated variations in the current mass flux result in minor unsteadiness in the flow over timescales in the order of 0.05 s and flow thickness variations in the order of +/- 10%, hence their quasi or nearly-steady nature (Rowley et al., 2014). The currents initially deposit planar or very shallow backset bedsets after the break in aeration, (Fig. 4.3b) at velocities of ~1-1.5 ms^{-1}. Within 0.4-0.8 s of deposition beginning, stoss-side aggrading shallow backset bedforms are deposited above and upstream of the planar bedsets as the current velocities decrease (Fig. 4.3c-d). Within 1.1-1.6 s of deposition beginning, with the current velocities below ~ 0.5 ms^{-1}, the upstream edge of the deposit steepens and collapses, with very steep backset bedsets deposited just prior to this, forming the stoss sides of steep backset bedforms (Fig. 4.3e-f). Current velocity and thickness data during deposition of the bedforms may be found in Supplementary Table B.1.

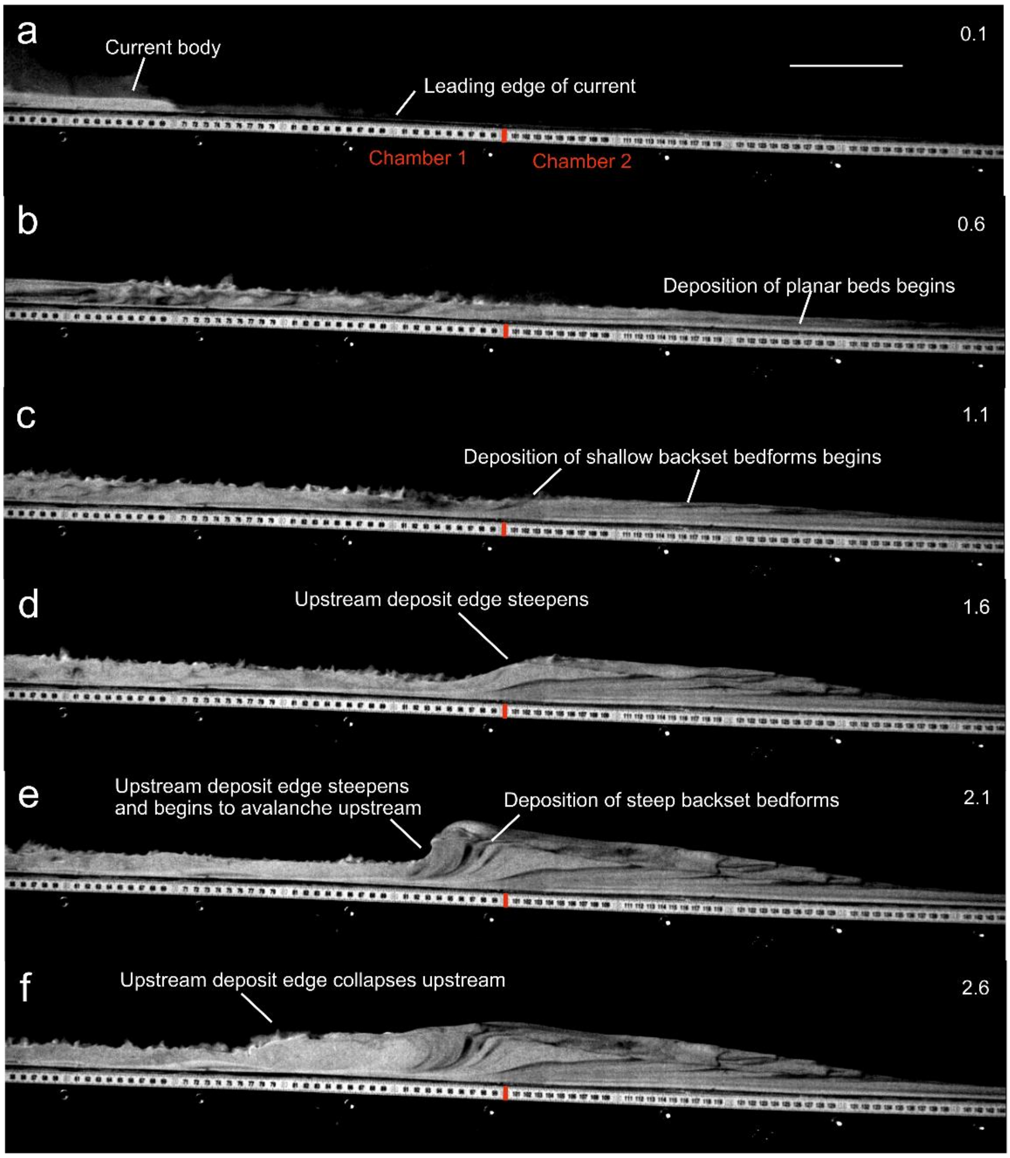

Figure 4.3 Timelapse of an experimental granular current. Scale bar = 10 mm. Deposition of backset bedforms is triggered by the current passing above a chamber aerated at 0.93 U_{mf_st} to one unaerated. See text for detailed description. Number in the top right of the frames is the time in seconds since the current entered the first frame.

4.2.3 Velocity and thickness control on bedform formation

Planar, shallow, and steep features fall into well-defined fields on a current velocity vs current thickness plot, suggesting that current velocity and thickness controls the sedimentary structures in the deposit (Fig. 4.4a). For a given current thickness planar bedsets are deposited at higher velocities (above 0.8 ms^{-1} in these experiments). Shallow backset bedforms are deposited at lower velocities, and steep backset bedforms are deposited at the lowest velocities (between 0.3-0.6 ms^{-1} in these experiments). With increasing current thickness, higher current velocities are required to remain in the shallow bedform and planar bedform stability fields. As a result of thickening within a steady current, bedform-induced deposits of different character can be formed without a requirement for a change in flow velocity. It is important to note that the deposit formed over the smallest aeration drop (0.66 U_{mf_st} to 0.53 $U_{mf\_st.}$) does not show steep backset bedforms, and only poorly developed shallow backset bedforms, suggesting the magnitude of the aeration drop and consequent velocity changes may also have some control.

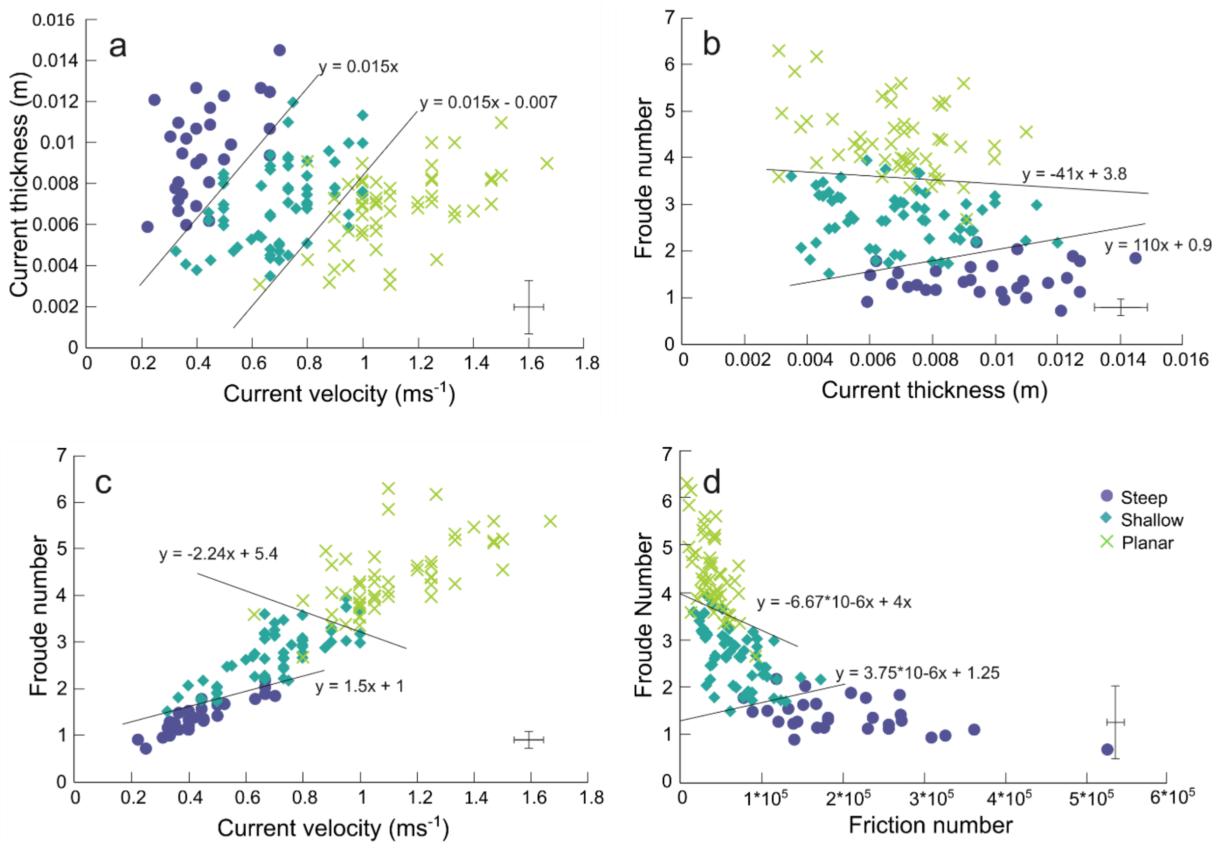

Figure 4.4 Phase diagrams showing the current conditions which control backset bedform formation, with plausible phase boundaries. **a** Velocity vs. thickness. **b** Thickness vs. Froude number. **c** Velocity vs. Froude number. **d** Friction number vs. Froude number. Representative (n = 20) error bars are located in the bottom right of each image (± 2 s.d.).

4.2.4 Phase fields

We define phase fields for the three types of bedforms using the Froude number (Fr) and the Friction Number (N_F). The Froude number (Fr) represents the ratio of kinetic to potential energy (Eq. 4.1).

$$Fr = U/(gH)^{1/2} \qquad \text{(Eq. 4.1)}$$

Where U = current velocity, g = gravity, and H = current thickness. The Friction Number (N_F) is the ratio of frictional to viscous stresses and is defined as Bagnold Number/Savage Number (Iverson & LaHusen, 1993; Iverson, 1997). The Savage number (N_S, Eq. 4.2) is the ratio of collisional stress to frictional stress (Savage & Hutter, 1989; Iverson, 1997), and the Bagnold number (N_B, Eq. 4.3) is the ratio of collisional stress to viscous fluid stress (Bagnold, 1954; Iverson, 1997).

$$N_S = \frac{\left(\frac{U}{H}\right)^2 \delta^2 \rho_s}{(\rho_s - \rho_f) g H tan\theta} \qquad \text{(Eq. 4.2)}$$

$$N_B = \frac{\left(\frac{U}{H}\right) \delta^2 \rho_s \varphi}{(1-\varphi)\mu_f} \qquad \text{(Eq. 4.3)}$$

where ρ_s = particle density ρ_f = fluid density δ = particle diameter θ = internal friction angle φ = solid volume fraction μ_f = fluid viscosity.

N_S in these experiments range from 0.00003-0.03, and N_B from 15-269. In natural PDCs, N_S has been estimated to range from 10^{-8}-10^{-9} (Roche, 2012), which similar to our experiments is in the frictional regime (Savage & Hutter, 1989) despite the difference of several orders of magnitude. Our N_B values overlap with those estimated for natural PDCs (10^0-10^2) (Roche, 2012).

Froude numbers were calculated for each tracked sediment package during its deposition. Different types of bedforms are formed under different ranges of Fr, with greater overlap between the planar bedset and shallow backset bedform fields than between the shallow and steep backset bedform fields (Fig. 4.4b-c). As anticipated, there is a good correlation (R = 0.843) between *Fr* and velocity (Fig. 4.4c), but with a noticeably greater data spread at higher (>0.8 ms^{-1}) velocities, whereas *H* exerts much less of a control on *Fr* (Fig. 4.4b).

Planar bedsets are mostly deposited at high *Fr* and low N_F, shallow backset bedforms at moderate *Fr* and N_F , and steep backset bedforms at low *Fr* and high N_F (Fig. 4.4d). The planar-shallow-steep sequence of bedform formation can therefore be seen as recording the transition of a fast, supercritical current dominated by viscous stresses to a slower current increasingly dominated by frictional stresses.

4.2.5 Similar bedforms in the field

The Pozzolane Rosse (PR) ignimbrite covers an area of more than 1600 km^2 around the Colli Albani volcano, Italy (Giordano & Dobran, 1994), and has been dated ($^{40}Ar/^{39}Ar$) at 456 ± 3 ka (Marra et al., 2009). It surmounts topography of 250 m to reach altitudes of 440 m (Giordano et al., 2010). The ignimbrite is generally massive, matrix-supported and poorly-sorted, with a noticeable paucity in fine ash. Emplacement temperatures have been estimated to be between 630 °C and 710 °C (Trolese et al., 2017).

Six samples were taken for this study from three localities (within 18-24 km of the vent; Fig. 4.5a) and two facies (massive, and undulated bedding as described in Giordano & Doronzo, 2017). Grains are dominantly poorly vesicular scoria with compositions plotting in the tephrite/basanite field (Conticelli et al., 2010). The grain size distribution of all samples is dominated by lapilli-sized grains and poor in the < 63 µm fraction (Fig. 4.5b, Supplementary Table B.2), which is consistent with samples from other studies (Fig. 4.5c), plotting in the fines-depleted flow field of Walker (1983). Therefore, we consider the parent PDC of the PR ignimbrite to be a good natural example of an analogue dense, granular current.

Rotating drum tests on the six samples taken from the PR (excluding grains > 0.0056 m) gave static minimum (Θ_{Smin}), maximum (Θ_{Smax}) and dynamic (Θ_{Dyn}) angles of repose of 35.3°, 51.7° and 45.2° respectively (Supplementary Figure B.1). Although these values are considerably higher than those obtained for the particles used in the experiments (Supplementary Figure B.2), (likely due to the variable grainsize and angularity of the ignimbrite grains), the scaling remains reasonable due to the larger particle sizes in the natural materials (see Eq. 4.2).

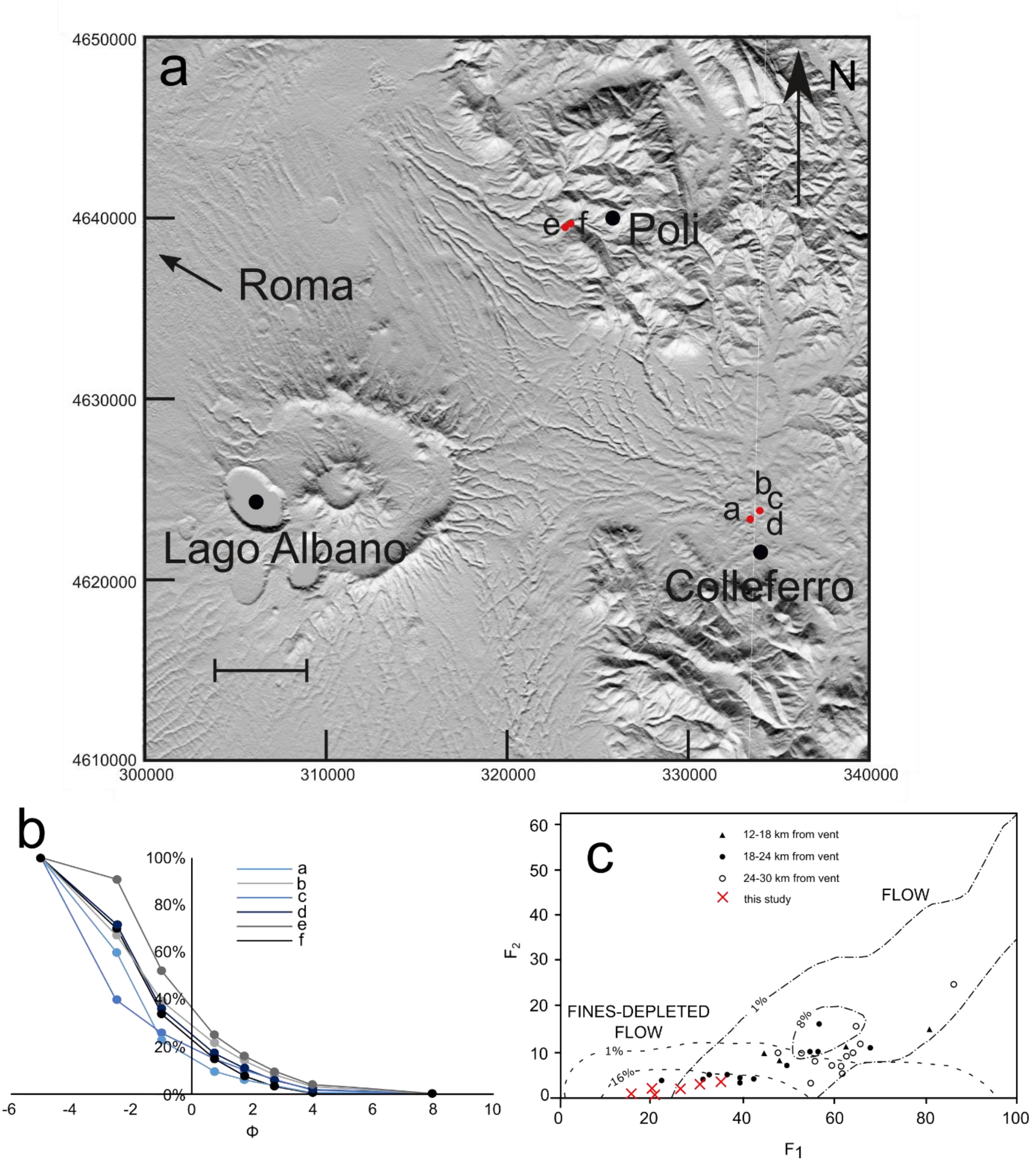

Figure 4.5 Grain size data for samples from the Pozzolane Rosse ignimbrite. **a** Map of sample locations. Scale bar = 5 km. Sample a is from the massive facies, sample b, c, and d from the undulated bedding facies, and sample e and f from backset bedforms within this facies. **b** Grain size distribution curves for samples from this study. Note the dominance of coarse grains and paucity in the <63 μm (4 ϕ) fraction. The grain size data are given in Supplementary Table B.2. **c** Plot of weight percentage finer than 63 μm (F_2) versus weight percentage finer than 1 mm (F_1), after Walker (1983). Black symbols are PR ignimbrite samples from Giordano and Dobran (1994), red crosses show the PR ignimbrite samples from this study.

Backset bedforms are found in the undulated bedding facies in the NE sector of the PR ignimbrite, where the depositing current left the radial plain and ran up into the Apennine mountains (Giordano & Doronzo, 2017). The undulated facies transitions laterally into the massive facies of the PR on scales of hundreds of metres, and both facies have the same grain size and compositional characteristics (Fig. 4.5b-c), thus we interpret them to be from the same parent PDC. The bedforms in the PR share similarities with our experimental deposits (c.f. Fig. 4.6a and Fig. 4.2a-c, Fig. 4.6c and Fig. 4.2d); and measured stoss angles for both natural and experimental bedforms span the same range (Fig. 4.6b). The stoss layers seen in the PR backset bedforms are never overturned upstream like some of the experimental deposits. Preservation of overturned beds in natural deposits may be difficult – upstream avalanching of material from this unstable bedform may be reincorporated into a sustained current, or they may be cryptic and not easily visible in natural material. Shallow stoss-sided bedforms are found in this facies (Fig. 4.6d) although they tend to have greater lee (due to the greater repose angles of the material) and stoss angles than experimental examples, where both are $<10°$ (Fig. 4.6b).

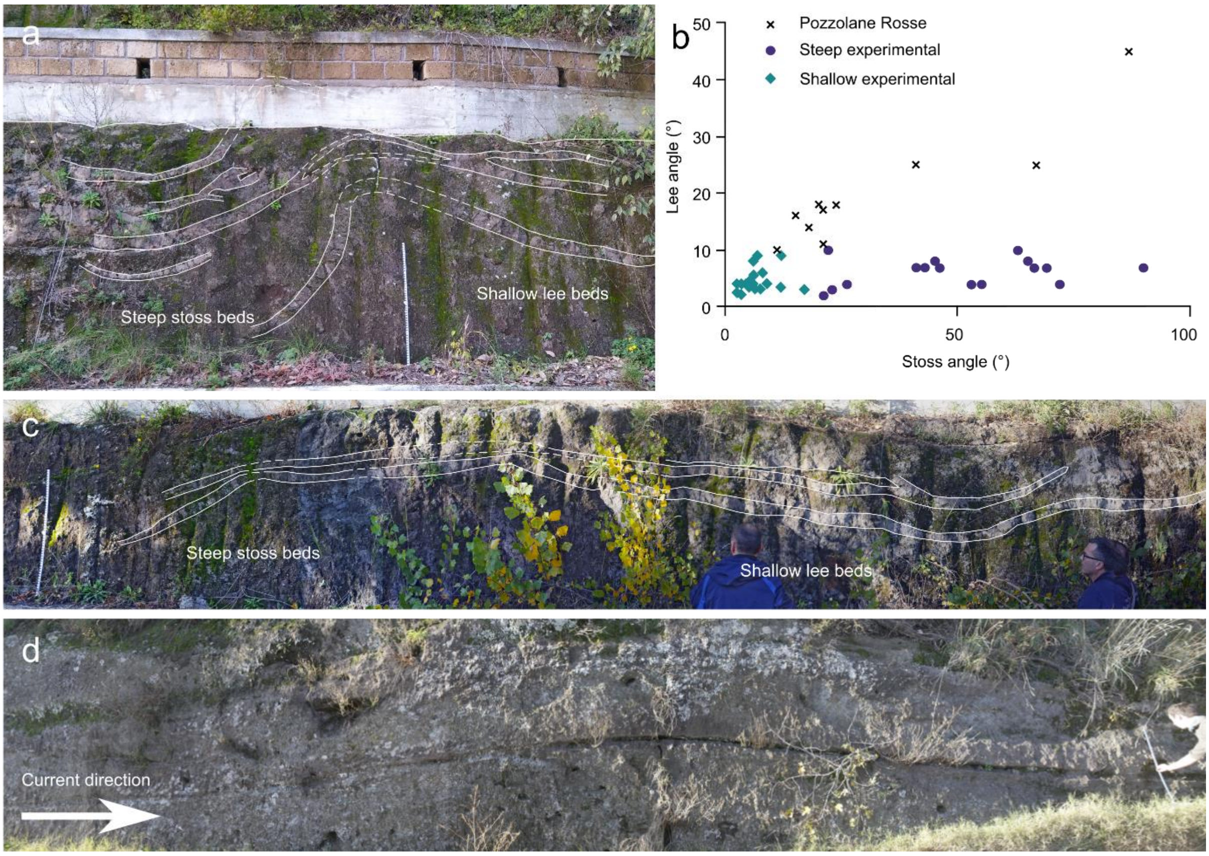

Figure 4.6 Field photos and data of the Pozzolane Rosse ignimbrite erupted from Colli Albani, Italy. The ruler is 1 m in length. Coordinates are for UTM 33T grid, using the WGS84 Datum. **a** steep stoss side backset bedform at 323348 4639535, c.f. **Fig. 4.2a-c**. **b** stoss and lee angles for PR and experimental backset bedforms. Several of these backset bedforms have similar stoss angles to our experimental features, however the lee angles are much steeper. **c** backset bedform directly upstream from **a**, c.f. **Fig. 4.2d**. **d** shallow bedform at 323037 4639270, thicker by ~15 cm over the stoss and crest compared to the lee.

4.3 Discussion

Our experimental deposits consist of planar bedsets and shallow and steep backset bedforms. The existing widespread interpretation of backset features in PDC deposits is that they are a product of upper flow regime/Froude supercritical flow within dilute PDCs (Fisher & Waters, 1969, 1970; Waters & Fisher, 1971; Crowe & Fisher, 1973; Cole & Scarpati, 1993; Brand & Clarke, 2012) , or that relatively steep backset bedforms are specifically a record of the formation and propagation of Froude jumps, where flow transforms from Froude supercritical (>1) to Froude subcritical, similar to fluvial chute-and-pool structures (Fisher & Waters, 1969; Schmincke et al., 1973; Fisher & Schmincke, 1984; Rowley et al., 1985; Cole &

Scarpati, 1993; Gençalioğlu-Kuşcu et al., 2007; Brand & Clarke, 2012; Brand et al., 2016) (Fig. 4.1a/1e and 4.1f). Our experimental currents show rapidly evolving Froude numbers (Fig. 4.4). Within the current body, planar beds are deposited at *Fr* 3-5, shallow backset bedforms at *Fr* 2-3, and steep backset bedforms at *Fr* 0.59-2. We show that an apparent Froude jump within the flow forms in the current during deposition of the steep backset bedforms (Fig. 4.7). As the experimental current is granular, we adopt the term granular jump (Boudet et al., 2007; Faug, 2015; Faug et al., 2015), which shares many characteristics with its hydraulic counterpart. However, the outgoing current only briefly has *Fr* < 1, due to thickening of the current directly prior to its being blocked, meaning that a granular jump, strictly defined as a flow transitioning from *Fr* >1 to *Fr* <1, exists here for only 0.1 - 0.2 seconds.

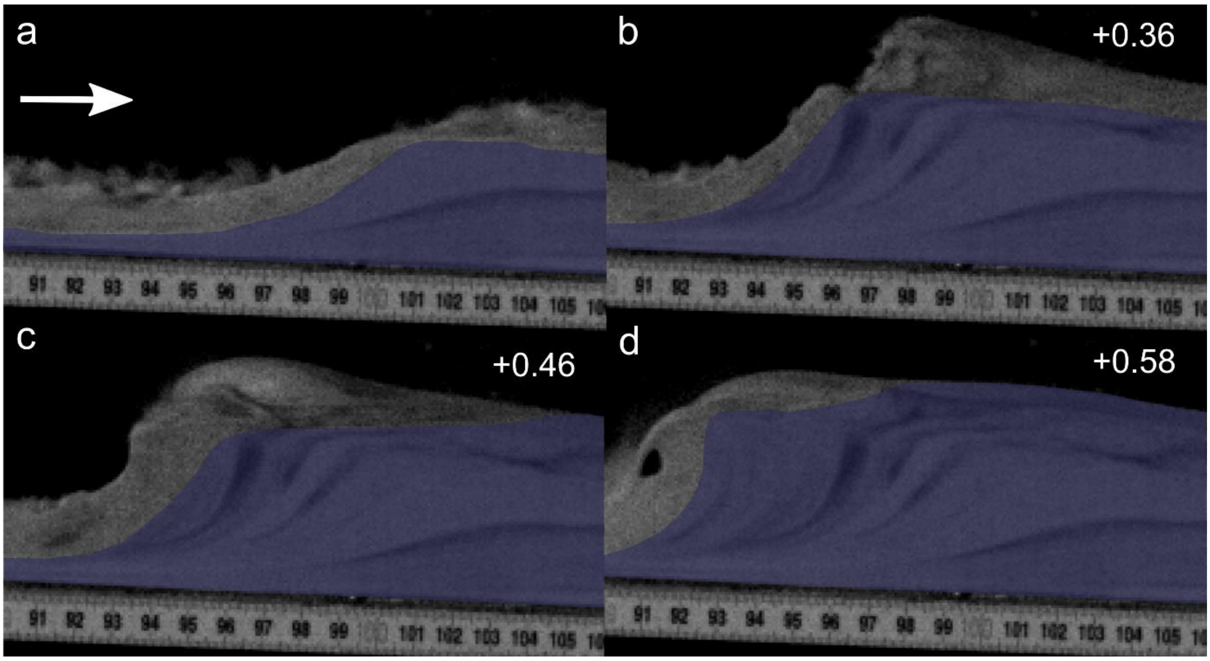

Figure 4.7 The formation and evolution of a granular bore. Numbers in the top right are seconds passed since the first frame. Shaded area shows stationary deposit. Flow direction left to right. **a** shows the initial formation of a steepening bump, with the incoming and outgoing current both supercritical. **b** shows the upstream propagation and further steepening of the bore, immediately after blocking of the outgoing current. **c** The bore propagates further upstream, the front steepening to vertical. **d** The front of the bore collapses upstream by avalanching.

As the sediment deposit grows in thickness, a critical point is reached where the incoming flow cannot surpass the positive slope, and the pseudo-jump propagates upstream as a granular bore (Faug, 2015), which travels at 0.14 ms^{-1} between 96 cm and 90 cm along the flume length. Here we use granular bore to describe the upstream propagation of the depositional front of the granular material, regardless of flow conditions. This process appears to be similar to the stoss-side blocking or granular jamming invoked to explain stoss-aggrading bedforms at Tungurahua (Douillet et al., 2013, 2018), where the granular current is simply blocked by topography with no particular fluid conditions necessary.

An interesting feature seen in the granular jump of Boudet et al. (2007) and our own currents is the steepening of stoss faces well beyond the repose angle at the front of the granular bore, and its collapse by avalanching (Fig. 4.7d). This is likely caused by rapid deposition from the incoming flow countering the effects of gravity sliding, and allowing the bedforms to steepen well beyond repose angle. Again, a similar phenomenon of very high sedimentation rates is used to explain near-vertical bedding at Tungurahua (Douillet et al., 2018). The particles deposited by the current as the deposit front steepens form our steep backset bedforms, with stoss angles up to 90°. This may explain why the smallest aeration drop in our experiments (0.66 U_{mf_st} to 0.53 U_{mf_st}) did not form steep backset bedforms – the drop was too small to promote the levels of deaeration and deceleration necessary for such rapid sedimentation. Our experimental data therefore call the widespread interpretation of backset bedforms recording Froude jumps within dilute PDCs into question, as we show that similar features can form in dense granular flows in relation to an extremely transient Froude jump, and more clearly related to stoss-side blocking.

Calculated N_S and N_B numbers indicate that planar bedsets are deposited under conditions closer to a collision-dominated flow regime (N_S > 0.1 and N_B >450, Iverson & Denlinger, 2001) than the backset bedforms (Supplementary Table B.1). The planar bedset deposition occurs beyond the transition to the unfluidised section of flume, and therefore they are deposited by a current which is experiencing more collisions between particles due to the loss of gas pore pressure. The backset bedforms are deposited closer to this transition point, where the current has a higher gas pore pressure and grain collisions are not as prevalent. A ratio of N_B to N_S (N_F) shows that frictional stresses are considerably higher than viscous shear stresses in the area of the currents depositing steep backset bedforms (Fig. 4.4d). As the current is waning at this point and relatively thick, this could result in sustained contacts between particles despite relatively high gas pore pressures.

The PR ignimbrite is generally massive and fines poor, which suggests that the flow-boundary zone conditions of the parent PDC were highly concentrated, likely close to the fluid escape-dominated and granular flow-dominated end-members of Branney and Kokelaar (2002). Additionally, the dense nature of the clasts, lack of fines and the lack of widespread stratification all suggest that the ignimbrite is the deposit of a dense, granular PDC. The presence of backset bedforms within the deposit, which are typically indicative of dilute, turbulent flow (pyroclastic surges), is therefore paradoxical. Rather, the backset bedforms must have been produced by some other process than turbulence within a dilute current.

The similarities between the structures in the PR ignimbrite and our experimental deposits formed by a dense granular current suggest that the depositional processes involved in both cases could be related. We interpret the undulated bedding facies - which includes the backset bedforms - to have been deposited by the same PDC as the rest of the PR ignimbrite. This is due to the traceable lateral transition between facies, the similarity between the grain size curves over a range of localities, and because the tephra is compositionally identical in the two lithofacies. Instead, the change in facies could be due to the onset of rapid deposition and stoss-side blocking related to the run-up of the PDC into the Apennine mountains (Fig. 4.5a). Giordano and Doronzo (2017) interpret the undulated bedding to the east of the volcano as the result of rapid sedimentation and a reduction in the lateral mass discharge rate caused by a palaeovalley perpendicular to flow. Our experimental steep stoss-sided bedforms are created in a waning flow regime after the cessation of basal gas injection and the resulting decrease in pore pressure results in rapid sedimentation, so these interpretations are consistent.

We propose a depositional model whereby shallow backset bedforms are deposited by supercritical flow, forming a topographic irregularity which slows the incoming current (Fig. 4.8a-b), causing stoss-side blocking, forming a granular bore and promoting rapid deposition (Fig. 4.8c). Continued deposition steepens the front of the bore until it collapses upstream through avalanching (Fig. 4.8d-e). Our work provides direct evidence that bedforms can be created by dense granular PDCs, and supports the stoss-side blocking process first suggested by Douillet et al. (2013, 2018) based on field deposits.

The upstream propagation of a granular bore, which is caused by the blocking of the current by the aggrading deposit, is a process which in nature could be exacerbated or triggered by pre-existing topography (Faug et al., 2015). The waning nature of the incoming flow at this point, and its relatively low Froude number, suggests that while most of these steep backset bedforms are technically recording the transition from supercritical to subcritical flow, both the shallow backset bedforms and planar beds are formed under increasingly supercritical conditions. It follows that shallow backset bedforms and planar bedsets may then be better indicators of supercritical flow conditions when interpreting dense PDC deposits. The proposed phase diagrams presented here are a major step towards quantitative links between PDC processes and their deposits.

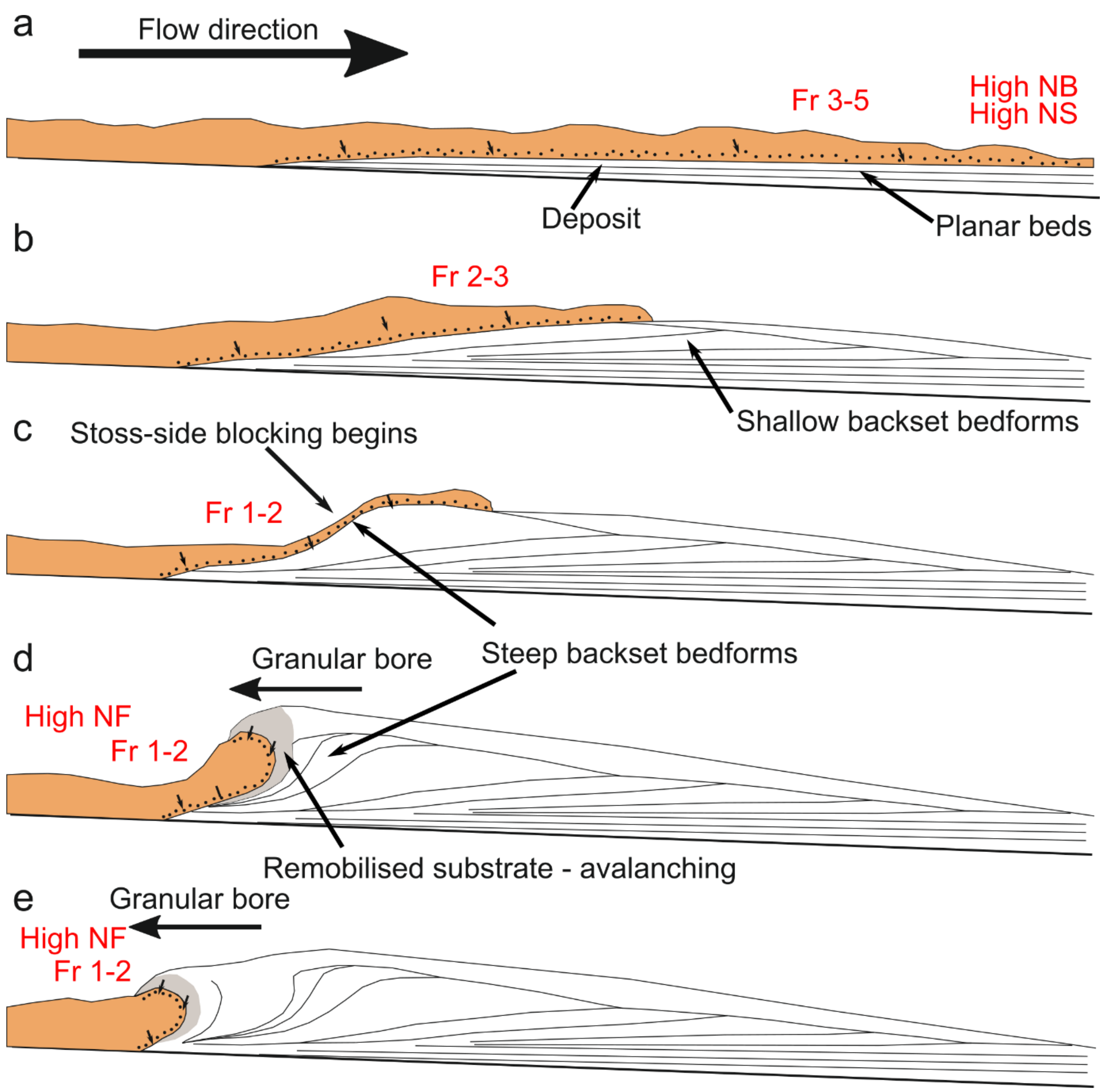

Figure 4.8 Schematic showing how different backset bedforms could be deposited by a PDC. Flow properties in red (*Fr*, N_S, N_B, N_F) refer to the Froude, Savage, Bagnold, and Friction Numbers respectively. See text for detailed description.

Bedforms can be the product of a dense granular flow and can form without any interference (e.g. tractional shear) from an overlying dilute turbulent layer. As the presence of bedforms (e.g. cross-stratification and backsets) has been commonly used as diagnostic evidence for dilute, turbulent currents, our findings have important implications for field interpretation – as different types of PDCs can react differently to topography the correct classification is necessary for hazard assessment. Other sedimentary characteristics such as field relations, grain size and sorting must be used in order to distinguish between the two PDC end-members. This challenge to the interpretation of the deposits of particulate granular currents is particularly relevant to other free-surface granular mass flows, including landslides, snow avalanches, and debris flows. Our experiments demonstrate that formation of different bedforms may by controlled by current thickness and current velocity which has important implications for hazard mapping, and the potential for further investigation to a) expand the bedform stability criteria identified here, and b) define palaeoflow conditions from recorded bedforms.

4.4 Methods

4.4.1 Flume set-up

We use the experimental flume of Smith et al. (2018), modified so that release of the particulate density current is controlled by a trapdoor instead of a horizontal lock gate (Fig. 4.9), such that colour stratification in the starting charge transmits to the flow and deposit. The base of the flume comprises one-meter long sections which can provide independently controlled gas fluxes through a porous baseplate in each section in order to fluidise any overpassing material. The flume was kept at an angle of 2°, to promote flow away from the impingement surface while maintaining a sub-horizontal surface.

The air-supply plumbing allows a gas flux to be fed through the base of the flume, producing sustained aeration of the current. In such thin (<0.03 m), rapidly degassing laboratory currents, this enables us to simulate the long-lived high gas pore pressures that characterize thicker PDCs (Rowley et al., 2014; Smith et al., 2018). The gas flux supplied through the base in each of the three sections of the channel was controlled to vary the aeration state of the currents, all of which were below the static minimum fluidisation velocity (U_{mf_st}), as complete fluidisation would result in non-deposition (Rowley et al., 2014).

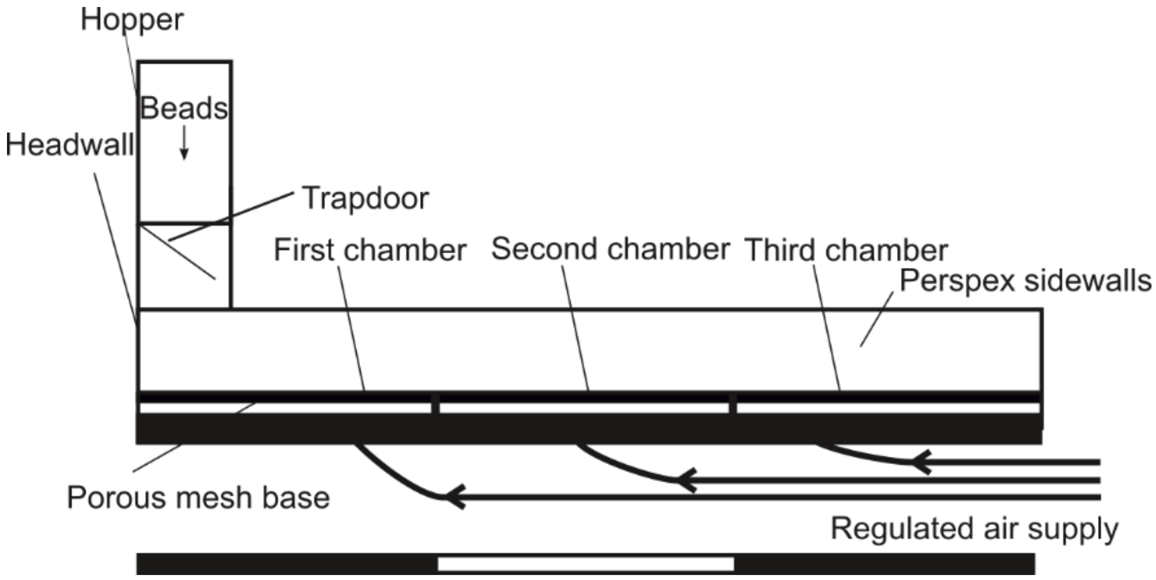

Figure 4.9 A longitudinal section view of the experimental flume. Scale bar = 3 m.

Various aeration states were used to trigger different flow behaviours. The first chamber (0.66-0.93 U_{mf_st}) always had higher gas flux than the second chamber (0-0.66 U_{mf_st}) to trigger deposition in the target area of the flume. The experiments were recorded using a high-speed camera at 200 frames per second. This video recorded a side-wall area of the channel at 1 m runout (across the contact between the first and second gas supply chambers), allowing for measurement of the flow conditions. From the opening of the trapdoor to the cessation of deposition each experimental run lasted approximately four seconds.

4.4.2 Experimental material and deposits

The experiments were performed using particles of spherical soda lime ballotini with grain sizes of 45-90 μm (average δ_{32} = 63.4 μm calculated from six samples across the material batch) similar to the particles used in previous experimental granular currents (Roche et al., 2004; Montserrat et al., 2012; Rowley et al., 2014). These ballotini belong to the Group A classification of Geldart (1973), comprising particles 45-90 μm which expand homogenously above U_{mf} until bubbles form, and which are non-cohesive. As PDCs contain dominantly

Group A particles, this allows dynamic similarity between the natural and experimental currents (Roche, 2012). Detailed mechanical properties of the ballotini are presented in Supplementary Table B.3, derived from rotating drum (Carrigy, 1970) and shearbox (BS 1377-7:1990) testing. These give cohesion values of 0 kPa, and an internal friction angle of 25.3° (Supplementary Figure B.3). Static minimum (Θ_{Smin}), maximum (Θ_{Smax}) and dynamic (Θ_{Dyn}) angles of repose are found to be of 11.7°, 31.9° and 20.9° respectively (Supplementary Figure B.2).

Due to the monodisperse nature of the materials, any internal structure is easily masked by lack of contrast between packages of sediment (Rowley et al., 2011). To this end the charge for each experiment was built up of layers of dyed beads so that flow packages could be tracked throughout flow and deposition, as used in Rowley et al. (2014). Reported velocities are calculated by tracking these coloured sediment packages in the body of the current immediately prior to their deposition.

When reporting the length of a bedform, the distance from the onset of the stoss-side lamina to the termination of the lee slope on the depositional surface was measured. Thickness refers to the distance between the lowest point of a lamina in the bedform to the highest point of a lamina in that same bedform (Fig. 4.1g and 4.1h). Bedform lengths and thicknesses are reported, as opposed to wavelengths and amplitudes, as we do not produce repetitive trains of bedforms. This is because of the short nature of the experiments – the current is not sustained for long enough, and doing so would require an unfeasible amount of material under the current set-up.

4.4.3 Error measurements

Errors (2 s.d.) for various measurements are as follows: current thickness: ± 0.0013 m. Current velocity: ± 0.055 ms^{-1} . *Fr:* ±0.17. N_F : ±67,000.

4.5 Additional Information

4.5.1 Data Availability

Data supporting the graphs in Fig. 4.4 is derived from raw video files and is available in Supplementary Table B.1. One experimental run is available as Supplementary Movie B.1. Four other videos are available upon reasonable request.

==

Chapter 5

5. Characterising the flow-boundary zone in fluidised granular currents

==

Pyroclastic Density Currents (PDCs) are hazardous flows of hot gas and volcanic particles which have a diverse range of flow behaviours and depositional mechanisms. Using flume experiments of defluidising granular currents, analogous to dense PDCs, the region known in the volcanological literature as the flow-boundary zone is examined. This is the lower part of the current/upper part of the deposit, and its behaviour is thought to control the characteristics of the deposit. Here, the top of the flow-boundary zone is defined as equal to the top of the exponential tail of the velocity profile through the current. Using the viscous law of the wall to acquire shear velocity and shear stress it is shown how variations in parameters in the flow-boundary zone control deposition. In waning currents, the flow-boundary zone transitions from thin, high-shear granular-flow dominated, to thick, low-shear fluid-escape dominated, during the deposition of a sequence of steepening bedforms. This process results in inverse grading at the base of the deposit as initial high shear allows effective vertical particle segregation. Attention is also drawn to how the near-wall viscous sublayer of turbulent fluid flows is analogous to the flow-boundary zone in granular currents. This work demonstrates that PDC deposits are controlled by the characteristics of the flow-boundary zone, as well as factors such as the current's response to topography.

5. 1 Introduction

Pyroclastic density currents (PDCs) are hot mixtures of gas and volcanic particles commonly generated during explosive volcanic eruptions. Their ability to travel at high speeds over large distances makes them a deadly natural hazard (Sulpizio et al., 2014). PDCs range on a spectrum from dense to dilute (Branney & Kokelaar, 2002), and both dense and dilute particle support mechanisms can exist simultaneously in the same current (Breard et al., 2016). Even high concentration PDCs, however, are unusually mobile (Hayashi & Self, 1992; Calder et al., 1999) due to the presence of high gas pore pressures (e.g. Roche, 2012; Breard et al., 2019; Lube et al., 2019) which decrease frictional forces between particles.

PDCs deposit by progressive aggradation, where deposits form by the sustained build up of particles sedimenting from the lower boundary of the current (Fisher, 1966; Branney & Kokelaar, 1992). Hence, the characteristics of the region adjacent to the boundary, the flow-boundary zone, control the characteristics of the resulting deposit (Branney & Kokelaar, 2002; Sulpizio & Dellino, 2008; Zrelak et al, 2020). For example, a moderate-high concentration 'granular flow-dominated' flow-boundary zone deposits massive lithofacies. Conversely, stratification is usually thought to be the result of deposition from low concentration 'traction-dominated' flow-boundary zones (Branney & Kokelaar, 2002). Although the presence of stratification and bedforms in PDC deposits has traditionally been ascribed to deposition from low concentration PDCs, recent experimental work (Rowley et al., 2014; Chapter 4) has shown that structures with complex internal surfaces can be deposited from dense granular currents when fluidised.

5.1.1 Definitions used for the velocity profile and the flow-boundary zone

Velocity profiles of depositing granular currents typically have a concave down, exponential tail close to zero velocity and a quasi-linear region leading up to maximum velocity (e.g. GDR MiDi, 2004; Lube et al., 2007; Forterre & Pouliquen, 2008; Mangeney et al., 2010; Farin et al., 2014; Wang et al. 2019). Much less work has been done on dense granular currents in which the interstitial fluid plays an important role, although velocity profiles of fluidised granular currents have been described before (e.g. Girolami et al., 2010; Roche et al., 2010; Breard & Lube, 2017; Jessop et al., 2017). Typically these profiles show that velocity is non-zero at the base of the current and increases either linearly or concave-up towards the free surface, although maximum velocity may be lower than this. An exponential tail, however, is not recognised.

Here, the flow-boundary zone is defined as the basal region showing increasing acceleration with height from the top of the static deposit (concave-down curve in Fig. 5.1), which is distinct from the quasi-linear velocity increase with height above this. Because the particle concentration in the current and deposit is similar, and due to the extremely slow motion of particles towards the base of the exponential tail of the velocity profile it is not feasible to define the base of the flow/top of the static deposit as the point of zero velocity. Instead this boundary is defined as the point at which the velocity is 1% of the maximum velocity of that profile. A similar concept was used successfully for dense granular flows by Wang et al. (2019). The flow-boundary zone, then, includes the lower region of the current, as well as the mobile portion of the deposit. The (quasi) linear region of the velocity profile, which typically becomes concave up close to maximum velocity (U_{max}), is referred to as the granular flow (Fig. 5.1). This is bounded at the top by the free surface and the transition to the dilute cloud, however this study focuses on the dense granular current and does not consider the area above U_{max}. U_{max} is used instead of surface velocity as in many other studies on granular currents because in the dense regions of PDCs U_{max} can be below the free surface.

Here the evolution of velocity profiles of a fluidised granular current from its non-depositional phase through deposition of various bedforms is reported. PIV analysis allows the imaging of the flow-boundary zone and the identification of an exponential tail in the velocity profiles of the depositional phase, showing that i) a flow-boundary zone exists and ii) there is no definitive boundary between current and deposit. The law of the wall for the viscous sublayer is then applied to obtain shear velocity and shear stress data and describe how changing parameters in the flow-boundary zone affect the characteristics of the deposit, as well granular segregation processes.

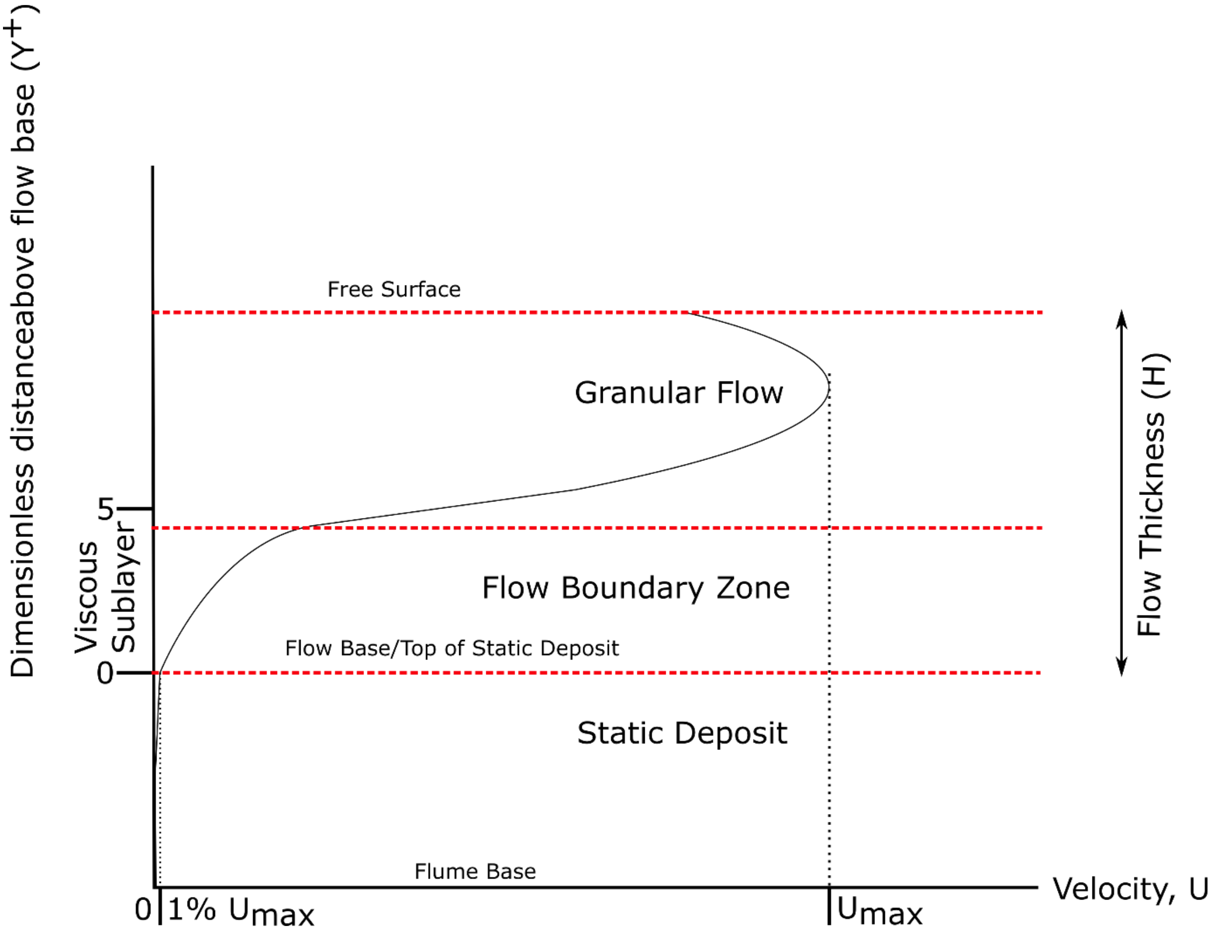

Figure 5.1 Schematic diagram of a velocity profile through a typical dense granular current. The profile is synthesised from various experiments (Taberlet et al., 2003; GDR MiDi, 2004; Girolami et al., 2010). See Table 5.1 for definitions.

Table 5.1 Terms, symbols, and definitions used in this chapter.

Term/Symbol	**Definition**
Flow-boundary zone	Zone of the velocity profile bounded by the top of the static deposit at the bottom and the transition to a linear velocity profile at the top.
Free Surface	Top surface of the Granular Flow.
g	Gravitational acceleration.
Granular Flow	Zone of the velocity profile bounded by the transition from flow-boundary zone to linear at the bottom, and the free surface at the top.
H	Thickness of the flow, from the base to the free surface.
(H-Y')/H	Height in the flow as proportion of H.
N_S	Savage number. Defined as $\frac{\rho_s\left(\frac{U}{H}\right)^2\delta^2}{(\rho_s-\rho_f)gH\tan\theta}$.
Re	Reynolds number. Defined as $\mathrm{Re} = \frac{U\rho H}{\mu}$.
Static deposit	Area between the flume base and the flow base.
Top of the static deposit/flow base	Height at which U = 1% U_{max}.
U	Velocity.
U_{max}	Maximum velocity below the free surface.
U_{mf_st}	Static minimum fluidisation velocity.
U^+	Dimensionless velocity. Defined as U/U*.
U*	Shear velocity. Defined as $\sqrt{\frac{U\mu_f}{Y\rho_f}}$.
V	Kinematic viscosity. Defined as $\mu f/\rho_f$.
Viscous Sublayer	Area between Y^+ 0 and 5.
Y	Distance above flow base.
Y'	Distance below free surface.
Y^+	Dimensionless distance from flow base. Defined as $(\rho_f U^* Y)/\mu$.
δ	Particle diameter.
Θ	Particle internal friction angle.
Θ_{Dyn}	Dynamic angle of repose.
μ	Bulk dynamic viscosity.
μ_f	Fluid dynamic viscosity.
ρ	Bulk density.
ρ_f	Fluid density.
ρ_s	Particle density.
τ	Shear stress. Defined as ${U^*}^2\rho_f$
τ_{max}	Maximum shear stress below the free surface.

5.2 Methods

5.2.1 Experimental Method

The experimental flume described in section 4.4.1 is used to simulate dense, granular PDCs and the formation of their deposits. The base of the flume comprises one-meter long sections which can provide independently controlled gas fluxes through a porous baseplate in each section in order to fluidise any overpassing material. The flume was kept at an angle of 2°, to promote flow away from the impingement surface while maintaining a sub-horizontal surface.

The air-supply plumbing allows a gas flux to be fed through the base of the flume, producing sustained aeration of the current. In such thin (<0.03 m), rapidly degassing laboratory currents, this enables the simulation of the long-lived high gas pore pressures that characterize thicker PDCs (Rowley et al., 2014; Chapter 3-4). Deposition was triggered by the absence of the gas flux in the second and third chambers of the flume. The first chamber always had a gas flux of 0.93 U_{mf_st}, so that experimental currents experienced significant deaeration after passing into the second chamber of the flume.

Experiments were recorded using a high-speed camera at 800 frames per second. This video recorded a side-wall area of the channel at 1 m runout (across the contact between the first and second gas supply chambers), allowing for measurement of the flow conditions. From the opening of the trapdoor to the cessation of deposition in the target area each experimental run lasted three to four seconds.

The experiments were performed using particles of spherical soda lime ballotini. The grain size distribution was bimodal, with one population of 45-90 μm (average δ_{32} = 63.4 μm calculated from six samples across the material batch) similar to the particles used in previous experimental granular currents (e.g. Roche et al., 2004; Montserrat et al., 2012; Rowley et al., 2014; Chapter 3-4). In order to accurately measure flow parameters, larger tracking particles, dyed black, were added to the sediment charge. This second population of 150-250 μm diameter particles comprised ~15% of the current. The 45-90 μm ballotini belong to the Group A classification of Geldart (1973), comprising particles which expand homogenously above U_{mf} until bubbles form, and which are non-cohesive. The fraction > 200 μm belongs to group B, where particles are less able to sustain a pore pressure (Roche et al., 2004), but this is only a small percentage of the entire particle mass. These particles do not affect the bulk Group A behaviour, as demonstrated in Roche et al. (2006); when the Group A fraction is >0.5 the whole current experiences Group A behaviour. As PDCs contain dominantly Group A particles, this allows dynamic similarity between the natural and experimental currents (Roche, 2012), ensuring that the experimental currents do not allow gas to escape too readily as would occur if the majority of particles were too cohesive or too coarse (Druitt et al., 2007). Detailed mechanical properties of the 45-90 μm particles are given in section 4.4.2.

The results reported here are taken from one experimental run. To test repeatability, the thickness of the deposit+current was measured from the base of the flume in five locations at four different points in time, for four separate currents. Analysis of Variance (ANOVA) tests show that for three of these points in time, the mean deposit+current thickness over all locations was similar across the repeats ($P > 0.05$). Raw data is presented in Supplementary Table C.1, and a visual comparison in Supplementary Figure C.1 (Appendix C). Only at 0.2 seconds was there a significant difference, due to current c being thinner at this point. As this is very soon after propagation began it is likely this difference in thickness resulted from unsteadiness caused by the initial impingement of the charge onto the base of the flume. Given the high P-values for the majority of the repeats it is reasonable to conclude that at a given point in time the average thickness of the current and its deposit does not vary significantly over multiple runs, variation over time is systematic and reproducible, and therefore the experimental run reported here is representative of its conditions.

5.2.2 Analytical Method

PIV analysis was carried out using the PIVlab toolbox for Matlab (Thielicke, 2014; Thielicke & Stamhuis, 2014), using the Fast-Fourier Transform (FFT) window deformation algorithm. This algorithm has been demonstrated to work in granular materials (Sarno et al., 2018).

Pixel (px) size in the analysed video frames was 9E-05 m, giving 1 px per frame = 0.07 m/s. Each analysis used four passes, with the interrogation window decreasing from 64 px in the first pass to 50 px, 36 px, and 22 px in the final pass. Using interrogation windows smaller than 22 px resulted in a very low signal to noise ratio. In a multi-pass analysis the interrogation window of the first pass should be three to four times the size of the maximum displacement between frames in order to reduce error (Sarno et al., 2018). As the vast majority of displacements in these granular currents are less than ~20 px (i.e. 1.4 m/s) this yields acceptable results.

Each analysis consisted of averaging five frames from the high speed video to generate a velocity field. Profiles of velocity magnitude were taken perpendicular to the free surface, and exported for analysis.

5.3 Results

5.3.1 Velocity fields and profiles

Deposits formed by the experimental granular currents were similar to those formed in the experiments described in Chapter 4. The formation of bedforms is marked by either diffuse stratification or by the angle of the surface of the aggrading deposit. Three types of bedform are identified: i) planar/very shallow backset (<2°) bedsets (Fig. 5.3b), ii) backset bedforms with shallow stoss sides less than the dynamic angle of repose ($< \Theta_{Dyn}$, Fig. 5.3c), and iii) backset bedforms with steep ($>\Theta_{Dyn}$) stoss sides (Fig. 5.3d).

Figure 5.2 shows representative velocity fields for the non-depositional phase of the current (Fig. 5.2a), and for the current during the deposition of planar, shallow, and steep bedforms (Fig. 5.2b-d).

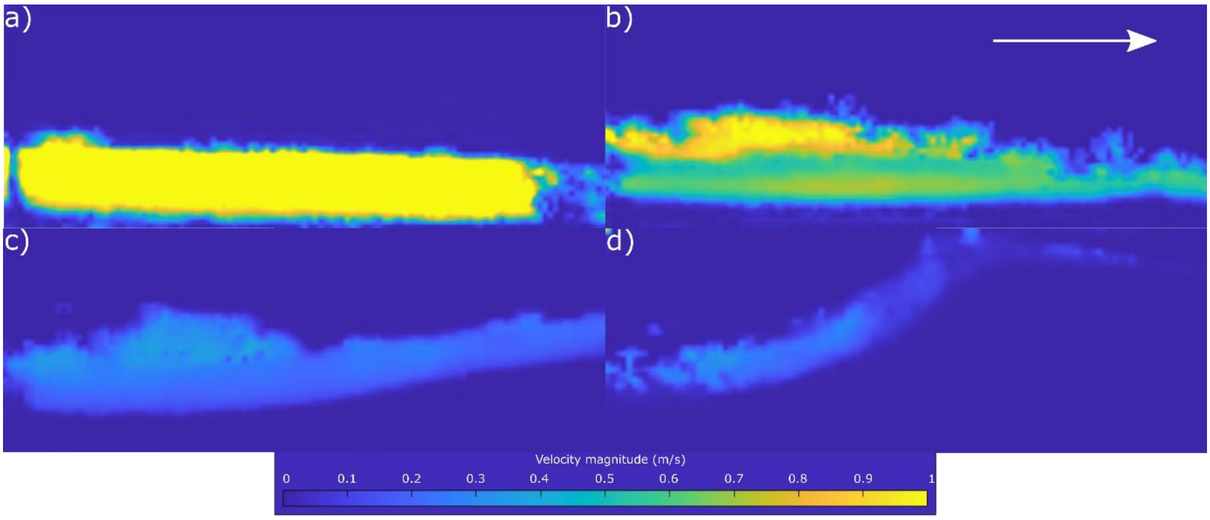

Figure 5.2 Representative velocity field for various phases of the the experimental granular current. **a** Non depositional phase. **b** During deposition of planar bedforms. **c** During deposition of shallow stoss-side bedforms. **d** During deposition of steep stoss-side bedforms. Note that velocities greater than 1 m/s are not shown here.

Figure 5.3 shows representative velocity profiles generated at regular intervals from the velocity fields, superimposed over video frames for the non-depositional phase of the current (Fig. 5.3a), and for the current during the deposition of planar, shallow, and steep bedforms (Fig. 5.3b-d). All velocity profiles can be found in Appendix C.

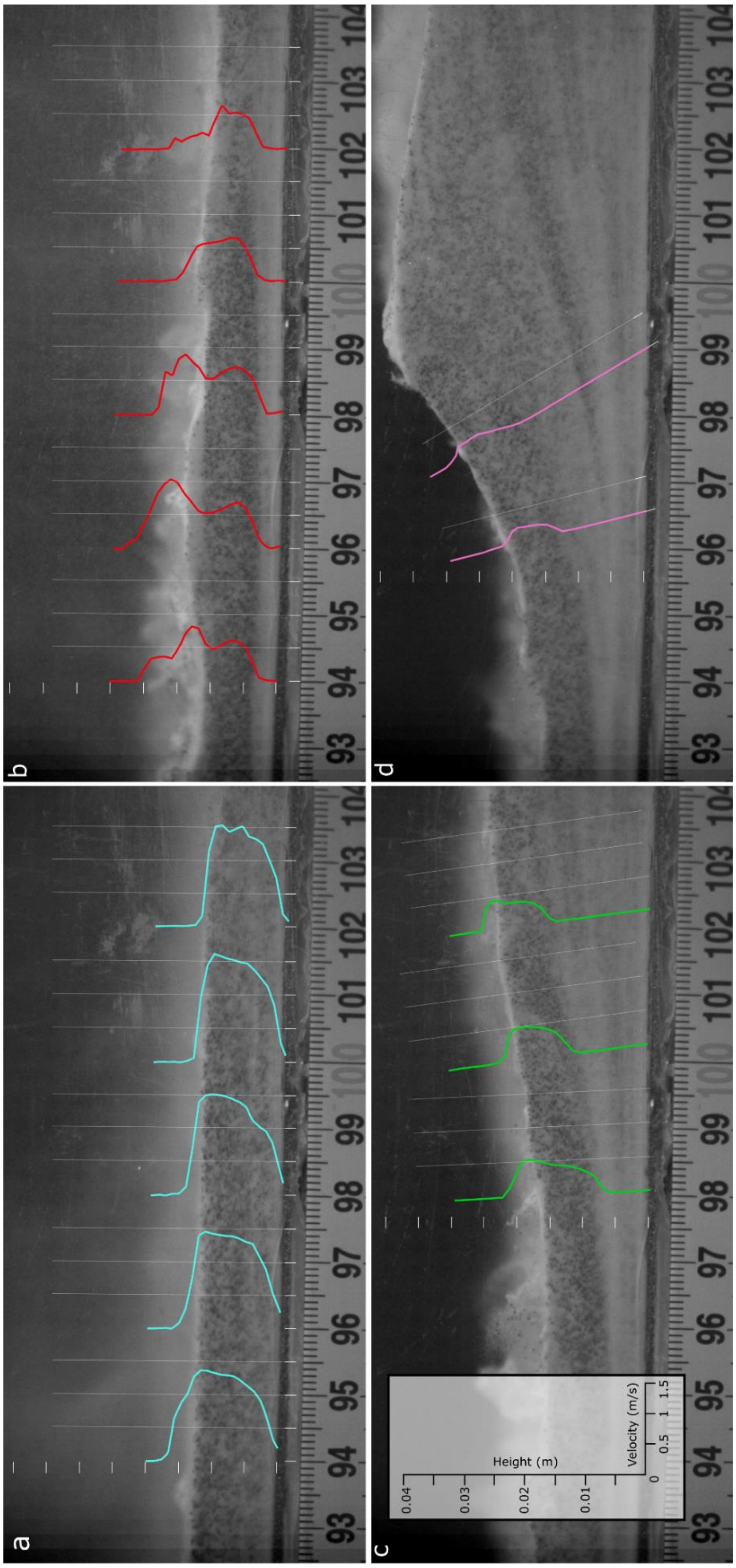

Figure 5.3 Snapshots of a granular current at different phases of its evolution, with velocity profiles superimposed on top, perpendicular to flow direction. **a** Non-depositional phase **b** Depositing planar bedforms **c** Depositing shallow stoss-side bedforms **d** Depositing steep stoss-side bedforms. Velocity intervals are 0.5 m/s and height intervals are 0.005 m, as seen on inset example. Height is above the flume base.

Velocity profiles from the non-depositional phase of the current consist of one or two quasi-linear gradients leading up from non-zero velocity at the base to U_{max}. Velocity profiles from close to the head of the current are very linear. There is occasionally a very small concave-down zone at the base of the velocity profiles from the non-depositional phase. The mean slip at the base of the non-depositional current is 0.46 m/s. Where the velocity profile consists of more than one quasi-linear gradient the upper one is considerably steeper, sometimes almost vertical (Fig. 5.3a). This is similar to the velocity profiles through the non-expanded fluidised granular currents of Girolami et al. (2010) and velocity profiles through the basal granular flow of Breard and Lube (2017). In Figure 5.3a, the two gradients are approximately concordant with inverse grading within the current, with almost uniform velocity in the coarser part of the current. The velocity profiles seen in the depositing phases of the current, meanwhile, generally consist of a concave down zone, with an exponential tail tending towards zero, and a quasi-linear or concave up profile leading to U_{max} above this (Fig. 5.3b-d).

Within the granular current, U_{max} decreases with increasing steepness of the bedforms being deposited (see also section 4.2.3). The gradient of the velocity profiles below U_{max} for the current in its depositional phase increases with increasing bedform steepness. The position of U_{max} as a proportion of flow thickness (H) varies. Expressed as (H-Y')/H, the average position of U_{max} across all phases of deposition is 0.76, but it can be lower than this, especially during the deposition of planar bedforms, where over 25% of recorded U_{max} were below 0.6 (ranges are plotted in Figure 5.4a). When the current is non-depositional or depositing shallow bedforms, U_{max} in velocity profiles is close to the free surface. The outliers in the non-depositional dataset are from less than 0.03s after the passage of the leading edge of the current. Velocity profiles from when the current is depositing planar bedforms show the most complexity and often have two velocity peaks, with U_{max} either very close to the free surface or ~60% flow thickness, resulting in a range from 0.57-1. For velocity profiles from when the current is depositing steep bedforms U_{max} is ~75% flow thickness, and has the most restricted range, of 0.61-0.83.

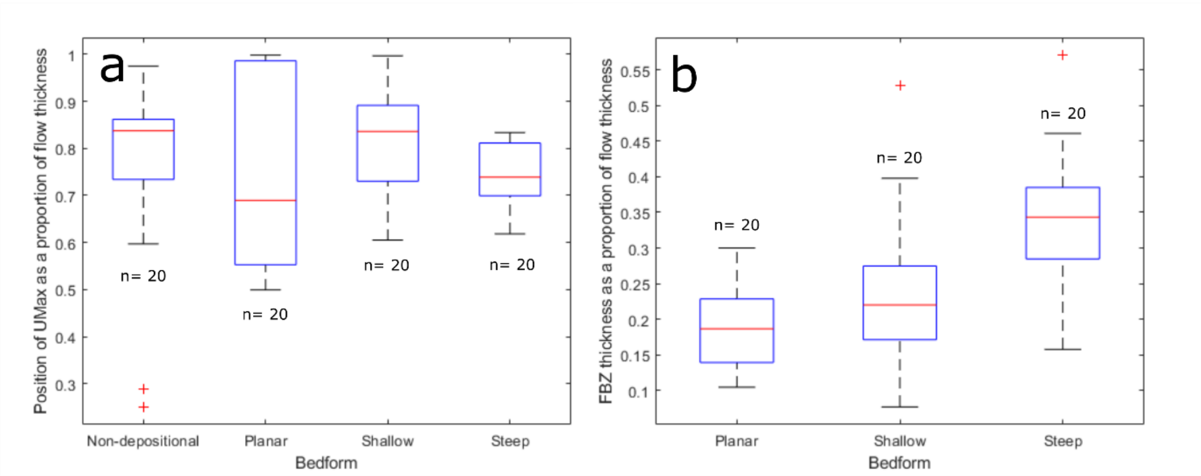

Figure 5.4 a Box plot showing the position U_{max} as a proportion of flow thickness, or (H-Y')/H, for different depositional phases of the current. Red line is the median, blue box is the interquartile range. Dashed lines indicate values less than the 1st quartile or greater than the 3rd quartile, and red crosses are outliers. **b** Box plot showing the position of the top of the flow-boundary zone as (H-Y')/H (and so its dimensionless thickness) for currents depositing different bedforms.

5.3.2 Quantifying the flow-boundary zone

5.3.2.1 By velocity profile

The top of the flow-boundary zone at any given point in the current is defined as the inflection point at which the velocity profile first begins to deviate (concave down) from the quasi-linear portion of the profile – the granular flow (see Fig. 5.1) – assuming that this point is both < 50% U_{max} and that the angle between the gradients is > 5°. This is to ensure that the flow-boundary zone top is chosen based on perturbations related to deposition of particles, and not minor fluctuations in velocity within the granular flow, or larger fluctuations more closely associated with U_{max}. No flow-boundary zones were defined for the non-depositional phase of the current; even where small concave down regions were present at the base of velocity profiles, because the base of the current at this point is travelling at far greater than zero velocity. The velocity within the flow-boundary zone generally tends exponentially towards zero, but when the current is depositing planar bedforms velocity may actually increase towards the flow base (e.g. profile at 98 cm in Figure 5.3b). As the current is still travelling relatively fast when depositing planar bedforms velocity rarely decreases to 1% of U_{max}, meaning that at many points the whole deposit is technically part of the flow-boundary zone although stationary to the naked eye.

Figure 5.4b shows the ranges of the thickness of the flow-boundary zone for velocity profiles of the current when depositing planar, shallow, and steep bedforms as a proportion of the flow thickness (H-Y'/H). The thickness of the flow-boundary zone increases slightly from the deposition of planar to shallow bedforms and significantly from the deposition of shallow to steep bedforms: the interquartile ranges of the shallow and steep bedform datasets do not overlap. Despite the small increase in flow-boundary zone thickness from deposition of planar to deposition of shallow bedforms, the flow-boundary zone of the current during deposition of shallow bedforms has a much greater range of thicknesses than during deposition of planar bedforms (0.05-0.4 compared to 0.12-0.32).

5.3.2.2 Application of the viscous Law of the Wall

Field studies have inferred that shear intensity in the flow-boundary zone is an important control on deposit characteristics (Branney & Kokelaar, 2002; Sulpizio et al., 2014; Pollock et al., 2019; Zrelak et al., 2020), but absolute values of shear parameters are difficult to establish from interpretation of deposits. Here this control is quantified by calculating shear velocity and shear stress values by treating the dense granular current as analogous to the wall-adjacent viscous sublayer in clean-water channel flows.

The Law of the Wall is used for estimating the velocity of turbulent (high *Re*) flow, parallel to the wall (or flow base). The Reynolds Number (*Re*) is the ratio of inertial to viscous forces and can be expressed as:

$$Re = \frac{U\rho H}{\mu} \qquad \text{(Eq. 5.1)}$$

where U is velocity, ρ is density, H is flow thickness, and μ is viscosity. For these experimental currents, using bulk flow values of U = 0.5 m/s, H = 0.01 m ρ = 2500 kg/m^3, and μ = 167 Pa gives *Re* = 0.075, significantly below the laminar-turbulent transition and demonstrating the clear dominance of viscous forces. Bulk ρ and μ values were calculated following Wohletz (1998), using a ρ_f of 1.225. The small scale of these experimental currents contributes to the very small *Re*, which is less than what would be expected in natural granular currents. In natural PDCs, typical U and H values range from 5-30 m/s and 1-50 m respectively (Roche, 2012). However even scaling the velocity and thickness up by a factor of 10 towards these more realistic values results in *Re* = 7.5, still far below the turbulent zone.

The viscous sublayer is the portion of the velocity profile in aqueous systems where viscous forces dominate. It can be estimated using part of the Law of the Wall expressed as follows:

$$\frac{\overline{U}}{U^*} = \frac{\rho_f U^* Y}{\mu_f} \qquad \text{(Eq. 5.2)}$$

where $\overline{U}$ is the time-averaged velocity, U* is shear velocity, ρ_f is fluid density, μ_f is fluid viscosity and Y is distance from the flow base (Southard, 2006). It can also be expressed as:

$$U^+ = Y^+ \qquad \text{(Eq. 5.3)}$$

where dimensionless velocity $U^+ = U/U^*$ and dimensionless distance from the flow base $Y^+ = (\rho_f U^* Y)/\mu$. Y^+ can also be written as:

$$Y^{+} = \frac{U^{*}Y}{V} \quad \text{(Eq. 5.4)}$$

where V is the kinematic fluid viscosity, μ_f/ρ_f.

Equation 5.2 is only applicable in the viscous sublayer, where $Y^+ < 5$. However due to the very low *Re* of these experimental granular currents it is likely to be valid throughout their thickness and provide a better approximation than the standard Law of the Wall. It must be noted, however, that Equation 5.2 is derived for dynamically smooth flow and that it may not be applicable to two-phase flow which is dynamically rough. Hence, the equation has been applied here purely to explore possible values of shear velocity and shear stress, and to show general flow behaviour across the experiment, and is not validated.

Equation 5.2 can be rearranged to provide shear velocity U*:

$$U^{*} = \sqrt{\frac{U\mu_f}{Y\rho_f}} \quad \text{(Eq. 5.5)}$$

and as shear stress τ is related to U* the following equation can then be used:

$$\tau = {U^{*}}^{2}\rho_f \quad \text{(Eq. 5.6)}$$

Figure 5.5 shows calculated U* and τ values for velocity profiles of the current during different stages of deposition. Values are presented as depth-averaged throughout the flow-boundary zone (Fig. 5.5d), the granular flow (Fig. 5.5c), and both together (Fig. 5.5a), as well as the basal values from the flow-boundary zone (Fig. 5.5f) and the granular flow (Fig. 5.5e) in depositional currents, and basal values from the non-depositional phase of the current (Fig. 5.5b).

Shear velocity and shear stress calculated as depth-averaged values for the whole velocity profile below U_{max} are higher in the non-depositional phase than in the depositional phases (Fig. 5.5a). The general trend shows that as U* and τ in both the granular flow and the flow-boundary zone decrease the current begins to deposit. As the current wanes and deposits bedforms of increasing steepness, U* and τ continue to decrease.

Depth-averaged U* and τ in the flow-boundary zone are lower than depth-averaged granular flow values (Fig. 5.5c and 5.5d). Planar bedforms are deposited when the current has high U* and τ (Fig. 5.5a, d and f) and a thin flow-boundary zone (Fig. 5.4b), where shear is noticeably higher at the base (Fig. 5.5f). Further decreases in U* and τ result in the deposition of shallow stoss-sided bedforms, also from a thin flow-boundary zone (Fig. 5.4b). The lowest U* and τ values are from when the current deposits steep stoss-sided bedforms, from a thicker flow-boundary zone (Fig. 5.4b). The highest U* and τ values are seen in the non-depositing current, and are higher in the basal section (Fig. 5.5b). There is very little overlap in U* and τ between the non-depositional and depositional phases of the current (Fig. 5.5a), whereas there is considerable overlap between these values during the deposition of the different bedforms.

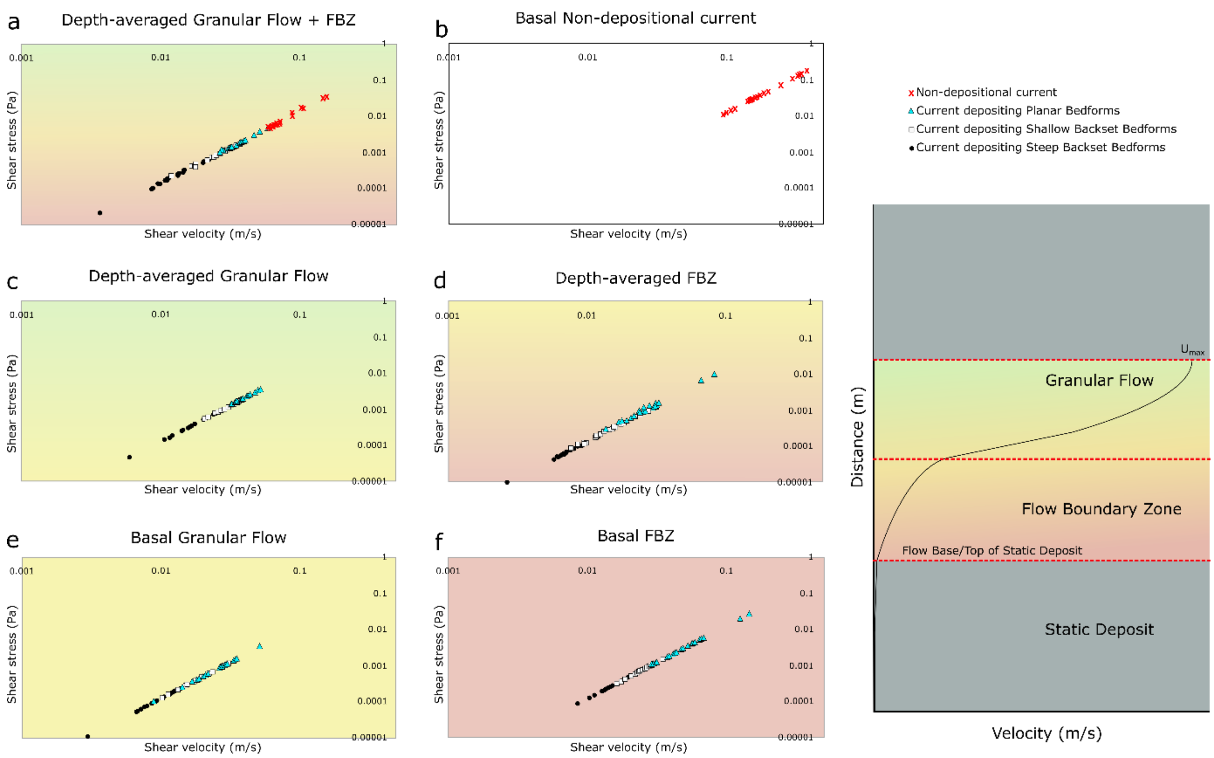

Figure 5.5 Shear velocity and shear stress values for an experimental current. Each data point represents either a single depth-averaged velocity profile or the basal point of a velocity profile. 20 velocity profiles were examined for each depositional phase (non-depositional, planar bedforms, shallow backset bedforms, and steep backset

bedforms). Shear velocity and shear stress decrease as steeper bedforms are deposited. **a** shows the values depth-averaged through the whole current. **b** shows the values at the base of the current while it is non-depositional. **c** shows the values depth-averaged through the granular flow part of the current only. **d** shows the values at the base of the granular flow part of the current only. **e** shows the values depth-averaged through the flow-boundary zone. **f** shows the values at the base of the flow-boundary zone. **g** is a modified version of Figure 5.1 showing the location on the velocity profile (of a depositing granular current) of the previous plots.

5.3.3 Savage Numbers

The Savage Number (N_S) is the ratio of collisional to frictional stresses within a granular current; lower numbers show the dominance of intergranular friction as a mechanism of momentum transfer. It can be written as:

$$N_S = \frac{\left(\frac{U}{H}\right)^2 \delta^2 \rho_s}{(\rho_s - \rho_f) g H \tan\theta} \qquad \text{(Eq. 5.7)}$$

where δ is particle diameter, ρ_s is particle density, g is gravitational acceleration and Θ is the particle internal friction angle. Figure 5.6 shows the range of N_S calculated from the velocity profiles of the current during the deposition of the three bedform types, and from the non-depositional phase.

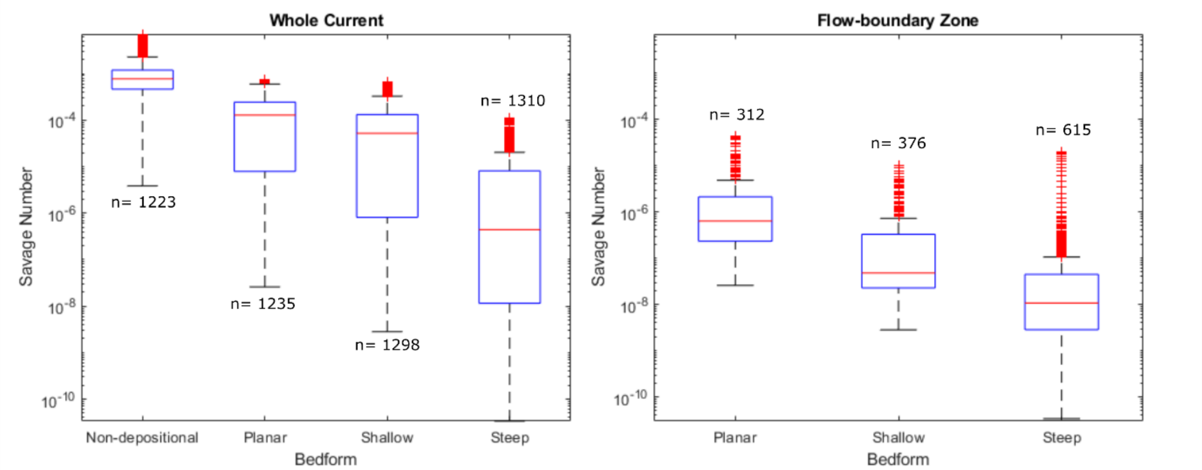

Figure 5.6 Box plots showing the ranges of Savage Numbers for the experimental current when depositing different bedforms and for the non-depositional current. **a** Through the whole current. **b** Through the flow-boundary zone only. Red line is the median, blue box is the interquartile range. Dashed lines indicate values less than the 1st quartile or greater than the 3rd quartile, and red crosses are outliers.

There is a decrease in N_S with increasing steepness of the bedform being deposited, which is more pronounced when looking solely at the flow-boundary zone. Here, velocity profiles in the current above planar, shallow, and steep bedforms have median N_S of 4 x 10^{-6}, 6 x 10^{-7}, and 6 x 10^{-8} respectively (Fig. 5.6b). The median N_S for velocity profiles from the non-depositional phase is 10^{-3}. This is higher than for any from the depositional phase, and importantly there is no overlap between the interquartile ranges of the non-depositional and depositional datasets, unlike between the three depositional datasets themselves.

5.4 Discussion

5.4.1 Velocity and shear stress profiles

The experimental granular currents follow a pattern of decreasing depth-averaged shear velocity and shear stress at one location as velocity decreases and the deposit aggrades, although there are some interesting features hidden by the depth-averaging. Shear stress, for example, typically increases downwards through the flow-boundary zone, even when velocity is consistently decreasing over the same interval (Fig. 5.7). This is especially evident during the deposition of planar bedforms (Fig. 5.5e- f). Above the flow-boundary zone, shear stress increases quasi-linearly over a short distance to τ_{max}, which is closer to the top of the flow-boundary zone than it is to U_{max} (Fig. 5.7).

The combination of these patterns means that shear stress is higher on average in the granular flow than the flow-boundary zone, but decreases throughout the lower granular flow, and the lowest shear stress is mostly seen in the mid-upper flow-boundary zone. At this location particles are furthest from both the static deposit and the fast upper granular flow.

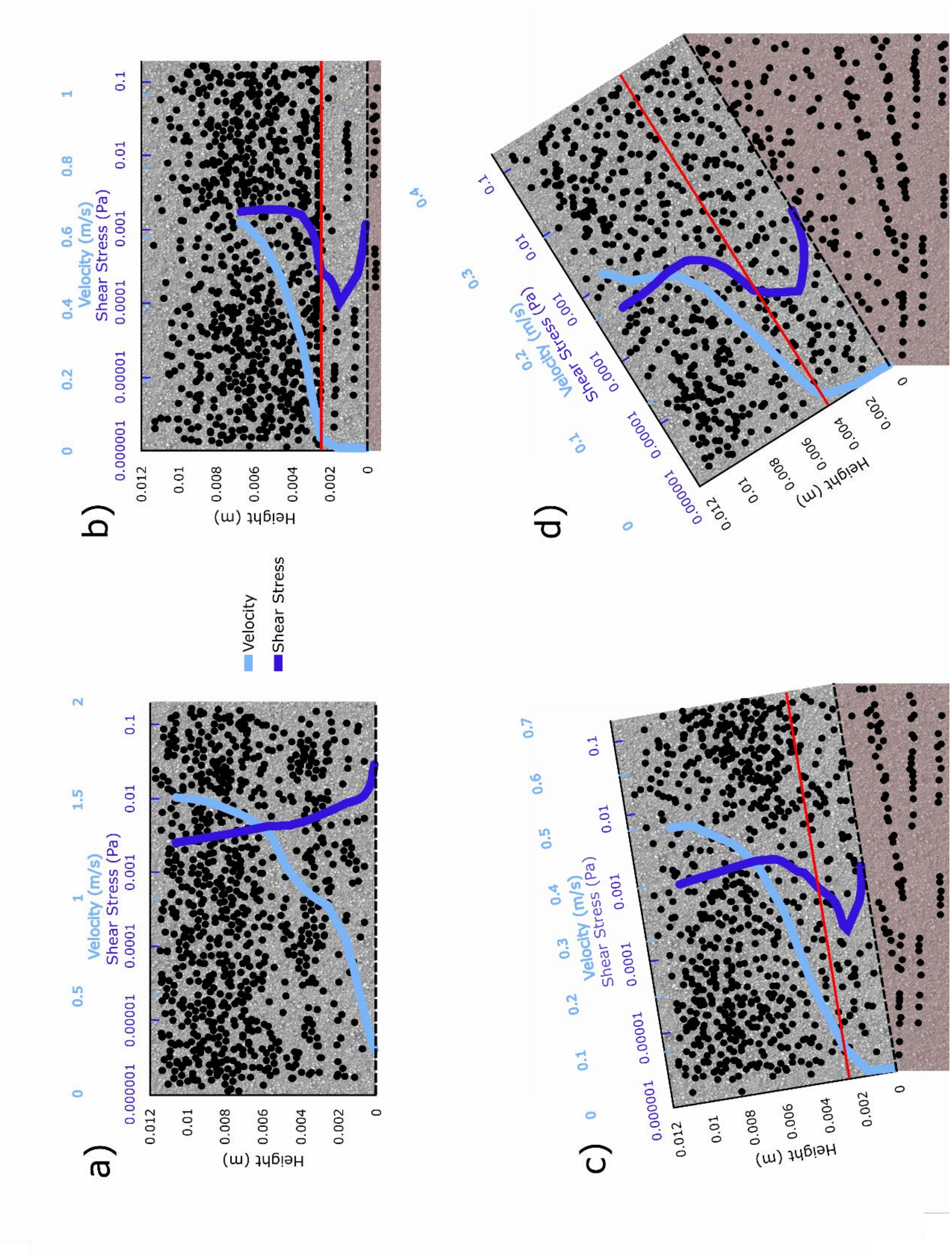

Figure 5.7 Schematic figures and representative velocity (pale blue) and shear stress (dark blue) profiles for the **a** non-depositional phase, deposition of **b** planar beds **c** shallow stoss-sided bedforms **d** steep stoss-sided bedforms. Height is from the flow base to U_{max}. These profiles are from the same snapshots seen in Figure 5.2 (a = 98 cm, b = 94 cm, c = 100 cm, d = 96 cm). The top of the flow-boundary zone is marked by a red line. Black dots represent the coarser particle fraction. Grey stipple is the moving current and mauve stipple the static deposit. Note different velocity scales.

The inflection point at the top of the flow-boundary zone is usually quite sharp (Fig. 5.7b + d), which implies poor coupling between the flow-boundary zone and the granular flow (Breard et al., 2016; Breard & Lube, 2017). In some cases the inflection point is much less sharp (Fig. 5.7c), suggesting low traction between the two zones. Although Figure 5.7c shows the velocity profile during deposition of shallow backset bedforms this behaviour is actually more common during deposition of steep bedforms, perhaps due to the overall waning of the current.

Shear velocity has been calculated for PDCs by numerous authors, although typically focusing on the dilute regime (e.g. Dellino et al., 2004; Dellino et al., 2008; Doronzo et al., 2010; Dioguardi & Dellino, 2014). The range of shear velocities derived is 0.62-3.07, considerably higher than values from this study, which range from 0.001 to 0.383. Estimates for subaqueous PDCs are 0.008-0.033 (Maeno & Imamura, 2007) and 0.022 (Doronzo & Dellino, 2010). These overlap with values from these experiments, possibly as similar to the granular currents, and unlike lofting dilute PDCs, they are denser than their surrounding fluid. Choux and Druitt (2002) suggest that shear velocity is 10-30% of average flow velocity. Although meant for dilute currents the lower limit is a reasonable approximation for the whole current depth-averaged shear velocities presented here when using average velocities of 1.2, 0.4, 0.3, and 0.1 m/s for the non-depositional through to steep backset bedform depositing phases. Therefore, the shear velocities and stresses presented here are representative of dense PDCs.

5.4.2 Particle Segregation

The experimental granular currents and their deposits were largely homogenous in grain size distribution, with the larger particles remaining well mixed within the dominant smaller particle population. However, there is some evidence of particle segregation. Transient inverse grading is visible during the non-depositional phase (Fig. 5.3a), especially close to the current head (Fig. 5.8). Inverse grading also exists at the base of the deposit (Fig. 5.3b), where dominantly finer particles have been deposited (although some deposition of coarser particles forms weak stratification).

Size segregation in dense granular currents is well documented, generally forming inversely graded deposits (e.g. Iverson & Vallance, 2001; Pittari et al., 2005; Gray, 2018). This is commonly attributed to gravity-driven segregation (Vallance & Savage, 2000; Gray et al., 2015; Baker et al., 2016; Gray 2018) in the form of kinetic sieving and squeeze expulsion (Middleton, 1970; Savage & Lun, 1988), where larger particles are forced towards the free surface, allowing the preferential deposition of smaller particles. The gravity-driven segregation that causes inverse grading is controlled by shear (Bridgwater et al., 1985; Savage & Lun, 1988; Branney & Kokelaar, 2002), so variations in the shear rate/ stress will affect the amount of vertical segregation taking place. As described in Branney and Kokelaar (2002), a decreasing shear rate, or increasing sedimentation rate, in a waning flow-boundary zone will allow progressively larger particles to deposit.

Particle segregation in the granular current may have been dampened due to the interstitial fluid. Due to the great density difference between the particles and the fluid (air), however, this effect is likely negligible (Thornton et al., 2006; Vallance & Savage, 2000). The inverse grading that is seen at the base of the deposit can be explained by unsteadiness in the current - initially high shear rates at the base of the current cause the larger particles to rise higher in the current and overpass, but as the current wanes lower shear rates (and perhaps an increasing deposition rate) prevent effective gravity-driven segregation, and deposition of both coarse and fine particles is allowed (Fig. 5.7 shows decreasing shear stress over time in one area of the flume).

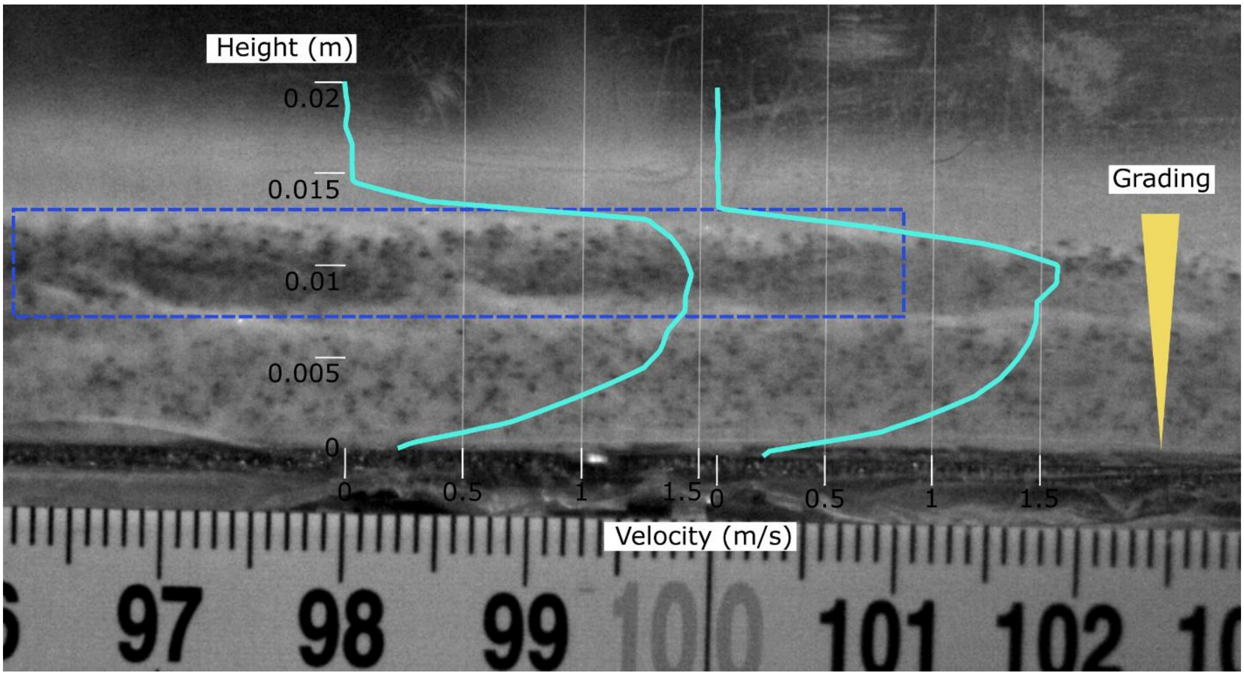

Figure 5.8 Inverse grading during the non-depositional phase, with velocity profiles. Blue box highlights the greater concentration of coarser particles. This snapshot is approximately 0.085 s behind the current head.

There is also some evidence of lateral grading in the final deposit – concentrations of coarse particles are seen at the free surface towards the distal end of the deposit, presumably due to their overpassing as described above. In one experimental run a higher concentration of coarse particles upstream of the steep backset bedforms was observed – this could be an effect of the stoss-side blocking/granular jamming mechanism described in Douillet et al. (2018) and section 4.3. Alternatively this could simply represent a concentration of coarse particles in the initial sediment charge.

5.4.3 Deposition of bedforms

Chapter 4 established that an upstream series of steepening bedforms are deposited by a rapidly defluidising granular current. Repeating those experiments here it is seen that as the current wanes and steeper bedforms are deposited, the flow-boundary zone becomes concomitantly thicker (Fig. 5.4b). Once deposition begins it continues as long as the current is in motion, without any pauses but at varying rates. This is different to the stepwise aggradation observed in previous experiments (section 3.4.4), although this work examines a very restricted and relatively proximal area.

Profiles of concentration are not taken through this current, but particle volume fraction is uniformly high. In terms of Branney and Kokelaar's (2002) classification of flow-boundary zones, therefore, only granular-flow dominated (Fig. 5.9c) and fluid-escape dominated (Fig. 5.9d) are applicable. During the deposition of planar bedforms, shear is still relatively high, especially at the base of the flow (Fig. 5.7b), resulting in a relatively thin flow-boundary zone, and it is not uncommon for the velocity gradient in the flow-boundary zone to start increasing downwards. This level of shearing increases particle-particle collisions and is recorded in the relatively high N_s (Fig. 5.6b). However, as mentioned above, segregation favouring the deposition of fine particles is active during this time so stratification is weak/absent. As there is relatively high shear at the base of the current and there is a clear interface between current and deposit, the flow-boundary zone during deposition of planar bedforms can be classified as granular-flow dominated (Fig. 5.9c; Branney & Kokelaar, 2002).

During the deposition of shallow backset bedforms shear at the base of the current has decreased as the current wanes, which also causes the cessation of the vertical segregation preventing deposition of coarse particles, resulting in relatively well-defined backset beds (Fig. 5.3c+d, Fig. 5.7c+d). Otherwise the processes are very similar as during the deposition of planar bedforms; there is not much difference in flow-boundary zone thickness (Fig. 5.4b), and it too could be classified as granular-flow dominated. Velocity profiles descend exponentially towards zero, and reach 1 % U_{max} relatively quickly.

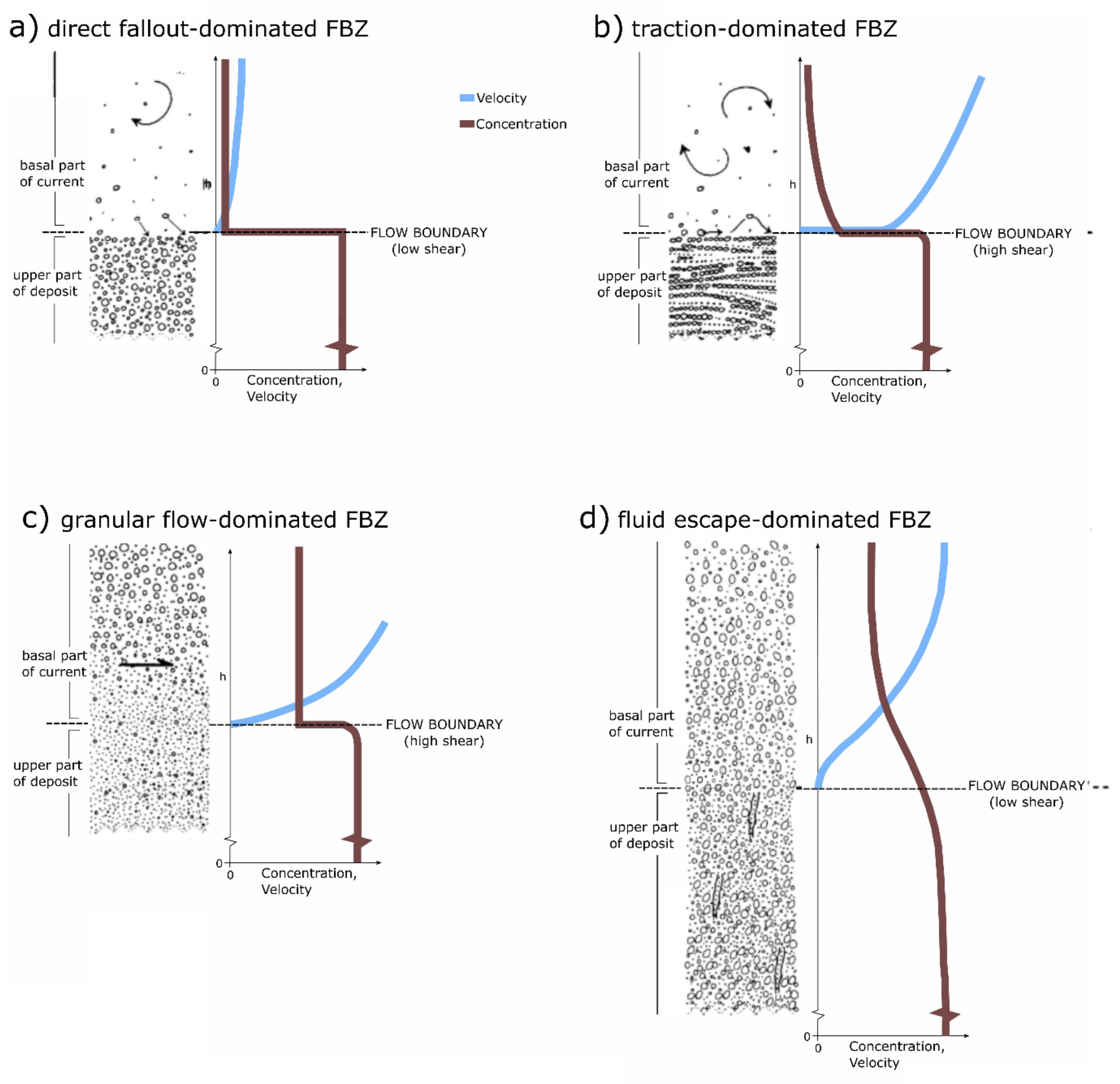

Figure 5.9 Schematic representations of the four end-member flow-boundary zones, modified from Branney and Kokelaar (2002) with velocity (blue) and concentration (brown) profiles.

When the steep backset bedforms are being deposited the current has slowed drastically due to blocking by the growing deposit, and there is no segregation of particles in the current or deposit due to the low shear (Fig. 5.7d). As the deposit is thick by this point it is more difficult for the upwards gas flux to reach the current and decrease frictional forces between particles. Nevertheless pore pressure is still present, as rapid deposition results in soft-sediment deformation from expulsion of the interstitial fluid. Despite the internal deformation, the lowest N_s recorded occur in this flow-boundary zone (Fig. 5.6b) suggesting a highly frictional regime. This all results in a deposit difficult to distinguish from the current, and the velocity profile, although already recording very small velocities, possesses a very long exponential tail before reaching 1% of U_{max}, (Fig. 5.7d) resulting in a very thick, sluggish flow-boundary zone (Fig. 5.4b). Due to the low shear, homogenous particle dispersal, and lack of a sharp interface between current and deposit, the flow-boundary zone here would be classified as fluid-escape dominated (Fig. 5.9d; Branney & Kokelaar, 2002). As the steep stoss-side layers seen in Chapter 4 are interpreted as resulting from rapid deposition and topographic blocking rather than traction, the low levels of shear in a fluid-escape dominated flow-boundary zone support this classification.

5.4.4 The flow-boundary zone vs. the viscous sublayer

Figure 5.10 shows a remarkable correlation between the height of the top of the flow-boundary zone and the height of the top of the viscous sublayer (calculated by treating the current as clear water). These were calculated independently; the top of the flow-boundary zone by an inflection point in the velocity profile, and the top of the viscous sublayer by the point at which $Y^+ = 5$. As seen in equations (3) and (4) Y^+ is dependent on velocity, which may account for the similarity. Nevertheless, as the viscous sublayer is a concept used for clear-water channel flow it is interesting that it delineates the slower, depositing zone of a dense granular current.

The calculations show that top of the viscous sublayer, if it existed in the experimental current, is systematically higher than the top of the flow-boundary zone. This could be because i) the top of the flow-boundary zone was underestimated and a higher inflection point should have been chosen or ii) the top of the viscous sublayer was overestimated – perhaps a larger μ should be used to account for pressurised, dusty gas. Alternatively the difference could simply be explained in that the law of the wall for the viscous sublayer is not strictly applicable to granular systems.

A much greater scatter in the data is seen for currents depositing steep bedforms than those depositing planar and shallow bedforms. As explained in section 4.3 and section 5.4.3, the planar-shallow-steep sequence of bedforms seems to record a current increasingly dominated by frictional stresses over viscous ones. Hence, the correlation becomes more nebulous as steep backset bedforms are deposited.

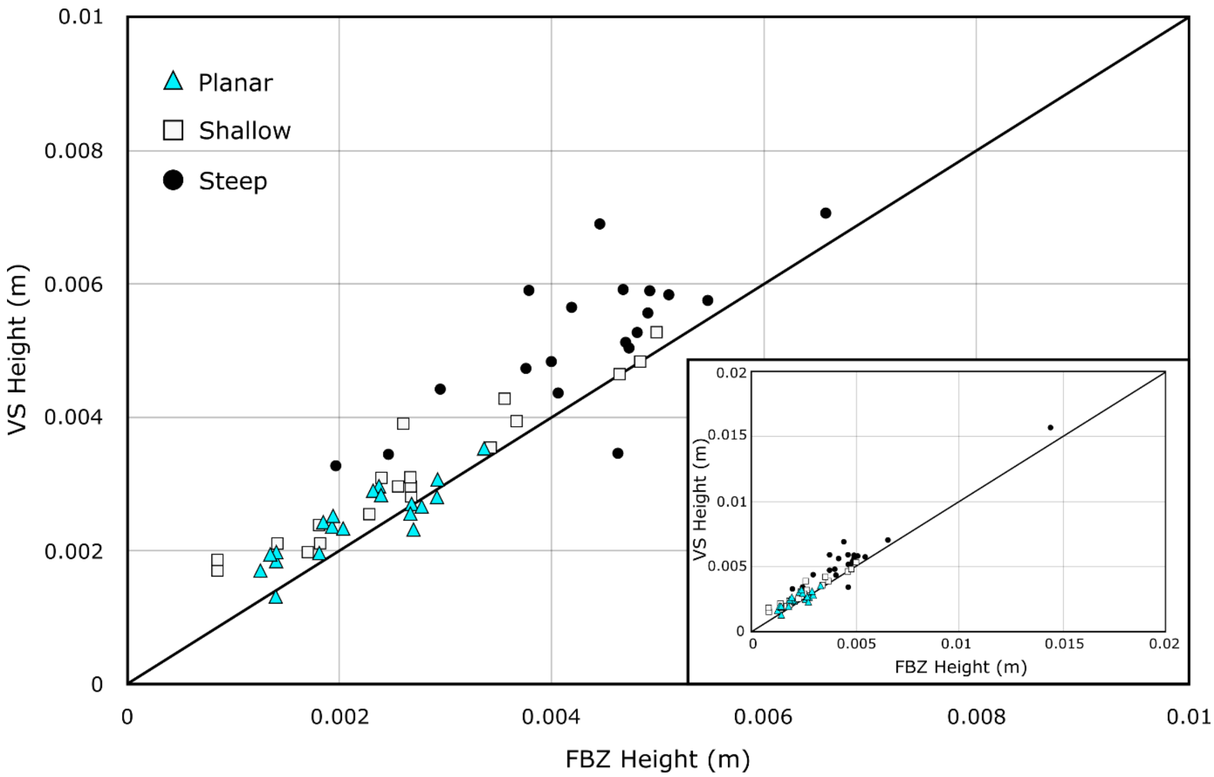

Figure 5.10 Correlation between the height of the top of the viscous sublayer and the height of the top of the flow-boundary zone for the current as various bedforms are deposited. Inset shows outlier in the top right.

5.5 Conclusions

The concept of the flow-boundary zone has been widely adopted in volcanology since its introduction (e.g. Sulpizio & Dellino, 2008; Brown & Branney, 2013; Sulpizio et al., 2014; Breard et al., 2015; Brown & Andrews, 2015), yet little work has been done to validate it experimentally. This study demonstrates that bedforms are not entirely restricted to traction-dominated flow-boundary zones as is commonly supposed, and that characteristics of granular-flow dominated and fluid-escape dominated flow-boundary zones are clearly seen in experimental dense granular currents.

The depositional sequence of planar-shallow-steep bedforms records the transition of the flow-boundary zone from granular-flow to fluid-escape dominated. The waning current, slowed by the steepening deposit, sees decreasing shear in the flow-boundary zone, which is manifested in decreasing effectiveness of particle size segregation. The experiments suggest that conditions in the flow-boundary zone drive the depositional behaviours as previously surmised from field studies. However other factors must also be taken into account when interpreting deposit structure, such as the angle of the aggrading deposit and the presence of topography (section 4.3). Once deposition begins it is continuous, although unsteady, showing that these currents deposit by gradual progressive aggradation. Furthermore, the viscous law of the wall yields shear velocities for these currents which are similar to those estimated for PDCs denser than their surrounding fluid, suggesting that this is an acceptable method to investigate dense granular currents close to the wall, and that results presented here are applicable to natural PDCs. It also correlates well with the suggested method of quantitatively defining the flow-boundary zone using the velocity profile.

Chapter 6

6. Quantifying the geometries of backset bedforms in pyroclastic density current deposits

Upstream-dipping, stoss-aggrading “backset” bedforms are commonly found in the deposits of pyroclastic density currents (PDCs). They are traditionally interpreted as recording the passage of highly energetic dilute PDCs, although recent work, including analogue experiments, has begun to challenge this. Backset bedforms in the field span a range of sizes and stoss and lee angles, so a robust dataset is required in order to validate experimental examples. Here, backset bedform geometry data is collated from a literature review and fieldwork, and this data is compared with experimental examples. Backset bedforms are generally symmetrical or have steep stoss and gentle lee slopes, although the first group is much more populated. Experimental backset bedforms overlap much of this data, and steep experimental backset bedforms show particular similarities with examples from Mt St Helens and Laacher See. Length and thickness are very well correlated and a numerical relationship is defined. Experimental backset bedforms plot on this trend but are not well correlated themselves, perhaps due to small sample numbers. The similarities in geometry between field and experimental backset bedforms allow the latter to be used in interpreting the flow and depositional conditions within PDCs. Finally, some recommendations regarding the reporting of backset bedforms in PDCs are made.

6.1 Introduction

Bedforms are often found in pyroclastic density current (PDC) deposits and a wide variety have been documented (e.g. Crowe & Fisher, 1973; Schmincke et al., 1973; Sigurdsson et al., 1987; Cole, 1991; Giannetti & Luongo, 1994; Douillet et al., 2013; Brand et al., 2016). The analogue experiments described in the previous two chapters produced planar bedforms as well as upstream-migrating backset bedforms, some of which have unusually steep stoss laminations. Stoss-aggrading structures have been described in PDC deposits by numerous authors using various terminology, including antidunes (e.g. Crowe & Fisher, 1973; Mattson & Alvarez, 1973; Giannetti & Luongo, 1994; Gençalioğlu-Kuşcu et al., 2007), regressive sandwaves (e.g. Allen, 1984; Cole, 1991; Cole & Scarpati, 1993), regressive climbing dunes (Douillet et al., 2013), and regressive dune bedforms (Brand et al., 2016). Bedforms of all the above types are referred to here as 'backset'. Some authors have also developed classification schemes for PDC bedforms which include non-genetic, non-descriptive terms for various backset bedforms (Allen, 1984; Cole, 1991; Schmincke et al., 1973).

Interpretations of such backset bedforms have evolved over time. In early work they were regarded as antidunes, indicative of trans- or supercritical flow (Crowe & Fisher, 1973; Schmincke et al., 1973), and despite challenges (Allen, 1984; Cas & Wright, 1987) this association persisted for some time (e.g. Giannetti & Luongo, 1994; Gençalioğlu-Kuşcu et al., 2007; Brand et al., 2009). In particular, backset bedforms with steep stoss-side laminations have been given the interpretative name *chute-and-pool*, implying formation by a hydraulic jump (e.g. Schmincke et al., 1973; Giannetti & De Casa, 2000; Brand & Clarke, 2012; Brand et al., 2016). Generally, bedforms and cross-stratification in PDC deposits have been used as a diagnostic feature for traction-dominated deposition by a dilute PDC (e.g. Walker, 1984; Branney & Kokelaar, 2002; Brown & Andrews, 2015; Dufek et al., 2015), although some have also been interpreted as being deposited by granular-dominated processes (Douillet et al., 2013, 2018; section 4.3).

As analogue modelling is now reproducing deposits with complex internal structures (Rowley et al., 2011, 2014; Chapters 4 & 5) and recognisable bedforms, it is important to have complementary field data with which to validate the experimental work. Such data should include length and thickness measurements of backset bedforms as well as the dip angles of lee and stoss laminations. These parameters are both easily comparable between field and experimental examples as well as holding fundamental information on flow and depositional conditions. For example, the size of bedforms in PDC deposits has been used in interpretation of flow energy (e.g. Sigurdsson et al., 1987; Brand et al., 2016; Pollock et al., 2019), and dip angles are used to interpret flow conditions (e.g. Schmincke et al., 1973; Cole, 1991; Brand et al., 2016). This study aims to produce a dataset of published, and new, data in order to i) compare the morphologies of backset bedforms across numerous PDC deposits, ii) allow the validation of the analogue models explored in previous chapters, and iii) provide a useful reference for volcanologists working on the interpretation of such features either in the lab or the field.

6.2 Methods

6.2.1 Data from the literature

Data was taken directly from tables, plots, and text, as well as from measuring backset bedforms in Figures 6.1-6.10, 6.12-6.21, 6.23-6.29, 6.31-6.33, and 6.35-6.38. Angles measured from photographs are the apparent dip unless the photo is orthogonal to the bedform, and are measured from either a depositional surface (short dashed red line) or the horizontal (no short dashed red line). Length and thickness were not always measured from photographs as complete structures and numerical scales are often not present. Furthermore, in the case of “chute-and-pool structures” the lee-side beds are often plane-parallel, making length measurements of the bedform difficult. Length and thickness are preferred over wavelength and amplitude because wavelength requires a series of bedforms to be measured and the amplitudes of individual laminae within a bedform commonly change upward (Schmincke et al., 1973; Douillet et al., 2013). Measurements given here cover a wide variety of named features, but have been chosen for either i) reported stoss aggradation/upstream crest migration ii) classification using “antidune”/”regressive” or a similar term, or iii) steep stoss-side bedding/laminae.

6.2.2 Data from the field

Data from the literature were supplemented with four field sites. Backset bedforms were measured in the field, or from field photographs (Fig. 6.11, 6.22, 6.30, 6.34). As above, internal angles were measured, as well as length and thickness where possible. Coordinates are UTM grid 32U (Germany), 33T (Italy), and 10T (USA).

Mt St Helens

The proximal bedded deposits of Mt St Helens, WA have been described by numerous authors (e.g. Rowley et al., 1985; Brand et al., 2016, 2017). They were deposited from PDCs derived from Plinian column collapses on May 20th 1980. Measurements were made in these deposits on the northern flank of the volcano (563369 5118802), above Loowit Falls, approximately 2.7 km from the vent. These deposits are poorly sorted, matrix-supported mixture of pumice and lithics containing abundant cobble-sized clasts. Compositionally, the lithic clasts are dominantly andesite from previous eruptive events (Brand et al., 2016).

Laacher See

Measurements of backset bedforms from Laacher See, Germany come from the Grey Laacher See Tuff, or LST 5, of Schmincke et al. (1973), the Upper Laacher See Tuff of Van Der Bogaard and Schmincke (1985). This tuff is interpreted as the product of the final phreatomagmatic phase of the climatic eruption of ~9000 BCE (Van Der Bogaard & Schmincke, 1985). Measurements were made ~2 km (378122 5584108), ~2.1 km (377913 5583841) and ~2.4 km (379133 5584545) from the centre of Laacher See, so somewhat more proximal than those reported by Schmincke et al. (1973). These deposits are poorly sorted and dominated by ash - lapilli sized grains, although coarser laminations are present which contain clasts up to 20 mm in diameter. Pumice clasts are poorly vesiculated, and lithic clasts consist of a mixture of juveniles and Devonian country rock (Schmincke et al., 1973).

Neapolitan Yellow Tuff

Measurements of backset bedforms were made in the Neapolitan Yellow Tuff (NYT) at several locations around Naples, Italy. The NYT was deposited by a caldera-forming eruption approximately 10000 BCE (Scarpati et al., 1993). Measurements were made at 419429 4518301, 424576 4527055, 433636 4519052, and 433080 4518453, 3.4-11.6 km from the inferred vent location (Cole & Scarpati, 1993). These deposits are poorly sorted with diameters of pumice clasts ranging from 2-87 mm and lithic clasts 5-17 mm, set in an ash matrix, which is trachytic-phonolitic in composition (Cole & Scarpati, 1993).

Astroni Crater

Astroni Crater is a volcanic edifice in Naples formed by a phreatomagmatic eruption approximately 1750 BCE. Measurements were made along a track incised through proximal deposits on the western flank of the crater (426913 4522177), 1.7 km from the vent. These deposits are very pumice-rich and trachytic-phonolitic in composition (Tonarini et al., 2009). Pumice clasts were angular and ranged from 8-47 mm in diameter, whereas lithic clasts ranged from 3-40 mm.

6.2.3 Data limitations

The extensive review of literature reporting upstream migrating/stoss-aggrading bedforms in PDC deposits has revealed the following common problems in presenting bedform geometry data:

- Bedform geometries are sometimes not reported at all, or only qualitatively.

- Bedform geometries are reported, but as ranges or representative values rather than tabulated original data.
- Only partial data is collected/reported, e.g. length and thickness measurements are given but no internal angles.
- Older literature reports wavelengths and amplitudes whereas new studies report bedform length and thickness.
- It is not always mentioned whether angles are measured from the horizontal or the depositional surface.
- Where photos of bedforms are included these are often taken subparallel to the rock face, meaning that there will be a discrepancy between the apparent and true dip of beds (leading to the underestimation of dip), but the angle between photo and the rock face is not recorded or reported.
- In photos, the rock face that a bedform is seen on may not be parallel to flow direction, but the angle of the discrepancy is rarely mentioned.
- In photos, flow direction is not always reported.
- Sometimes bedforms are only represented schematically rather than including photos or detailed sketches.
- The vast majority of measurements made are only 2D and do not take into account that bedforms exist in three dimensions.

6.3 Geometry of backset bedforms in PDC deposits

6.3.1 Description of bedforms

Dune-like bedforms proximal to Ubehebe Craters, CA (Fig. 6.1-6.2), were interpreted as antidunes by Fisher and Waters (1969, 1970) and Crowe and Fisher (1973), who suggested that they preserved the upper flow regime conditions experienced by pyroclastic base surges. Upstream-migrating dunes within ~2 km of Taal volcano, Philippines (Fig. 6.3), are also interpreted as antidunes, where cohesiveness was thought to be important in stoss accretion (Waters & Fisher, 1971). Likewise, sub-vertical bedding at Capelinhos, Azores (Fig. 6.4) is interpreted to be caused by sediment from a "wet" surge being plastered against obstacles (Waters & Fisher, 1971).

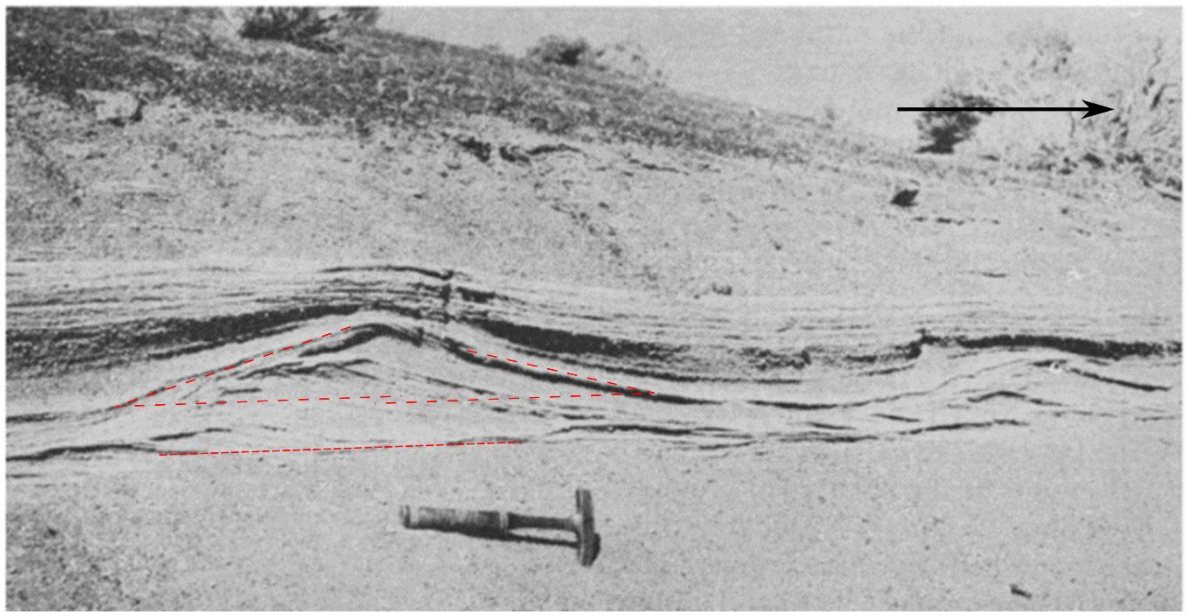

Figure 6.1 "Antidunes" at Ubehebe Craters, CA, USA. (Fisher & Waters, 1969). Flow direction left to right. Measured bedform angles shown as red dashed lines, measured from reference surface (short dashed red line).

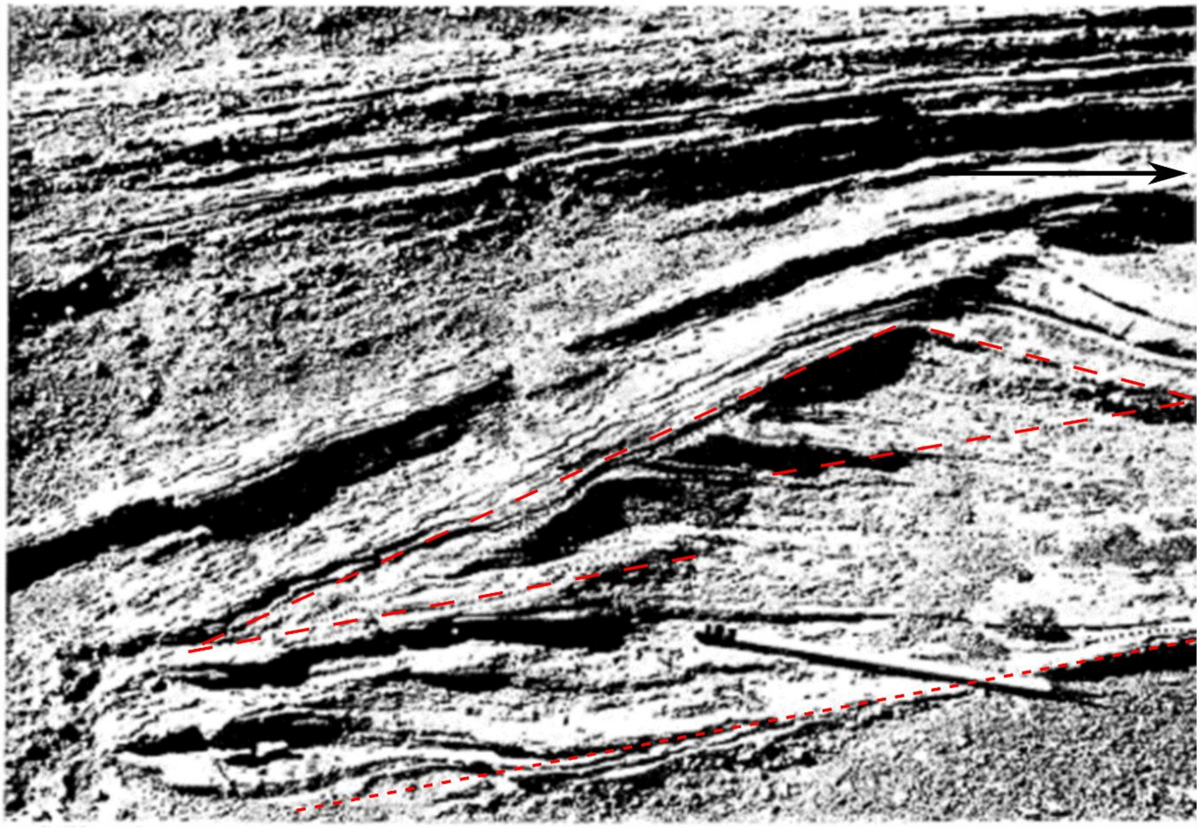

Figure 6.2 “Antidune” at Ubehebe Craters, CA, USA (Fisher & Waters, 1970). Flow direction left to right.

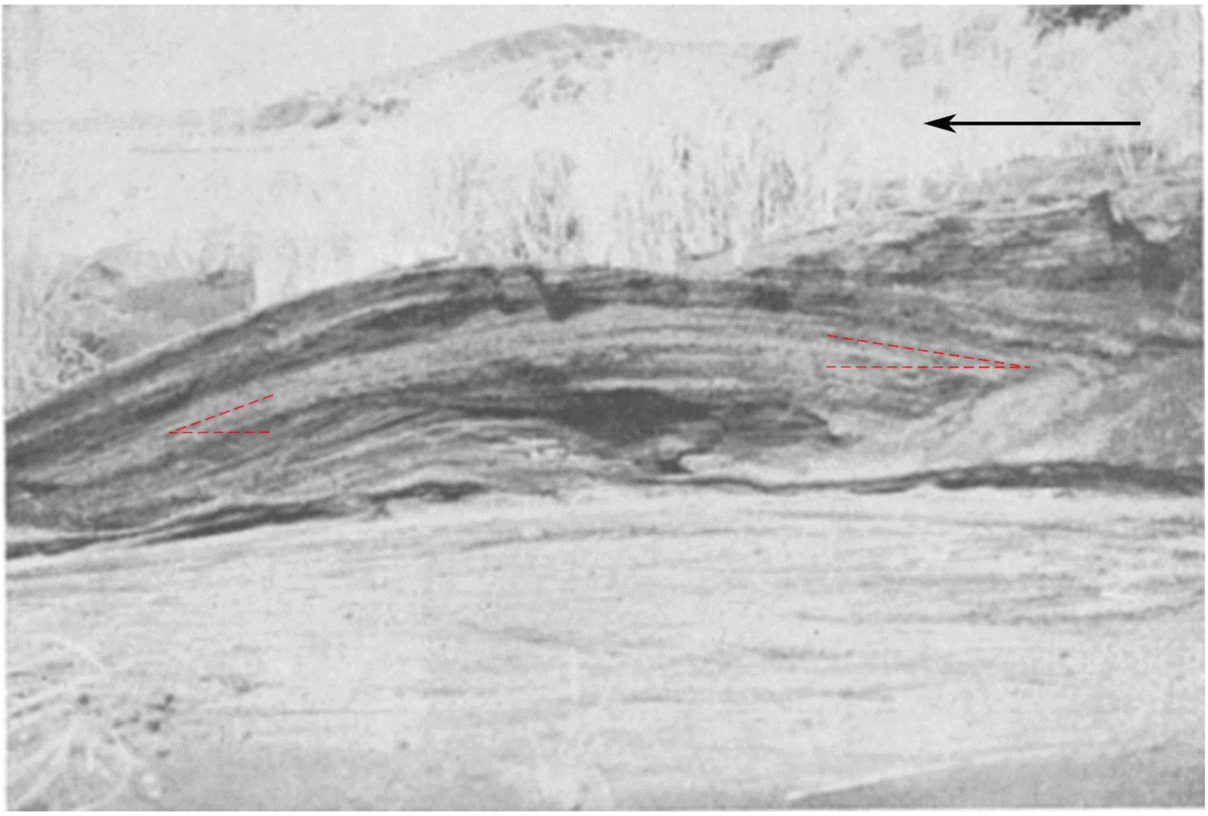

Figure 6.3 “Dune” showing upstream migration, Taal, Philippines (Waters & Fisher, 1971). Flow direction right to left.

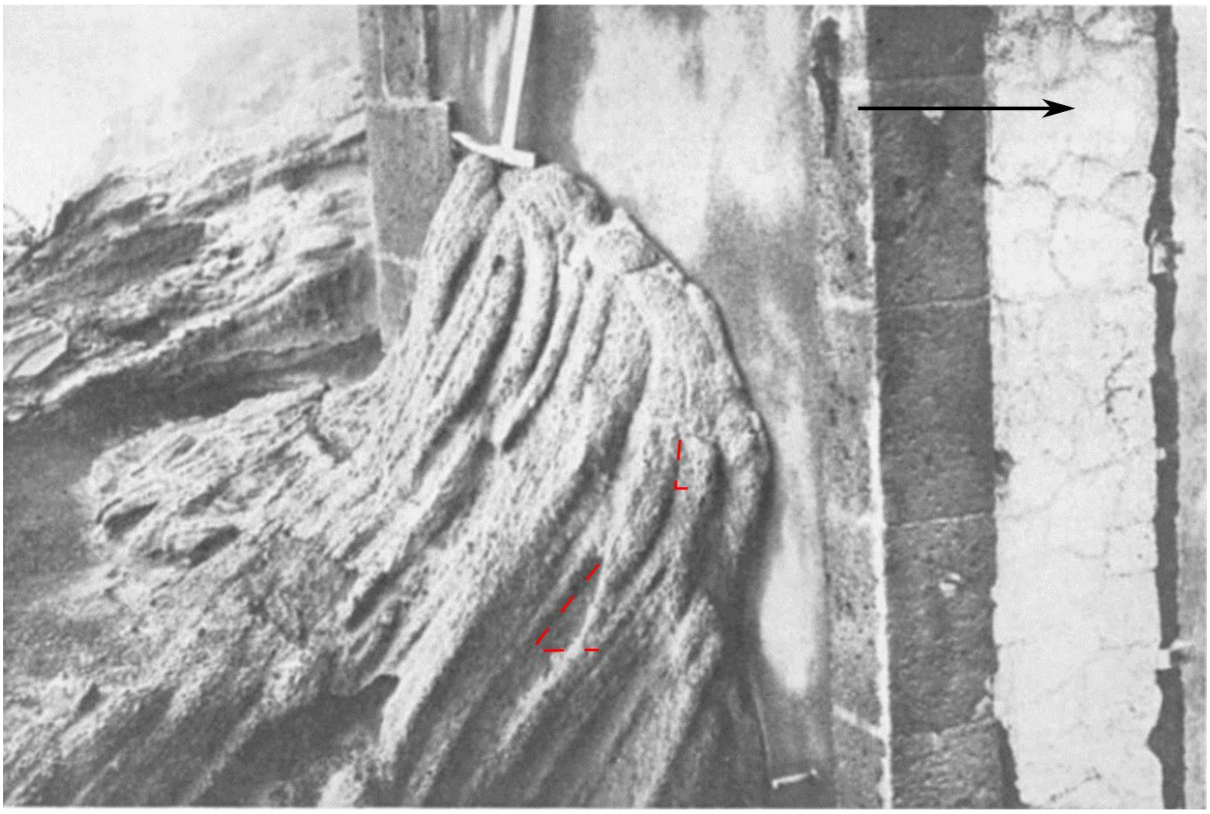

Figure 6.4 Near vertical "base-surge beds" against a lighthouse wall, Capelinhos, Azores (Waters & Fisher, 1971). Flow direction left to right.

Schmincke et al. (1973) identify dune-like structures at Laacher See, Germany, as chute-and-pool structures (Fig. 6.5-6.8) and antidunes (Fig. 6.9-6.10), recording deposition from surges of very high flow energies. These metre-scale bedforms are found within several kilometres of the source in successions 10 + m thick. A backset bedform measured by the author and similar to these "antidunes" is seen in Figure 6.11. Larger bedforms (Fig. 6.12-6.13) in the Roman Volcanic Province, Italy, are also interpreted as antidunes deposited from surges by Mattson and Alvarez (1973). These were produced by phreatic eruptions, which are also interpreted to have formed surges which deposited chute-and-pool structures (Fig. 6.14) at Tocomar, Argentina (Petrinovic & Colombo Piñol, 2006).

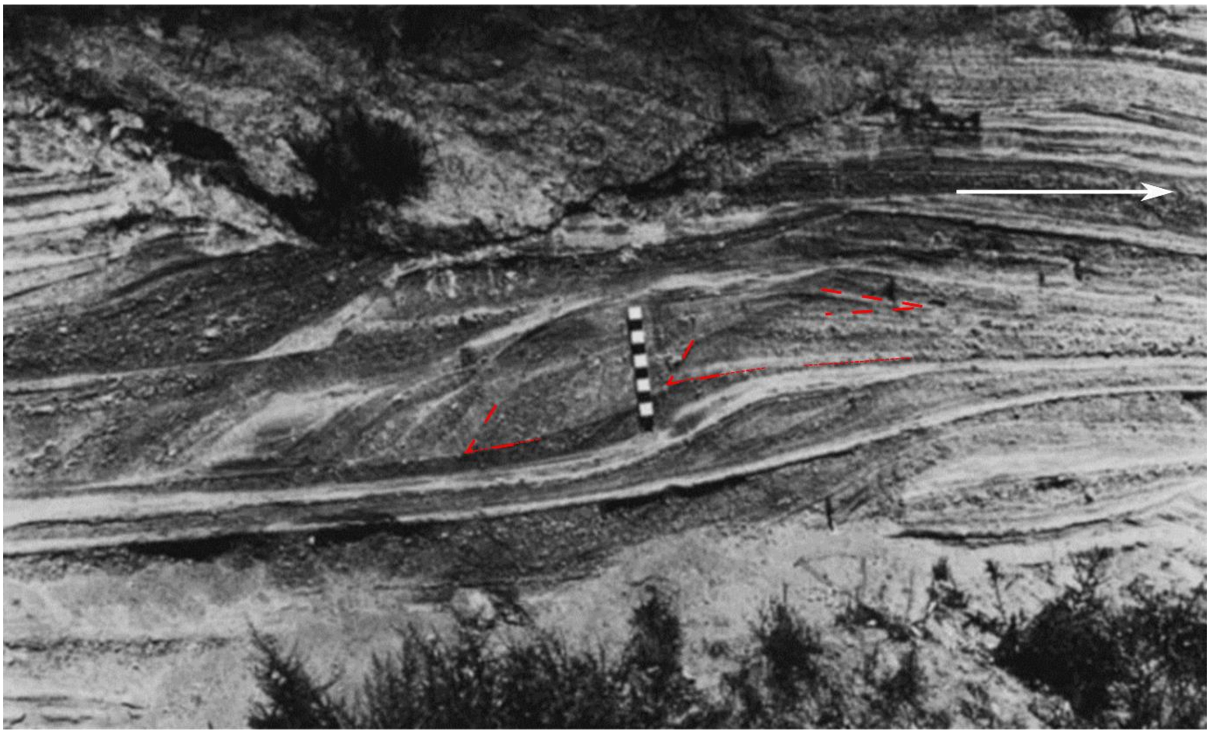

Figure 6.5 "Chute and pool structure", Laacher See, Germany (Schmincke et al., 1973). Flow direction left to right.

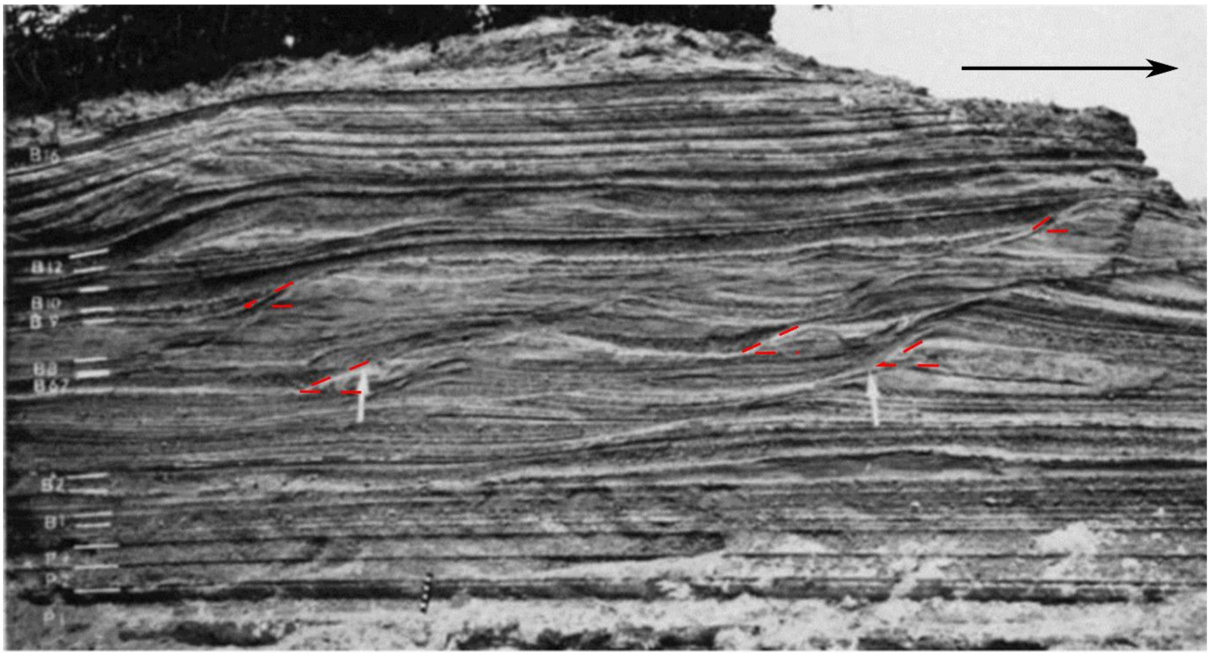

Figure 6.6 "Arrows indicate particularly prominent backset beds of chute and pool structures", Laacher See, Germany (Schmincke et al., 1973). Flow direction left to right.

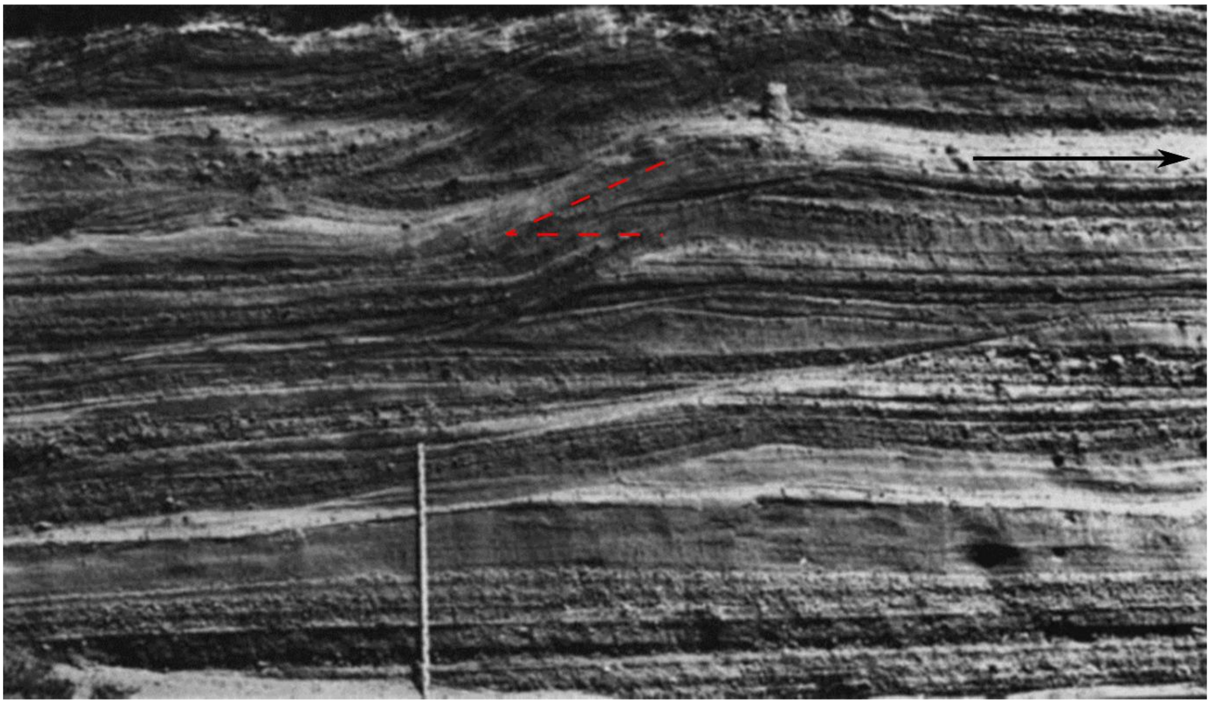

Figure 6.7 “Chute and pool structure”, Laacher See, Germany (Schmincke et al., 1973). Flow direction left to right.

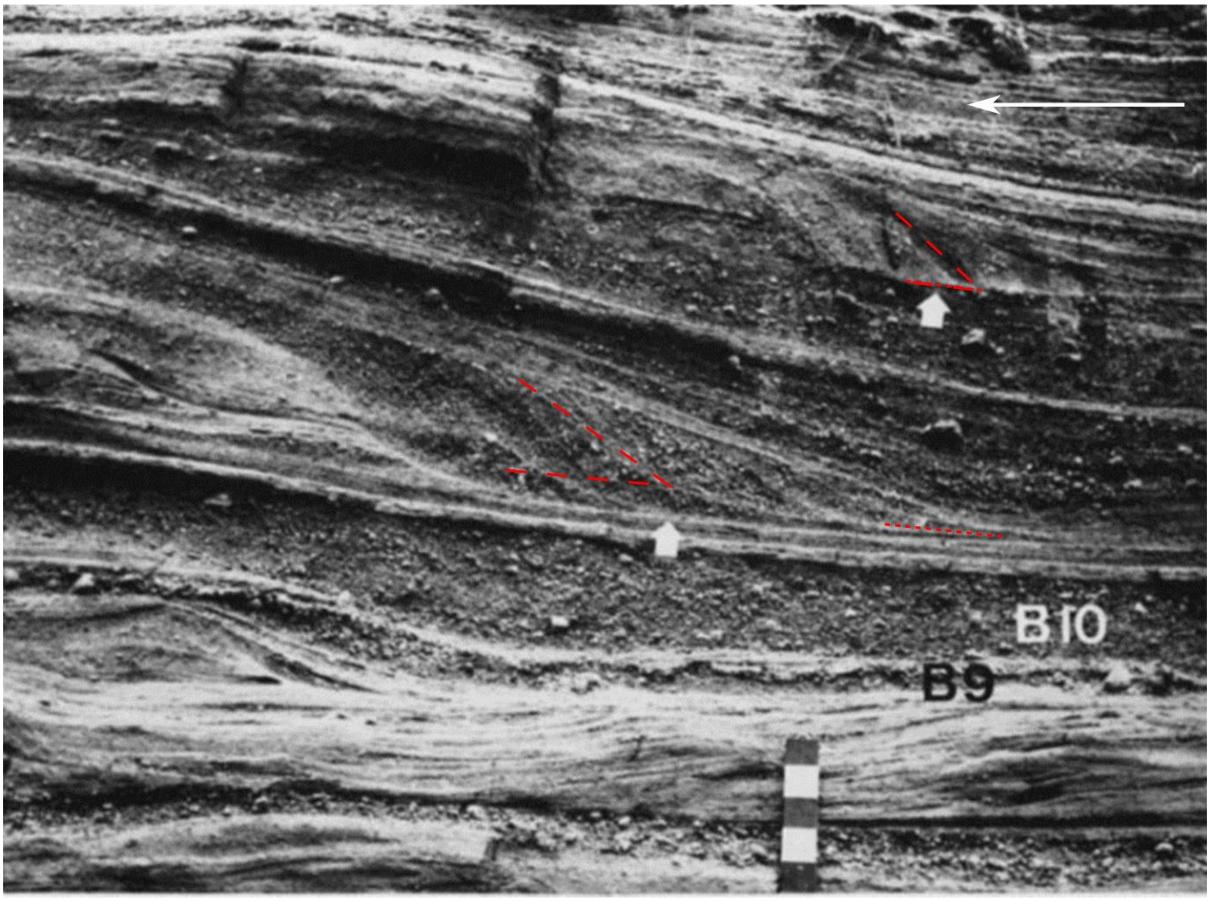

Figure 6.8 “Stoss-side beds of two chute-and-pool structures”, Laacher See, Germany (Schmincke et al., 1973). Flow direction right to left.

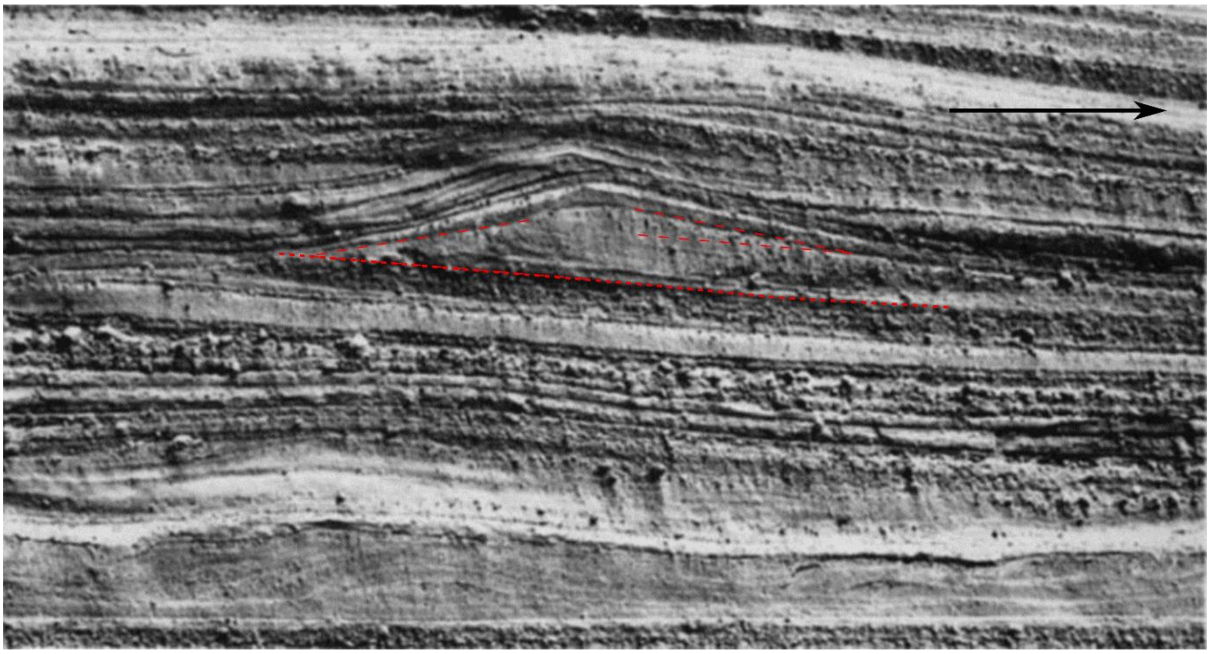

Figure 6.9 "Type III dune" ("probably within the antidune phase"), Laacher See, Germany (Schmincke et al., 1973). Flow direction left to right.

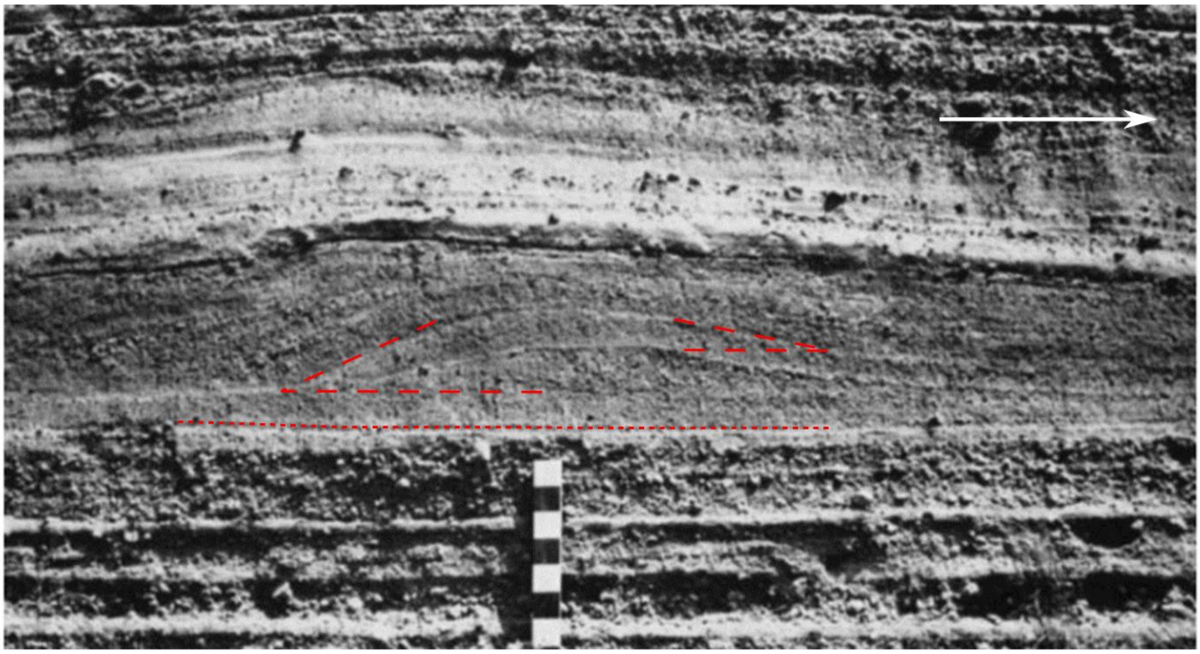

Figure 6.10 "Antidune bedding", Laacher See, Germany (Schmincke et al., 1973). Flow direction left to right.

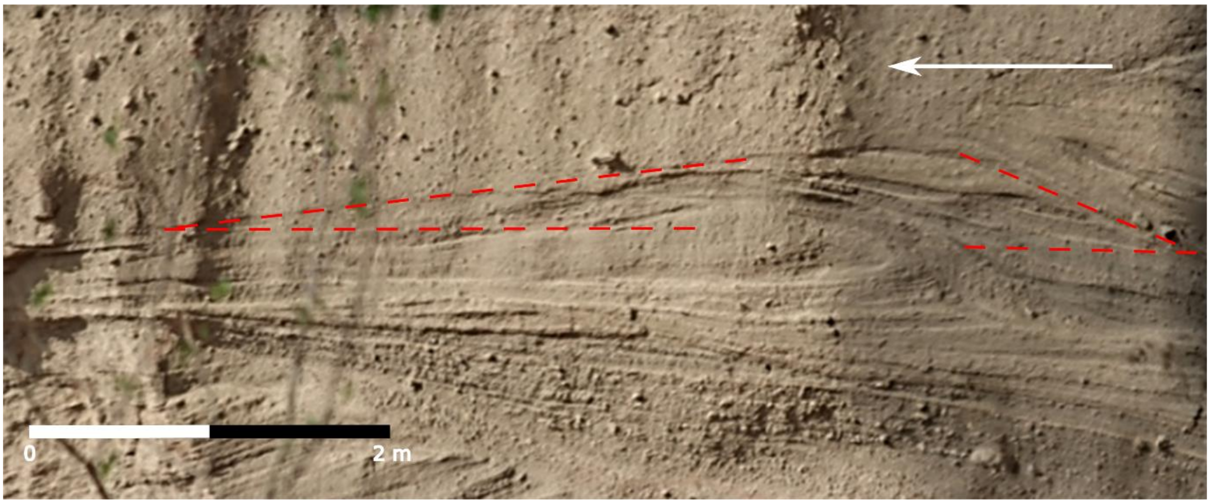

Figure 6.11 Backset bedform, Laacher See, Germany. Flow direction right to left. Facing 260° at 378122 5584108 UTM grid 32U.

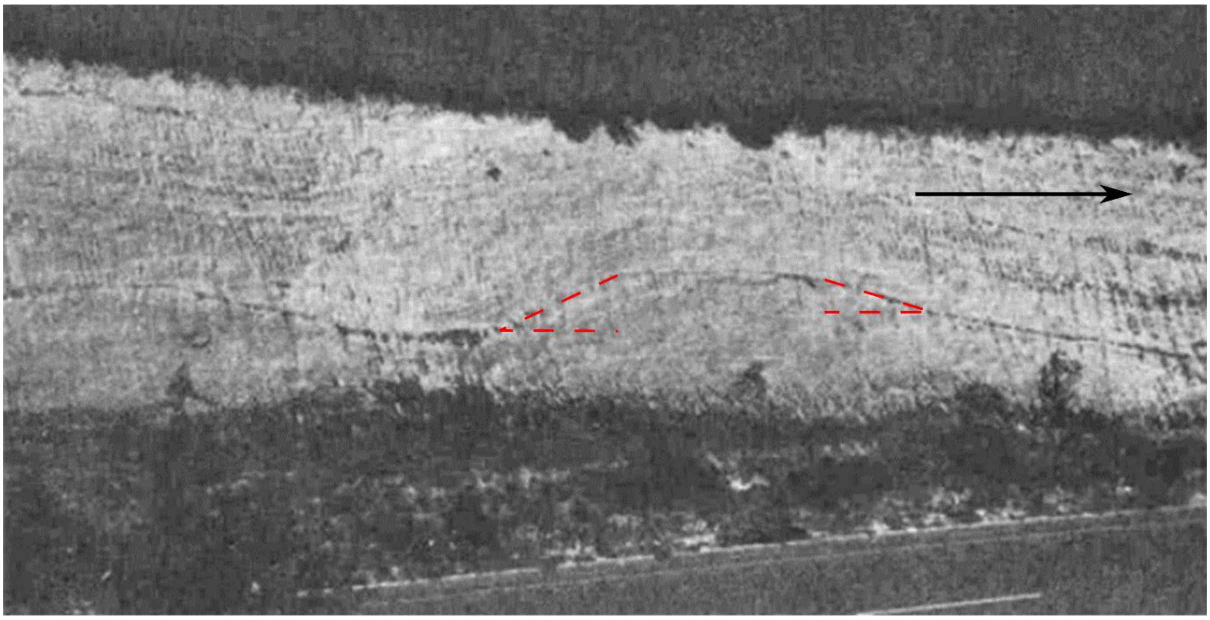

Figure 6.12 “Antidune”, Baccano Crater, Italy (Mattson & Alvarez, 1973). Flow direction left to right.

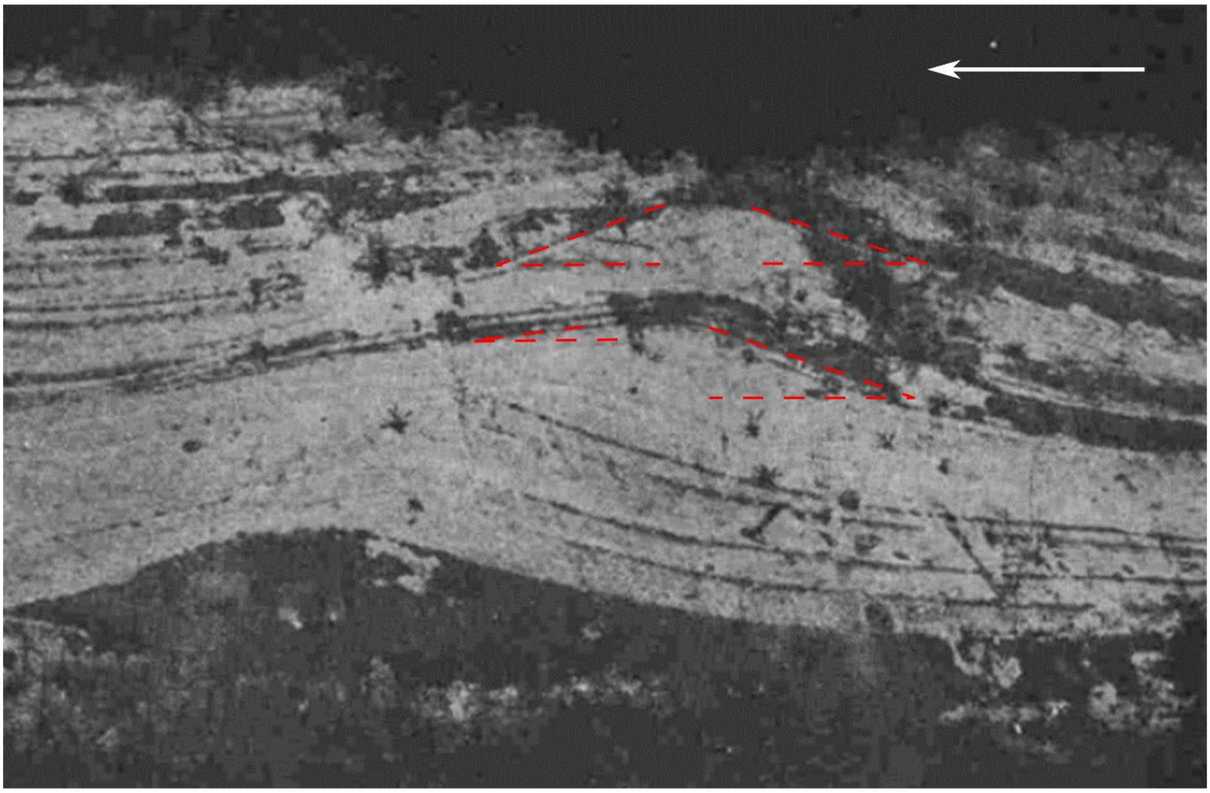

Figure 6.13 “Antidune”, Matignano Tuff, Italy (Mattson & Alvarez, 1973). Flow direction right to left.

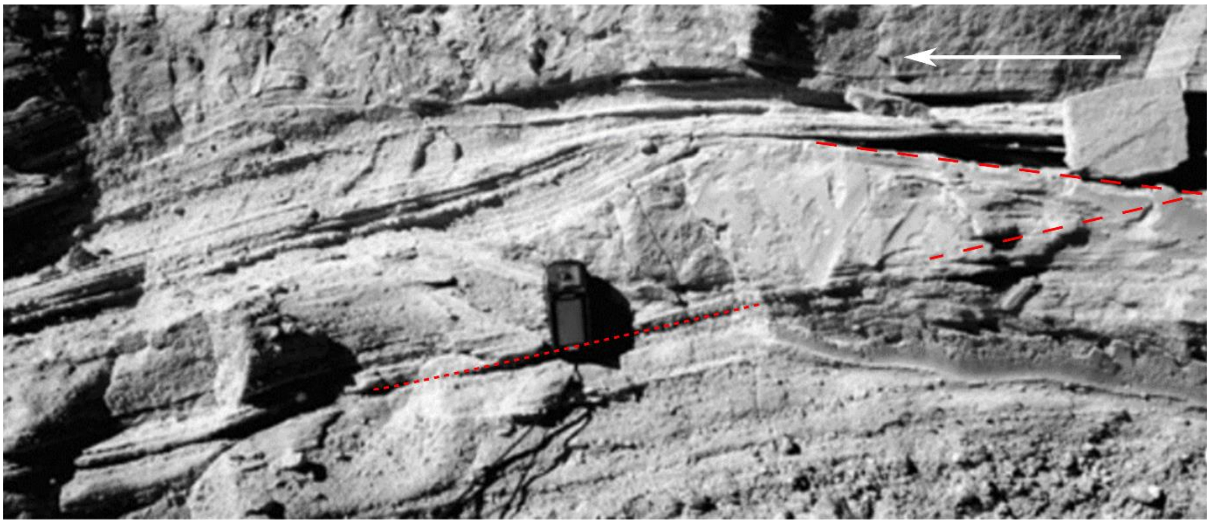

Figure 6.14 “Chute and pool structure”, Tocomar Volcanic Center, Argentina (Petrinovic & Colombo Piñol, 2006). Assumed flow direction right to left.

Many backset bedforms are identified in the proximal bedded deposits of Mt St Helens, WA. Rowley et al. (1985) identify chute-and-pool structures formed in very high flow regimes (Fig. 6.15), noting that their steep stoss sides indicate rapid deposition, and/or the presence of damp cohesive ash. Bedforms with steep stoss sides (Fig. 6.16-6.21) are classified at regressive bedforms by Brand et al. (2016), who also interpret them as recording high energy, supercritical conditions as well as rapid deposition, and note that they decrease in size as the depositional slope shallows. A backset bedform from these deposits measured by the author is shown in Figure 6.22. Rapid deposition is interpreted as the primary factor in the deposition of a high relief bedform in the El Abrigo ignimbrite, Tenerife (Fig. 6.23), which shows stoss aggradation over 25 km from source (Bryan et al., 1998).

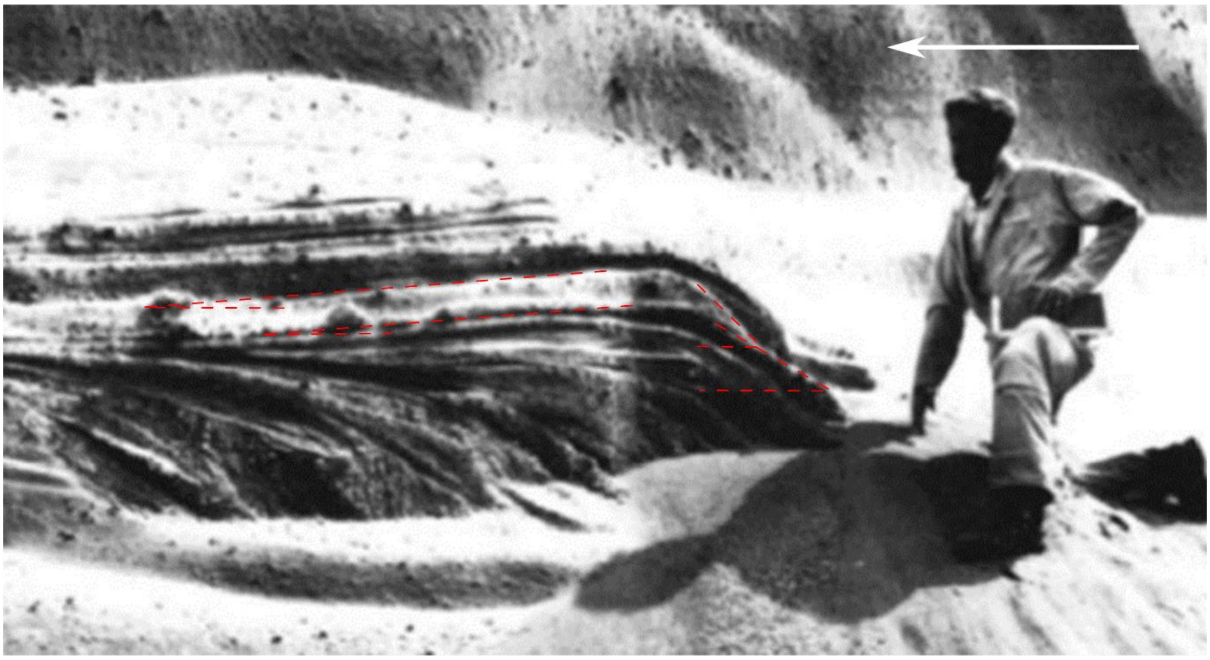

Figure 6.15 “Antidune”, Mt St Helens, WA, USA (Rowley et al., 1985). Flow direction right to left.

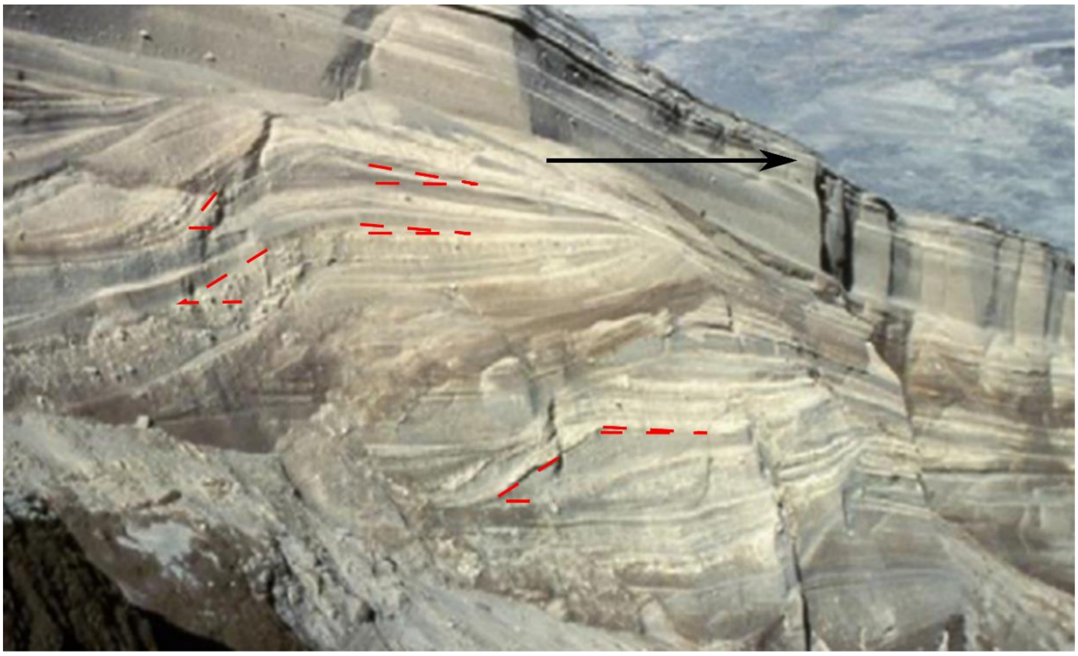

Figure 6.16 "Regressive bedforms", Mt St Helens, WA, USA (Brand et al., 2016). Flow direction left to right.

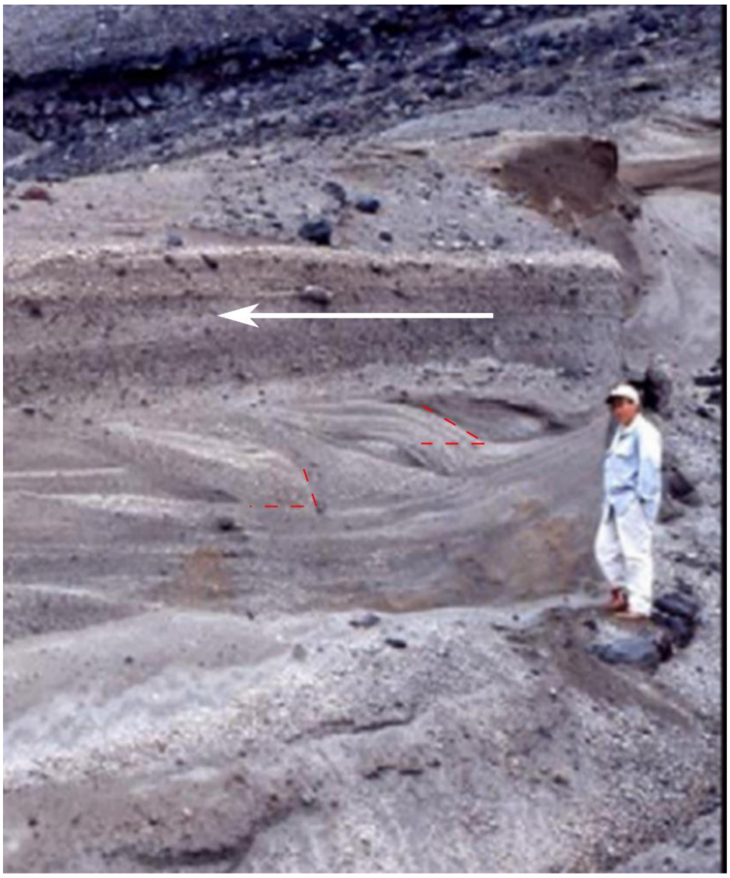

Figure 6.17 "Regressive bedforms", Mt St Helens, WA, USA (Brand et al., 2016). Flow direction right to left.

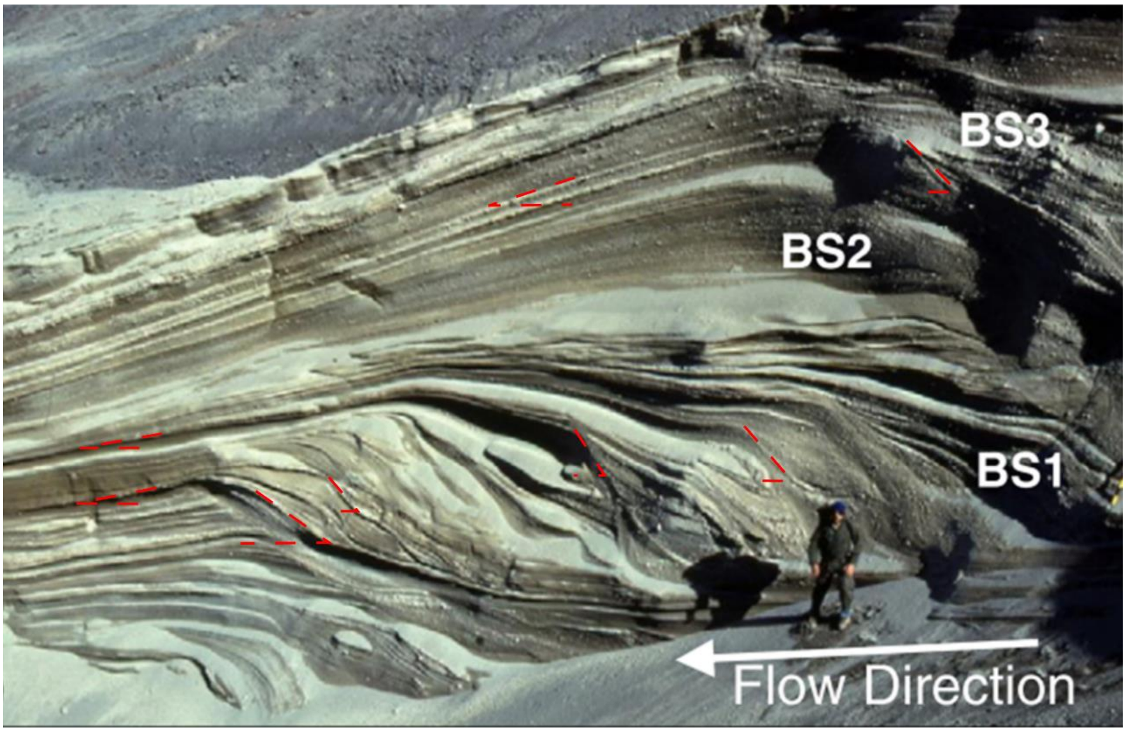

Figure 6.18 “Compound bedform”, Mt St Helens, WA, USA (Brand et al., 2016). Flow direction right to left.

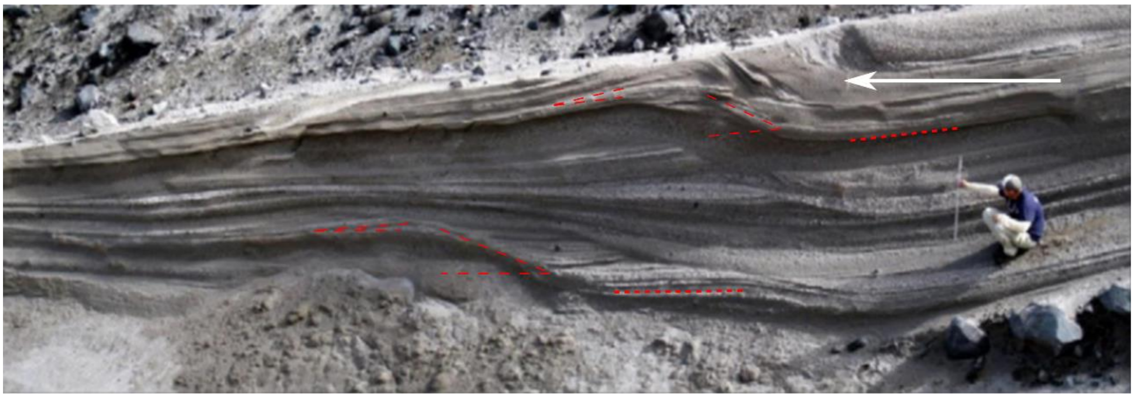

Figure 6.19 “Regressive bedform”, Mt St Helens, WA, USA (Brand et al., 2016). Flow direction right to left.

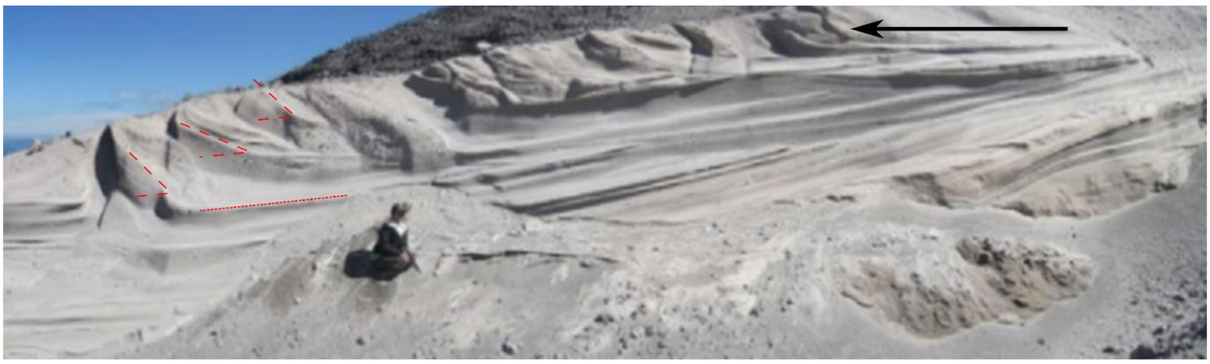

Figure 6.20 “Regressive bedform”, Mt St Helens, WA, USA (Brand et al., 2016). Flow direction right to left.

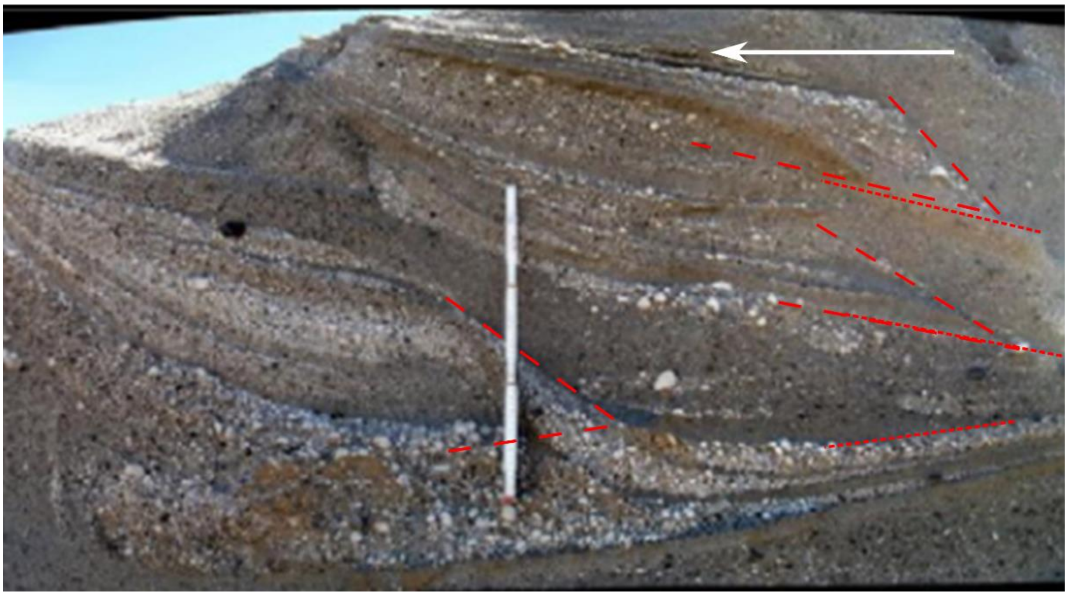

Figure 6.21 “Regressive bedform”, Mt St Helens, WA, USA (Brand et al., 2016). Flow direction right to left.

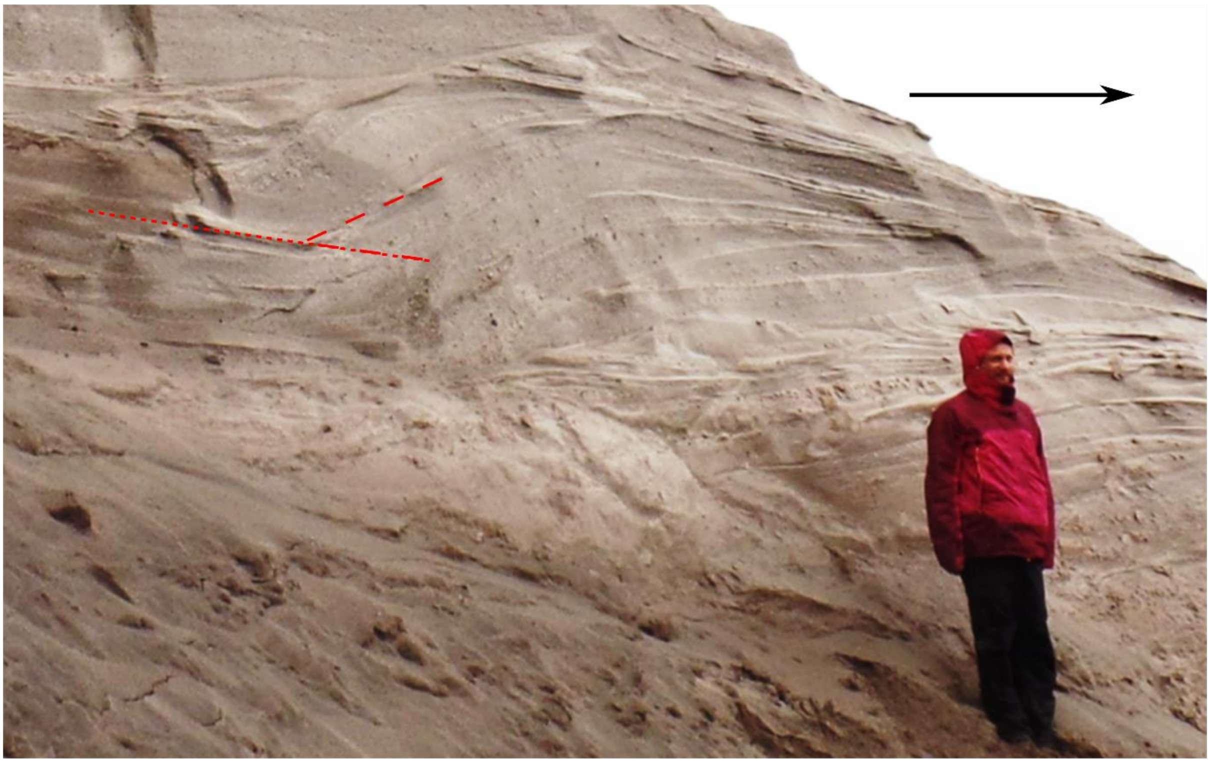

Figure 6.22 Backset bedform, Proximal Bedded Deposits, Mount St Helens, WA, USA. Flow direction left to right. Facing 315° at 563369 5118802 UTM grid 10T.

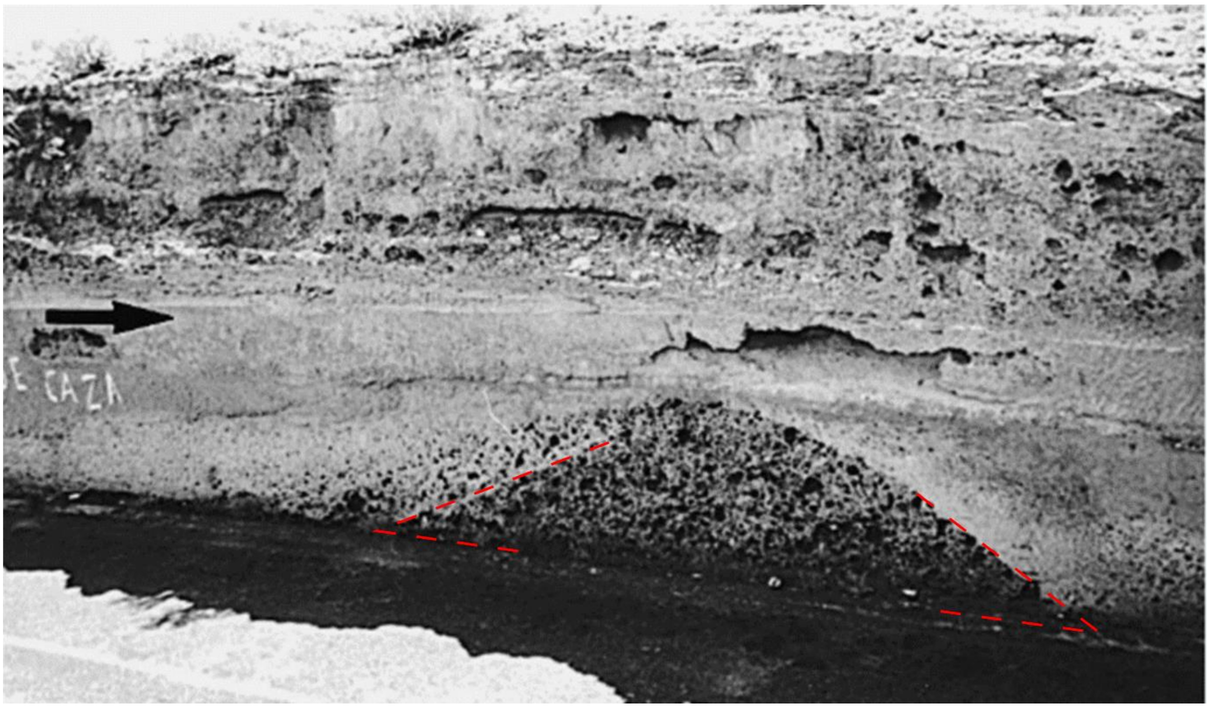

Figure 6.23 “High relief bedform”, El Abrigo Ignimbrite, Tenerife (Bryan et al., 1998). Flow direction left to right.

At Roccamonfina volcano, Italy, many structures interpreted as antidunes and chute-and-pool structures are found (Fig. 6.24-6.26). Chute-and-pool structures are identified by Valentine and Giannetti (1995) and Giannetti and De Casa (2000) approximately 7 km from the centre of the crater, and more proximally by Giannetti and Luongo (1994), who also record dozens of antidunes in an intracaldera facies. Cole (1991) records similar bedforms to chute-and-pool structures, which they call regressive sand-waves. Interpreted as recording the upper flow regime conditions, another regressive sand-wave from Sugarloaf Mountain, AZ is shown in Figure 6.27. Regressive sand-waves are also described in the Neapolitan Yellow Tuff, Italy, 10+ km from the inferred vent (Fig. 6.28-6.29). Cole and Scarpati (1993) interpret these as forming in the same way chute-and-pool structures, and suggest that although turbulent, the depositing currents had a highly concentrated basal layer. Another backset bedform seen in the Neapolitan Yellow Tuff is shown in Figure 6.30. The largest “sand-waves” are described proximal to El Chichon, Mexico by Sigurdsson et al. (1987), who interpret them as deposited by the concentrated basal layer of pyroclastic surges, with erosive turbulence forming steep stoss faces.

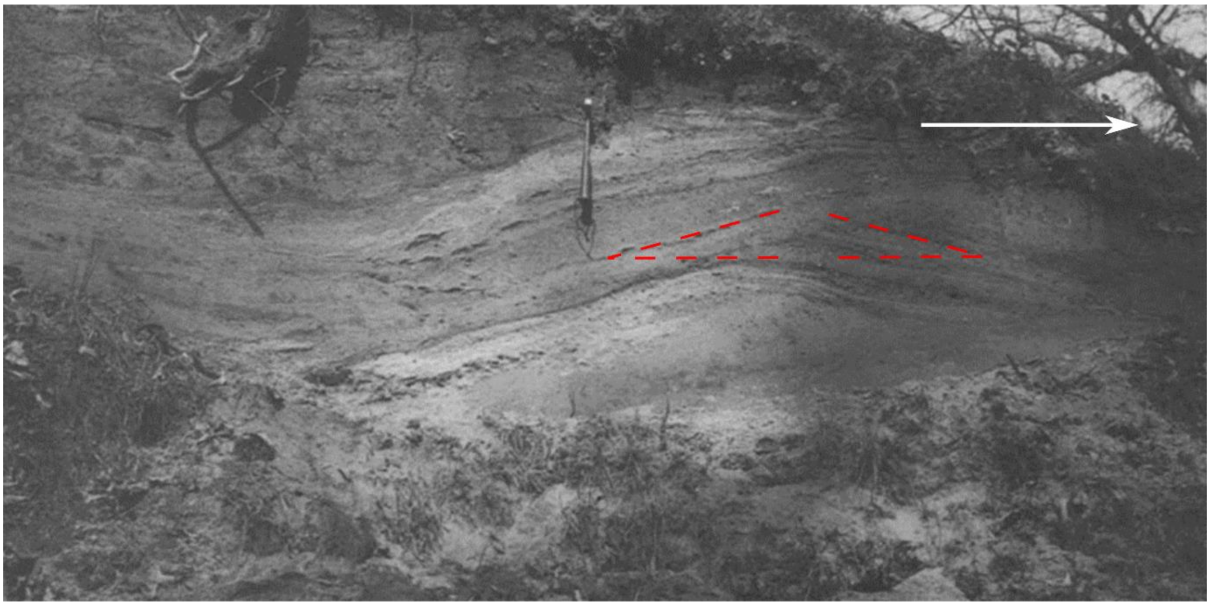

Figure 6.24 “Chute-and-pool structures”, Roccamonfina, Italy (Giannetti & Luongo, 1994). Flow direction left to right.

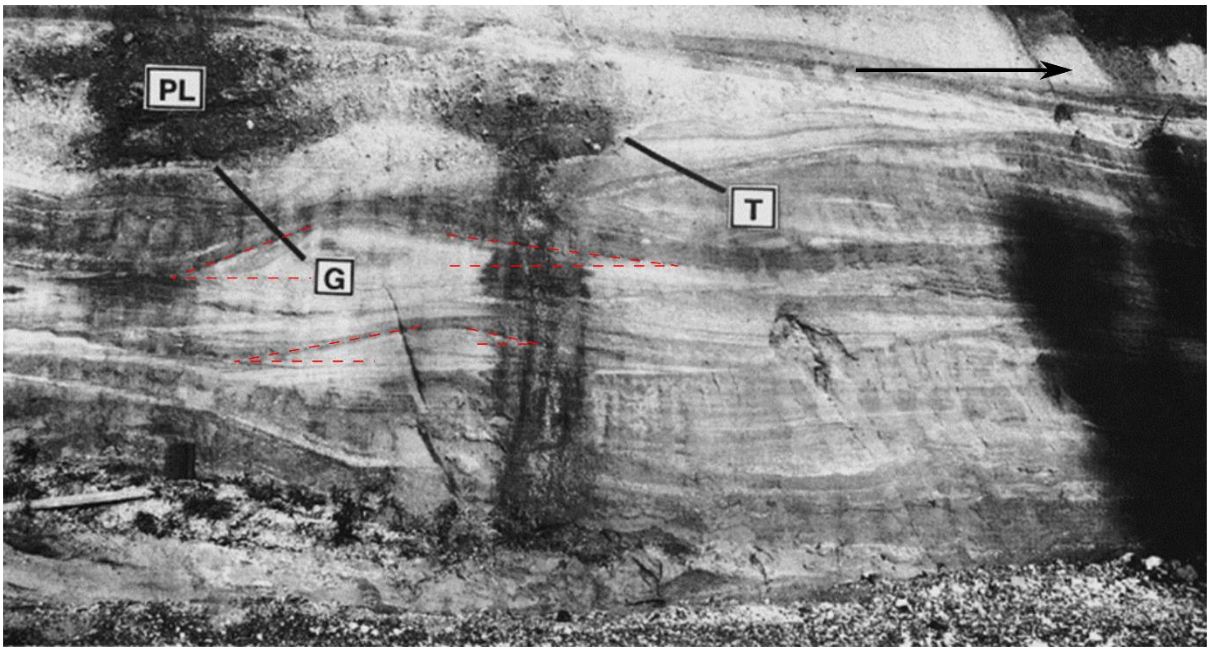

Figure 6.25 “Pyroclastic surge deposits…spectacular dune, antidune, chute-and-pool, and other features”, Roccamonfina, Italy (Valentine & Giannetti, 1995). Presumed flow direction left to right.

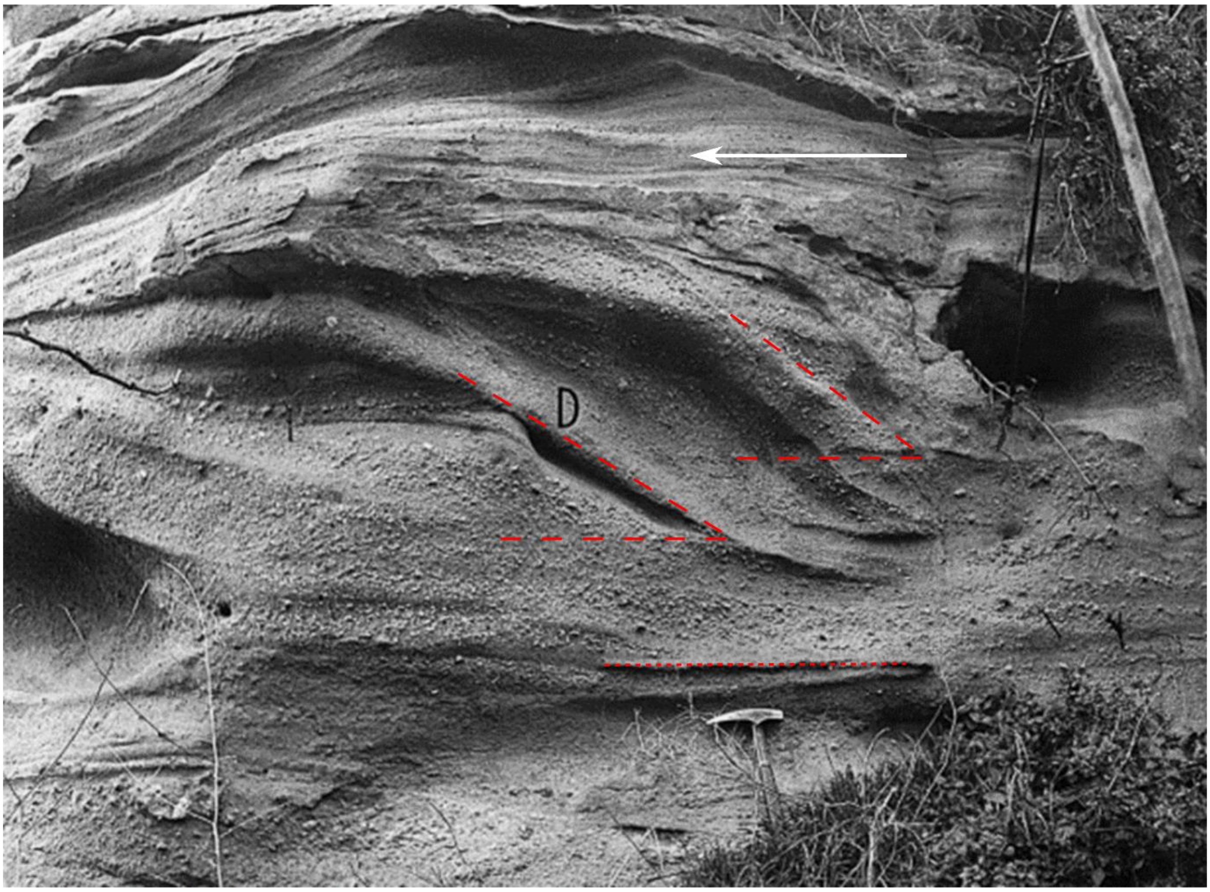

Figure 6.26 “Chute-and-pool structures”, Roccamonfina, Italy (Giannetti & De Casa, 2000). Flow direction right to left.

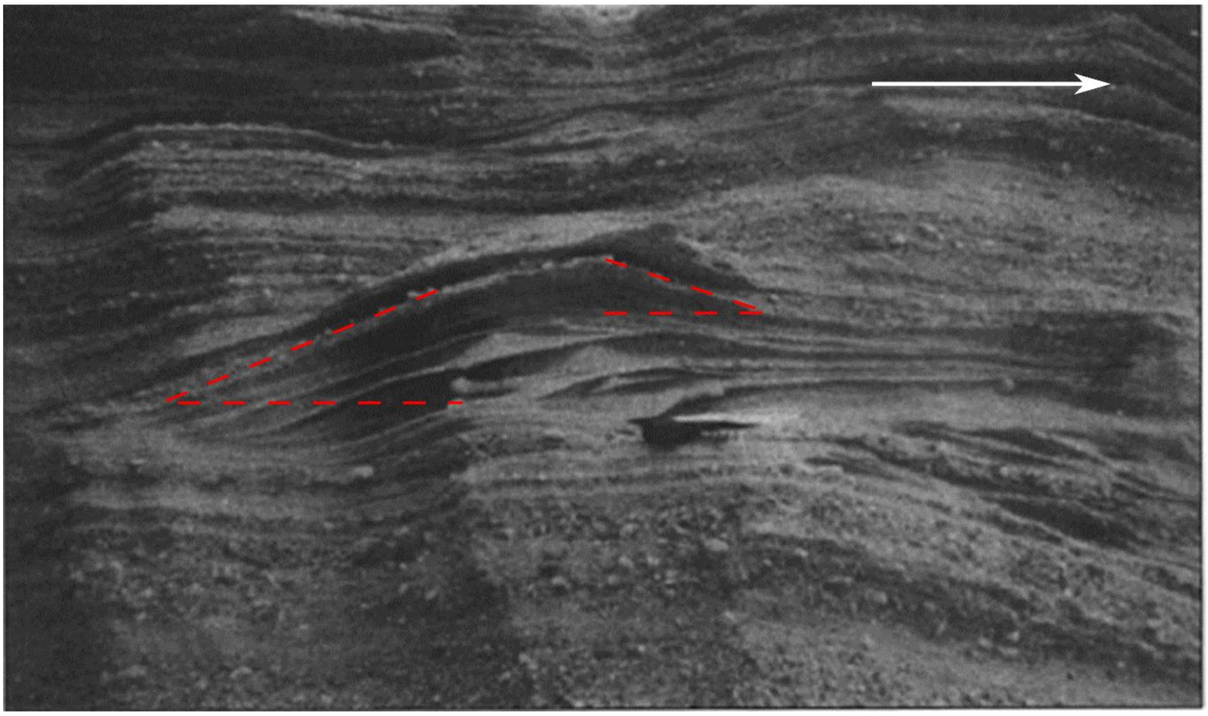

Figure 6.27 “Regressive sand-wave structure”, Sugarloaf Mountain, AZ, USA (Cole, 1991). Flow direction left to right.

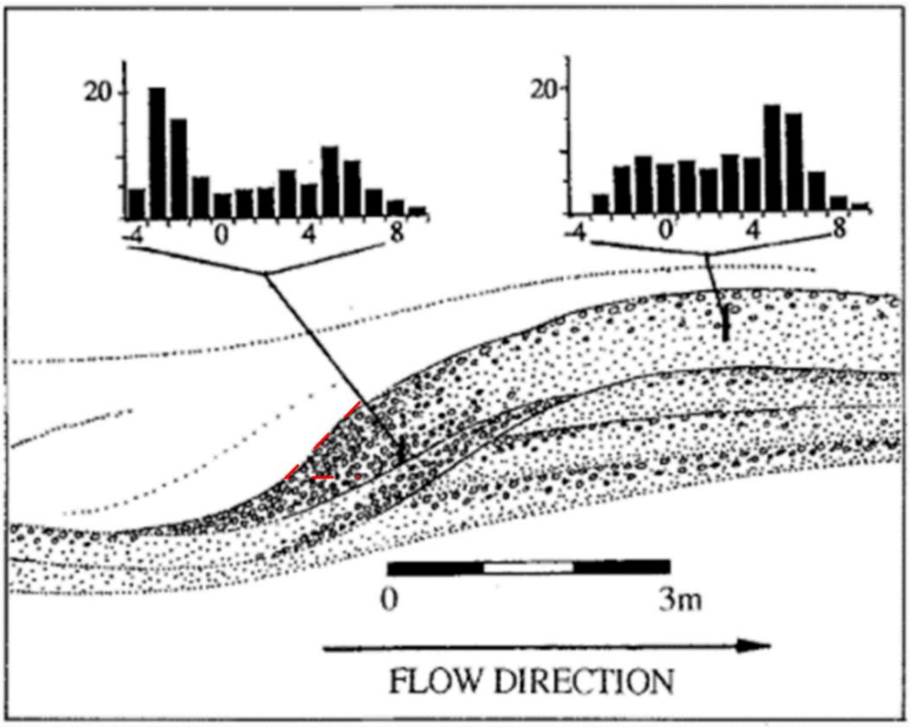

Figure 6.28 “Sand-wave structure”, Neapolitan Yellow Tuff, Italy (Cole & Scarpati, 1993). Flow direction left to right.

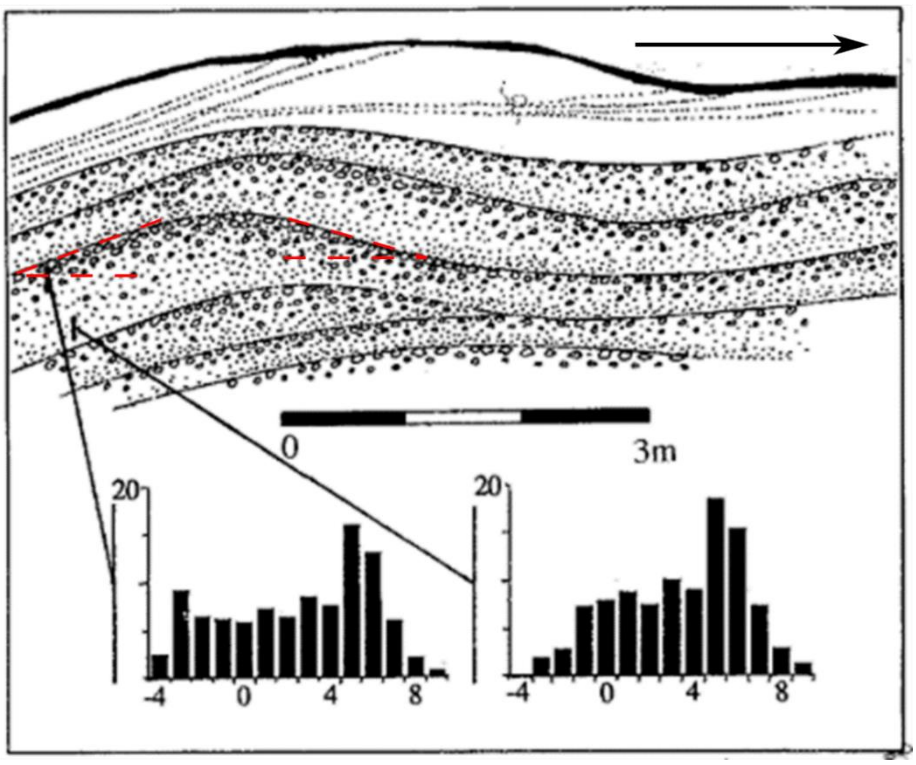

Figure 6.29 “Regressive sand-wave structure”, Neapolitan Yellow Tuff, Italy (Cole & Scarpati, 1993). Flow direction left to right, obliquely.

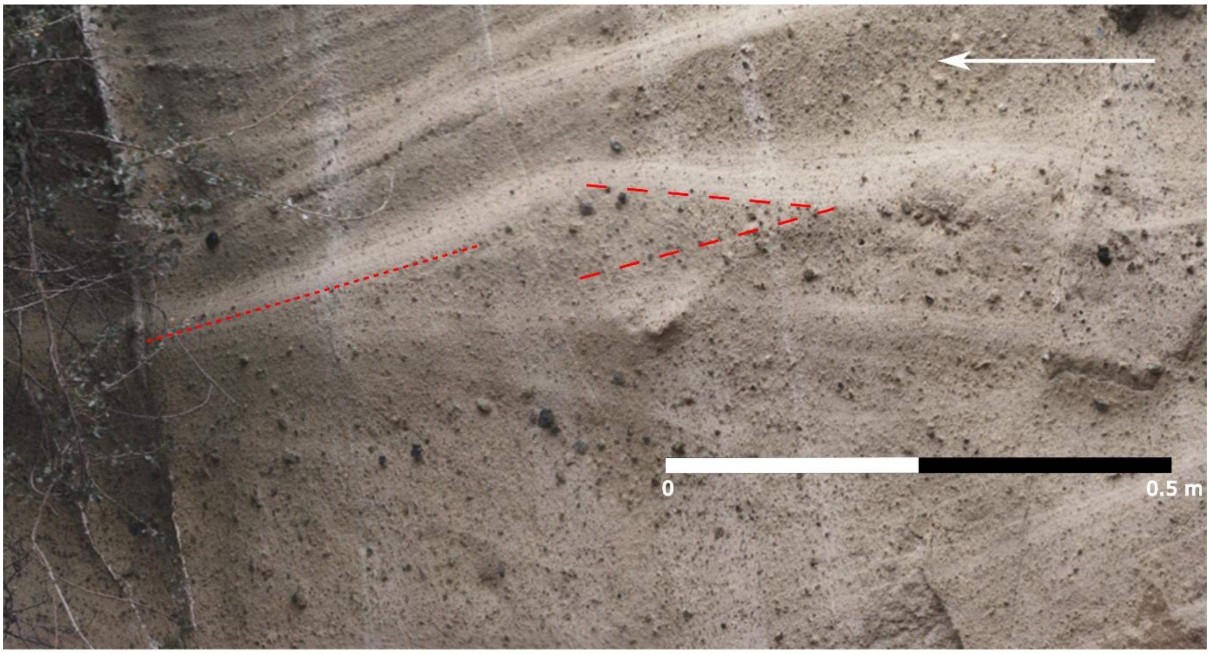

Figure 6.30 Backset bedform, Torregaveta, Italy. Flow direction right to left, obliquely towards viewer. Facing 350° at 419442 4518301 UTM grid 33T.

Bedforms interpreted as antidunes (Fig. 6.31-6.32) and chute-and-pool structures (Fig. 6.33) are found in the rim of Cora Maar, Turkey, in the 40 m thick crater rim deposits. Gençalioğlu-Kuşcu et al. (2007) like previous authors, interpret these as caused by changes in the flow regime of surges. A backset bedform found in the rim of Astroni Crater, Naples, is shown in Figure 6.34.

Figure 6.31 “Large scale climbing antidunes”, Cora Maar, Turkey (Gençalioğlu-Kuşcu et al., 2007). Flow direction left to right.

Figure 6.32 “Type III dune structure”, Cora Maar, Turkey (Gençalioğlu-Kuşcu et al., 2007). Assumed flow direction left to right.

Figure 6.33 “Chute and pool”, Cora Maar, Turkey (Gençalioğlu-Kuşcu et al., 2007). Flow direction left to right.

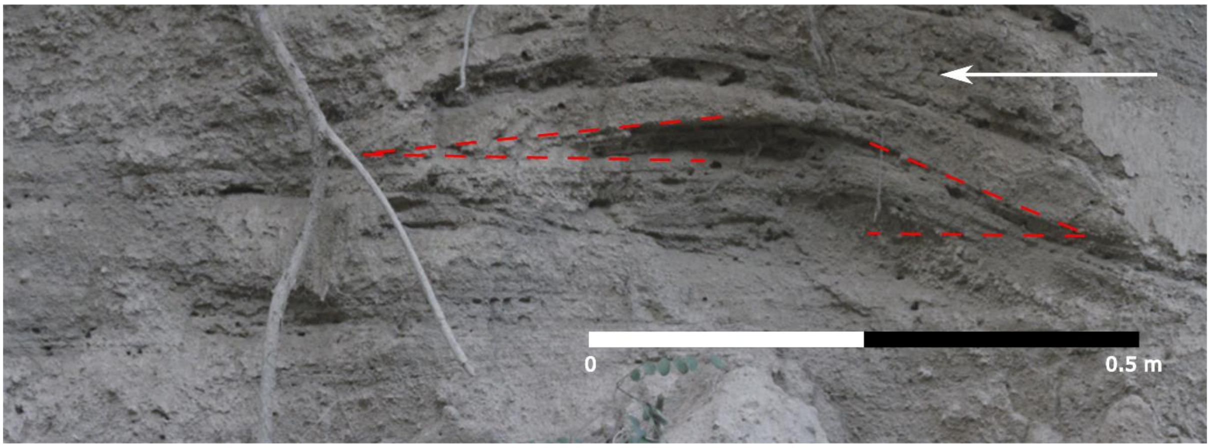

Figure 6.34 Backset bedform, Astroni Crater, Naples, Italy. Flow direction right to left. Facing 343° at 426913 4522177 UTM grid 33T.

Bedforms with very steeply dipping upstream beds are seen at Narbona Pass Maar, NM (Fig. 6.35) and at the Table Rock Complex, OR (Fig. 6.36), in both cases within 2 km of source. Brand et al. (2009) and Brand and Clarke (2012) interpret these as chute-and-pool structures recording the presence of supercritical flow.

Figure 6.35 “Chute-and-pool structure”, Narbona Pass Maar, NM, USA (Brand et al., 2009). Flow direction left to right.

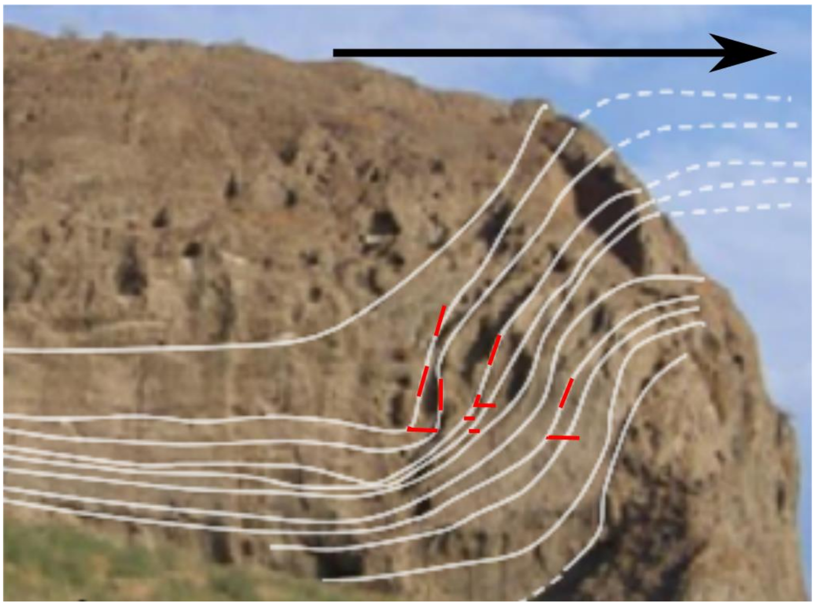

Figure 6.36 “Chute-and-pool feature”, Table Rock Complex, OR, USA (Brand & Clarke, 2012). Flow direction left to right.

Dozens of stoss-aggrading bedforms are described by Douillet et al. (2013, 2018) from the 2006 eruption of Tungurahua, Ecuador, where PDCs formed from destabilization of pyroclastic material near the vent. Those described by Douillet et al. (2013) are split into three groups based on 3D morphology – transverse, lunate, and elongate, with elongate bedforms found only proximally. These are interpreted as forming due to topographic blocking and truncative bursts of turbulence rather than recording highly energetic flow conditions. The three types of bedform have quite steep lee angles compared to other examples. Of the backset bedforms reported by Douillet et al. (2018), erosive-based backsets (Fig. 6.37) are thought to form by the same processes, and the stoss aggradation seen in Figure 6.38 is interpreted as due to the hindering of saltation on the stoss slope.

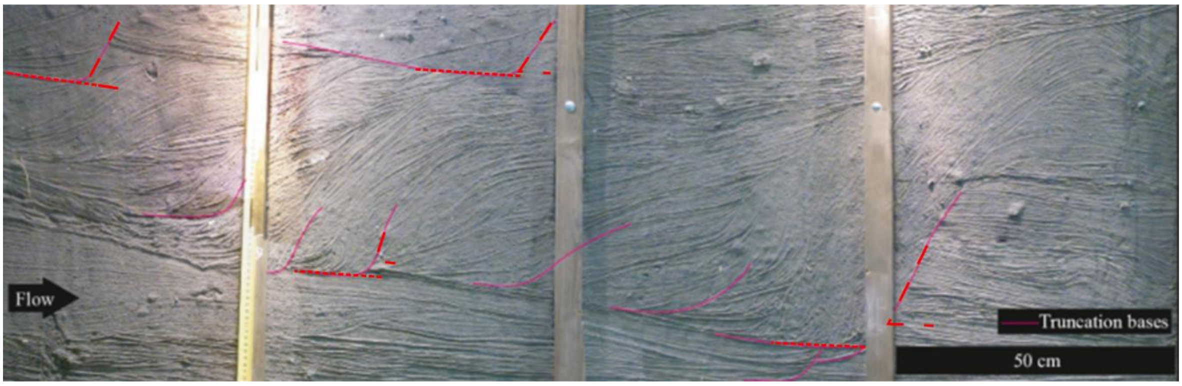

Figure 6.37 “Erosive-based backsets”, Tungurahua, Ecuador (Douillet et al., 2018). Flow direction left to right.

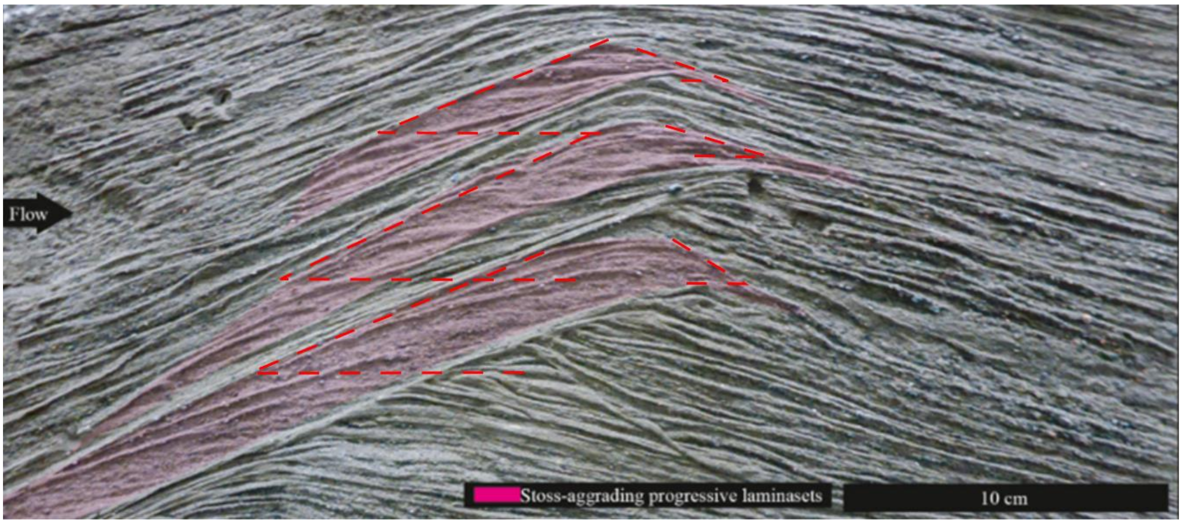

Figure 6.38 “Stoss-aggrading progressive laminasets”, Tungurahua, Ecuador (Douillet et al., 2018). Flow direction left to right.

6.3.2 Bedform geometries

There is a large spread of data for backset bedform angles (Fig. 6.39) but with two distinct trends – somewhat symmetrical lee/stoss and moderate-to-high stoss/low lee. The majority of backset bedforms reported here follow the first trend, and are usually interpreted as antidunes. The majority of these have lee angles less than 20°, with almost all of those with greater lee angles being formed by the 2006 eruption of Tungurahua. The backset bedforms comprising the second trend are typically reported as chute-and-pool structures - most of these steep backset bedforms either have plane-parallel lee sides or their lee sides are unreported/missing.

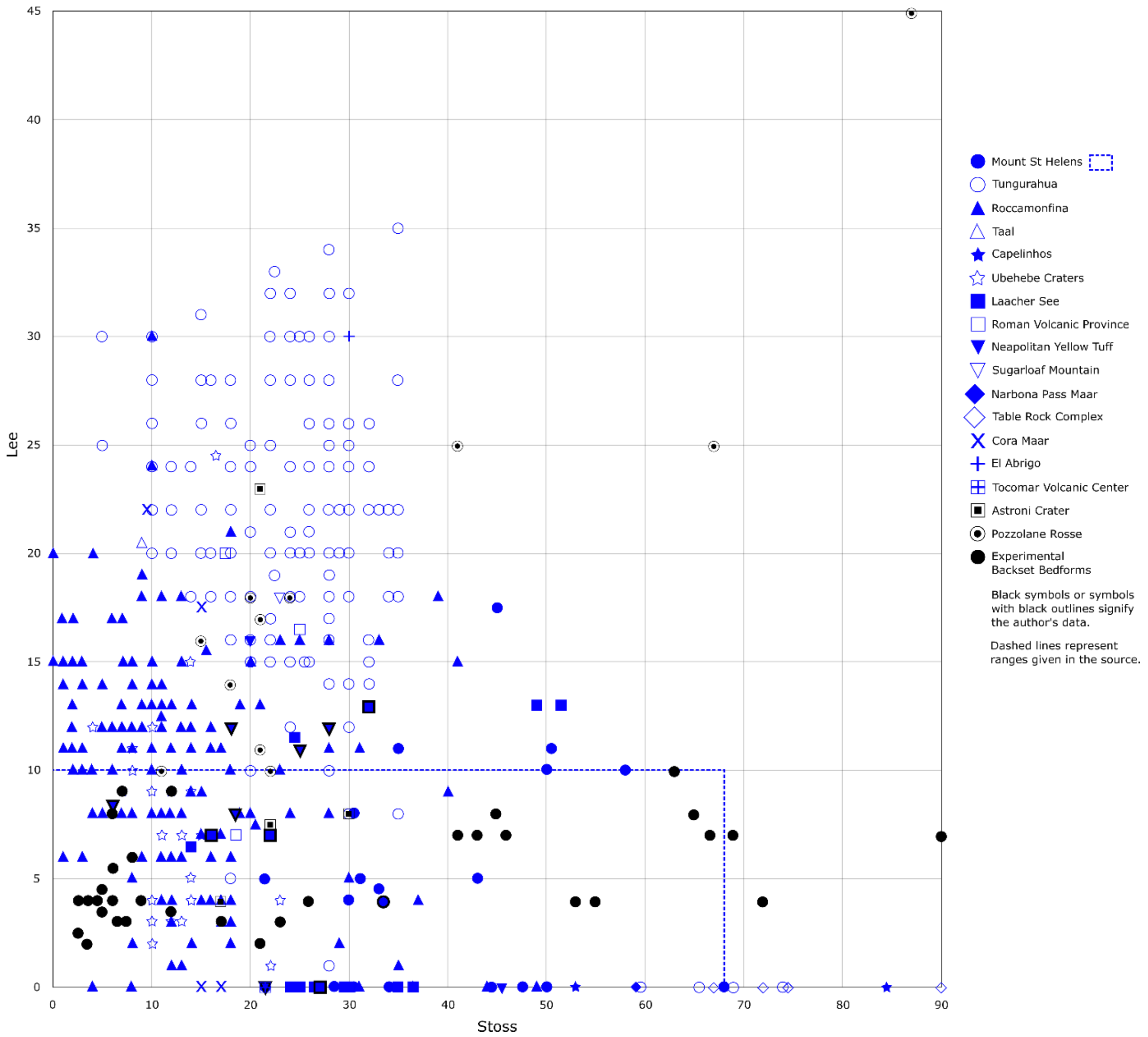

Figure 6.39 Stoss and lee angles of backset bedforms taken from the literature plotted against the experimental backset bedforms from Chapter 4. Black outlines show measurements taken from the author's field photos. See Supplementary Table D.1 in Appendix D for data sources and information on how angles were measured.

A plot of backset bedform length (L) vs. thickness (H) defines a trend with $R^2 = 0.7$ (Fig. 6.40), which gives the relationship H = 0.1L. This logarithmic trend has been recognised by multiple authors who have interpreted controls on decreasing length and height in various ways including decreasing sediment coarseness (Crowe & Fisher, 1973; Sigurdsson et al., 1987), decreasing velocity/flow energy with distance from the vent (Crowe & Fisher, 1973; Schmincke et al., 1973; Sigurdsson et al., 1987; Brand et al., 2016), and decreasing slope angle (Schmincke et al., 1973; Brand et al., 2016).

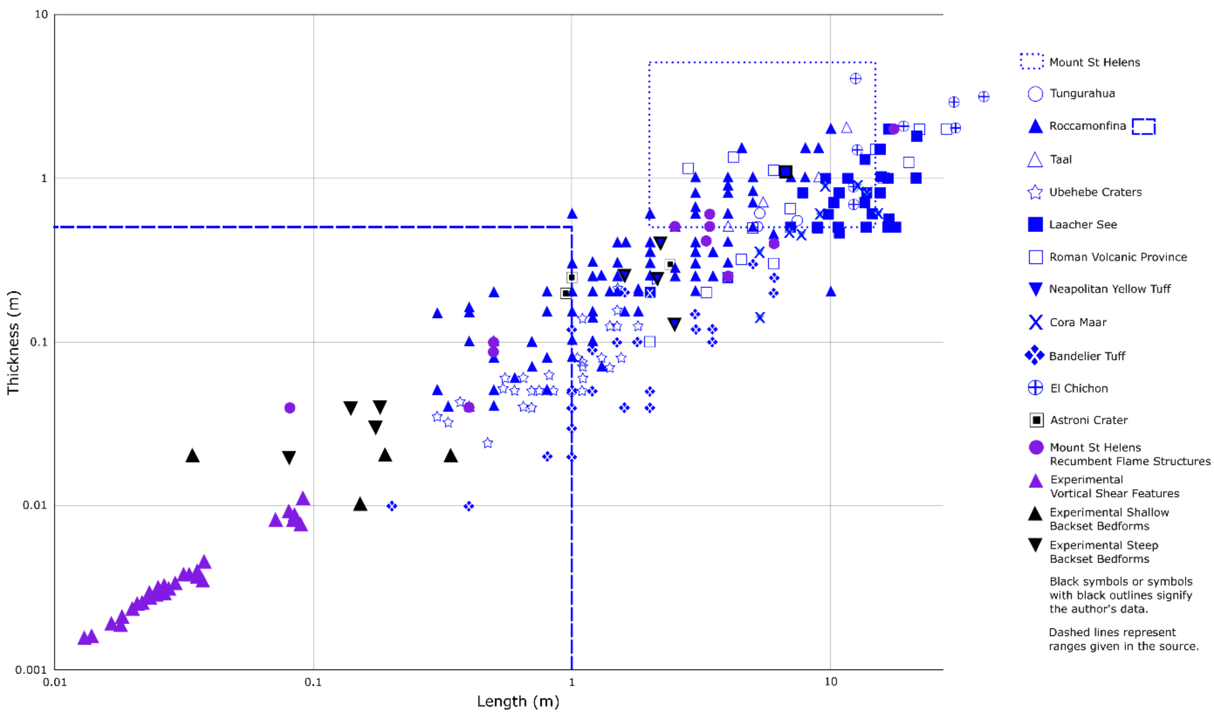

Figure 6.40 Backset bedform length vs. thickness for bedforms taken from the literature and the experimental ones described in Chapter 4. Black outlines show measurements taken from the author's field photos. This dataset also includes reported wavelengths (sources marked in Supplementary Table D.1 with *) and amplitudes (sources marked in Supplementary Table D.1 with +). See Supplementary Table D.1 in Appendix D for data sources.

6.4 Validation of experimental deposits

6.4.1 Bedform angles

The experimental steep backset bedforms have stoss angles greater than 20° and lee angles less than 10°. Similar natural features do exist, but not many backset bedforms from the field plot close to the experimental ones (Fig. 6.39). The lack of natural bedforms with steep stoss-sides and gentle lee sides is probably due to polydispersity in grain size and shape in nature, as opposed to the spherical, fine-grained, monodisperse particles used in the experiments which have a low angle of repose. Particles used in the experiments in this thesis have a dynamic angle of repose of 20.9° (section 4.4.2), whereas particles from the Pozzolane Rosse ignimbrite have a dynamic angle of repose of 45° (section 4.2.5), allowing them to form steeper lee slopes. Bedforms in aeolian deposits have been found to be more stable when comprised of coarser grains (Weitz et al., 2018), and less stable where a 50-150 µm fraction is present. The experimental bedforms are comprised of this fraction of particles, which may explain their gentle lee slopes. Furthermore, liquefaction of the bed due to high pore pressures is thought to play a role in the formation of gentle lee slopes in a fluvial environment (Hendershot et al., 2016). It is possible that a process similar to this could take place during the deposition of the experimental bedforms. If high pore pressures were trapped in the aggrading deposit (possible due to the impermeability of the mixture) a semi-fluidised top of the deposit which is able to move on slopes less than the angle of repose could exist. This process would not take place on the stoss side due to the impact of the current directly against the aggrading bed.

Steep backset experimental bedforms do, however, have similar stoss and lee angles to some field examples, particularly those from Mt St Helens and Laacher See (Fig. 6.39). In both cases the backset bedforms at these localities have been interpreted as recording high energy, supercritical flow conditions (Schmincke et al., 1973; Rowley et al., 1985; Brand et al., 2016), in contrast to the similar experimental structures formed in waning flow by topographic blocking (section 4.3). However, these field studies also highlight the importance of rapid deposition, which occurs in the analogue experiments due to a sudden drop in pore pressure. At Laacher See and Mt St Helens “chute-and-pool” structures are found in proximal deposits (< 2.5-3 km). These deposits were formed from the collapse of eruption columns, creating heavily laden, high energy density flows (Schmincke et al., 1973) and concentrated PDCs (Brand et al., 2016) that rapidly shed sediment in proximal areas. Numerical modelling by Sweeney and Valentine (2017) and Valentine and Sweeney (2018) shows that concentrated currents can form from the proximal collapse of eruption columns containing dominantly poorly coupled (i.e. coarse) particles.

Shallow backset experimental bedforms share similar angles with backset bedforms from Roccamonfina, Italy (Fig. 6.39). The majority of measurements at Roccamonfina are taken from the Trachyte Tuff of Garofali (GTT) (Giannetti & Luongo, 1994), which is an intracaldera facies originating from several vents. Despite its proximal location it has been interpreted that there was no ‘significant’ eruption column during the emplacement of the GTT due to the lack of fall deposits. Unlike Laacher See and Mt St Helens, therefore, there would not have been deposition in proximal areas as a result of column collapse. The data from Ubehebe Craters, CA plot nearby as well. Crowe and Fisher (1973) interpret these backset bedforms as indicative of a high flow regime, but also recognise the importance of rapid deposition and the increasing ratio of suspension fallout to tractional movement. This is similar to the decreasing shear/increasing sedimentation rate seen in the transition from planar through to shallow and steep backset experimental bedforms described in section 5.4.

6.4.2 Bedform thickness vs. length

The experimental backset bedforms plot on the trend of backset bedform thickness vs. length measurements taken from the literature (Fig. 6.40). Although they show no statistical correlation (probably due to the low sample size) they nevertheless plot where expected at the lower end of the trend. The experimental backset bedforms consist of fine particles - in subaqueous systems, bedform size has been shown to be dependent on grain size, with greater potential bedform sizes in coarser-grained sediments (Flemming, 2000). In addition, the experimental currents travelled slower than natural ones, as well as being an order of magnitude thinner, highlighting the controls of flow depth and velocity on bedform size. As a comparison, the largest backset bedforms presented here, proximal to El Chichon (Sigurdsson et al., 1987), are interpreted as been deposited from surges with a ~35 m thick boundary-layer (seven times as thick as distal surges), with flow velocity as the primary control on bedform size.

Experimental shear-derived vortical features (Rowley et al., 2011) also plot on the observed trend, and similar recumbent structures observed at Mt St Helens (Pollock et al., 2019) overlap multiple different data sets. Height vs. length relationships round to H =0.1L and H = 0.2L respectively, which are very close to that for the literature-derived backset bedforms (H = 0.1L). In both these cases the flows were dense and rapid deposition took place, as occurred in deposition of steep backset experimental bedforms (Chapter 4). However, these vortical and recumbent structures are interpreted as forming under high shear, whereas shear is low during the deposition of the steep backset experimental bedforms (section 5.4).

Some authors recognise an effect of increasing slope angle on increasing bedform size and stoss angle (Brand et al., 2016), but in other cases steep stoss-side bedforms are seen to be deposited on gentle (<5°) slopes (e.g. Bryan et al., 1998; Brand & Clarke, 2012; section 4.2.5). The slope that bedforms are deposited on is not often recorded in the literature, but some ranges for various volcanoes are displayed in Figure 6.41. From the available data, there does not seem to be any relationship between backset bedform geometry and depositional surface angle across multiple settings. For example steep stoss angles are found on steep (Mt St Helens) and shallow slopes (Table Rock). Steep lee angles are found on steep (Tungurahua) and shallow (Pozzolane Rosse) slopes. Small backset bedforms are deposited on shallow slopes (experimental), and large backset bedforms are deposited on shallow slopes (Baccano Crater, Roman Volcanic Province) and steep slopes (Mt St Helens). There are no small backset bedforms (< 1 m length and 0.1 m thickness) deposited on steep (> 20°) slopes, but this may just reflect the lack of data. Brand et al. (2016) suggest that steep backset bedforms are found on steep slopes because these are proximal to source and PDCs are more high-energy here. In view of the data presented here this suggests that slope angle may have some contribution to bedform geometry but that other controls such as flow energy and topographic blocking are stronger.

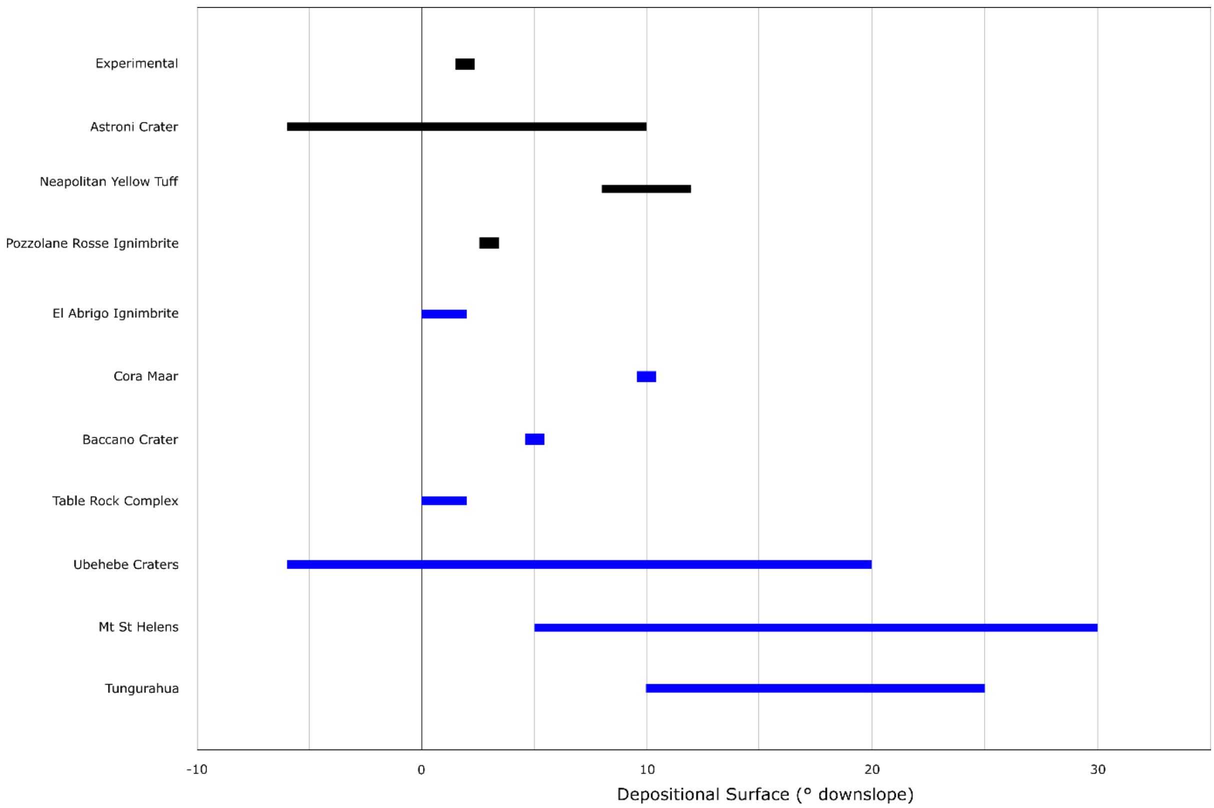

Figure 6.41 Ranges of depositional surfaces backset bedform have been found on. See Supplementary Table D.1 in Appendix D for data sources, blue bars are from the literature and black bars from the author.

6.5 Conclusions

This chapter has shown that backset bedforms possess a wide range of stoss and lee angles, but tend to have either steep (>20°) stoss and gentle (<20°) lee or be generally symmetrical. For length vs. thickness, meanwhile, backset bedforms from the field plot on a single trend which can be defined as H = 0.1L. Numerous mechanisms have been invoked by different authors for the deposition of backset bedforms, such as high flow regime conditions (Crowe & Fisher, 1973), transition from supercritical to subcritical flow (Schmincke et al., 1973), and topographic blocking (Douillet et al., 2018; section 4.3). Although backset bedforms can be created in waning flow conditions it is not clear that the interpretations of these experimental structures can be carried over to all natural features based purely on geometrical similarities. While high flow energy is a common explanation for backset bedforms of this type, rapid deposition is commonly cited as a reason for their formation and preservation (e.g.

Schmincke et al., 1973; Brand et al., 2016; Douillet et al., 2018; Pollock et al., 2019). Douillet et al. (2018) and the experiments in Chapter 4 also cite the importance of rapid deposition in preserving steep stoss angles in field and experimental bedforms, respectively, showing that there may be similarities between overall very different interpretations. Regardless of specific formation mechanisms, however, it is important that experimental and natural backset bedforms overlap significantly in measurements of length vs. thickness and stoss vs. lee angles, and that they form on overlapping ranges of depositional slopes. Despite the experimental currents being much thinner and slower, the fact that the experimental backset bedforms plot either side of the H = 0.1L trend suggests that the experimental currents in this thesis are a good analogue of natural dense PDCs, and that experimental backset bedforms can be used to infer flow conditions inside them.

6.5.1 Recommendations for recording PDC bedform geometries in the field

Future work would much benefit from more standardised reporting of bedform geometries, as well as metadata for published field photographs. Volcanologists can benefit from such data for both interpreting field deposits, and to design numerical and analogue models. Further field data on backset bedform angles, for example, will help to make clear whether the two trends identified in Figure 6.39 are “real”, and constrain the differences between shallow and steep backset bedforms. Likewise, more information on the depositional surfaces such bedforms are deposited on will allow greater understanding of what triggers their formation. Some suggestions are given below:

- Data should be presented in tables and plots. Ranges and representative values given in the text should be additional to this rather than stand-alone.
- If dip measurements are not the true dip this should be noted.
- It should be made clear whether dips are measured from the depositional surface or from the horizontal, and the angle of the depositional surface should be noted.

- Field photographs should include coordinates and the direction of view.
- Field photographs should be taken orthogonally to the bedform wherever possible.
- Flow direction should always be marked on field photographs.

==

Chapter 7

7. Synthesis and concluding remarks

==

The experiments presented in this thesis have investigated the variable aeration of sustained granular currents, analogous to pyroclastic density currents (PDCs), their depositional processes, and the characteristics of their deposits. They provide increased understanding of the importance of high pore pressures in controlling PDC behaviour and deposit morphology, as well as calling into question traditional interpretations of upstream-dipping bedforms in PDC deposits. Furthermore, the enigmatic flow-boundary zone has been identified and characterised for dense granular currents. Some outstanding issues are discussed below. Specific conclusions are then presented, in the format of answering the research questions given in section 1.4 , and finally some suggestions for future work are made.

7.1 Discussion

7.1.1 Scaling

Although scaling issues were dealt with separately in each results chapter, a table is provided here to briefly summarise how a range of parameters and dimensionless numbers from these experiments commonly overlap with their natural counterparts. This shows that the experimental granular currents described in the previous chapters are well-scaled for dense PDCs, which allows conclusions drawn about the former to be applied, carefully, to the latter.

Table 7.1 Parameters of natural dense PDCs (data from Roche, 2012) compared with the experimental currents in this work. *Range for the ash matrix only. **Values derived from the ranges for the Bagnold and Savage Numbers. +From Chapter 4 experiments only.

Parameter	Dense PDCs	These experiments
Particle Diameter (m)	$2x10^{-5}$ – $5x10^{-4}$*	$4.5x10^{-5}$ – $2.5x10^{-4}$
Particle Density (kgm^{-3})	500-2500	2500
Particle Volume Fraction	0.3-0.6	0.6
Fluid Density (kgm^{-3})	~1	1.225 - 2
Fluid Viscosity ($kgm^{-1}s^{-1}$)	~10^{-5}	$1.78x10^{-5}$
Acceleration due to Gravity (ms^{-1})	9.81	9.81
Flow Thickness (m)	10^{0} – $5x10^{1}$	10^{-3} – $1.2x10^{-1}$
Flow Length (m)	10^{3}-10^{4}	0.5-3
Flow Front Velocity (ms^{-1})	5-30	1.5 – 2.5
Slope Angle (°)	0-30	2 - 4
Froude Number	1.6-3	0.7 - 7
Bagnold Number	10^{0}-10^{2}	15 -269^{+}
Savage Number	10^{-9} – 10^{-8}	$3x10^{-11}$ – $3x10^{-2}$
Friction Number	**10^{7} – 10^{11}	$8x10^{3}$ – $5x10^{5+}$

Particle size and density were chosen specifically in order to provide dynamic similarity with natural, low permeability dense PDCs which possess long-lived high pore pressures (section 2.5.4.2; Roche, 2012). The particle volume fraction was not varied between experiments and given the high mass fluxes must have approached the maximum concentration for randomly packed spheres of 0.63 (Song et al., 2008). The flow thickness, length, and speed are all constrained by the small size of the experiments compared to nature, but sustained fluidisation (Rowley et al., 2014) prevents the expected rapid loss of pore pressure. The interstitial fluid was compressed air with a density slightly greater than 1. Slope angle was varied slightly to simulate runout on gentle slopes far away from a PDC's source.

The Froude Number was defined in section 3.4.4 and is the ratio of kinetic to potential energy - flows < 1 are defined as subcritical and flows > 1 are supercritical. Experimental values presented here are generally < 4 in the body of the flow, but can be as high as 7 towards the flow front. The Bagnold Number was defined in section 2.3.3 and is the ratio of collisional to viscous stresses. The Savage Number was defined in section 2.3.1 and is the ratio of collisional to frictional forces. The Friction Number is defined as the ratio of the Bagnold Number and the Savage Number, and so represents the ratio of frictional to viscous stresses (Iverson, 1997). While the experimental and natural ranges here do not overlap this is probably due to the low resolution of experiments in Chapter 4 leading to the underestimation of H, giving relatively high Savage Numbers (see section 7.1.2).

7.1.2 Phase field discrepancy

The experiments described in Chapters 4 and 5 were run under the same fluidisation conditions and resulted in deposits consisting of three types of bedforms – planar, shallow backset, and steep backset. However, there is a discrepancy in their conditions of formation. The bedforms from the Chapter 5 experiments are deposited from currents at lower velocities and greater thicknesses than those from the Chapter 4 experiments (Fig. 7.1). They do, however demonstrate the same general trend, although this is weak as regards current thickness. There are several possible reasons for this discrepancy:

- Different current thicknesses. In the Chapter 4 experiments the resolution was too low to identify the flow-boundary zone. Due to the low velocities in this area it would have appeared to be part of the static deposit, decreasing apparent current thickness. The Chapter 5 experiments include the flow-boundary zone, increasing the thickness of the current. This also accounts for the larger Savage Numbers reported in Chapter 4. This issue highlights a need for a constant criteria for defining the base of the current in situations where the current and deposit are very similar in concentration and difficult to differentiate at lower resolutions.

- Different measurement techniques. The higher-resolution video used in the Chapter 5 experiments, along with the tracking particles, allowed the calculation of velocities using PIV, which was not possible in the Chapter 4 experiments. Some of the difference in velocities between the two sets of experiments can therefore be explained by the fact that it was measured in different ways, with a greater error in the lower-resolution Chapter 4 experiments.

- Different window of the flume. Much of the planar bed data from the Chapter 4 experiments comes from 20-30 cm further downstream than in the Chapter 5 experiments (blue box in Fig. 7.2), and was therefore deposited by the earlier, faster portion of the current. This is because the Chapter 5 experiments aimed to gather high resolution video of all 3 bedforms so only a small area was examined.

- Different grain size distributions. The Chapter 5 experiments use a bimodal grain size distribution as opposed to the monodisperse currents in Chapter 4. It is possible the inclusion of coarser particles resulted in greater permeability and pore pressure diffusion, leading to slower (or more rapidly decelerating) currents. However, Roche et al. (2006) showed that small concentrations of coarser particles should not affect the bulk Group A behaviour.

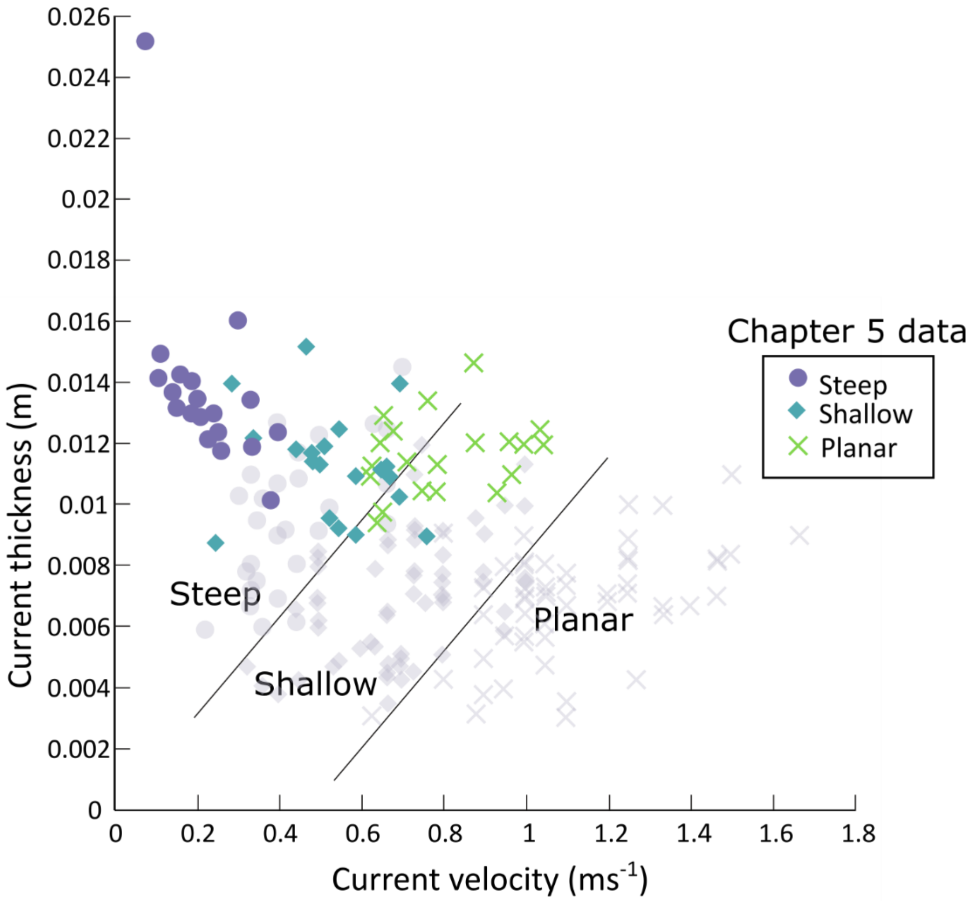

Figure 7.1 Bedform phase diagram modified from section 4.2.3, showing data from Chapter 5 experiments superimposed on the phase fields defined by the Chapter 4 experiments, with original data in faded grey. The velocities given here for the Chapter 5 data are the maximum velocities.

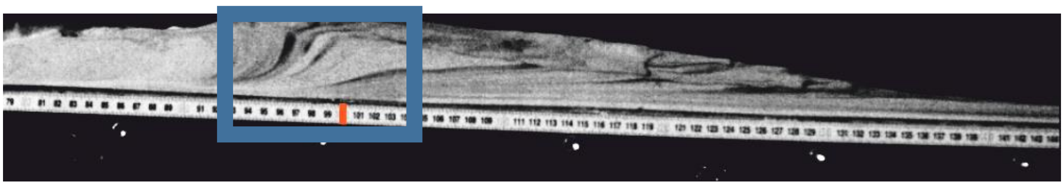

Figure 7.2 Longitudinal view of an experimental deposit from Chapter 4. For comparison, the blue box highlights the area of the flume in which analysis of the Chapter 5 experiments takes place.

7.1.3 Gradual or stepwise progressive aggradation?

The experiments in Chapter 3 show a series of pulses overrunning the flow front, suggesting that deposition may be taking place by stepwise aggradation (section 3.4.4). As the currents are monodisperse and made up of particles of one colour it is impossible to evaluate how deposition occurs well behind the flow front. Stepwise aggradation occurs when periods of deposition alternate with periods of non-deposition (Fig. 7.3; Branney & Kokelaar, 1992). The behaviour of the pulses at the flow front is reminiscent of a model proposed by Sulpizio and Dellino (2008), where each pulse of a dense PDC is rapidly deposited (almost "emplaced"), resulting in a stepped graph of deposit thickness vs. time. Stepwise aggradation has also been invoked for PDCs at Mt St Helens (Pollock et al., 2019), as the calculated rate of deposition is too high for the deposits in question so periods of non-deposition must also have occurred, as well as for block-and-ash-flows (Charbonnier & Gertisser, 2011; Macorps et al., 2018).

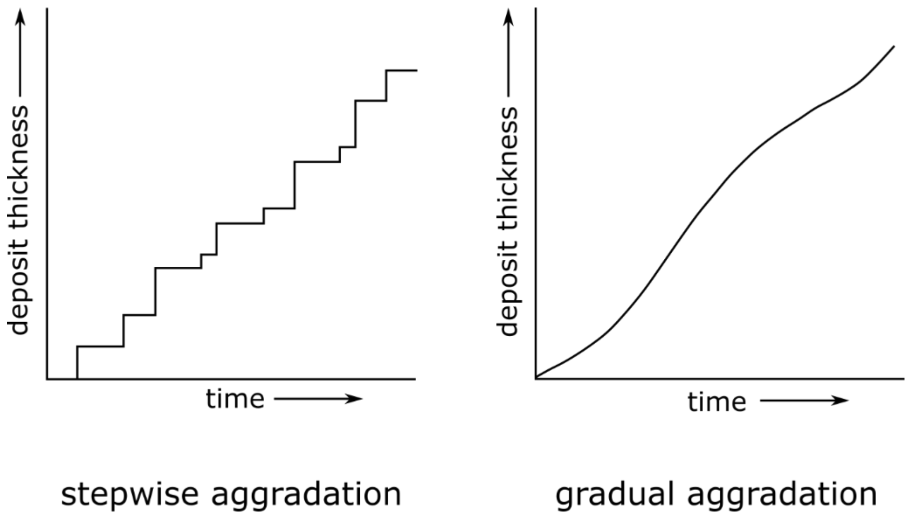

Figure 7.3 Stepwise and gradual progressive aggradation (Branney & Kokelaar, 1992).

However, in the high-resolution experiments in Chapter 5 it is clear that once deposition has begun it continues, not necessarily as a steady rate but without periods of non-deposition (gradual aggradation, Fig. 7.3). The pulsating behaviour is also not apparent in the relatively proximal window examined – in the Chapter 3 experiments the overriding pulses were visible relatively distally. It seems to be the case, therefore, that deposition occurs by gradual progressive aggradation in the body of the current and stepwise in distal areas by emplacement of successive pulses. Further experiments focused on high-resolution imaging of distal deposition would be needed to confirm this, however. This reinforces that no one location of a PDC is representative of the whole and that different depositional mechanisms can be active depending on local conditions.

7.1.4 Why aren't there more natural examples of steep bedforms?

Section 6.3 shows that although the experimental steep backset bedforms have realistic stoss and lee angles compared to natural examples there are relatively few natural bedforms with their exact angles. There are several possible, related reasons that the exact dimensions of the steep experimental bedforms reported here either do not occur or are not preserved often in nature (summarised in Fig. 7.4):

- As mentioned in section 4.2.5, bedforms may be cryptic, i.e. difficult or impossible to distinguish from the surrounding deposit due to similarities in grain size and colour (Fig. 7.4), and depending on deposition rate very steep stoss beds may collapse and be reincorporated into the current before the deposit is stable.
- The experimental steep backset bedforms are interpreted as forming from stoss-side blocking during waning flow (section 4.3), which is triggered by a rapid loss of pore pressure forming an aggrading sediment pile. Rapid deaeration can happen in numerous ways in natural currents (section 3.4.4) but the existence of suitable topographic barriers already in place could also trigger the stoss-side blocking process. On the slopes of volcanoes there will be a limited amount of locations where such a process could take place, especially in multiple-PDC, or sustained PDC events, where earlier deposition will result in smoothed topography (Brown & Branney, 2013) with less obstacles to trigger such a process as happened in the experiments (Fig. 7.4).

- The experimental currents consisted of spherical particles of one (Chapter 3 & 4) or two (Chapter 5) sizes. This resulted in lee slopes with relatively gentle slopes, due to the low angle of repose of the experimental materials. PDCs are liable to be poorly sorted and contain very irregular fragments of juveniles and lithics, with higher angles of repose. Section 4.2.5 shows that samples of the Pozzolane Rosse ignimbrite have dynamic angles of repose of 45°. Therefore, bedforms deposited by natural PDCs will generally have greater lee angles than experimental ones, which is seen in section 6.3.
- Erosion by PDCs is known to occur both on steep slopes (>~25°, Brand et al., 2016), and in areas of slope changes and due to local topographic effects (Calder et al., 2000; Brand et al., 2016). Hence, if any steep backset bedforms were deposited due to blocking of the current in a topographically rough area then they could be eroded, either by the same current or a subsequent one (Fig. 7.4).
- Bedform size is related to distance from source and thought to be a product of flow energy (section 2.4.1). This means that large bedforms will be deposited on a volcanoes flanks, which is the case at Mt St Helens (Brand et al., 2016). However, this makes them more liable to erosion, either by the same current or a subsequent one. Also, the experimental bedforms are thicker than the thickness of the depositing dense current. As the dense basal currents of PDCs can be many meters thick (Roche, 2012) natural examples could be very large, especially in proximal locations, which would make them hard to recognise, especially if the crest has been eroded. Such a problem was noted by Sigurdsson et al. (1987) at El Chichon. Conversely, as bedform size decreases with distance a point will come where they are too small to identify (Fig. 7.4).

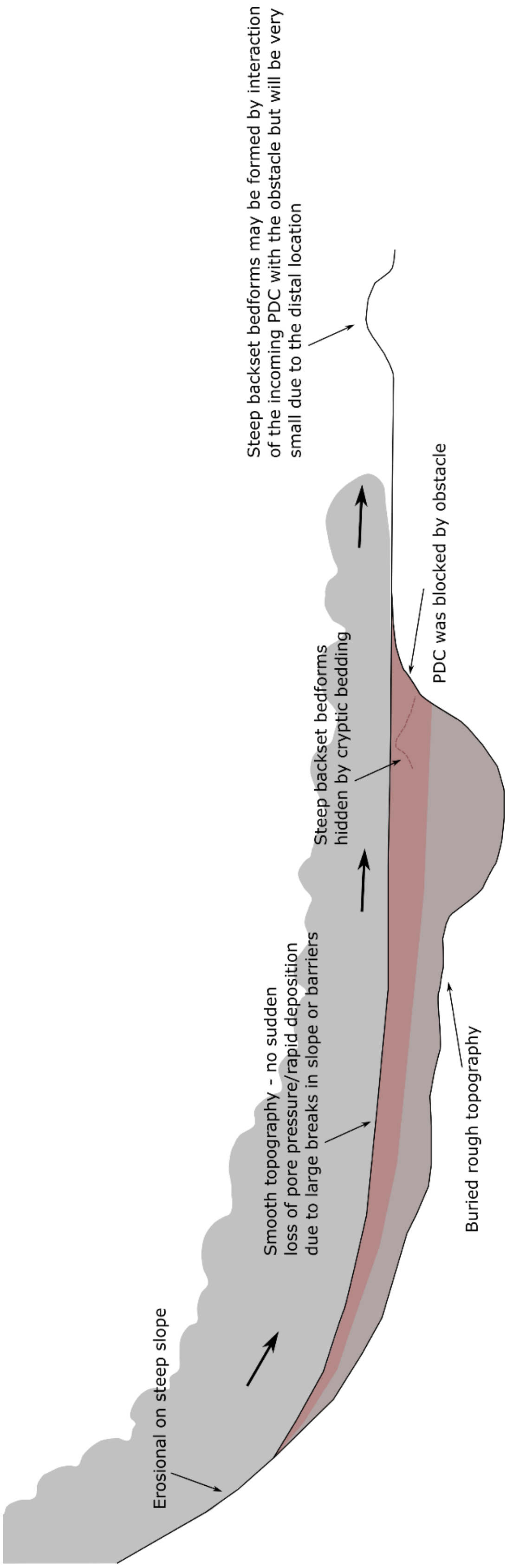

Figure 7.4 Schematic diagram (not to scale) showing reasons why steep backset bedforms are not often found in PDC deposits.

Some of these suggestions are applicable even to the traditional interpretation of steep backset bedforms, that they record supercritical flow conditions.

7.2 Main findings

Can heterogeneous fluidisation of granular currents be replicated in the lab and what effect does this have on flow parameters?

PDCs are intrinsically heterogeneous in time and space, and with numerous possible methods of fluidisation, there will be variability of pore pressure magnitude within a current. In Chapter 3, experiments are presented that examine the effect of variable fluidisation in granular currents for the first time.

High initial gas fluxes produce currents which travel as supercritical pulses, with average Froude Numbers of 7 (section 3.4.4). These are seen at the current head and in the first pulse, and are higher than in other experiments simulating dense PDCs (e.g. Roche et al., 2002, 2004, 2008), reflecting the higher energy in currents initiated from collapse from a hopper as opposed to dam-break initiation. This collapse-type initiation more accurately replicates sustained, quasi-steady PDCs which form from fountaining and column-collapse. Moderate sustained gas fluxes produce currents with at least equal runouts to those with high initial fluxes that are subsequently decreased (section 3.3.1). The sustained basal gas injection results in slower, more realistic pore pressure diffusion timescales compared to dam-break experiments, where pore pressure diffusion is fast and runout distances short (Roche, 2012).

Although the greatest flow front velocities are reached by currents with the highest degree of proximal aeration, high initial fluxes that are subsequently decreased also result in flow front velocities which decline more rapidly than currents with moderate sustained gas fluxes. As aeration drops are not immediately reflected in velocities, currents can continue to accelerate for a short period after undergoing an aeration drop (section 3.3.1). Assuming that a dense

PDC is sufficiently fine-grained/poorly sorted (Breard et al., 2019) for high pore pressures to be retained, a situation can be envisaged where it is not immediately slowed by deaeration caused by e.g. loss of fines (Bareschino et al., 2007) at a break in slope (Sulpizio et al., 2016). If an assumption that PDCs would decelerate at that point had been built into local hazard assessment more people than realised could be at risk. The morphology of the resulting deposit also depends on pore pressure magnitude and variation. Sustained, moderate aeration results in greater runout distances and thin deposits, while thick wedges are formed by currents that undergo large aeration drops (section 3.3.3). These findings are relevant as high pore pressures can be generated in PDCs in numerous ways (e.g. Sparks, 1978; Wilson, 1980; Chédeville & Roche, 2014; Lube et al., 2020), and mechanisms can vary in time and space.

What is the effect of slope angle on the behaviour of sustained, variably fluidised granular currents?

PDCs travel down the steep flanks of volcanoes and may propagate great distances on sub-horizontal substrates, therefore it is important to quantify how changes in gradient effect current dynamics. In Chapter 3, it is shown that increasing the slope angle from 2° to 4° is able to increase the runout distance of currents by over 50%. Currents which undergo low levels of sustained aeration for their entire runout distance see the greatest increases in runout distance with slope angle. Currents travelling on a 4° slope are also able to sustain higher flow front velocities for longer (section 3.4.3). Therefore, even gentle gradients far from the steep upper flanks of a volcano can prolong high PDC velocities and runout distances. Fieldwork suggests that erosion and entrainment commonly occurs on steep slopes (e.g. Calder et al., 2000; Brand et al., 2016; Pollock et al., 2016), and although this has been seen to substantially increase runout distance in dry granular currents (Mangeney et al., 2010; Farin et al., 2014), it is not clear if this would be seen in variably fluidised/defluidising granular currents as well. In these experiments erosion was not noted, presumably as the gradient was too shallow to generate the required basal shear stress.

How do conditions in variably fluidised granular currents control deposition (and vice versa)?

Chapter 3 shows that the magnitude of an aeration drop controls deposit morphology, with large drops forming thick wedges of sediment and uniform moderate aeration forming thin sheets. Uniform low aeration (<~0.5 U_{mf_st}) forms thick deposits upstream (section 3.3.3), as also seen in Rowley et al. (2014) and the initially fluidised dam-break experiments of Roche et al. (2002).

In Chapter 4, focusing the video on the point of a large aeration drop allows investigation of how thick wedge-shaped deposits form. Rapid deposition caused by the aeration drop results in an aggrading sediment pile (section 4.2.2). Initially currents are able to surpass this and continue downstream, but once a critical height has been reached the current is forced to propagate upstream as a granular bore (section 4.3), which is also seen in other work on the interaction of granular currents with barriers, e.g. Faug (2015), who defines a phase field for the formation of granular bores. In the Chapter 4 experiments, the incoming current begins to propagate upstream as a bore when the sediment pile is ~ 4 cm thick. Using a thickness of 0.08 cm for the incoming current gives an obstacle/current thickness ratio of 5. As well as *Fr*, this is lower than predicted by Faug's (2015) phase diagram for the formation of granular bores – these parameters instead fall into their 'granular dead zone' regime, where a quasi-static stagnant zone forms upstream of the obstacle, there is no marked difference in thickness and some material is able to overflow the obstacle. Nevertheless in the experiments described here a bore clearly propagates upstream and is noticeably thicker than the incoming current. It is possible that this phase diagram is not relevant to these experiments as here the incoming currents are aerated and very mobile, less likely to form a quasi-static region upstream of an obstacle. The granular bore is recorded in the deposit as steep, upstream dipping beds (section 4.3).

Deposition from PDCs is significantly affected by topography (e.g. Sulpizio et al., 2008b; Cas et al., 2011; Brown & Branney, 2013; Sulpizio et al., 2014), and these experiments provide further evidence local obstacles can result in thick deposits from decelerating currents. An important point to be raised is that due to constriction by the sidewalls the incoming experimental currents were not able to flow around the obstacle, as has been interpreted as occurring in the field (Brown & Branney, 2013). Therefore granular bores may be more likely to occur in restricted, channelized environments. It is also notable that until a certain obstacle height was achieved, much of the granular current was able to flow across it without rapidly decelerating. The processes envisaged in section 4.3 could be triggered for natural PDCs by e.g. dearation and rapid deposition due to rough topography or breaks in slope, but because local topography may be smoothed out by depositing PDCs this is more likely to occur earlier in eruptions.

Can recognisable bedforms be deposited by these currents, and are different bedforms systematically deposited under different flow conditions?

A wide range of bedforms are found in PDC deposits, but until now there has been no work aimed at experimentally quantifying the conditions under which they form. In Chapter 4, it is shown that three different types of bedform are deposited after a current undergoes a large aeration drop (section 4.2.1). Initially these are planar beds, followed by shallow backset bedforms, and finally steep backset bedforms deposited in waning flow by a granular bore (section 4.3). A series of phase diagrams are presented, quantifying the flow conditions in which each bedform is deposited (Fig. 4.4). This is highly relevant because of general acceptance that backset bedforms record the transition from supercritical to subcritical flow conditions (e.g. Schmincke et al., 1973; Cole, 1991; Brand & Clarke, 2012; Brand et al., 2016), and a widespread association of dunes and bedforms of any type with dilute, turbulent PDCs (e.g. Crowe & Fisher, 1973; Branney & Kokelaar, 2002; Gençalioğlu-Kuşcu et al., 2007; Sulpizio et al., 2008b; Brand et al., 2009; Brown & Andrews, 2015), although recently similar conclusions to those reached here have been drawn from fieldwork (Douillet et al., 2013, 2018). In the experiments presented here, during deposition the dense granular currents are usually supercritical, and the steep backset bedforms appear to be the result of granular bores caused by topographic blocking of the current (section 4.3). Interpreting PDC deposits accurately is very important as different types of PDC have different associated hazards (Cole et al., 2015), so if some "dilute" PDC deposits can alternatively be interpreted as "dense" PDC deposits this has implications for hazard assessment.

If so, are these comparable to bedforms in PDC deposits and are the laboratory conditions realistic?

In Chapter 4 the experimental bedforms are validated using field examples from the Pozzolane Rosse ignimbrite, Italy. Due to its sedimentology and field relations this is interpreted as the deposit from a dense current, similar to the experimental ones (section 4.2.5). Bedforms found in the Pozzolane Rosse show steeply dipping stoss beds with angles comparable to those seen in the experiments, although the lee angles are steeper (probably due to the high repose angle of the natural material). The bedforms in the Pozzolane Rosse, therefore, are suitable to compare with the experimental ones, and the geography of the

Pozzolane Rosse suggests that its bedforms may also have been formed due to a similar topographic blocking process as seen in the experiments (section 4.3).

Chapter 6 extends this comparison of experimental and field bedforms; gathering bedform geometry data from PDC deposits described in the literature. In terms of stoss and lee angles, the field which the experimental steep backset bedforms plot in is not well populated, although there is some overlap, especially with bedforms from the proximal bedded deposits of Mt St Helens (Fig. 6.39). Furthermore, the experimental bedforms plot close to the clearly defined bedform length vs. thickness relationship of H = 0.1L (Fig. 6.40). This strongly supports the experimental bedforms as valid analogues of actual PDC deposits.

Backset bedforms in the field can show a variety of sorting and grading patterns. For example, steeply dipping backset beds described by Brand et al. (2016) are internally massive, attributed to rapid deposition. Rowley et al. (1985) describe antidunes as finer grained and better sorted than surrounding deposits. Cole and Scarpati (1993) describe backset layers in chute and pool structures which are enriched in coarser material due to the inhibition of turbulent sorting by a concentrated boundary layer. Grain size variation in bedforms has not been examined in these experiments except briefly in Chapter 5, and only using two grain sizes. In comparison to the above examples the process described in section 5.4.2 involves the inhibition of particle segregation due to decreasing shear and increasing deposition rate in the flow-boundary zone. This results in both fine and coarse particles passing though the flow boundary and forming the shallow and steep backset bedforms, giving them an internally massive appearance (with some stratification in the shallow backset bedforms). With a greater grain size distribution used in experiments it can be anticipated that more complex patterns will emerge.

Can the flow-boundary zone concept be experimentally quantified in fluidised granular currents? Do the currents deposit via gradual progressive aggradation?

The flow-boundary zone is a widely applied concept in the study of PDC deposits, but the different flow-boundary zone classes are not based on quantitative flow parameters. In Chapter 5, experiments identical to those in Chapter 4 are repeated, but at a higher resolution and with seeding of the currents with larger tracking particles. This allows velocity profiles to be constructed at any point in the current using PIV analysis (section 5.3.1). In combination with shear parameters obtained using the viscous law of the wall (section.5.3.2.2), it is possible to identify the flow-boundary zone, as the exponential tail of the velocity profile during the deposition of bedforms, and characterise its changes over time (section 5.4.1). Calculated shear velocities are similar to those estimated in the literature for subaqueous PDCs, and noticeably smaller than those estimated for dilute PDCs (section 5.4.1). As shear velocity and shear stress in the flow-boundary zone decrease, the flow-boundary zone itself increases in thickness, sometimes approaching 0.5 current thickness (Fig. 5.4b), and progressively steeper backset bedforms are deposited.

Once deposition begins it appears to continue without interruption, supporting a model of gradual progressive aggradation from the body of the current, which contrasts with recent work proposing stepwise progressive aggradation (Sulpizio et al., 2014; Pollock et al., 2019; Zrelak et al., 2020), which may occur more distally.

7.3 Recommendations for future work

As well as advancing understanding of flow and depositional processes, one of the aims of experimental modelling is to provide realistic data for numerical modelling, particularly that involving hazard assessment. The present study has made several noticeable advances, but due to the simplified system next steps should focus on determining whether the conclusions made here are applicable in currents with different compositions and boundary conditions. Possible future research includes:

Expanding the bedform stability criteria defined in Chapter 4.

Section 7.1.2 highlighted that even a small change in grain-size distribution may have an effect on the bedform phase fields, although in combination with other changes. Also, bedforms in PDC deposits display a wide range of sorting and grading patterns. Therefore more work should be carried out using granular currents of various grain-size distributions to examine how this effects bedform stability, and whether different criteria are needed to define these bedforms based on grain size. Furthermore the possibility of slope angle affecting bedform type and size has been noted in section 6.4, so future experiments of this type should investigate a range of slope angles, including steep (~20°) ones.

Using natural pyroclastic material.

Many lab-scale experiments have been carried out using natural particles rather than synthetic (section 2.5.4.2), although not involving heterogeneous aeration or bedform formation. As these mixtures are dominated by the same particle size as that used in the experiments here it would be expected that the same behaviour would be observed, were pyroclastic material used to repeat these experiments. This would be an important step in validating the interpretations made in this thesis. A side-effect of this would be currents with a more "natural" grain size distribution, which would hopefully reproduce complex grading patterns seen in PDC bedforms and which have only been reproduced here very simply.

Using particles of various densities.

PDCs are known to be density stratified (section 2.2), but the experiments presented here have used particles of the same density. Experiments may use particles of two densities to replicate the flow behaviours described in this thesis, but in order to accurately describe segregation processes grain sizes should be monodisperse. Although the entire granular current is already highly concentrated, denser particles should be concentrated at the base and be expected to be deposited preferentially, leading to concentrations at the base of the deposits and on the stoss sides of bedforms.

Continuing to record PDC bedforms in the field.

Much of the literature describing PDC bedforms is now over three decades old, and although there is excellent recent work which focuses on quantitative descriptions of such features, it is somewhat scarce, which is not likely to be because they have all been discovered! Therefore field volcanologists should endeavour to make detailed recordings of bedforms in PDC deposits rather than simply noting their presence.

References

Alexander, J., Bridge, J.S., Cheel, R.J. & Leclair, S.F. (2001) Bedforms and associated sedimentary structures formed under water flows over aggrading sand beds. *Sedimentology*, 48, 133–152.

Allen, J. (1984) *Sedimentary structures: their character and physical basis, vol. 2.* Amsterdam: Elsevier.

Andrews, B.J. (2014) Dispersal and air entrainment in unconfined dilute pyroclastic density currents. *Bulletin of Volcanology*, 76, 852. Available online: https://link.springer.com/article/10.1007/s00445-014-0852-4 [Accessed 14/11/2016].

Andrews, B. & Manga, M. (2011) Effects of topography on pyroclastic density current runout and formation of coignimbrites. *Geology*, 39, 1099–1102.

Andrews, B. & Manga, M. (2012) Experimental study of turbulence, sedimentation and coignimbrite mass partitioning in dilute pyroclastic density currents. *Journal of Volcanology and Geothermal Research*, 225-226, 30–44.

Auker, M.R., Sparks, R.S.J., Siebert, L., Crossweller, H.S. & Ewert, J. (2013) A statistical analysis of the global historical volcanic fatalities record. *Journal of Applied Volcanology*, 2, 2. Available online: https://link.springer.com/article/10.1186/2191-5040-2-2 [Accessed 12/5/2019].

Bagnold, R.A. (1954) Experiments on a gravity-free dispersion of large solid spheres in a Newtonian fluid under shear. *Proceedings of the Royal Society of London, Series A*, 225, 49–63.

Baker, J., Gray, N., & Kokelaar, P. (2016) Particle size-segregation and spontaneous levee formation in geophysical granular flows. *International Journal of Erosion Control Engineering*, 9(4), 174–178.

Barberi, F., Innocenti, F., Lirer, L., Munno, R., Pescatore, T., & Santacroce, R. (1978) The campanian ignimbrite: a major prehistoric eruption in the Neapolitan area (Italy). *Bulletin Volcanologique*, 41(1), 10–31.

Bareschino, P., Gravina, T., Lirer, L., Marzocchella, A., Petrosino, P., Salatino, P. (2007) Fluidization and de-aeration of pyroclastic mixtures: the influence of fines content, polydispersity and shear flow. *Journal of Volcanology and Geothermal Research*, 164, 284–292.

Baxter, P. (1990) Medical effects of volcanic eruptions. *Bulletin of Volcanology*, 52, 532–544.

Belousov, A., Voight, B. & Belousova, M. (2007) Directed blasts and blast-generated pyroclastic density currents: A comparison of the Bezymianny 1956, Mount St Helens 1980, and Soufrière Hills, Montserrat 1997 eruptions and deposits. *Bulletin of Volcanology*, 69(7), 701–740.

Boudet, J.F., Amarouchene, Y., Bonnier, B. & Kellay, H. (2007) The granular jump. *Journal of Fluid Mechanics*, 572, 413–431.

Bouma, A.H. (1962) *Sedimentology of some flysch deposits*. Amsterdam: Elsevier.

Bouma, A.H., Normark, W.R. & Barnes, N.E. (1985) *Submarine fans and related turbidite systems*. New York: Springer.

Brand, B.D. & White, C.M. (2007) Origin and stratigraphy of phreatomagmatic deposits at the Pleistocene Sinker Butte Volcano, Western Snake River Plain, Idaho. *Journal of Volcanology and Geothermal Research*, 160(3–4), 319–339.

Brand, B.D. & Clarke, A.B. (2012) An unusually energetic basaltic phreatomagmatic eruption: Using deposit characteristics to constrain dilute pyroclastic density current dynamics. *Journal of Volcanology and Geothermal Research*, 243–244, 81–90.

Brand, B.D., Clarke, A.B. & Semken, S. (2009) Eruptive conditions and depositional processes of Narbona Pass Maar volcano, Navajo volcanic field, Navajo Nation, New Mexico (USA). *Bulletin of Volcanology*, 71(1), 49–77.

Brand, B.D., Bendaña, S., Self, S. & Pollock, N. (2016) Topographic controls on pyroclastic density current dynamics: insight from 18 May 1980 deposits at Mount St. Helens, Washington (USA). *Journal of Volcanology and Geothermal Research*, 321, 1–17.

Brand, B.D., Pollock, N., Sarocchi, D., Dufek, J. & Clynne, M.A. (2017) Field-trip guide for exploring pyroclastic density current deposits from the May 18, 1980, eruption of Mount St. Helens, Washington. *USGS Scientific Investigations Report 2017-5022-C*. Available online: https://pubs.er.usgs.gov/publication/sir20175022C [Accessed 8/8/2017].

Branney, M.J. & Kokelaar, P. (1992) A reappraisal of ignimbrite emplacement: progressive aggradation and changes from particulate to non-particulate flow during emplacement of high grade ignimbrite. *Bulletin of Volcanology*, 54, 504–520.

Branney, M.J. & Kokelaar, P. (2002) *Pyroclastic density currents and the sedimentation of ignimbrites*. Geological Society, London, Memoirs, 27, 1-143.

Breard, E.C.P. & Lube, G. (2017) Inside pyroclastic density currents—uncovering the enigmatic flow structure and transport behaviour in large-scale experiments. *Earth and Planetary Science Letters*, 458, 22–36.

Breard, E.C.P., Lube, G., Cronin, S.J., & Valentine, G.A. (2015). Transport and deposition processes of the hydrothermal blast of the 6 August 2012 Te Maari eruption, Mt. Tongariro. *Bulletin of Volcanology*, 77, 100. Available online: https://link.springer.com/article/10.1007/s00445-015-0980-5 [Accessed 30/1/2017].

Breard, E.C.P., Lube, G., Jones, J.R., Dufek, J., Cronin, S.J., Valentin,e G.A. & Moebis, A. (2016) Coupling of turbulent and non-turbulent flow regimes within pyroclastic density currents. *Nature Geoscience*, 9, 767–771.

Breard, E.C.P., Dufek, J., Lube, G. (2018) Enhanced mobility in concentrated pyroclastic density currents: an examination of a self-fluidization mechanism. *Geophysical Research Letters*, 45, 654–664.

Breard, E.C.P., Jones, J.R., Fullard, L., Lube, G., Davies, C. & Dufek, J. (2019) The permeability of volcanic mixtures—implications for pyroclastic currents. *Journal of Geophysical Research: Solid Earth*, 124(2), 1343–1360.

Bridge, J.S. & Demicco, R.V. (2008) *Earth surface processes, landforms and sediment deposits*. Cambridge: Cambridge University Press.

Bridgwater, J., Foo, W.S. & Stephens, D.J. (1985) Particle mixing and segregation in failure zones-theory and experiment. *Powder Technology*, 41(2), 147–158.

Brown, M.C. (1962) Nuées ardentes and fluidization. *American Journal of Science*, 260, 467–470.

Brown, R.J. & Branney, M.J. (2004a) Bypassing and diachronous deposition from density currents: evidence from a giant regressive bed form in the Poris ignimbrite, Tenerife, Canary Islands. *Geology*, 32, 445–448.

Brown, R.J. & Branney, M.J. (2004b) Event-stratigraphy of a caldera-forming ignimbrite eruption on Tenerife: The 273 ka Poris Formation. *Bulletin of Volcanology*, 66(5), 392–416.

Brown, R.J. & Branney, M.J. (2013) Internal flow variations and diachronous sedimentation within extensive, sustained, density-stratified pyroclastic density currents flowing down gentle slopes, as revealed by the internal architectures of ignimbrites on Tenerife. *Bulletin of Volcanology*, 75(7), 727. Available online: https://link.springer.com/article/10.1007/s00445-013-0727-0 [Accessed 14/11/2016].

Brown, R.J. & Andrews, G.D.M. (2015) Deposits of pyroclastic density currents. In: Sigurdsson, H., Houghton, B., Rymer, H., Stix, J., McNutt, S. (Eds.) *The Encyclopedia of Volcanoes*, 2nd edition. Amsterdam: Academic Press, 631-648.

Brown, R.J., Kokelaar, B.P. & Branney, M.J. (2007) Widespread transport of pyroclastic density currents from a large silicic tuff ring: the Glaramara tuff, Scafell caldera, English Lake District, UK. *Sedimentology*, 54, 1163-1189.

Brown, S.K., Auker, M.R. & Sparks R.S.J. (2015) Populations around Holocene volcanoes and development of a Population Exposure Index. In: Loughlin, S.C., Sparks, R.S.J., Brown, S.K., Jenkins, S.F. & Vye-Brown, C. (Eds.) *Global Volcanic Hazards and Risk*. Cambridge: Cambridge University Press, 223–32.

Brown, S.K., Jenkins, S.F., Sparks, R.S.J., Odbert, H. & Auker, M.R. (2017) Volcanic fatalities database: analysis of volcanic threat with distance and victim classification. *Journal of Applied Volcanology*, 6, 15. Available online: https://appliedvolc.biomedcentral.com/articles/10.1186/s13617-017-0067-4 [Accessed 18/06/2020].

Bryan, S.E., Cas, R.A.F. & Martí, J. (1998) Lithic breccias in intermediate volume phonolitic ignimbrites, Tenerife (Canary Islands): constraints on pyroclastic flow depositional processes. *Journal of Volcanology and Geothermal Research*, 81(3–4), 269–296.

Burgissier, A. & Bergantz, G.W. (2002) Reconciling pyroclastic flow and surge: the multiphase physics of pyroclastic density currents. *Earth and Planetary Science Letters*, 202, 405–418.

Bursik, M.I. & Woods, A.W. (1996) The dynamics and thermodynamics of large ash flows. *Bulletin of Volcanology*, 58(2–3), 175–193.

Bursik, M., Patra, A., Pitman, E.B., Nichita, C., Macias, J.L., Saucedo, R. & Girina, O. (2005) Advances in studies of dense volcanic granular flows. *Reports on Progress in Physics*, 68(2), 271–301.

Calder, E.S., Cole, P.D., Dade, W.B., Druiit, T.H., Hoblitt, R.P., Huppert, H.E., Ritchie, L., Sparks, R.S.J. & Young, S.R. (1999) Mobility of pyroclastic flows and surges at the Soufriere Hills Volcano, Montserrat. *Geophysical Research Letters*, 26, 534–540.

Calder, E.S., Wagner, K. & Ogburn, S.E. (2015) Volcanic hazard maps. In: Loughlin, S.C., Sparks, R.S.J., Brown, S.K., Jenkins, S.F. & Vye-Brown, C. (Eds.) *Global Volcanic Hazards and Risk*. Cambridge: Cambridge University Press, 335–341.

Campbell, C.S. (1990) Rapid granular flows. *Annual Review of Fluid Mechanics*, 22, 13–34.

Carey, S. & Sigurdsson, H. (1987). Temporal variations in column height and magma discharge rate during the 79 A.D. eruption of Vesuvius (Italy). *Geological Society of America Bulletin*, 99(2), 303–314.

Cartigny, M.J.B., Ventra, D., Postma, G. & Van Den Berg, J.H. (2014) Morphodynamics and sedimentary structures of bedforms under supercritical-flow conditions: new insights from flume experiments. *Sedimentology*, 21, 712–748.

Carrigy, M.A. (1970) Experiments on the angles of repose of granular materials. *Sedimentology*, 14, 147–158.

Cas, R.A.F. & Wright, J.V. (1987) *Volcanic Successions: Modern and Ancient*. London: Allen and Unwin.

Cas, R.A.F., Wright, H.M.N., Folkes, C.B., Lesti, C., Porreca, M., Giordano, G., Viramonte, J.G. (2011) The flow dynamics of an extremely large volume pyroclastic flow, the 2.08-Ma Cerro Galán Ignimbrite, NW Argentina, and comparison with other flow types. *Bulletin of Volcanology*, 73, 1583–1609.

Cashman, K.V. & Sparks, R.S.J. (2013) How volcanoes work: A 25 year perspective. *Bulletin of the Geological Society of America*, 125(5–6), 664–690.

Charbonnier, S.J. & Gertisser, R. (2011). Deposit architecture and dynamics of the 2006 block-and-ash flows of Merapi Volcano, Java, Indonesia. *Sedimentology*, 58, 1573–1612.

Charbonnier, S.J. & Gertisser, R. (2012) Evaluation of geophysical mass flow models using the 2006 block-and-ash flows of Merapi Volcano, Java, Indonesia: Towards a short-term hazard assessment tool. *Journal of Volcanology and Geothermal Research*, 231–232, 87–108.

Chédeville, C. & Roche, O. (2014) Autofluidization of pyroclastic flows propagating on rough substrates as shown by laboratory experiments. *Journal of Geophysical Research*: *Solid Earth*, 119, 1764–1776.

Chédeville, C. & Roche, O. (2015). Influence of slope angle on pore pressure generation and kinematics of pyroclastic flows: insights from laboratory experiments. *Bulletin of Volcanology*, 77, 96. Available online: https://link.springer.com/article/10.1007/s00445-015-0981-4 [Accessed 14/11/2016].

Chédeville, C. & Roche, O. (2018) Autofluidization of collapsing bed of fine particles: Implications for the emplacement of pyroclastic flows. *Journal of Volcanology and Geothermal Research*, 368, 91–99.

Choux, C.M. & Druitt, T.H. (2002) Analogue study of particle segregation in pyroclastic density currents, with implications for the emplacement mechanisms of large ignimbrites. *Sedimentology*, 49(5), 907–928.

Clarke, A.B., Voight, B., Neri, A. & Macedonio, G. (2002) Transient dynamics of vulcanian explosions and column collapse. *Nature*, 415(6874), 897–901.

Cole, P.D. (1991) Migration direction of sand-wave structures in pyroclastic-surge deposits: implications for depositional processes. *Geology*, 19, 1108–1111.

Cole, P.D. & Scarpati, C. (1993) A facies interpretation of the eruption and emplacement mechanisms of the upper part of the Neapolitan Yellow Tuff, Campi Flegrei, southern Italy. *Bulletin of Volcanology*, 55, 311–326.

Cole, P.D., Calder, E.S., Druitt, T.H., Hoblitt, R., Robertson, R., Sparks, R.S.J. & Young, S.R. (1998) Pyroclastic flows generated by gravitational instability of the 1996-97 lava dome at Soufriere Hills Volcano, Montserrat. *Geophysical Research Letters*, 25(18), 3425–3428.

Cole, P.D., Calder, E.S., Sparks, R.S.J., Clarke, A.B., Druitt, T.H., Young, S.R., Herd, R.A., Harford, C.L. & Norton, G.E. (2002) Deposits from dome-collapse and fountain-collapse pyroclastic flows at Soufrière Hills Volcano, Montserrat. In: Druitt, T.H. & Kokelaar, B.P. (Eds.) *The Eruption of Soufrière Hills Volcano, Montserrat, from 1995 to 1999*. Geological Society, London, Memoirs, 21, 231–262.

Cole, P.D., Neri, A. & Baxter, P.J. (2015) Hazards from Pyroclastic Density Currents. In: Sigurdsson, H., Houghton, B., Rymer, H., Stix, J., McNutt, S. (Eds.) *The Encyclopedia of Volcanoes*, 2nd edition. Amsterdam: Academic Press, 943-956.

Conticelli, S., Boari, E., Avanzinelli, R., De Benedetti, A.A., Giordano, G., Mattei, M., Melluso, L. & Morra, V. (2010) Geochemistry, isotopes and mineral chemistry of the Colli Albani volcanic rocks: constraints on magma genesis and evolution. In: Funiciello, R. & Giordano, G. (Eds.) *The Colli Albani Volcano, Special Publications of IAVCEI, 3*. The Geological Society, London, 107-139.

Crandell, D.R. & Hoblitt, R.P. (1986). Lateral blasts at Mount St. Helens and hazard zonation. *Bulletin of Volcanology*, 48, 27–37.

Crowe, B. & Fisher, R. (1973) Sedimentary structures in base-surge deposits with special reference to cross-bedding, ubehebe craters, death valley, California. *Bulletin of the Geological Society of America*, 84, 663–682.

Dade, W.B., Huppert, H.E. (1996) Emplacement of the Taupo ignimbrite by a dilute turbulent flow. *Nature*, 381, 509–512.

de Gennes, P.G. (1999) Granular matter: a tentative view. *Reviews of Modern Physics*, 71(2), S374–S382.

Delannay, R., Valance, A., Mangeney, A., Roche, O. & Richard, P. (2017) Granular and particle-laden flows: from laboratory experiments to field observations. *Journal of Physics D: Applied Physics*, 50(5), 053001. Available online: https://iopscience.iop.org/article/10.1088/1361-6463/50/5/053001 [Accessed 12/8/2019].

Dellino, P., Isaia, R. & Veneruso, M. (2004) Turbulent boundary layer shear flows as an approximation of base surges at Campi Flegrei (Southern Italy). *Journal of Volcanology and Geothermal Research*, 133(1–4), 211–228.

Dellino, P., Zimanowski, B., Büttner, R., La Volpe, L., Mele, D. & Sulpizio, R. (2007) Large-scale experiments on the mechanics of pyroclastic flows: Design, engineering, and first results. *Journal of Geophysical Research: Solid Earth*, 112(4). B04202. Available online: https://agupubs.onlinelibrary.wiley.com/doi/full/10.1029/2006JB004313 [Accessed 2/12/2016].

Dellino, P., Mele, D., Sulpizio, R., La Volpe, L. & Braia, G. (2008) A method for the calculation of the impact parameters of dilute pyroclastic density currents based on deposit particle characteristics. *Journal of Geophysical Research: Solid Earth*, 113, B07206. Available online: https://agupubs.onlinelibrary.wiley.com/doi/full/10.1029/2007JB005365 [Accessed 3/7/2019]

Dellino, P., Dioguardi, F., Zimanowski, B., Büttner, R., Mele, D., La Volpe, L., Sulpizio, R., Doronzo, D.M., Sonder, I., Bonasia, R., Calvari, S. & Marotta, E. (2010) Conduit flow experiments help constraining the regime of explosive eruptions. *Journal of Geophysical Research, 115(B4)*, B04204. Available online: https://agupubs.onlinelibrary.wiley.com/doi/10.1029/2009JB006781 [Accessed 21/8/2020].

Dellino, P., Dioguardi, F., Doronzo, D.M. & Mele, D. (2020) A discriminatory diagram of massive versus stratified deposits based on the sedimentation and bedload transportation rates. Experimental investigation and application to pyroclastic density currents. *Sedimentology*, 67(4), 2013–2039.

Dioguardi, F. & Dellino, P. (2014) PYFLOW: A computer code for the calculation of the impact parameters of Dilute Pyroclastic Density Currents (DPDC) based on field data. *Computers and Geosciences*, 66, 200–210.

Dobran, F., Neri, A. & Macedonio, G. (1993) Numerical simulation of collapsing volcanic columns. *Journal of Geophysical Research*, 98, 4231–4259.

Doronzo, D.M. & Dellino, P. (2010) A fluid dynamic model of volcaniclastic turbidity currents based on the similarity with the lower part of dilute pyroclastic density currents: Evaluation of the ash dispersal from ash turbidites. *Journal of Volcanology and Geothermal Research*, 191(3–4), 193–204.

Doronzo, D.M. & Dellino, P. (2011) Interaction between pyroclastic density currents and buildings: Numerical simulation and first experiments. *Earth and Planetary Science Letters*, 310(3–4), 286–292.

Doronzo, D.M. & Dellino, P. (2013) Hydraulics of subaqueous ash flows as deduced from their deposits: 2. Water entrainment, sedimentation, and deposition, with implications on pyroclastic density current deposit emplacement. *Journal of Volcanology and Geothermal Research*, 258, 176–186.

Doronzo, D.M., Valentine, G.A., Dellino, P. & de Tullio, M.D. (2010) Numerical analysis of the effect of topography on deposition from dilute pyroclastic density currents. *Earth and Planetary Science Letters*, 300(1–2), 164–173.

Dorrell, R.M., Peakall, J., Darby, S.E., Parsons, D.R., Johnson, J., Sumner, E.J., Wynn, R.B., Özsoy, E. & Tezcan, D. (2019) Self-sharpening induces jet-like structure in seafloor gravity currents. *Nature Communications*, 10, 1381. Available online: https://www.nature.com/articles/s41467-019-09254-2 [Accessed 12/8/2019].

Douillet, G.A., Pacheco, D.A., Kueppers, U., Letort, J., Tsang-Hin-Sun, È., Bustillos, J., Hall, M., Ramón, P., Dingwell, D.B. (2013) Dune bedforms produced by dilute pyroclastic density currents from the August 2006 eruption of Tungurahua volcano, Ecuador. *Bulletin of Volcanology*, 75, 762. Available online: https://link.springer.com/article/10.1007/s00445-013-0762-x [Accessed 14/11/2016].

Douillet, G.A., Bernard, B., Bouysson, M., Chaffaut, Q., Dingwell, D.B., Gegg, L., Hoelscher, I., Kueppers, U., Mato, C., Ritz, V.A., Schlunegger, F. & Witting, P. (2018) Pyroclastic dune bedforms: macroscale structures and lateral variations. Examples from the 2006 pyroclastic currents at Tungurahua (Ecuador). *Sedimentology*, 66, 1531–1559.

Doyle, E.E., Hogg, A.J. & Mader, H.M. (2011) A two-layer approach to modelling the transformation of dilute pyroclastic currents into dense pyroclastic flows. *Proceedings of the Royal Society A*, 467(2129), 1348–1371.

Druitt, T.H. (1992) Emplacement of the 18 May 1980 lateral blast deposit ENE of Mount St. Helens, Washington. *Bulletin of Volcanology*, 54, 554–572.

Druitt, T.H. (1995) Settling behaviour of concentrated dispersions and some volcanological applications. *Journal of Volcanology and Geothermal Research*, 65, 27–39.

Druitt, T.H. (1998) *Pyroclastic density currents*. Geological Society, London, Special Publications, 145, 145–182.

Druitt, T.H. & Sparks, R.S.J. (1982) A proximal ignimbrite breccia facies on Santorini, Greece. *Journal of Volcanology and Geothermal Research*, 13, 147–171.

Druitt, T.H., Calder, E.S., Cole, P.D., Hoblitt, R.S., Loughlin, S.C., Norton, G.E., Ritchie, L.J., Sparks, R.S.J., Voight, B. (2002) Small-volume, highly mobile pyroclastic flows formed by rapid sedimentation from pyroclastic surges at Soufrière Hills Volcano, Montserrat: an important volcanic hazard. In: Druitt, T.H. & Kokelaar, B.P. (Eds.) *The Eruption of Soufrière Hills Volcano, Montserrat, from 1995 to 1999*. Geological Society, London, Memoirs, 21, 263–279.

Druitt, T.H., Avard, G., Bruni, G., Lettieri, P., Maez, F. (2007) Gas retention in fine-grained pyroclastic flow materials at high temperatures. *Bulletin of Volcanology*, 69, 881–901.

Dufek, J. (2016) The fluid mechanics of pyroclastic density currents. *Annual Review of Fluid Mechanics*, 48, 459–485.

Dufek, J., Esposti Ongaro, T. & Roche, O. (2015) Pyroclastic density currents: processes and models. In: Sigurdsson, H., Houghton, B., Rymer, H., Stix, J., McNutt, S. (Eds.) *The Encyclopedia of Volcanoes*, 2nd edition. Amsterdam: Academic Press, 617-629.

Eames, I. & Gilbertson, M. (2000) Aerated granular flow over a horizontal rigid surface. *Journal of Fluid Mechanics*, 424, 169–195.

Esposti Ongaro, T., Clarke, A.B., Voight, B., Neri, A., & Widiwijayanti, C. (2012) Multiphase flow dynamics of pyroclastic density currents during the May 18, 1980 lateral blast of Mount St. Helens. *Journal of Geophysical Research: Solid Earth*, 117(6), B06208. Available online: https://agupubs.onlinelibrary.wiley.com/doi/full/10.1029/2011JB009081 [Accessed 20/8/2020]

Faccanoni, G. & Mangeney, A. (2013) Exact solution for granular flows. *International Journal for Numerical and Analytical Methods in Geomechanics*, 37(10), 1408–1433.

Farin, M., Mangeney, A. & Roche, O. (2014) Fundamental changes of granular flow dynamics, deposition, and erosion processes at high slope angles: insights from laboratory experiments. *Journal of Geophysical Research: Solid Earth*, 119, 504–532.

Faug, T. (2015) Depth-averaged analytic solutions for free-surface granular flows impacting rigid walls down inclines. *Physical Review E*, 92, 062310. Available online: https://journals.aps.org/pre/abstract/10.1103/PhysRevE.92.062310 [Accessed 20/4/2019].

Faug, T., Childs, P., Wyburn, E. & Einav, I. (2015) Standing jumps in shallow granular flows down smooth inclines. *Physics of Fluids*, 27, 073304. Available online: https://aip.scitation.org/doi/10.1063/1.4927447 [Accessed 20/04/2019].

Fenner, C.N. (1923) The origin and mode of emplacement of the great tuff deposit in the Valley of Ten Thousand Smokes. *National Geographic Society Contributed Technical Papers, Katmai Series*, 1:1

Fielding, C.R. (2006) Upper flow regime sheets, lenses and scour fills: extending the range of architectural elements for fluvial sediment bodies. *Sedimentary Geology*, 190, 227–240.

Fierstein, J. & Hildreth, W. (1992).The plinian eruptions of 1912 at Novarupta, Katmai National Park, Alaska. *Bulletin of Volcanology*, 54, 646–684.

Fisher, R.V. (1966) Mechanism of deposition from pyroclastic flows. *American Journal of Science*, 264(5), 350-363.

Fisher, R.V. (1995) Decoupling of pyroclastic currents: hazards assessments. *Journal of Volcanology and Geothermal Research*, 66(1–4), 257–263.

Fisher, R. & Waters, A. (1969) Bed forms in base-surge deposits: lunar implications. *Science*, 26, 1349–1352.

Fisher, R. & Waters, A. (1970) Base surge bed forms in maar volcanoes. *American Journal of Science*, 268, 157–180.

Fisher, R.V. & Schmincke, H.-U. (1984) *Pyroclastic Rocks*. Berlin: Springer-Verlag.

Fisher, R.V., Schmincke, H.-U. & Van Bogaard, P. (1983) Origin and emplacement of a pyroclastic flow and surge unit at Laacher See, Germany. *Journal of Volcanology of Geothermal Research*, 17, 375–392.

Fisher, R.V., Orsi, G., Ort, M. & Heikan, G. (1993) Mobility of a large-volume pyroclastic flow - emplacement of the Campanian ignimbrite, Italy. *Journal of Volcanology and Geothermal Research*, 56(3), 205–220.

Flemming, B.W. (2000) The role of grain size, water depth and flow velocity as scaling factors controlling the size of subaqueous dunes. In: Trentesaux A & Garlan T (Eds.) *Proceedings, marine sandwave dynamics, international workshop, March 23-24 2000, University of Lille 1, France*, 55-60.

Forterre, Y. & Pouliquen, O. (2008) Flows of Dense Granular Media. *Annual Review of Fluid Mechanics*, 40(1), 1–24.

Freundt, A. & Schmincke, H.-U. (1986) Emplacement of small-volume pyroclastic flows at Laacher See (East-Eifel, Germany). *Bulletin of Volcanology*, 48(1), 39–59.

GDR MiDi (2004) On dense granular flows. *European Physical Journal E*, 14(4), 341–365.

Geldart, D. (1973). Types of gas fluidization. *Powder Technology*, 7, 285–292.

Gençalioğlu-Kuşcu, C., Atilla, C., Cas, R.A.F. & Kuşcu, I. (2007) Base surge deposits, eruption history, and depositional processes of a wet phreatomagmatic volcano in Central Anatolia (Cora Maar). *Journal of Volcanology and Geothermal Research*, 159, 198–209.

Giannetti, B. & Luongo, G. (1994) Trachyandesite scoria-flow and associated trachyte pyroclastic flow and surge at Roccamonfina Volcano (Roman Region, Italy). *Journal of Volcanology and Geothermal Research*, 59(4), 313–334.

Giannetti, B. & De Casa, G. (2000) Stratigraphy, chronology, and sedimentology of ignimbrites from the white trachytic tuff, Roccamonfina Volcano, Italy. *Journal of Volcanology and Geothermal Research*, 96(3–4), 243–295.

Gibilaro, L.G., Gallucci, K., Di Felice, R. & Pagliai, P. (2007) On the apparent viscosity of a fluidized bed. *Chemical Engineering Science*, 62, 294–300.

Gilbertson, M.A., Jessop, D.E. & Hogg, A.J. (2008) The effects of gas flow on granular currents. *Philosophical Transactions of the Royal Society A*, 366, 2191–2203.

Giordano, G. (1998) The effect of paleotopography on lithic distribution and facies associations of small volume ignimbrites: the WTT Cupa (Roccamonfina volcano, Italy). *Journal of Volcanology and Geothermal Research*, 87, 255–273.

Giordano, G. & Dobran, F. (1994) Computer simulations of the Tuscolano Artemisio's second pyroclastic flow unit (Alban Hills, Latium, Italy). *Journal of Volcanology and Geothermal Research*, 61, 69–94.

Giordano, G. & Doronzo, D.M. (2017) Sedimentation and mobility of PDCs: a reappraisal of ignimbrites' aspect ratio. *Scientific Reports*, 7, 4444. Available online: https://www.nature.com/articles/s41598-017-04880-6 [Accessed 18/4/2018].

Giordano, G., De Benedetti, A.A., Diana, A., Diano, G., Esposito, A., Fabbri, M., Gaudioso, F., Marasco, F., Mazzini, I., Miceli, M., Mincione, V., Porreca, M., Rodani, S., Rosa, C., Vinkler, A.P., Caprilli, E., Taviani, S., Trigari, A., Bilardello, D., Malinconico, S., Sabato Ceraldi, T., Funiciello, R., Mattei, M., De Rita, D., Parotto, M. & Cas, R.A.F. (2010) Stratigraphy, volcano tectonics and evolution of the Colli Albani volcanic field. In: Funiciello, R. & Giordano, G. (Eds.) *The Colli Albani Volcano, Special Publications of IAVCEI, 3*. The Geological Society, London, 43-98.

Girolami, L., Druitt, T.H., Roche, O. & Khrabrykh, Z. (2008) Propagation and hindered settling of laboratory ash flows. *Journal of Geophysical Research: Solid Earth*, 113, B02202. Available online: https://agupubs.onlinelibrary.wiley.com/doi/full/10.1029/2007JB005074 [Accessed 14/11/2016]

Girolami, L., Roche, O., Druitt, T. & Corpetti, T. (2010) Particle velocity fields and depositional processes in laboratory ash flows, with implications for the sedimentation of dense pyroclastic flows. *Bulletin of Volcanology*, 72, 747–759.

Girolami, L., Druitt, T.H. & Roche, O. (2015) Towards a quantitative understanding of pyroclastic flows: Effects of expansion on the dynamics of laboratory fluidized granular flows. *Journal of Volcanology and Geothermal Research*, 296, 31–39.

Goldhirsch, I. (2003) Rapid granular flows. *Annual Review of Fluid Mechanics*, 35(1), 267–293.

Goldhirsch, I. (2008) Introduction to granular temperature. *Powder Technology*, 182(2), 130–136.

Gray, J.M.N.T. (2018) Particle segregation in dense granular flows. *Annual Review of Fluid Mechanics*, 50(1), 407–433.

Gray, J.M.N.T., Tai, Y.-C. & Noelle, S. (2003) Shock waves, dead zones and particle-free regions in rapid granular free-surface flows. *Journal of Fluid Mechanics*, 291, 161–181.

Gray, J.M.N.T., Gajjar, P. & Kokelaar, P. (2015) Particle-size segregation in dense granular avalanches. *Comptes Rendus Physique*, 16(1), 73–85.

Gueugneau, V., Kelfoun, K., Roche, O. & Chupin, L. (2017) Effects of pore pressure in pyroclastic flows: numerical simulation and experimental validation. *Geophysical Research Letters*, 44, 2194–2202.

Gueugneau, V., Kelfoun, K. & Druitt, T. (2019) Investigation of surge-derived pyroclastic flow formation by numerical modelling of the 25 June 1997 dome collapse at Soufrière Hills Volcano, Montserrat. *Bulletin of Volcanology*, 81, 25. Available online: https://link.springer.com/article/10.1007%2Fs00445-019-1284-y [Accessed 24/8/2020].

Guzmán, S., Doronzo, D.M., Martí, J. & Seggiaro, R. (2020) Characteristics and emplacement mechanisms of the Coranzulí ignimbrites (Central Andes). *Sedimentary Geology*, 405, 105699. Available online: https://www.sciencedirect.com/science/article/abs/pii/S0037073820301147 [Accessed 9/7/2020].

Hayashi, J. & Self, S. (1992) A comparison of pyroclastic flow and debris avalanche mobility. *Journal of Geophysical Research*, 97, 9063–9071.

Hendershot, M.L., Venditti, J.G., Bradley, R.W., Kostaschuk, R.A., Church, M. & Allison, M.A. (2016) Response of low-angle dunes to variable flow. *Sedimentology*, 63(3), 743–760.

Hernando, I.R., Petrinovic, I.A., Gutiérrez, D.A., Bucher, J., Fuentes, T.G. & Aragón, E. (2019) The caldera-forming eruption of the quaternary Payún Matrú volcano, Andean back-arc of the southern volcanic zone. *Journal of Volcanology and Geothermal Research*, 384, 15–30.

Huppert, H.E. & Simpson, J.E. (1980) The slumping of gravity currents. *Journal of Fluid Mechanics*, 99(4), 785–799.

Huppert, H.E. Turner, J.S., Carey, S.N., Sparks, R.S.J. & Hallworth, M.A. (1986) A laboratory simulation of pyroclastic flows down slopes. *Journal of Volcanology and Geothermal Research*, 30, 179–199.

Iverson, R.M. (1997) The physics of debris flows. *Reviews of Geophysics*, 35, 245–296.

Iverson, R.M. & LaHusen, R.G. (1993) Friction in debris flows: inferences from large-scale flume experiments. *Hydraulic Engineering*, 93, 1604–1609.

Iverson, R.M. & Denlinger, R.P. (2001) Flow of variably fluidized granular masses across three-dimensional terrain: 1. Coulomb mixture theory. *Journal of Geophysical Research*, 106, 537–552.

Iverson, R.M. & Vallance, J.W. (2001) New views of granular mass flows. *Geology*, 29(2), 115–118.

Jessop, D.E., Hogg, A.J., Gilbertson, M.A. & Schoof, C. (2017) Steady and unsteady fluidised granular flows down slopes. *Journal of Fluid Mechanics*, 827, 67–120.

Jop, P., Forterre, Y. & Pouliquen, O. (2005) Crucial role of sidewalls in granular surface flows: Consequences for the rheology. *Journal of Fluid Mechanics*, 541(i), 167–192.

Jop, P., Forterre, Y. & Pouliquen, O. (2006) A constitutive law for dense granular flows. *Nature*, 441(7094), 727–730.

Jopling, A.V. & Richardson, E.V. (1966) Backset bedding developed in shooting flow in laboratory experiments. *Journal of Sedimentary Petrology*, 36, 821–825.

Kelfoun, K. (2011) Suitability of simple rheological laws for the numerical simulation of dense pyroclastic flows and long-runout volcanic avalanches. *Journal of Geophysical Research: Solid Earth*, 116(8), B08209. Available online: https://agupubs.onlinelibrary.wiley.com/doi/full/10.1029/2010JB007622 [Accessed 24/8/2020].

Kelfoun, K., Samaniego, P., Palacios, P. & Barba, D. (2009). Testing the suitability of frictional behaviour for pyroclastic flow simulation by comparison with a well-constrained eruption at tungurahua volcano (Ecuador). *Bulletin of Volcanology*, 71(9), 1057–1075.

Kelly, R.W., Dorrell, R.M., Burns, A.D. & McCaffrey, W.D. (2019) The structure and entrainment characteristics of partially confined gravity currents. *Journal of Geophysical Research: Oceans*, 124(3), 2110–2125.

Kennedy, J.F. (1963). The mechanics of dunes and antidunes in erodible bed channels. *Journal of Fluid Mechanics*, 16, 521–544.

Kieffer, S.W. (1981) Fluid dynamics of the May 18 blast at Mount St. Helens. In: Lipman, P.W. & Mullineaux, D.R. (Eds.) *The 1980 eruptions of Mount St. Helens, Washington*. US Geological Survey Professional Paper, 1250, 379-401.

Kleinhans, M.G. (2004) Sorting in grain flows at the lee side of dunes. *Earth-Science Reviews*, 65(1–2), 75–102.

Kneller, B.C., Bennett, S.J. & McCaffrey, W.D. (1999) Velocity structure, turbulence and fluid stresses in experimental gravity currents. *Journal of Geophysical Research*, 104(1998), 5381–5391.

Kunii, D. & Levenspiel, O. (1991) *Fluidization Engineering*, 2nd edition. Oxford: Butterworth Heinemann.

Lajeunesse, E., Mangeney-Castelnau, A. & Vilotte, J.P. (2004) Spreading of a granular mass on a horizontal plane. *Physics of Fluids*, 16(7), 2371–2381.

Le Roux, J.P. (2003) Can dispersive pressure cause inverse grading in grain flows? - Discussion. *Journal of Sedimentary Research*, 73(2), 333–334.

Legros, F. (2002) Can dispersive pressure cause inverse grading in grain flows? *Journal of Sedimentary Research*, 72(1), 166–170.

Li, L. & Ma, W. (2011) Experimental study on the effective particle diameter of a packed bed with non-spherical particles. *Transport in Porous Media*, 89, 35–48.

Loughlin, S.C., Luckett, R., Ryan, G., Christopher, T., Hards, V., De Angelis, S., Jones, L. & Strutt, M. (2010) An overview of lava dome evolution, dome collapse and cyclicity at Soufrière Hills Volcano, Montserrat, 2005-2007. *Geophysical Research Letters*, 37(9), 4–9.

Lowe, D.R. (1976) Grain Flow and Grain Flow Deposits. *SEPM Journal of Sedimentary Research*, 46(1), 188–199.

Lube, G., Huppert, H.E., Sparks, R.S.J. & Hallworth, M.A. (2004) Axisymmetric collapses of granular columns. *Journal of Fluid Mechanics*, 508, 175–199.

Lube, G., Huppert, H.E., Sparks, R.S.J. & Freundt, A. (2005) Collapses of two-dimensional granular columns. *Physical Review E*, 72, 04130. Available online: https://journals.aps.org/pre/abstract/10.1103/PhysRevE.72.041301 [Accessed 28/6/2017].

Lube, G., Cronin, S.J., Platz, T., Freundt, A., Procter, J.N., Henderson, C. & Sheridan, M.F. (2007) Flow and deposition of pyroclastic granular flows: A type example from the 1975 Ngauruhoe eruption, New Zealand. *Journal of Volcanology and Geothermal Research*, 161(3), 165–186.

Lube, G., Huppert, H.E., Sparks, R.S.J. & Freundt, A. (2011) Granular column collapses down rough, inclined channels. *Journal of Fluid Mechanics*, 675, 347–368.

Lube, G., Breard, E.C.P., Cronin, S.J. & Jones, J. (2015) Synthesizing large-scale pyroclastic flows: Experimental design, scaling, and first results from PELE. *Journal of Geophysical Research: Solid Earth*, 120(3), 1487-1502.

Lube, G., Breard, E.C.P., Jones, J., Fullard, L., Dufek, J., Cronin, S.J. & Wang, T. (2019) Generation of air lubrication within pyroclastic density currents. *Nature Geoscience*, 12, 381–386.

Lube, G., Breard, E.C.P., Esposti-Ongaro, T., Dufek, J. & Brand, B. (2020) Multiphase flow behaviour and hazard prediction of pyroclastic density currents. *Nature Reviews Earth & Environment*, 1, 348-365.

Macorps, E., Charbonnier, S.J., Varley, N.R., Capra, L., Atlas, Z. & Cabré, J. (2018) Stratigraphy, sedimentology and inferred flow dynamics from the July 2015 block-and-ash flow deposits at Volcán de Colima, Mexico. *Journal of Volcanology and Geothermal Research*, 349, 99–116.

Maeno, F. & Imamura, F. (2007) Numerical investigations of tsunamis generated by pyroclastic flows from the Kikai caldera, Japan. *Geophysical Research Letters*, 34(23), L23303. Available online: https://agupubs.onlinelibrary.wiley.com/doi/full/10.1029/2007GL031222 [Accessed 8/7/2020].

Mangeney, A., Roche, O., Hungr, O., Mangold, N., Faccanoni, G. & Lucas, A. (2010) Erosion and mobility in granular collapse over sloping beds. *Journal of Geophysical Research: Earth Surface*, 115(3), F03040. Available online: https://agupubs.onlinelibrary.wiley.com/doi/full/10.1029/2009JF001462 [Accessed 14/11/2016].

Marra, F., Karner, D.B., Freda, C., Gaeta, M. & Renne, P. (2009) Large mafic eruptions at Alban Hills Volcanic District (Central Italy): chronostratigraphy, petrography and eruptive behavior. *Journal of Volcanology and Geothermal Research*, 179, 217–232.

Mastrolorenzo, G., Petrone, P.P., Pagano, M., Incoronato, A., Baxter, P.J., Canzanella, A. & Fattore, L. (2001) Herculaneum victims of Vesuvius in ad 79. *Nature*, 410(6830), 769–770.

Mattson, P.H. & Alvarez, W. (1973) Base surge deposits in Plesitocene volcanic ash near Rome. *Bulletin of Volcanology*, 37, 553–572.

McClelland, E., Wilson, C.J.N. & Bardot, L. (2004) Palaeotemperature determinations for the 1.8-ka Taupo ignimbrite, New Zealand, and implications for the emplacement history of a high-velocity pyroclastic flow. *Bulletin of Volcanology*, 66(6), 492–513.

McTaggart, K.C. (1960) The mobility of nuées ardentes. *American Journal of Science*, 258, 369–382.

McTaggart, K.C. (1962) Nuees Ardentes and fluidization - a reply. *American Journal of Science*, 260, 470-476.

Middleton, G.V. (1965) Antidune cross-bedding in a large flume. *Journal of Sedimentary Petrology*, 35, 922–927.

Middleton, G.V. (1970) Experimental studies related to problems of flysch sedimentation. In: Lajoie, J. (Ed.) *Flysch Sedimentology in North America*. Geological Association of Canada Special Paper, 7, 253-272.

Middleton, G.V. & Southard, J.B. (1984) Mechanics of sediment movement. In: *Short course notes: 3*. Tulsa: Society of Economic Paleontologists and Mineralogists.

Montserrat, S., Tamburrino, A., Roche, O. & Niño, Y. (2012) Pore fluid pressure diffusion in defluidizing granular columns. *Journal of Geophysical Research: Earth Surface*, 117, F02034. Available online: https://agupubs.onlinelibrary.wiley.com/doi/full/10.1029/2011JF002164 [Accessed 19/7/2018].

Montserrat, S., Tamburrino, A., Roche, O., Niño, Y. & Ihle, C.F. (2016) Enhanced run-out of dam-break granular flows caused by initial fluidization and initial material expansion. *Granular Matter*, 18, 11. Available online: https://link.springer.com/article/10.1007/s10035-016-0604-6 [Accessed 14/11/2016].

Moore, J.G. (1967) Base surge in recent volcanic eruptions. *Bulletin of Volcanology*, 30, 337–363.

Muzzio, F.J., Shinbrot, T. & Glasser, B.J. (2002) Powder technology in the pharmaceutical industry: The need to catch up fast. *Powder Technology*, 124(1–2), 1–7.

Nedderman, R.M. (1992) *Statics and Kinematics of Granular Materials*. Cambridge: Cambridge University Press.

Normark, W.R., Hess, G.R., Stow, D.A.V. & Bowen, A.J. (1980) Sediment waves on the Monterey Fan levee: a preliminary physical interpretation. *Marine Geology*, 37, 1–18.

Ogawa, S. (1978) Multitemperature theory of granular materials. In: Cowin, S.C. & Satake, M. (Eds.) *Proceedings of the US-Japan seminar on continuum-mechanical and statistical approaches in the mechanics of granular materials*. Tokyo: Gakujutsu Bunken Fukyukai, 208-217.

Orton, G.J. (1996) Volcanic Environments. In: Reading, H.G. (Ed.) *Sedimentary Environments: Processes, Facies and Stratigraphy*, 3rd edition. Oxford: Blackwell, 485-567.

Pacheco-Hoyos, J.G., Aguirre-Díaz, G.J. & Dávila-Harris, P. (2018) Boiling-over dense pyroclastic density currents during the formation of the ~ 100 km3 Huichapan ignimbrite in Central Mexico: Stratigraphic and lithofacies analysis. *Journal of Volcanology and Geothermal Research*, 349, 268–282.

Petrinovic, I.A. & Colombo Piñol, F. (2006) Phreatomagmatic and phreatic eruptions in locally extensive settings of Southern Central Andes: The Tocomar Volcanic Centre (24°10′S-66°34′W), Argentina. *Journal of Volcanology and Geothermal Research*, 158(1–2), 37–50.

Pittari, A., Cas, R.A.F. & Martí, J. (2005) The occurrence and origin of prominent massive, pumice-rich ignimbrite lobes within the Late Pleistocene Abrigo Ignimbrite, Tenerife, Canary Islands. *Journal of Volcanology and Geothermal Research*, 139(3–4), 271–293.

Platzman, E.S., Sparks, R.S.J. & Cooper, F.J .(2020) Fabrics, facies, and flow through a large-volume ignimbrite: Pampa De Oxaya, Chile. *Bulletin of Volcanology*, 82, 8. Available online: https://link.springer.com/article/10.1007/s00445-019-1345-2 [Accessed 15/7/2020]

Pollock, N.M., Brand, B.D. & Roche, O. (2016) The controls and consequences of substrate entrainment by pyroclastic density currents at Mount St Helens, Washington (USA). *Journal of Volcanology and Geothermal Research*, 325, 135–147.

Pollock, N.M., Brand, B.D., Rowley, P.J., Sarocchi, D. & Sulpizio, R. (2019) Inferring pyroclastic density current flow conditions using syn-depositional sedimentary structures. *Bulletin of Volcanology*, 81, 46. Available online: https://link.springer.com/article/10.1007/s00445-019-1303-z [Accessed 6/8/2019].

Ponce, J.J. & Carmona, N.B. (2011) Miocene deep-marine hyperpycnal channel levee complexes, Tierra Del Fuego, Argentina: facies associations and architectural elements. In: Slatt, R.M. & Zavala, C. (Eds.) *Sediment transfer from shelf to deep water - revisting the delivery system*. AAPG Studies in Geology, 61, 75–93.

Prescott, J.K. (2001) Powder Handling. In: Levin, M. (Ed.) *Pharmaceutical process scale-up*. New York: Marcel Dekker, 133-149.

Rader, E., Geist, D., Geissman, J., Dufek, J. & Harpp, K. (2015). Hot clasts and cold blasts: thermal heterogeneity in boiling-over pyroclastic density currents. In: Ort, M.H, Porreca, M. & Geissman, J.W. (Eds.) *The use of palaeomagnetism and rock magnetism to understand volcanic processes*. Geological Society, London, Special Publications, 396, 67–86.

Reynolds, D.H. (1954) Fluidisation as a geological process and its bearing on the problems of intrusive granites. *American Journal of Science*, 252, 577–613.

Richard, P., Valance, A., Métayer, J.F., Sanchez, P., Crassous, J., Louge, M. & Delannay, R. (2008) Rheology of confined granular flows: Scale invariance, glass transition, and friction weakening. *Physical Review Letters*, 101(24), 248002. Available online: https://journals.aps.org/prl/abstract/10.1103/PhysRevLett.101.248002 [Accessed 28/7/2020].

Roche, O. (2012) Depositional processes and gas pore pressure in pyroclastic flows: an experimental perspective. *Bulletin of Volcanology*, 74, 1807–1820.

Roche, O., Gilbertson, M.A., Phillips, J.C. & Sparks, R.S.J. (2002) Experiments on deaerating granular flows and implications for pyroclastic flow mobility. *Geophysical Research Letters*, 29, 40-1–40-4.

Roche, O., Gilbertson, M.A., Phillips, J.C. & Sparks, R.S.J. (2004) Experimental study of gas-fluidized granular flows with implications for pyroclastic flow emplacement. *Journal of Geophysical Research: Solid Earth*, 109, B10201. Available online: https://agupubs.onlinelibrary.wiley.com/doi/full/10.1029/2003JB002916 [Accessed 8/11/2016].

Roche, O., Gilbertson, M.A., Phillips, J.C. & Sparks, R.S.J. (2006) The influence of particle size on the flow of initially fluidised powders. *Powder Technology*, 166(3), 167–174.

Roche, O., Montserrat, S., Niño, Y. & Tamburrino, A. (2008) Experimental observations of water-like behavior of initially fluidized, dam break granular flows and their relevance for the propagation of ash-rich pyroclastic flows. *Journal of Geophysical Research: Solid Earth*, 113(12), B12203. Available online: https://agupubs.onlinelibrary.wiley.com/doi/full/10.1029/2008JB005664 [Accessed 8/11/2016].

Roche, O., Montserrat, S., Niño, Y. & Tamburrino, A. (2010) Pore fluid pressure and internal kinematics of gravitational laboratory air-particle flows: insights into the emplacement dynamics of pyroclastic flows. *Journal of Geophysical Research: Solid Earth*, 115, B12203. Available online: https://agupubs.onlinelibrary.wiley.com/doi/full/10.1029/2009JB007133 [Accessed 8/11//2016].

Roche, O., Niño, Y., Mangeney, A., Brand, B., Pollock, N. & Valentine, G.A. (2013) Dynamic pore-pressure variations induce substrate erosion by pyroclastic flows. *Geology*, 41, 1107–1110.

Roche, O., Buesch, D.C. & Valentine, G.A. (2016) Slow-moving and far-travelled dense pyroclastic flows during the Peach Spring super-eruption. *Nature Communications*, 7, 10890. Available online: https://www.nature.com/articles/ncomms10890 [Accessed 22/11/2016].

Roche, O. & Carazzo, G. (2019) The contribution of experimental volcanology to the study of the physics of eruptive processes, and related scaling issues: A review. *Journal of Volcanology and Geothermal Research*, 384, 103–150.

Rowley, P.D., Kuntz, M.A. & MacLeod, N.S. (1981) Pyroclastic-flow deposits. The 1980 eruptions of Mount St. Helens, Washington. *USGS Professional Paper*, 1250, 489-512.

Rowley, P.D., MacLeod, N.S., Kuntz, M.A. & Kaplan, A.M. (1985) Proximal bedded deposits related to pyroclastic flows of May 18, 1980, Mount St. Helens, Washington. *Geological Society of America Bulletin*, 96, 1373–1383.

Rowley, P.J., Kokelaar, P., Menzies, M. & Waltham, D. (2011) Shear-derived mixing in dense granular flows. *Journal of Sedimentary Research*, 81, 874–884.

Rowley, P.J., Roche, O., Druitt, T.H. & Cas, R. (2014) Experimental study of dense pyroclastic density currents using sustained, gas-fluidized granular flows. *Bulletin of Volcanology*, 76, 855. Available online: https://link.springer.com/article/10.1007/s00445-014-0855-1 [Accessed 30/09/2016].

Rycroft, C.H., Grest, G.S., Landry, J.W. & Bazant, M.Z. (2006) Analysis of granular flow in a pebble-bed nuclear reactor. *Physical Review E*, 74(2), 021306. Available online: https://journals.aps.org/pre/abstract/10.1103/PhysRevE.74.021306 [Accessed 28/7/2019].

Saleh, K., Golshan, S. & Zarghami, R. (2018). A review on gravity flow of free-flowing granular solids in silos – Basics and practical aspects. *Chemical Engineering Science*, 192, 1011-1035.

Sarno, L., Carravetta, A., Tai, Y.C., Martino, R., Papa, M.N. & Kuo, C.Y. (2018) Measuring the velocity fields of granular flows – Employment of a multi-pass two-dimensional particle image velocimetry (2D-PIV) approach. *Advanced Powder Technology*, 29(12), 3107–3123.

Sarocchi, D., Sulpizio, R., Macias, J.L. & Saucedo, R. (2011) The 17 July 1999 block-and-ash flow (BAF) at Colima Volcano: new insights on volcanic granular flows from textural analysis. *Journal of Volcanology and Geothermal Research*, 204, 40–56.

Savage, S.B. & Lun, C.K. (1988) Particle size segregation in inclined chute flow of dry cohesionless granular solids. *Journal of Fluid Mechanics*, 189(1), 311-335.

Savage, S.B. & Hutter, K. (1989) The motion of a finite mass of granular material down a rough incline. *Journal of Fluid Mechanics*, 199, 177–215.

Savage, S.B. & Oger, L. (2013) Airslide flows, Part 1-Experiments, review and extension. *Chemical Engineering Science*, 91, 35–43.

Scarpati, C., Cole, P. & Perrotta, A. (1993) The Neapolitan Yellow Tuff - A large volume multiphase eruption from Campi Flegrei, Southern Italy. *Bulletin of Volcanology*, 55, 343–356.

Scarpati, C., Sparice, D. & Perrotta, A. (2015) Facies variation in the Campanian Ignimbrite. *Rendiconti Online Societa Geologica Italiana*, 33, 83–87.

Schmincke, H.-U., Fisher, R.V. & Waters, A.C. (1973) Antidune and chute and pool structures in the base surge deposits of the Laacher See area, Germany. *Sedimentology*, 20, 553–574.

Schwarzkopf, L.M., Schmincke, H.-U. & Cronin, S.J. (2005) A conceptual model for block-and-ash flow basal avalanche transport and deposition, based on deposit architecture of 1998 and 1994 Merapi flows. *Journal of Volcanology and Geothermal Research*, 139, 117–134.

Scott, W.E., Hoblitt, R.P., Torres, R.C., Self, S., Martinez, M.L. & Nillos, T. (1996) Pyroclastic Flows of the June 15, 1991, Climactic Eruption of Mount Pinatubo. In: Newhall, C.G. & Punongbayan, R.S. (Eds.) *Fire and Mud: Eruptions and Lahars of Mount Pinatubo, Philippines*. Seattle: University of Washington Press, 545-570.

Self, S. (2006) The effects and consequences of very large explosive volcanic eruptions. *Philosophical Transactions of the Royal Society A*, 364, 2073–2097.

Siegert, S., Branney, M.J. & Hecht, L. (2017) Density current origin of a melt-bearing impact ejecta blanket. *Geology*, 45, 855–858.

Sigurdsson, H., Carey, S. & Fisher, R.V. (1987) The 1982 eruptions of El Chichon volcano, Mexico (3): Physical properties of pyroclastic surges. *Bulletin of Volcanology*, 49, 467–488.

Smellie, J.L., Rocchi, S., Johnson, J.S., Di Vincenzo, G. & Schaefer, J.M. (2018) A tuff cone erupted under frozen-bed ice (northern Victoria Land, Antarctica): linking glaciovolcanic and cosmogenic nuclide data for ice sheet reconstructions. *Bulletin of Volcanology*, 80, 12. Available online: https://link.springer.com/article/10.1007/s00445-017-1185-x [Accessed 5/8/2020].

Smith, G., Williams, R., Rowley, P. & Parsons, D. (2018) Investigation of variable aeration of monodisperse mixtures: implications for pyroclastic density currents. *Bulletin of Volcanology*, 80, 67. Available online: https://link.springer.com/article/10.1007/s00445-018-1241-1 [Accessed 30/08/2018].

Smith, G., Rowley, P., Williams, R., Giordano, G., Trolese, M., Silleni, A., Parsons, D. & Capon, S. (2020) A bedform phase diagram for dense granular currents. *Nature Communications*, 11, 2873. Available online https://www.nature.com/articles/s41467-020-16657-z [Accessed 8/6/2020].

Smith, N.J. & Kokelaar, B.P. (2013) Proximal record of the 273 ka Poris caldera-forming eruption, Las Cañadas, Tenerife. *Bulletin of Volcanology*, 75(11), 768. Available online: https://link.springer.com/article/10.1007/s00445-013-0768-4 [Accessed 9/7/2020].

Sohn, Y. K. (1997) On traction-carpet sedimentation. *Journal of Sedimentary Research*, 67(3), 502–509.

Song, C., Wang, P. & Makse, H.A. (2008) A phase diagram for jammed matter. *Nature*, 453(7195), 629–632.

Southard, J.B. (2006). 12.090 Introduction to fluid motions, sediment transport, and current-generated sedimentary structures. Massachusetts Institute of Technology: *MIT*

OpenCourseWare. Available online: https://ocw.mit.edu/courses/earth-atmospheric-and-planetary-sciences/12-090-introduction-to-fluid-motions-sediment-transport-and-current-generated-sedimentary-structures-fall-2006 [Accessed 25/05/2020].

Southern, S.J., Kane, I.A., Warchoł, M.J., Porten, K.W. & McCaffrey, W.D. (2017) Hybrid event beds dominated by transitional-flow facies: Character, distribution and significance in the maastrichtian springar formation, north-west vøring basin, Norwegian Sea. *Sedimentology*, 64(3), 747–776.

Sparks, R.S.J. (1976) Grain size variations in ignimbrites and implications for the transport of pyroclastic flows. *Sedimentology*, 23, 147–188.

Sparks, R.S.J. (1978) Gas release rates from pyroclastic flows: an assessment of the role of fluidisation in their emplacement. *Bulletin of Volcanology*, 41, 1–9.

Sparks R.S.J. (1983) Mont Pelee, Martinique: May 8 and 20, 1902, pyroclastic flows and surges - discussion. *Journal of Volcanology and Geothermal Research*, 19, 175–184.

Sparks, R.S.J., Self. S, & Walker, G.P.L. (1973) Products of ignimbrite eruptions. *Geology*, 1(3), 115–118.

Sparks, R.S.J., Bonnecaze, R.T., Huppert, H.E., Lister, J.R., Hallworth, M.A., Mader, H. & Phillips, J. (1993) Sediment-laden gravity currents with reversing buoyancy. *Earth and Planetary Science Letters*, 114(2–3), 243–257.

Sulpizio, R. & Dellino, P. (2008) Depositional mechanisms and pulsating behaviour of pyroclastic density currents. In: Marti, L. & Gottsman, J. (Eds.) *Caldera volcanism: analysis, modelling and response*. Developments in volcanology, 10. Amsterdam: Elsevier, 57–96.

Sulpizio, R., Dellino, P., Mele, D. & La Volpe, L. (2008a) Generation of pyroclastic density currents from pyroclastic fountaining or transient explosions: insights from large scale experiments. *IOP Conference Series: Earth and Environmental Science*, 3, 012020. Available online: https://iopscience.iop.org/article/10.1088/1755-1307/3/1/012020/meta [Accessed 8/8/2019].

Sulpizio, R., De Rosa, R. & Donato, P. (2008b) The influence of variable topography on the depositional behaviour of pyroclastic density currents: The examples of the Upper Pollara eruption (Salina Island, southern Italy). *Journal of Volcanology and Geothermal Research*, 175, 367-385.

Sulpizio, R., Dellino, P., Doronzo, D.M. & Sarocchi, D. (2014) Pyroclastic density currents: State of the art and perspectives. *Journal of Volcanology and Geothermal Research*, 283, 36–65.

Sulpizio, R., Castioni, D., Rodriguez-Sedano, L.A., Sarocchi, D. & Lucchi, F. (2016) The influence of slope-angle ratio on the dynamics of granular flows: insights from laboratory experiments. *Bulletin of Volcanology*, 78, 77. Available online: https://link.springer.com/article/10.1007/s00445-016-1069-5 [Accessed 22/11/2016].

Sumner, E.J. & Paull, C.K. (2014) Swept away by a turbidity current in Mendocino submarine canyon, California. *Geophysical Research Letters*, 41, 7611-7618.

Sumner, E.J., Amy, L.A. & Talling, P.J. (2008) Deposit structure and processes of sand deposition from decelerating sediment suspensions. *Journal of Sedimentary Research*, 78(8), 529–547.

Sumner, E.J., Talling, P.J., Amy, L.A., Wynn, R.B., Stevenson, C.J. & Frenz, M. (2012) Facies architecture of individual basin-plain turbidites: Comparison with existing models and implications for flow processes. *Sedimentology*, 59(6), 1850–1887.

Sumner, E.J., Peakall, J., Parsons, D.R., Wynn, R.B., Darby, S.E., Dorrell, R.M., McPhail, S.D., Perrett, J., Webb, A. & White, D. (2013) First direct measurements of hydraulic jumps in an active submarine density current. *Geophysical Research Letters*, 40, 5904-5908.

Sweeney, M.R. & Valentine, G.A. (2017) Impact zone dynamics of dilute mono- and polydisperse jets and their implications for the initial conditions of pyroclastic density currents. *Physics of Fluids*, 29(9), 093304. Available online: https://aip.scitation.org/doi/10.1063/1.5004197 [Accessed 31/8/2019].

Taberlet, N., Richard, P., Valance, A., Losert, W., Pasini, J.M., Jenkins, J.T. & Delannay R. (2003) Superstable granular heap in a thin channel. *Physical Review Letters*, 91(26), 264301. Available online: https://journals.aps.org/prl/abstract/10.1103/PhysRevLett.91.264301 [Accessed 28/7/2019].

Talling, P.J., Allin, J., Armitage, D.A., Arnott, R.W.C., Cartigny, M.J.B., Clare, M.A., Felletti, F., Covault, J.A., Girardclos, S., Hansen, E., Hill, P.R., Hiscott, R.N., Hogg, A.J., Hughes Clarke, J., Jobe, Z.R., Malgesini, G., Mozzato, A., Naruse, H., Parkinson, S., Peel, F.J., Piper, D.J.W., Pope, E., Postma, G., Rowley, P., Sguazzini, A., Stevenson, C.J., Sumner, E.J., Sylvester, Z., Watts, C. & Xu, J. (2015) Key future directions for research on turbidity currents and their deposits. *Journal of Sedimentary Research*, 85, 153-169.

Tanguy. J.-C., Ribière, C.H., Scarth, A. & Tjetjep, W. (1998) Victims from volcanic eruptions: a revised database. *Bulletin of Volcanology*, 60, 137–144.

Thielicke, W. (2014) *The flapping flight of birds - analysis and application*. PhD thesis. Rijksuniversiteit Groningen. Available online: http://irs.ub.rug.nl/ppn/382783069 [Accessed 10/3/2020].

Thielicke, W. & Stamhuis, E.J. (2014) PIVlab – Towards user-friendly, affordable and accurate digital Particle Image Velocimetry in MATLAB. *Journal of Open Research Software*, 2(1), e30. Available online: https://openresearchsoftware.metajnl.com/articles/10.5334/jors.bl/ [Accessed 10/8/2019].

Thornton, A.R., Gray, J.M.N.T. & Hogg, A.J. (2006) A three-phase mixture theory for particle size segregation in shallow granular free-surface flows. *Journal of Fluid Mechanics*, 550, 1–25.

Tonarini, S., D'Antonio, M., Di Vito, M.A., Orsi, G. & Carandente, A. (2009) Geochemical and B-Sr-Nd isotopic evidence for mingling and mixing processes in the magmatic system that fed the Astroni volcano (4.1-3.8 ka) within the Campi Flegrei caldera (southern Italy). *Lithos*, 107, 135-151.

Torres, R.C., Self, S. & Martinez, M.L. (1996) Secondary pyroclastic flows from the June 15, 1991, ignimbrite of Mount Pinatubo. In: Newhall, C.G. & Punongbayan, R.S. (Eds.) *Fire and Mud: Eruptions and Lahars of Mount Pinatubo, Philippines*. Seattle: University of Washington Press, 665–678.

Trolese, M., Giordano, G., Cifelli, F., Winkler, A. & Mattei, M. (2017) Forced transport of thermal energy in magmatic and phreatomagmatic large volume ignimbrites: paleomagnetic evidence from the Colli Albani volcano, Italy. *Earth and Planetary Science Letters*, 478, 179–191.

Valentine, G.A. (1987) Stratified flow in pyroclastic surges. *Bulletin of Volcanology*, 49, 616–630.

Valentine, G.A. (2020) Initiation of dilute and concentrated pyroclastic currents from collapsing mixtures and origin of their proximal deposits. *Bulletin of Volcanology*, 82, 20. Available online: https://link.springer.com/article/10.1007/s00445-020-1366-x [Accessed 25/03/2020].

Valentine, G.A. & Wohletz, K.H. (1989) Numerical models of Plinian eruption columns and pyroclastic flows. *Journal of Geophysical Research*, 94(B2), 1867–1887.

Valentine, G.A. & Giannetti, B. (1995) Single pyroclastic beds deposited by simultaneous fallout and surge processes: Roccamonfina volcano, Italy. *Journal of Volcanology and Geothermal Research*, 64(1–2), 129–137.

Valentine, G.A. & Sweeney, M.R. (2018) Compressible flow phenomena at inception of lateral density currents fed by collapsing gas-particle mixtures. *Journal of Geophysical Research: Solid Earth*, 123(2), 1286–1302.

Valentine, G.A., Buesch, D.C. & Fisher, R.V. (1989) Basal layered deposits of the Peach Springs Tuff, northwestern Arizona, USA. *Bulletin of Volcanology*, 51, 395–414.

Vallance, J.W. & Savage, S.B. (2000) Particle segregation in granular flows down chutes. In: Rosato, A. & Blackmore, D. (Eds.) *IUTAM symposium on segregation in granular flows. Solid mechanics and its applications*, 81. Dordrecht: Springer, 31–51.

Van Der Bogaard, P. & Schmincke, H.-U. (1985) Laacher See tephra: a widespread isochronous late Quaternary tephra layer in central and northern Europe. *Geological Society of America Bulletin*, 96(12), 1554–1571.

Vidales, A.M., Ippolito, I., Benegas, O.A., Aguirre, F., Nocera, O.C. & Baudino, M.R. (2006) Granular components of cement: Influence of mixture composition. *Powder Technology*, 163(3), 196–201.

Walker, G.P.L. (1983) Ignimbrite types and ignimbrite problems. *Journal of Volcanology and Geothermal Research*, 17, 65–88.

Walker, G.P.L. (1984) Characteristics of dune-bedded pyroclastic surge bedsets. *Journal of Volcanology and Geothermal Research*, 20, 281–296.

Walker, G.P.L., Wilson, C.J.N. & Froggatt, P.C. (1980a) Fines-depleted ignimbrite in New Zealand - The product of a turbulent pyroclastic flow. *Geology*, 8(5), 245–249.

Walker, G.P.L., Heming, R.F & Wilson, C.J.N. (1980b) Low-aspect ratio ignimbrites. *Nature*, 283. 287-287.

Wang, N., Lu, H., Xu, J., Guo, X. & Liu, H. (2019). Velocity profiles of granular flows down an inclined channel. *International Journal of Multiphase Flow*, 110(I), 96–107.

Wang, Z.L., Finlay, W.H., Peppler, M.S. & Sweeney, L.G. (2006). Powder formation by atmospheric spray-freeze-drying. *Powder Technology*, 170(1), 45–52.

Waters, A.C. & Fisher, R.V. (1971) Base surges and their deposits: Capelinhos and Taal volcanoes. *Journal of Geophysical Research*, 76, 5596–5614.

Weitz, C.M., Sullivan, R.J., Lapotre, M.G.A., Rowland, S.K., Grant, J.A., Baker, M. & Yingst, R.A. (2018) Sand Grain Sizes and Shapes in Eolian Bedforms at Gale Crater, Mars. *Geophysical Research Letters*, 45(18), 9471–9479.

Whitney, J.A. & Stormer, J.C. (1985) Mineralogy, petrology, and magmatic conditions from the fish canyon tuff, central san juan volcanic field, Colorado. *Journal of Petrology*, 26(3), 726–762.

Williams, R., Branney, M.J., Barry, T.L. (2014) Temporal and spatial evolution of a waxing then waning catastrophic density current revealed by chemical mapping. *Geology*, 42, 107–110.

Wilson, C.J.N. (1980) The role of fluidization in the emplacement of pyroclastic flows: an experimental approach. *Journal of Volcanology and Geothermal Research*, 8, 231–249.

Wilson, C.J.N. (1985) The Taupo eruption, New Zealand: II. The Taupo Ignimbrite. *Philosophical Transanctions of the Royal Society A*, 314, 229–310.

Wilson, C.J.N. (1997) Emplacement of Taupo ignimbrite. *Nature*, 385, 306–307.

Wilson, C.J.N. & Walker G.P.L. (1982) Ignimbrite depositional facies: the anatomy of a pyroclastic flow. *Journal of the Geological Society of London*, 139, 581–592.

Wilson, C.J.N. & Hildreth, W. (2003) Assembling an ignimbrite: Mechanical and thermal building blocks in the Bishop Tuff, California. *Journal of Geology*, 111(6), 653–670.

Wilson, C.J.N., Houghton, B.F., Kamp, P.J.J. & McWilliams, M.O. (1995) An exceptionally widespread ignimbrite with implications for pyroclastic flow emplacement. *Nature*, 378, 605–607.

Wohletz, K.H. (1998) Pyroclastic surges and compressible two-phase flow. In: Freundt, A. & Rosi, M. (Eds.) *From Magma to Tephra: Modelling physical processes of explosive volcanic eruptions*. Developments in Volcanology, 4, 247-312.

Wohletz, K.H. & Sheridan, M.F. (1979) A model of pyroclastic surge. In: Chapin, C.E. & Elston, W.E. (Eds.) *Ash-flow tuffs*. Geological Society of America Special Papers, 180, 177–194.

Woods, A.W. & Bursik, M.I. (1994) A laboratory study of ash flows. *Journal of Geophysical Research*, 99(B3), 4375–4394.

Wright, J.V. & Walker, G.P.L. (1981) Eruption, transport and deposition of ignimbrite: A case study from Mexico. *Journal of Volcanology and Geothermal Research*, 9(2–3), 111–131.

Yamamoto, T., Takarada, S., Suto, S. (1993) Pyroclastic flows from the 1991 eruption of Unzen volcano, Japan. *Bulletin of Volcanology*, 55, 166–175.

Zrelak, P.J., Pollock, N.M., Brand, B.D., Sarocchi, D. & Hawkins, T. (2020) Decoding pyroclastic density current flow direction and shear conditions in the flow boundary zone via particle-fabric analysis. *Journal of Volcanology and Geothermal Research*, 402, 106978. Available online: https://www.sciencedirect.com/science/article/abs/pii/S0377027320300524 [Accessed 18/8/2020].

197

==

Appendix A – Supplementary Material for Chapter 3

==

Supplementary Table A.1 Grain size data and statistics for the particles used in the experiments. Six samples were taken from across the material batch and subjected to particle size analysis using a QICPIC.

Sample	**Run**	**Median diameter (µm)**	**Mean (µm)**	**Squared difference**	**Variance**	**Standard Deviation**
1	1	64.4		0.7		
	2	63.2	63.9	0.5	0.3	0.5
	3	64.1		0.1		
2	1	65.4		0.3		
	2	65.6	66.0	0.2	0.5	0.7
	3	67.0		1.0		
3	1	59.9		3.6		
	2	62.6	61.8	0.5	1.9	1.4
	3	63.0		1.4		
4	1	58.2		0.6		
	2	58.7	59.0	0.1	0.7	0.8
	3	60.1		1.3		
5	1	53.4		11.0		
	2	49.7	50.0	0.2	6.6	2.6
	3	47.1		8.6		
6	1	48.4		9.2		
	2	44.3	45.4	1.1	4.8	2.1
	3	43.4		4.0		
7	1	65.4		0.2		
	2	65.7	64.9	0.5	0.8	0.9
	3	63.7		1.5		
8	1	69.1		1.3		
	2	67.3	67.9	0.3	0.7	0.8
	3	67.3		0.3		

https://link.springer.com/article/10.1007/s00445-018-1241-1#Sec15

Online Resource A.1 High-speed video of an experimental current on a 4° slope under 0.93-0-0 U_{mf_st} conditions. Annotated frames are seen in **Fig. 3.4**.

==

Appendix B – Supplementary Material for Chapter 4

==

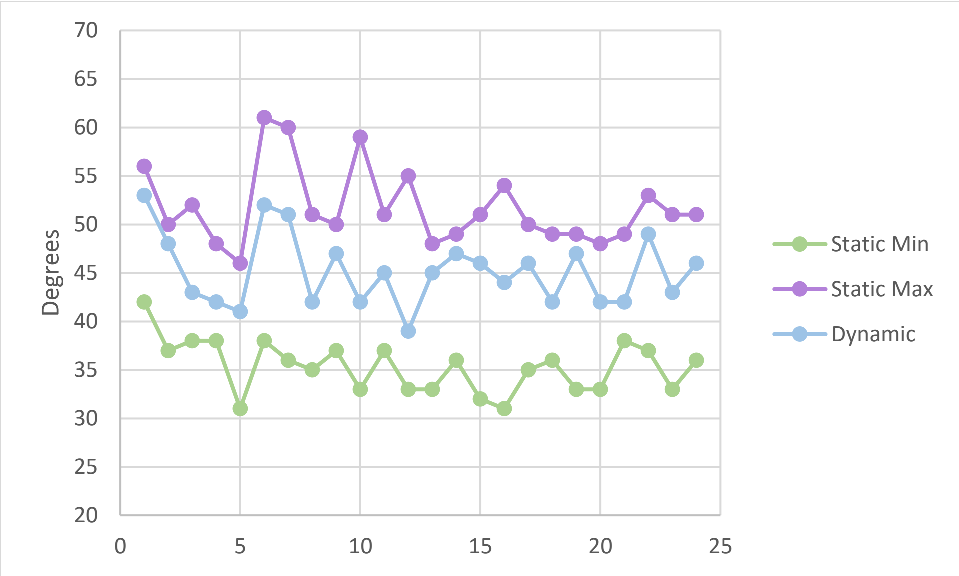

Supplementary Figure B.1 Results of rotating drum tests on Pozzolane Rosse ignimbrite samples. Dynamic, maximum and minimum static repose angles are given. X axis is test number.

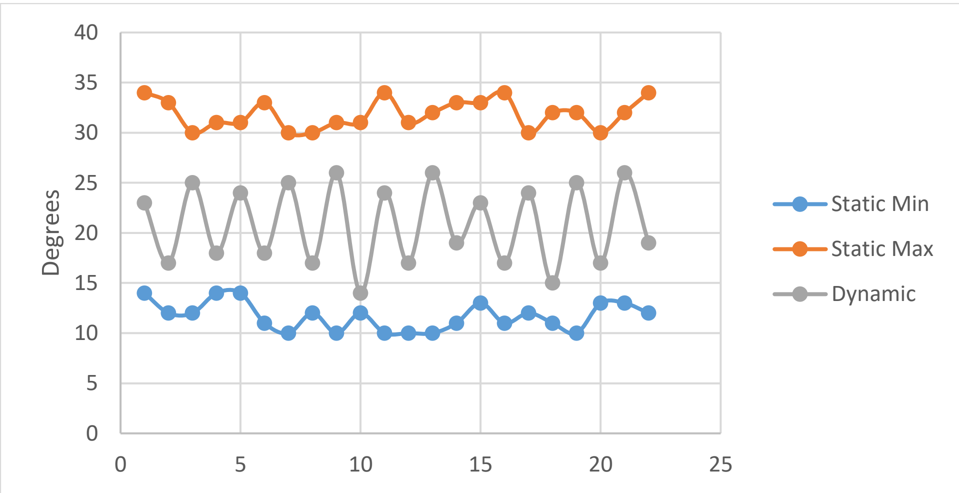

Supplementary Figure B.2 Results of rotating drum tests on ballotini samples. Dynamic, maximum and minimum static repose angles are given. X axis is test number.

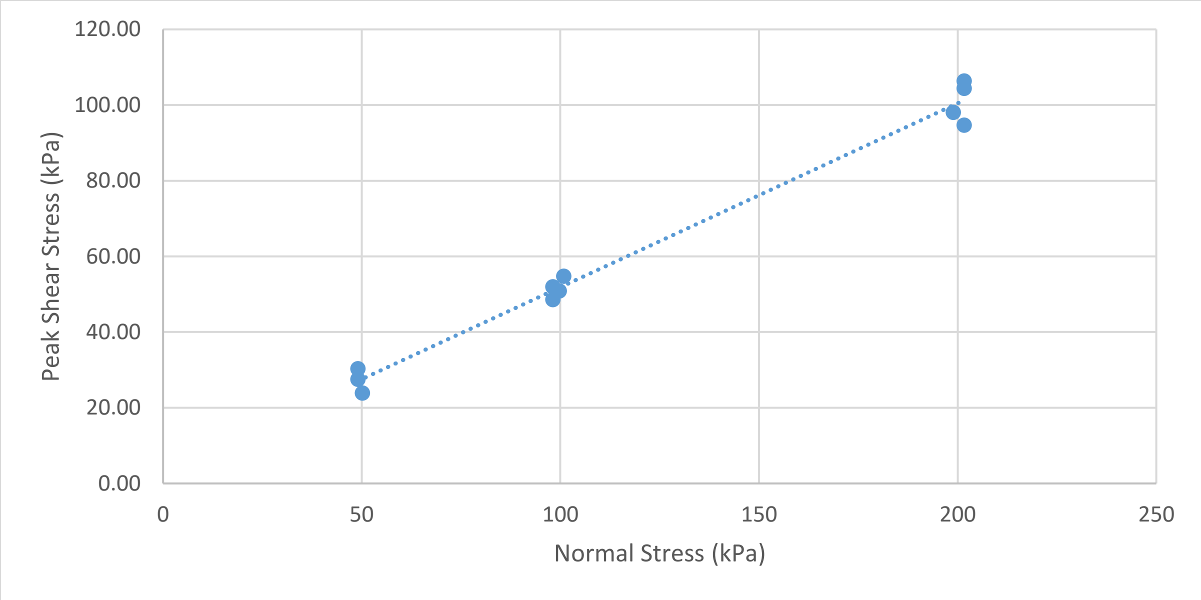

Supplementary Figure B.3 Results of shearbox testing on ballotini samples. Cohesion value given by intersect with y-axis. Internal friction angle given by value of slope.

Supplementary Table B.1 Experimental current data for five runs.

Run	Bedform	Current velocity	Current thickness	Froude Number	Savage number	Bagnold Number	Friction Number
1	Steep Regressive	0.44	0.0081	1.6	0.0003	41.6	132552
		0.36	0.0060	1.5	0.0005	46.0	88893
		0.22	0.0059	0.9	0.0002	28.6	140654
		0.40	0.0090	1.3	0.0002	33.7	181828
		0.35	0.0075	1.3	0.0002	35.4	144308
		0.33	0.0110	1.0	0.0001	23.0	325943
		0.40	0.0107	1.2	0.0001	28.4	257005
		0.36	0.0102	1.1	0.0001	27.0	256902
		0.44	0.0062	1.8	0.0007	54.4	77661
		0.33	0.0078	1.2	0.0002	31.6	168089
	Shallow Regressive	0.75	0.0120	2.2	0.0003	47.4	172399
		0.73	0.0093	2.4	0.0006	59.8	105901
		0.73	0.0078	2.7	0.0010	71.3	74494
		0.80	0.0075	2.9	0.0013	80.9	63135
		0.50	0.0068	1.9	0.0007	55.8	83039
		0.50	0.0070	1.9	0.0006	54.2	87996
		0.60	0.0053	2.6	0.0020	85.9	42037
		0.53	0.0047	2.5	0.0023	86.1	37190
		0.45	0.0043	2.2	0.0022	79.4	36894
		0.33	0.0047	1.5	0.0009	52.4	61031
		0.95	0.0100	3.0	0.0008	72.1	94517
		0.63	0.0079	2.3	0.0007	60.8	88482

		0.70	0.0050	3.2	0.0033	106.2	32068
		0.70	0.0043	3.4	0.0052	123.5	23718
		0.63	0.0054	2.8	0.0022	89.0	41342
		0.80	0.0070	3.1	0.0016	86.7	54997
		0.44	0.0062	1.8	0.0007	54.4	77661
		0.90	0.0078	3.3	0.0014	87.5	60699
		0.80	0.0071	3.0	0.0015	85.5	56580
		0.80	0.0068	3.1	0.0017	89.2	51899
		0.76	0.0068	2.9	0.0016	84.8	54631
		0.80	0.0075	2.9	0.0013	80.9	63135
		0.67	0.0065	2.6	0.0014	77.8	56905
		0.67	0.0064	2.7	0.0014	79.0	55168
		0.50	0.0060	2.1	0.0010	63.2	64650
	Planar	1.00	0.0057	4.2	0.0046	133.1	29173
		1.27	0.0043	6.2	0.0170	223.4	13107
		0.90	0.0050	4.1	0.0055	136.5	24942
		1.05	0.0048	4.8	0.0084	165.9	19703
		0.80	0.0043	3.9	0.0068	141.1	20753
		1.10	0.0031	6.3	0.0343	269.1	7845
		1.10	0.0036	5.9	0.0219	231.7	10579
		0.88	0.0032	5.0	0.0200	208.6	10448
		0.63	0.0031	3.6	0.0112	153.8	13728
		0.95	0.0040	4.8	0.0119	180.1	15123
		1.05	0.0057	4.4	0.0050	139.7	27784
		1.33	0.0064	5.3	0.0057	158.0	27584
		1.00	0.0069	3.8	0.0026	109.9	42750
		1.00	0.0055	4.3	0.0051	137.9	27162
		0.95	0.0057	4.0	0.0041	126.4	30709
		0.90	0.0038	4.7	0.0125	179.6	14407
2	Steep Regressive	0.63	0.0127	1.8	0.0002	37.8	228670
		0.50	0.0092	1.7	0.0003	41.2	151999
		0.33	0.0072	1.3	0.0003	35.1	139644
		0.67	0.0107	2.1	0.0003	47.3	154203
		0.40	0.0069	1.5	0.0004	44.0	106874
		0.53	0.0099	1.7	0.0002	40.2	167628
		0.33	0.0081	1.2	0.0002	31.2	176736
		0.67	0.0125	1.9	0.0002	40.4	210449
		0.40	0.0127	1.1	0.0001	23.9	362061
		0.25	0.0121	0.7	0.0000	15.7	525854
	Shallow Regressive	1.00	0.0113	3.0	0.0006	66.9	115468
		0.90	0.0091	3.0	0.0009	75.2	82255
		0.73	0.0071	2.8	0.0013	78.3	61723
		0.73	0.0077	2.7	0.0010	72.2	72596
		0.50	0.0062	2.0	0.0009	61.2	69032
		0.67	0.0048	3.1	0.0034	105.3	31032
		0.40	0.0038	2.1	0.0025	79.8	32415

		0.95	0.0065	3.8	0.0028	110.8	39934
		0.70	0.0051	3.1	0.0031	104.1	33364
		0.67	0.0044	3.2	0.0044	114.9	26075
		0.73	0.0045	3.5	0.0050	123.6	24795
		0.36	0.0041	1.8	0.0016	67.3	41508
		0.63	0.0055	2.7	0.0020	86.2	43459
		0.80	0.0051	3.6	0.0041	119.0	29193
		0.67	0.0035	3.6	0.0088	144.5	16499
		0.70	0.0047	3.3	0.0040	113.0	28336
		0.95	0.0059	3.9	0.0037	122.1	32901
		0.55	0.0049	2.5	0.0022	85.1	39198
		0.67	0.0045	3.2	0.0041	112.4	27274
		1.67	0.0090	5.6	0.0032	140.4	43639
		1.25	0.0083	4.4	0.0023	114.2	49486
		1.25	0.0089	4.2	0.0019	106.5	56899
		1.50	0.0084	5.2	0.0032	135.4	42238
		1.25	0.0082	4.4	0.0024	115.6	48301
		1.47	0.0082	5.2	0.0033	135.7	41165
		1.10	0.0078	4.0	0.0022	107.0	49663
	Planar	1.50	0.0110	4.6	0.0014	103.4	72432
		1.25	0.0100	4.0	0.0013	94.8	71833
		1.00	0.0082	3.5	0.0015	92.5	60376
		0.95	0.0080	3.4	0.0015	90.1	60491
		1.25	0.0071	4.7	0.0037	133.5	36211
		1.25	0.0074	4.6	0.0033	128.1	39336
		1.10	0.0067	4.3	0.0034	124.5	36643
		1.20	0.0071	4.5	0.0034	128.2	37720
		0.67	0.0125	1.9	0.0002	40.4	210449
		0.67	0.0094	2.2	0.0005	53.8	119009
		0.53	0.0099	1.7	0.0002	40.2	167628
		0.35	0.0095	1.1	0.0001	27.9	231533
	Steep Regressive	0.70	0.0145	1.9	0.0001	36.6	269695
		0.45	0.0117	1.3	0.0001	29.2	273145
		0.45	0.0109	1.4	0.0001	31.3	237069
		0.50	0.0123	1.4	0.0001	30.8	271691
		0.42	0.0092	1.4	0.0002	34.3	182399
3		0.73	0.0110	2.2	0.0003	50.6	148156
		1.00	0.0100	3.2	0.0008	75.8	89791
		0.88	0.0096	2.9	0.0007	69.5	94036
		0.50	0.0085	1.7	0.0003	44.6	129749
	Shallow Regressive	1.00	0.0076	3.7	0.0019	99.8	51863
		0.90	0.0075	3.3	0.0016	91.0	56120
		1.00	0.0075	3.7	0.0020	101.1	50508
		0.80	0.0078	2.9	0.0012	78.3	67414
		0.80	0.0070	3.1	0.0016	86.7	54997
		0.67	0.0087	2.3	0.0006	58.1	101945

		0.80	0.0091	2.7	0.0007	66.7	92945
	Planar	1.47	0.0083	5.1	0.0032	134.0	42175
		1.40	0.0067	5.5	0.0055	158.5	28791
		1.00	0.0073	3.7	0.0022	103.9	47850
		1.47	0.0070	5.6	0.0053	158.9	29998
		0.90	0.0064	3.6	0.0026	106.7	40865
		1.05	0.0061	4.3	0.0041	130.5	31820
		1.33	0.0100	4.3	0.0015	101.1	67344
		1.00	0.0081	3.5	0.0016	93.6	58912
		1.00	0.0090	3.4	0.0012	84.3	72731
		1.05	0.0073	3.9	0.0024	109.1	45571
		0.90	0.0073	3.4	0.0018	93.5	53166
4	Steep Regressive	0.31	0.0103	1.0	0.0001	22.7	309594
		0.33	0.0067	1.3	0.0003	37.7	120922
	Shallow Regressive	0.67	0.0089	2.3	0.0005	56.8	106686
		0.50	0.0083	1.8	0.0004	45.7	123715
		0.73	0.0092	2.4	0.0006	60.5	103636
		0.80	0.0084	2.8	0.0009	72.2	79196
	Planar	0.80	0.0091	2.7	0.0007	66.7	92945
		1.00	0.0070	3.8	0.0025	108.3	43998
		1.05	0.0081	3.7	0.0018	98.3	56107
5	Shallow Regressive	0.67	0.0094	2.2	0.0005	53.8	119009
		0.73	0.0089	2.5	0.0006	62.5	96987
		0.50	0.0080	1.8	0.0004	47.4	114933
		0.44	0.0066	1.7	0.0006	51.1	88005
	Planar	1.10	0.0074	4.1	0.0025	112.7	44700
		1.20	0.0068	4.6	0.0039	133.8	34600
		1.05	0.0071	4.0	0.0026	112.2	43108
		1.00	0.0065	4.0	0.0031	116.7	37937
		1.05	0.0070	4.0	0.0027	113.8	41903
		1.33	0.0067	5.2	0.0050	150.9	30231

Supplementary Table B.2 Grain size data for samples from the Pozzolane Rosse ignimbrite.

	Fraction (mm)	Mass (g)	Proportion	Cumulative Percentage	Fraction (phi)
Sample A	>5.6	13.40	0.40	100.00%	-5.00
	2-5.6	12.45	0.37	59.89%	-2.49
	600-2	4.38	0.13	22.63%	-1.00
	300-600	1.19	0.04	9.52%	0.74
	150-300	0.94	0.03	5.96%	1.74
	63-150	0.75	0.02	3.15%	2.74
	<63	0.30	0.01	0.90%	3.99
		SUM		0	7.97
		33.41			
Sample B	>5.6	11.80	0.33	100.00%	-5.00
	2-5.6	9.99	0.28	67.12%	-2.49
	600-2	6.39	0.18	39.28%	-1.00
	300-600	2.60	0.07	21.47%	0.74
	150-300	2.17	0.06	14.21%	1.74
	63-150	1.92	0.05	8.18%	2.74
	<63	1.02	0.03	2.83%	3.99
		SUM		0	7.97
		35.89			
Sample C	>5.6	17.60	0.60	100.00%	-5.00
	2-5.6	4.04	0.14	39.67%	-2.49
	600-2	3.21	0.11	25.83%	-1.00
	300-600	1.38	0.05	14.82%	0.74
	150-300	1.23	0.04	10.09%	1.74
	63-150	1.21	0.04	5.87%	2.74
	<63	0.51	0.02	1.74%	3.99
		SUM		0	7.97
		29.17			
Sample D	>5.6	8.50	0.28	100.00%	-5.00
	2-5.6	10.78	0.36	71.71%	-2.49
	600-2	5.54	0.18	35.84%	-1.00
	300-600	1.96	0.07	17.40%	0.74
	150-300	1.49	0.05	10.89%	1.74
	63-150	1.26	0.04	5.95%	2.74
	<63	0.53	0.02	1.75%	3.99
		SUM		0	7.97
		30.05			
Sample E	>5.6	2.60	0.09	100.00%	-5.00
	2-5.6	10.99	0.39	90.84%	-2.49
	600-2	7.71	0.27	52.12%	-1.00
	300-600	2.53	0.09	24.98%	0.74
	150-300	1.85	0.07	16.07%	1.74

	63-150	1.66	0.06	9.56%	2.74
	<63	1.06	0.04	3.72%	3.99
		SUM		0	7.97
		28.39			
Sample F	>5.6	7.50	0.30	100.00%	-5.00
	2-5.6	8.97	0.36	69.91%	-2.49
	600-2	4.76	0.19	33.91%	-1.00
	300-600	1.79	0.07	14.82%	0.74
	150-300	1.10	0.04	7.66%	1.74
	63-150	0.66	0.03	3.26%	2.74
	<63	0.16	0.01	0.63%	3.99
		SUM		0	7.97
		24.93			

Supplementary Table B.3 Supplementary mechanical data for ballotini.

	50kPa				100kPa			200kPa		
	Test 1	**Test 2**	**Test 3**	**Test 4**	**Test 1**	**Test 2**	**Test 3**	**Test 1**	**Test 2**	**Test 3**
Sample Height (mm)	3.87	3.21	4.44	8.13	4.89	6.35	3.15	3.32	5.85	4.86
	3.44	3.81	6.2	4.99	5.55	6.46	4.78	6.15	2.01	2.92
	3.40	3.2	5.21	4.06	3.61	6.4	6.54	2.87	5.76	7.09
	4.23	3.26	5.76	2.74	2.9	4.29	9.37	4.87	6.39	5.76
Av. Sample Height (mm)	3.74	3.37	5.40	4.98	4.24	5.88	5.96	4.30	5.00	5.16
Consolidation (mm)	0.392	0.2	0.204	0.227	0.665	0.51	0.404	0.821	0.637	0.746
Mass (kg)	1.84	1.8	1.8	1.8	3.66	3.6	3.6	7.3	7.4	7.4
Force (N)	18.05	17.66	17.66	17.66	35.90	35.32	35.32	71.61	72.59	72.59
Shear rate (mm/min)	0.5	0.5	0.5	0.5	0.5	0.5	0.5	0.5	0.5	0.5
Area (m^2)	0.0036	0.0036	0.0036	0.0036	0.0036	0.0036	0.0036	0.0036	0.0036	0.0036
Load (N/m^2)	5014	4905	4905	4905	9973.5	9810	9810	19892.5	20165	20165
Lever effect	10	10	10	10	10	10	10	10	10	10
Normal Stress (kPa)	50.14	49.05	49.05	49.05	99.735	98.1	98.1	198.925	201.65	201.65
Peak Shear Force (N)	86	109	99	97	183	175	187	353	383	341
Shear Stress (kPa)	23.89	30.28	27.50	26.94	50.83	48.61	51.94	98.06	106.39	94.72
Pre-consolidation Volume (mm^3)	78804	80118	72801	74322	76995	71100	70794	76761	74241	73683
Pre-consolidation Bulk Density (g/cm^3)	1.45	1.57	1.53	1.64	1.56	1.54	1.66	1.74	1.67	1.56
Post-consolidation Volume (mm^3)	77392.8	79398	72067	73505	74601	69264	69340	73805.4	71948	70997
Post-consolidation Bulk Density (g/cm^3)	1.48	1.58	1.55	1.66	1.61	1.58	1.70	1.81	1.72	1.62
Sample Mass (g)	114.44	125.72	111.38	122.23	120.01	109.17	117.6	133.33	123.65	115.13

https://www.nature.com/articles/s41467-020-16657-z#Sec13

Supplementary Movie B.1 Video of an experimental granular current. Deposition is triggered by the transition of the current to an unaerated chamber at 1 m mark (approximately half way across the frame). This is a video of the current seen in **Fig. 4.3**.

==

Appendix C – Supplementary Material for Chapter 5

==

Supplementary Table C.1 Thicknesses (mm) of the combined current and deposit at various locations and times. Time is given in seconds since the current entered the frame, and correspond to the four frames in Supplementary Figure C.1. ANOVA tests show that, at given times, average thicknesses of current + deposit belong to the same population except for those at time 0.2s.

		Location (cm)						
Time (s)	Current	94	96	98	100	102	Mean Thickness of current + deposit (mm)	*P-value*
0.2	a	13.5	13	12.7	12.4	12	12.72	1.07E-05
	b	12.8	13.1	12.5	12.5	12.8	12.74	
	c	10.5	9.8	10.1	11	11.4	10.56	
	d	12.4	12.9	12.3	12	11.6	12.24	
0.57	a	14	15.5	12.6	13.3	12	13.48	0.106483
	b	12.7	12.5	11.5	12.1	12.5	12.26	
	c	13.3	12.4	13.7	12.5	13.1	13	
	d	12.6	13.1	11.8	12.5	12.1	12.42	
1.19	a	14.8	15.3	16.7	19.4	23.7	17.98	0.966647
	b	13.4	14.5	15.5	19.3	22.1	16.96	
	c	14.3	14.4	15.7	19.2	21.4	17	
	d	14	14.8	15.2	19.8	23.1	17.38	
1.7	a	15.8	23.4	33.8	40.2	38.1	30.26	0.884209
	b	16.1	20.8	33.1	35.1	33.7	27.76	
	c	13.8	19	30.7	32.5	31.9	25.58	
	d	15.3	21.2	34.8	36.1	35.2	28.52	

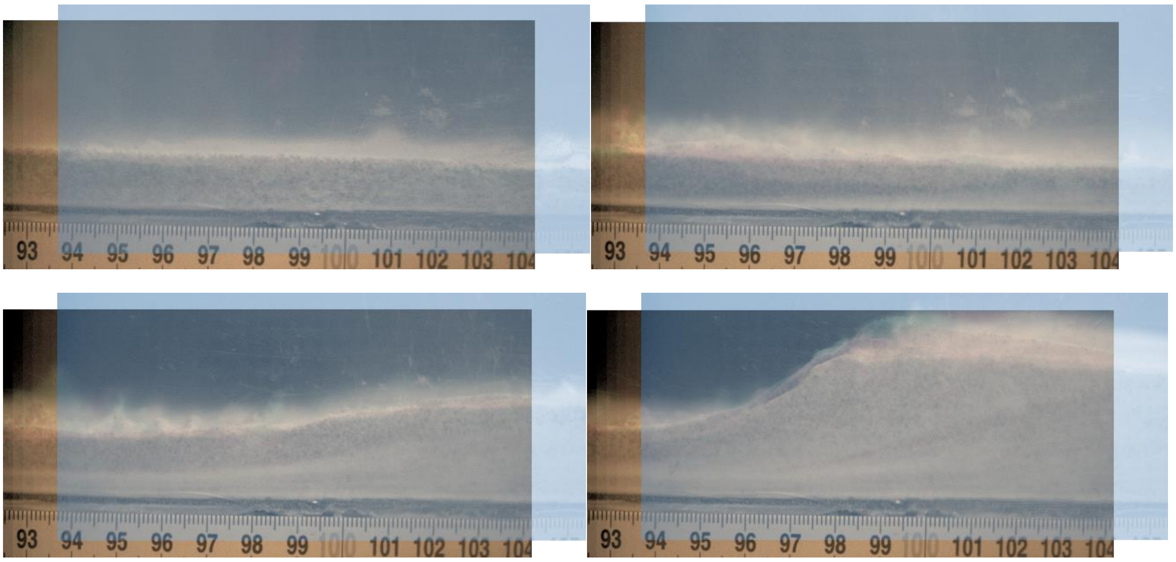

Supplementary Figure C.1 Three currents (a, b, and c of Table 2) at the four separate stages in time: **a** non-depositional, **b** depositing planar beds, **c** depositing shallow backset bedforms, and **d** depositing steep backset bedforms. In each panel the same amount of time has elapsed since each current entered the target area.

Velocity and shear stress profiles

Height is above flow base (top of flume base/static deposit) to U_{max}.

Top of the flow-boundary zone marked in red.

Non-depositional current velocity and shear stress profiles

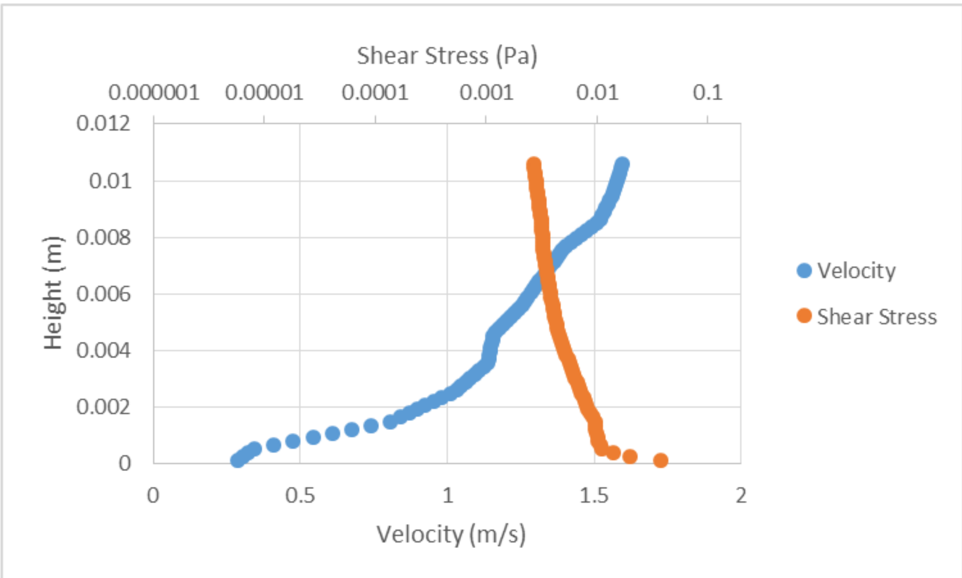

Supplementary Figure C.2 0.155 seconds from flow entering the frame. 94 cm along the flume.

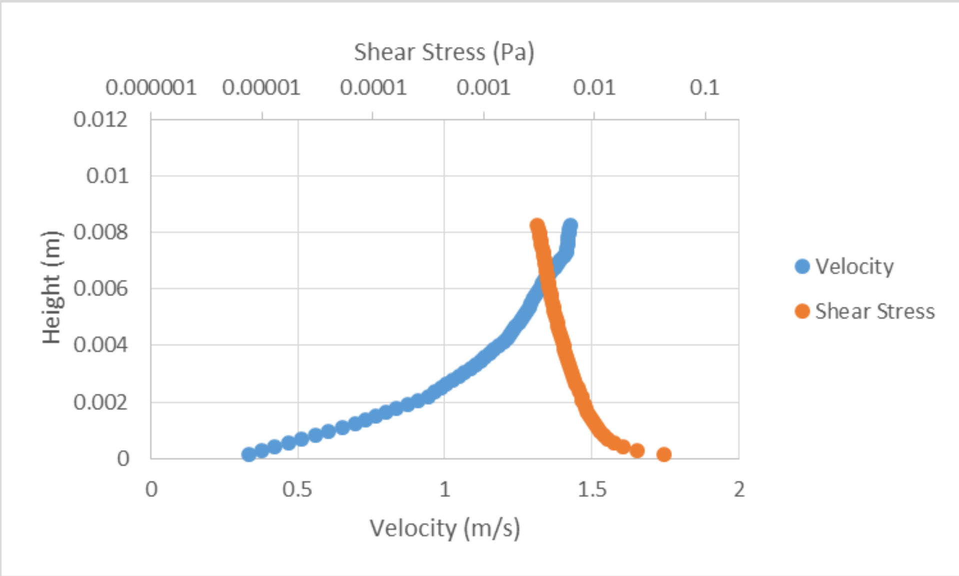

Supplementary Figure C.3 0.155 seconds from flow entering the frame. 96 cm along the flume.

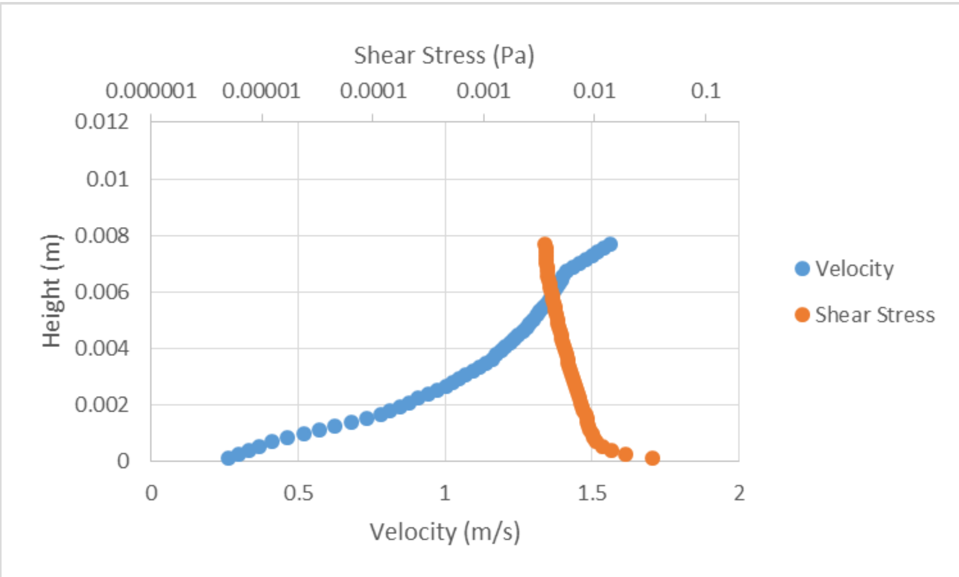

Supplementary Figure C.4 0.155 seconds from flow entering the frame. 98 cm along the flume.

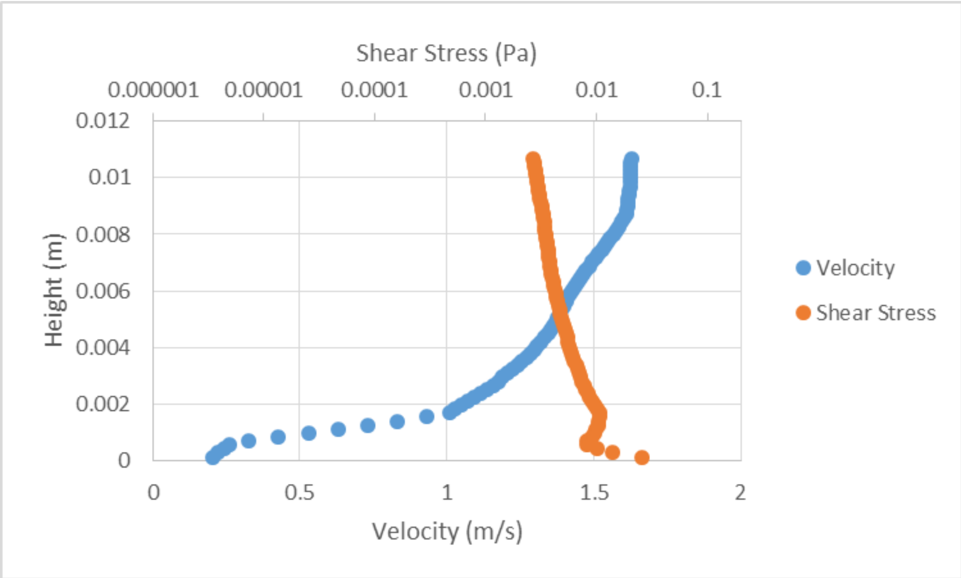

Supplementary Figure C.5 0.155 seconds from flow entering the frame. 100 cm along the flume.

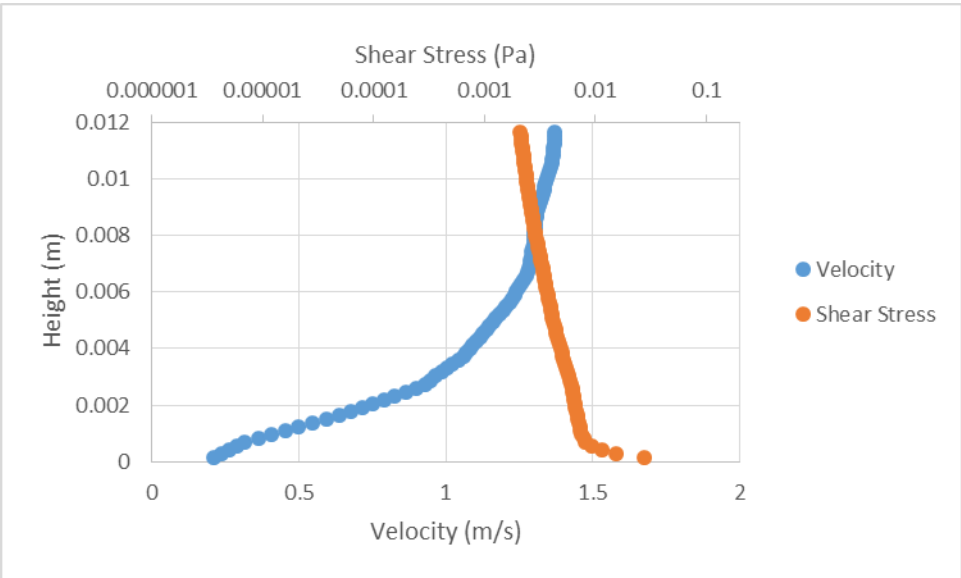

Supplementary Figure C.6 0.21 seconds from flow entering the frame. 94 cm along the flume.

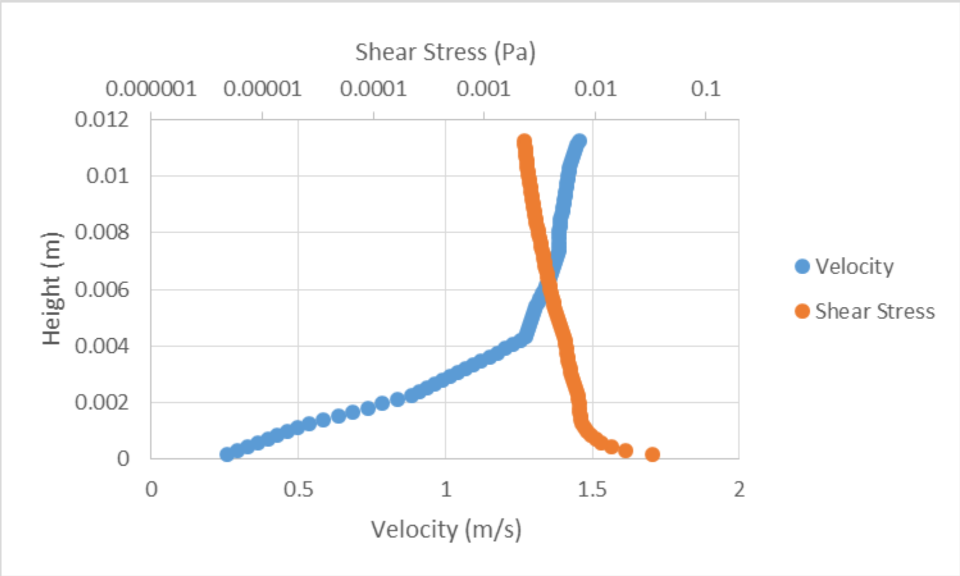

Supplementary Figure C.7 0.21 seconds from flow entering the frame. 96 cm along the flume.

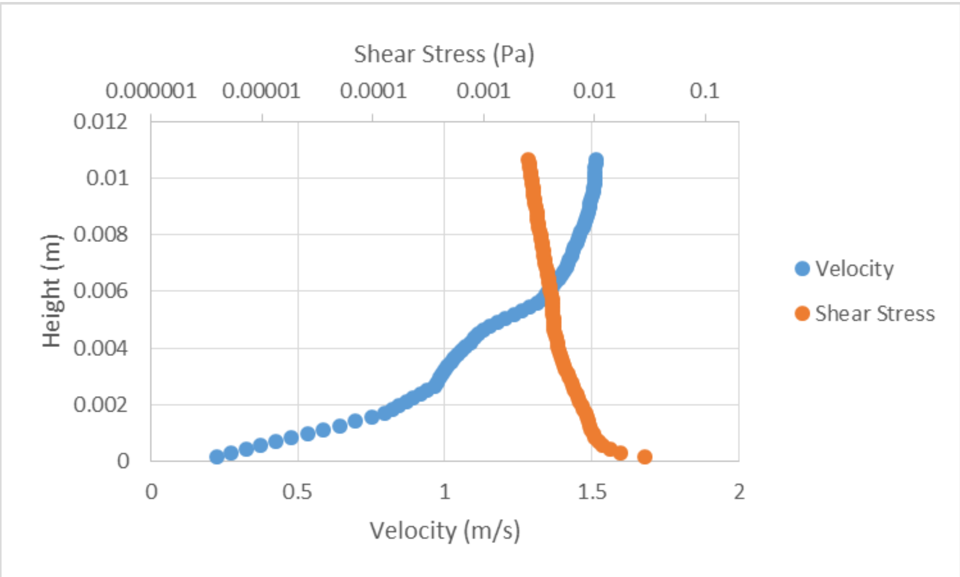

Supplementary Figure C.8 0.21 seconds from flow entering the frame. 98 cm along the flume.

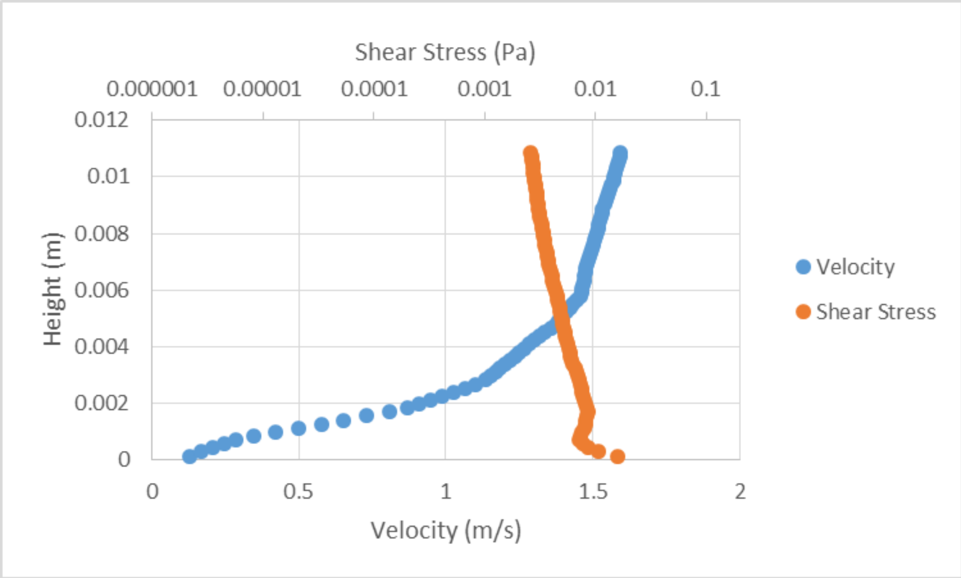

Supplementary Figure C.9 0.21 seconds from flow entering the frame. 100 cm along the flume.

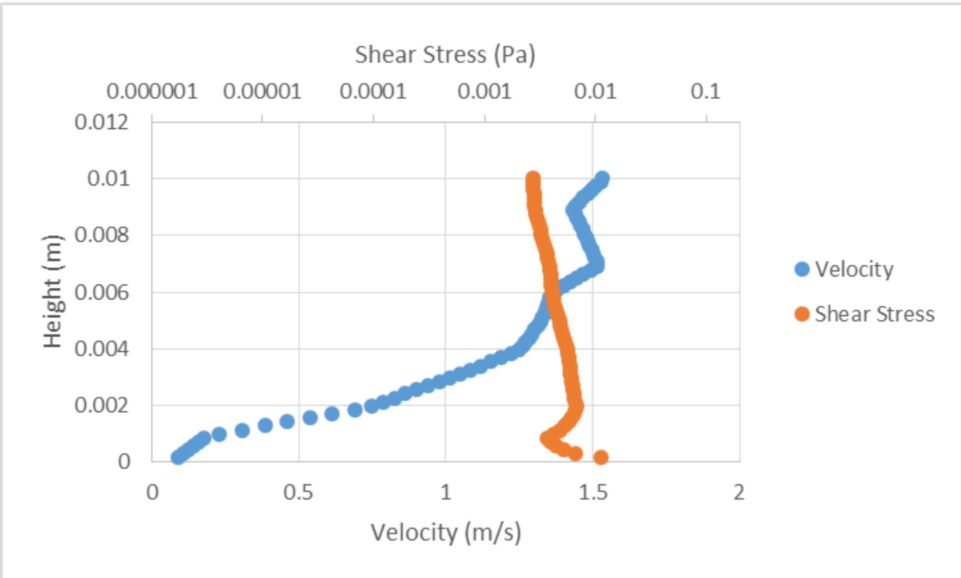

Supplementary Figure C.10 0.21 seconds from flow entering the frame. 102 cm along the flume.

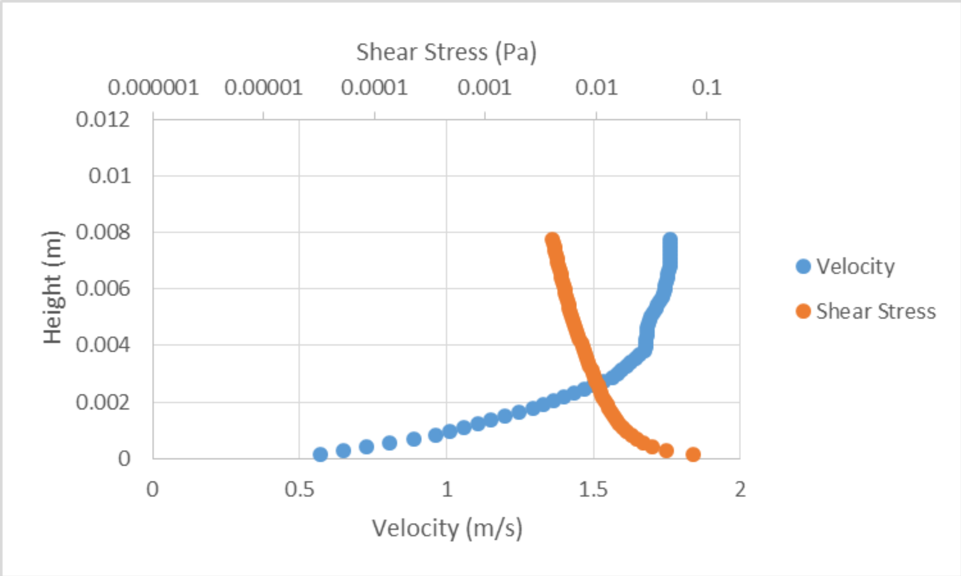

Supplementary Figure C.11 0.099 seconds from flow entering the frame. 94 cm along the flume.

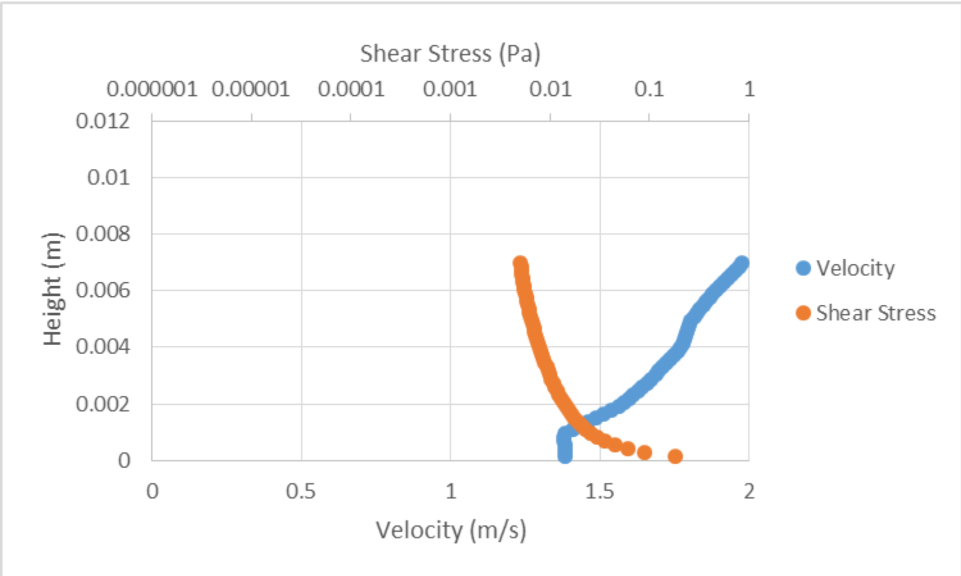

Supplementary Figure C.12 0.099 seconds from flow entering the frame. 96 cm along the flume.

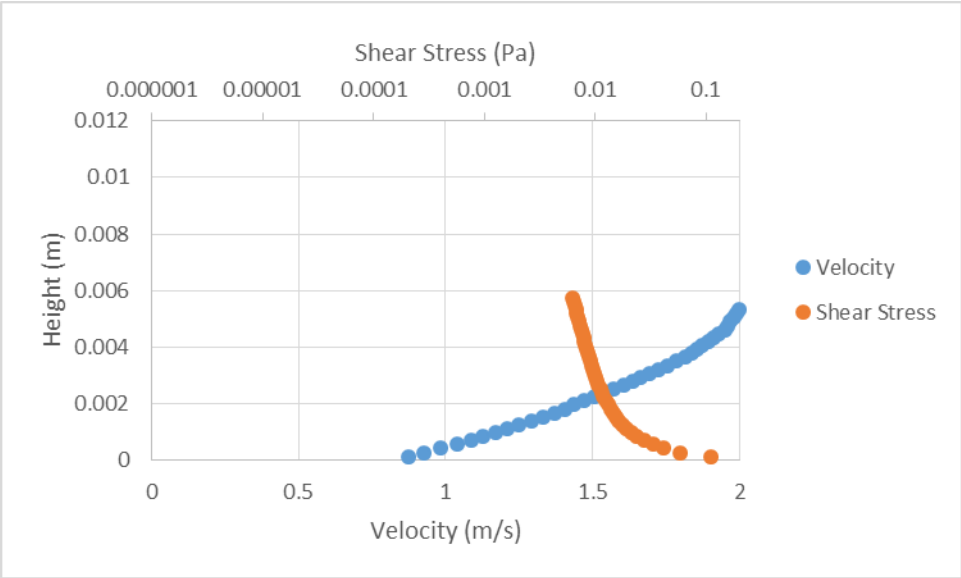

Supplementary Figure C.13 0.099 seconds from flow entering the frame. 98 cm along the flume.

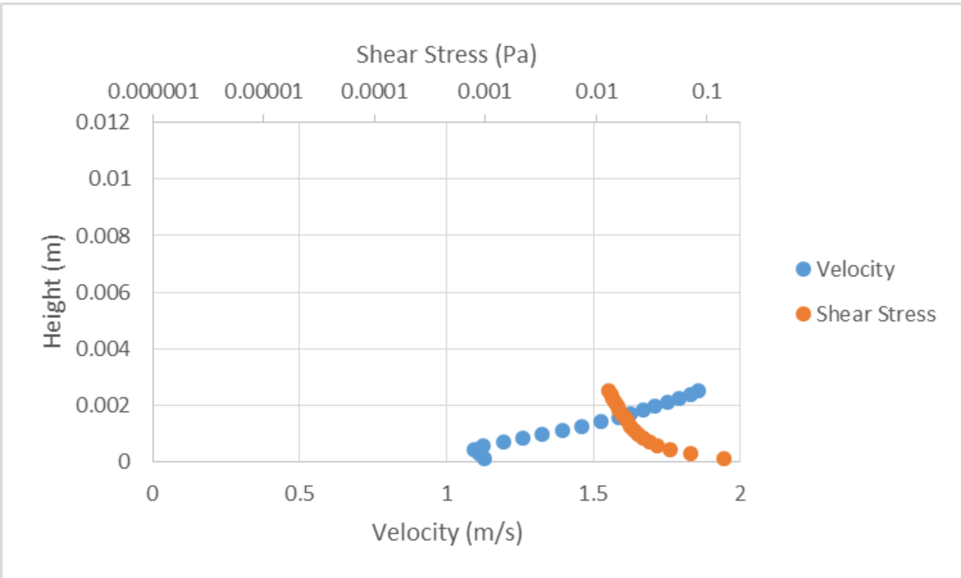

Supplementary Figure C.14 0.099 seconds from flow entering the frame. 100 cm along the flume.

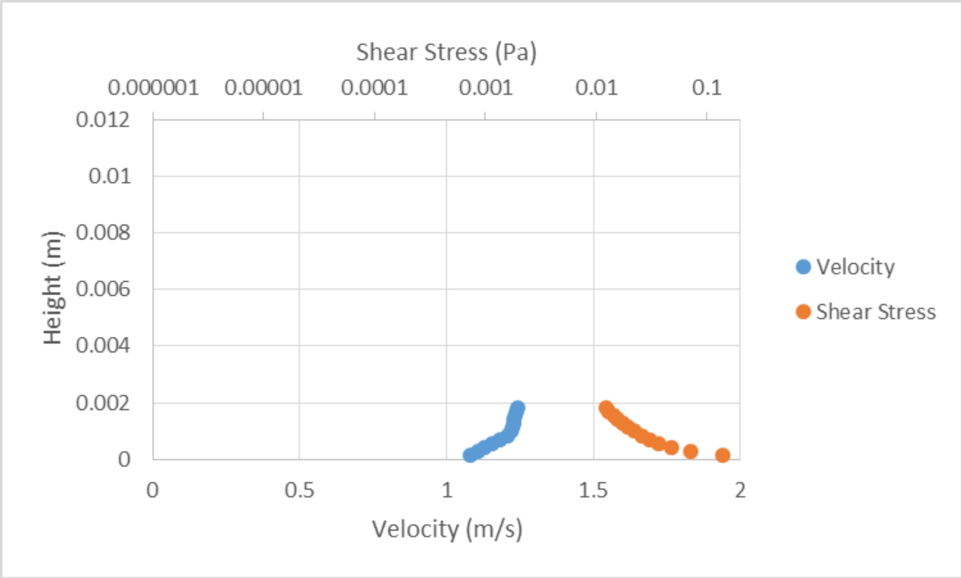

Supplementary Figure C.15 0.099 seconds from flow entering the frame. 102 cm along the flume.

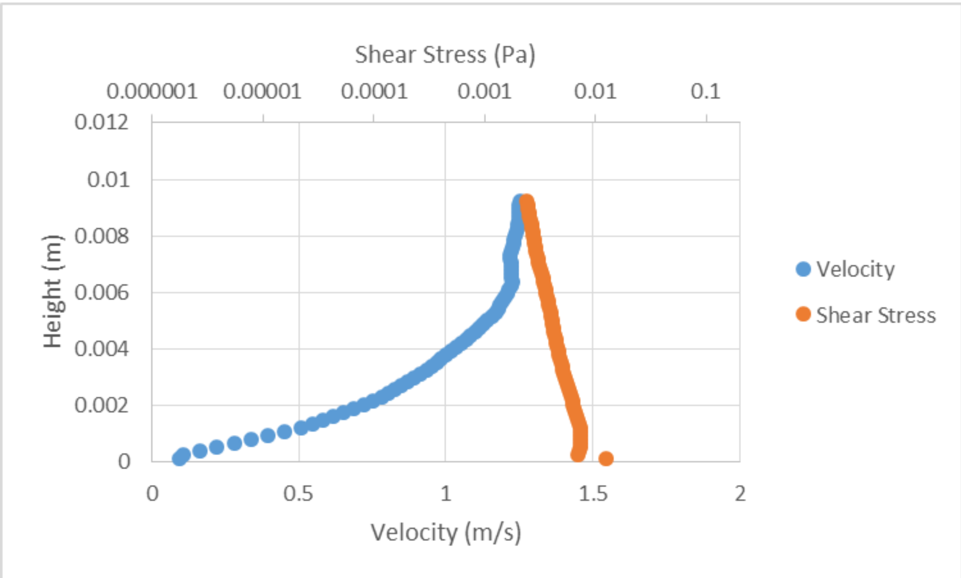

Supplementary Figure C.16 0.255 seconds from flow entering the frame. 94 cm along the flume.

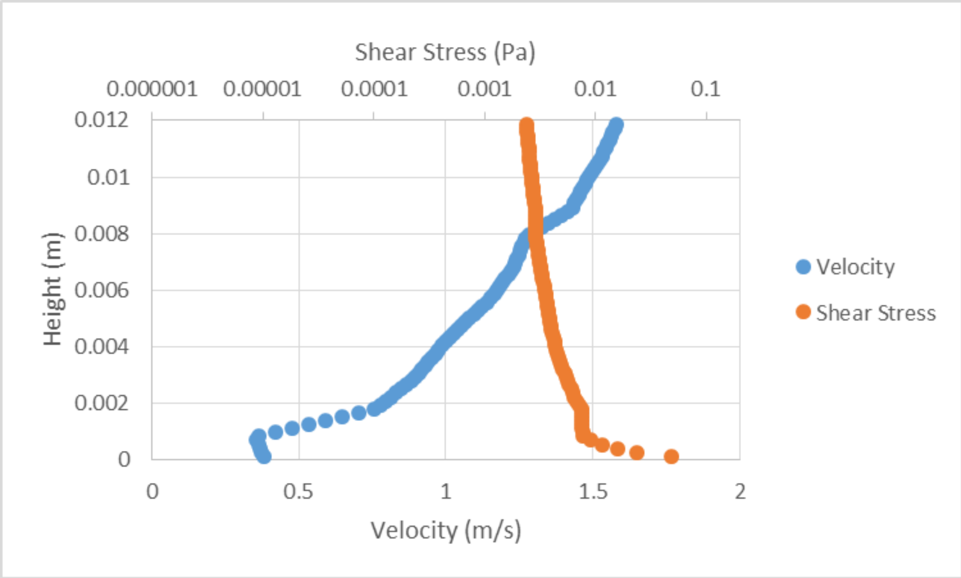

Supplementary Figure C.17 0.255 seconds from flow entering the frame. 96 cm along the flume.

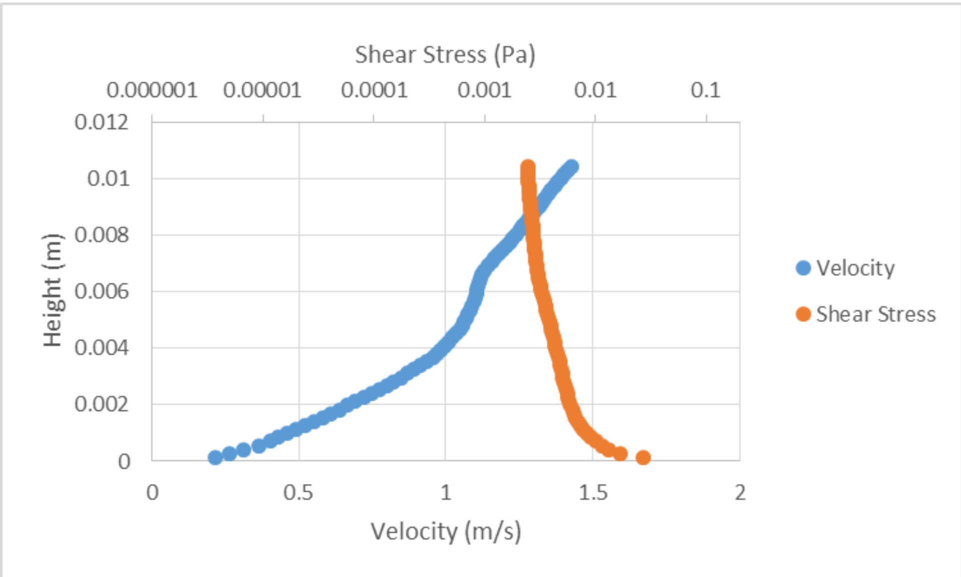

Supplementary Figure C.18 0.255 seconds from flow entering the frame. 98 cm along the flume.

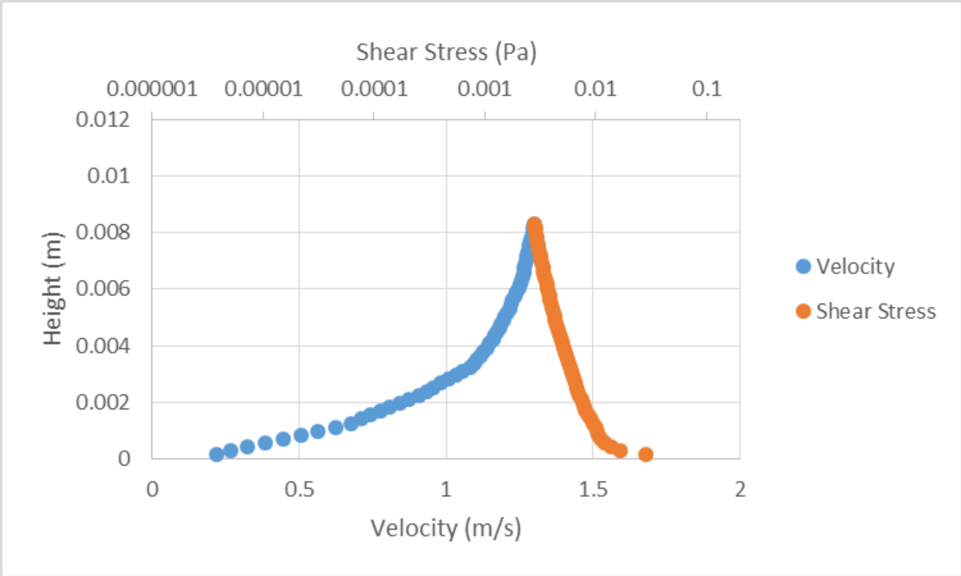

Supplementary Figure C.19 0.255 seconds from flow entering the frame. 100 cm along the flume.

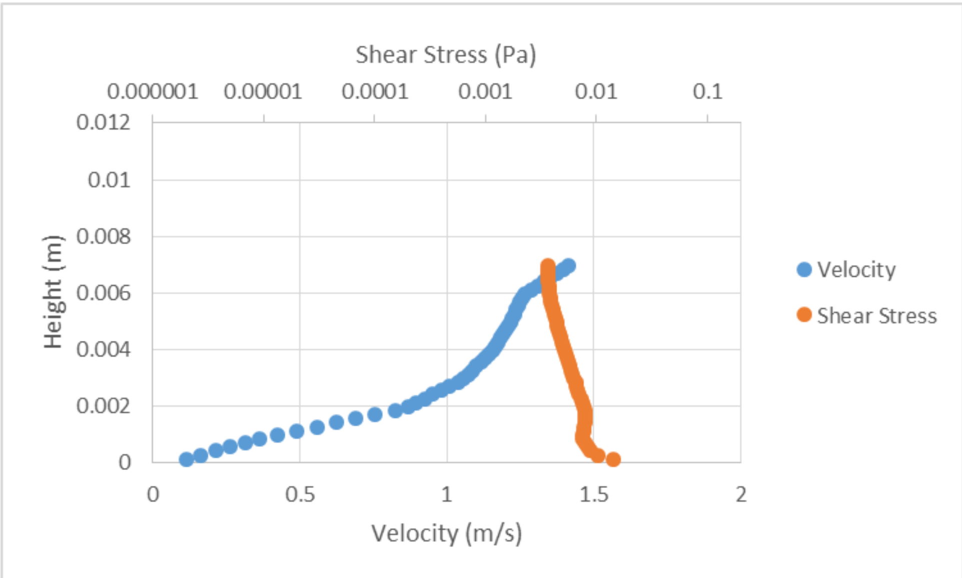

Supplementary Figure C.20 0.255 seconds from flow entering the frame. 102 cm along the flume.

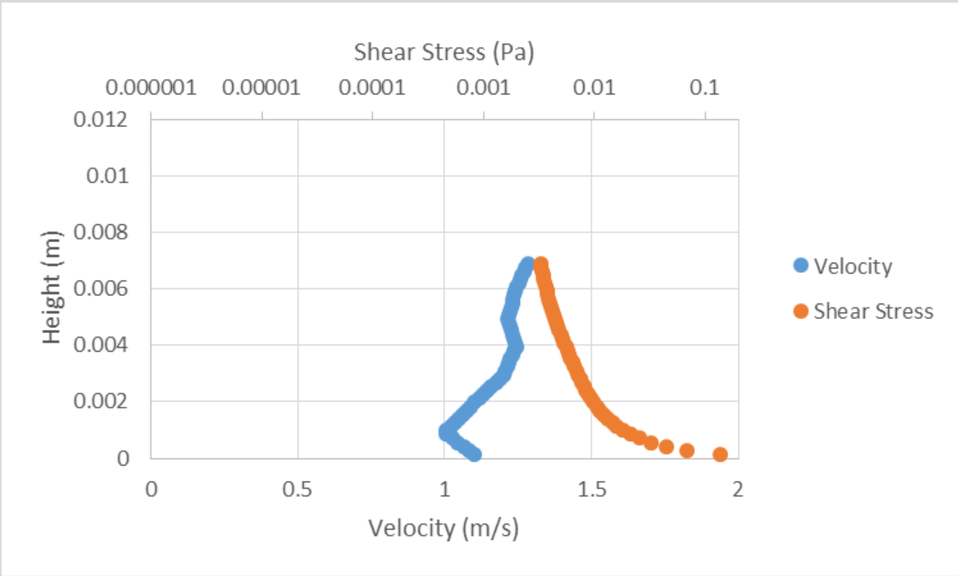

Supplementary Figure C.21 0.13 seconds from flow entering the frame. 102 cm along the flume.

Current depositing planar bedforms velocity and shear stress profiles

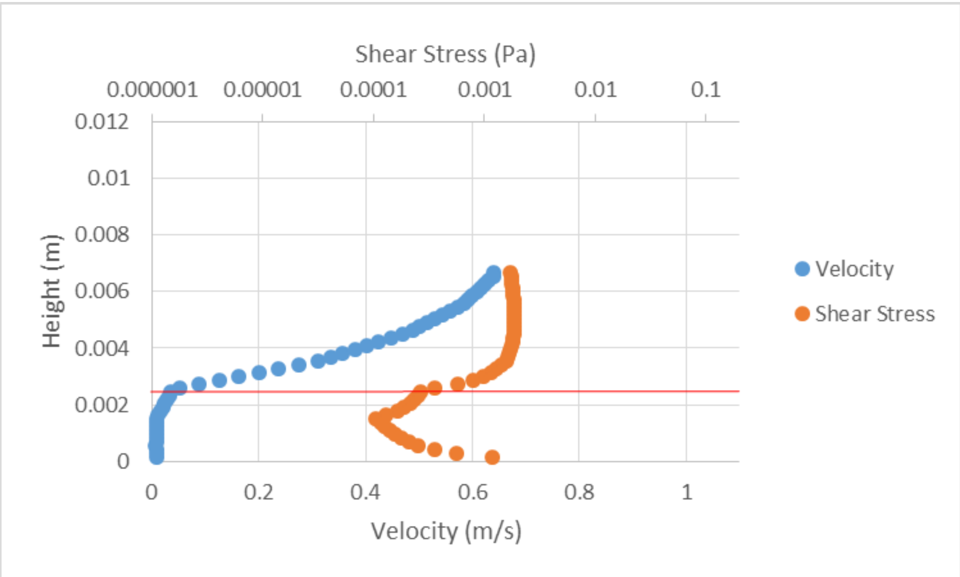

Supplementary Figure C.22 0.524 seconds from flow entering the frame. 94 cm along the flume.

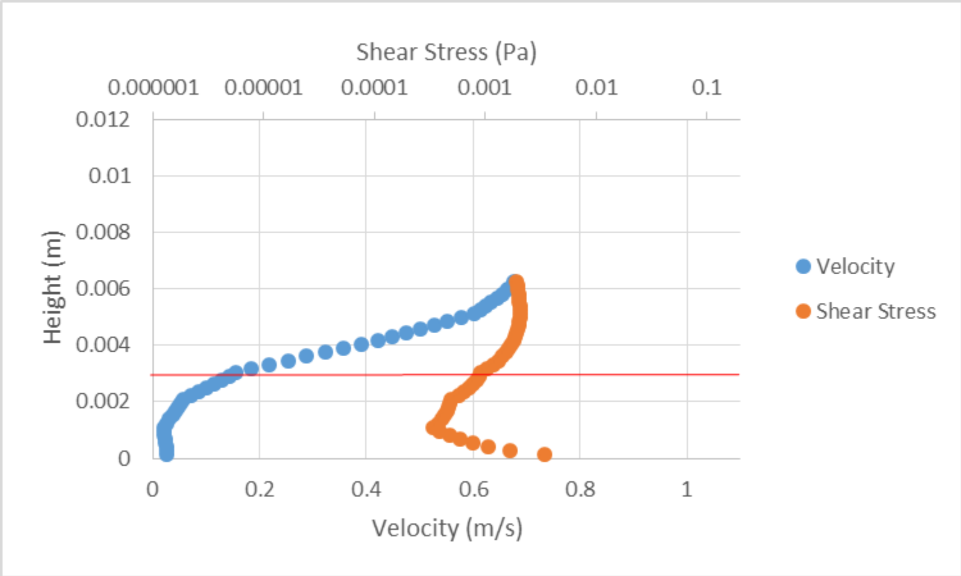

Supplementary Figure C.23 0.524 seconds from flow entering the frame. 96 cm along the flume.

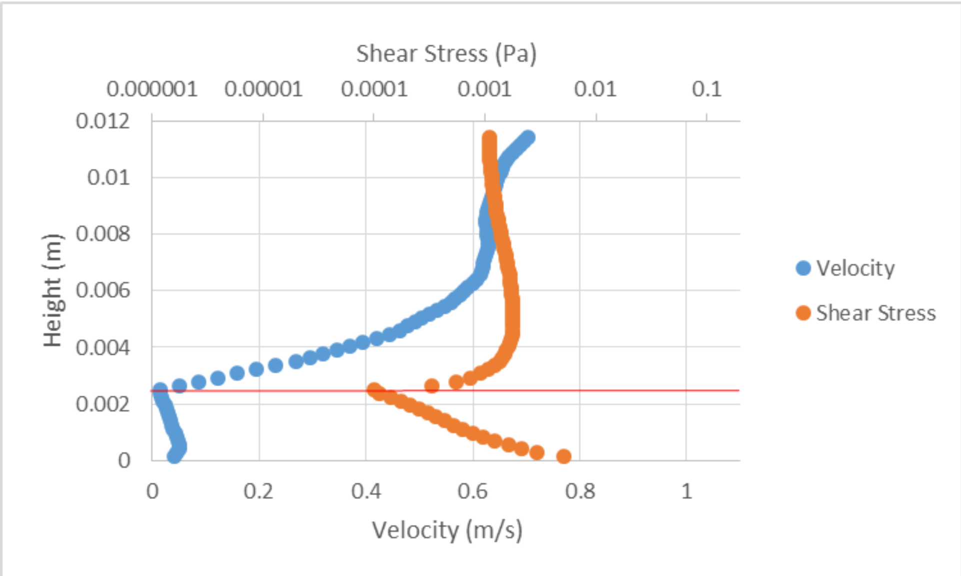

Supplementary Figure C.24 0.524 seconds from flow entering the frame. 98 cm along the flume.

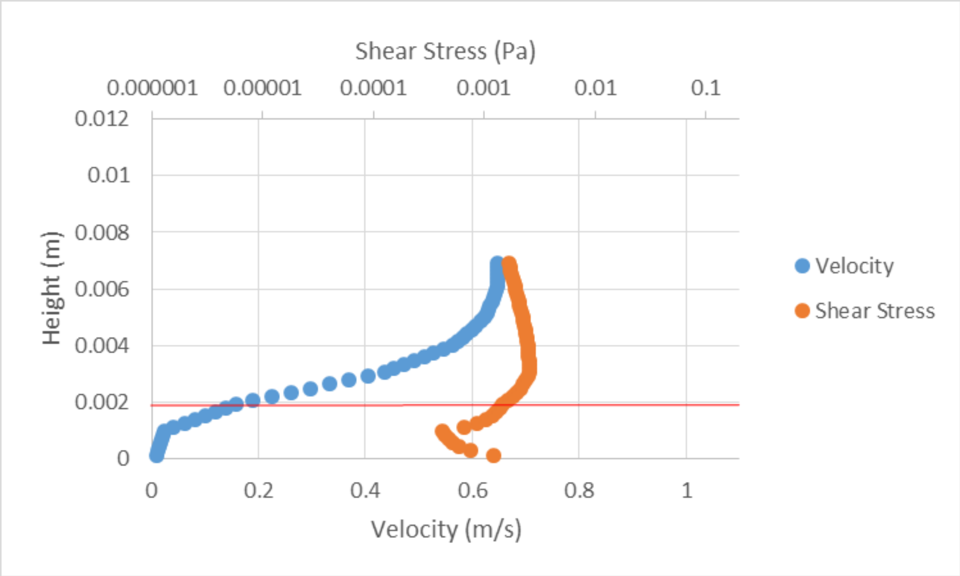

4226

4227 **Supplementary Figure C.25** 0.524 seconds from flow entering the frame. 100 cm along the flume.

4228

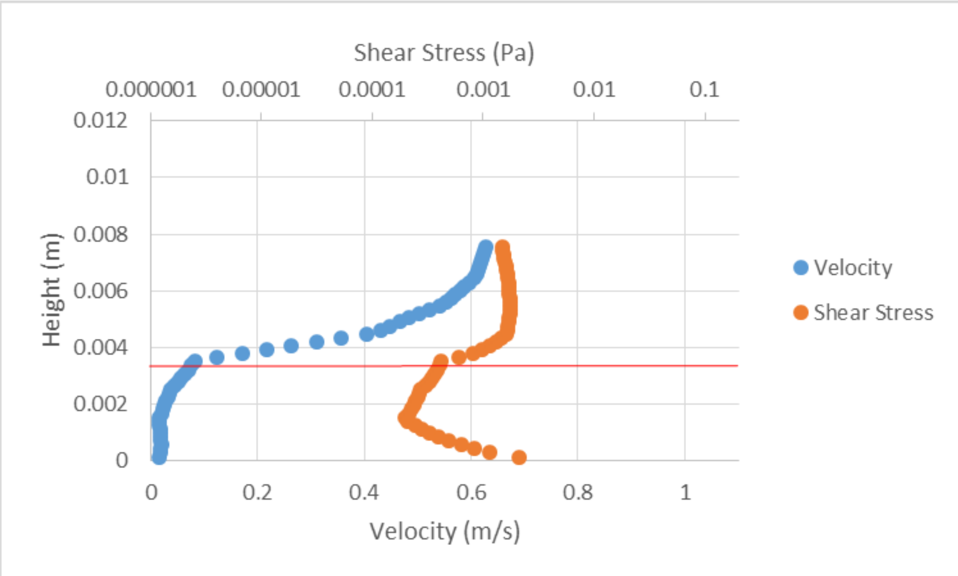

4229

4230 **Supplementary Figure C.26** 0.524 seconds from flow entering the frame. 102 cm along the flume.

4231

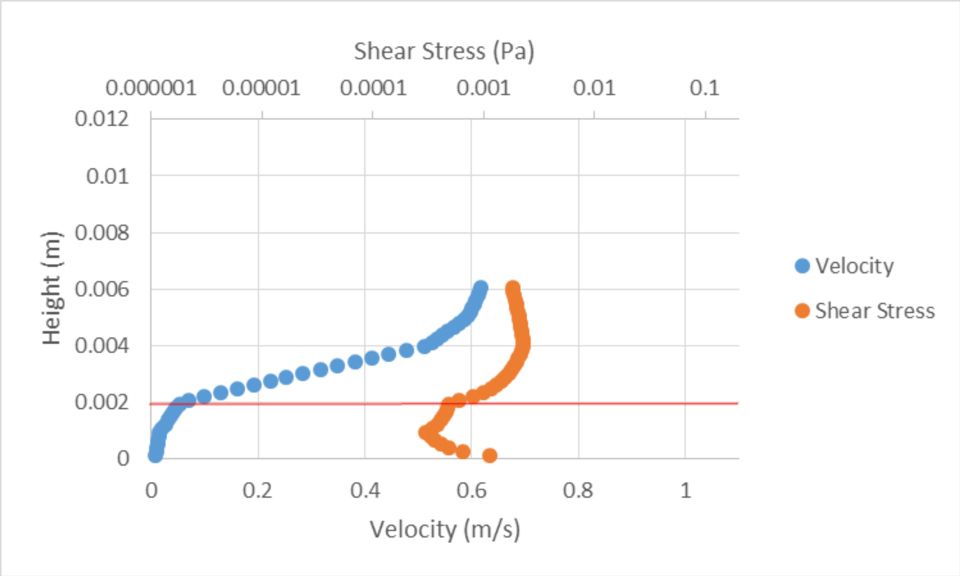

Supplementary Figure C.27 0.586 seconds from flow entering the frame. 94 cm along the flume.

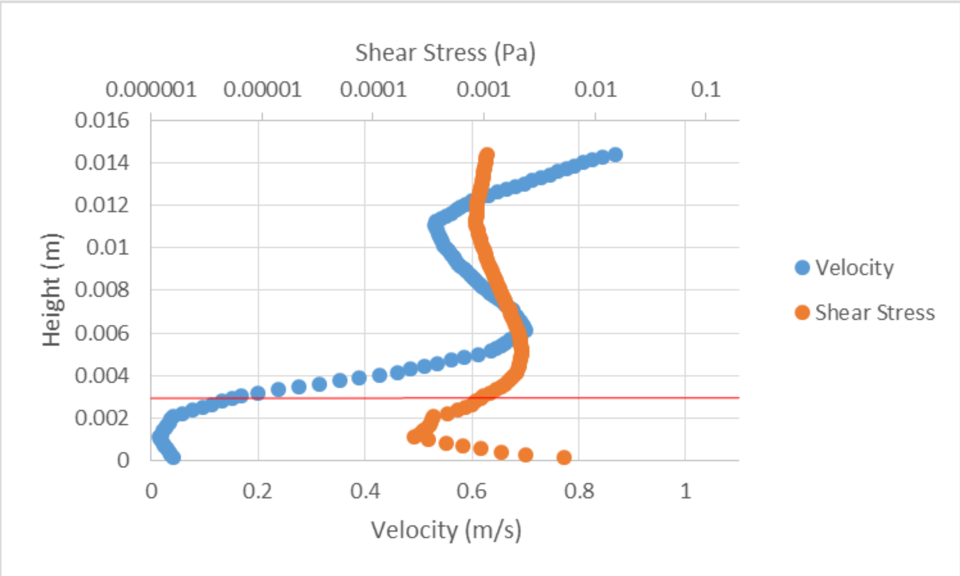

Supplementary Figure C.28 0.586 seconds from flow entering the frame. 96 cm along the flume.

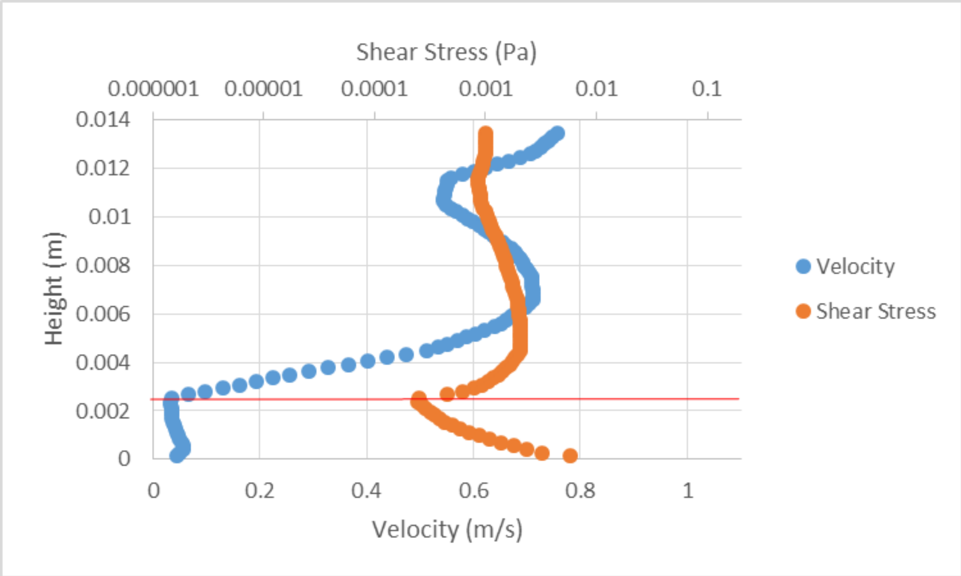

Supplementary Figure C.29 0.586 seconds from flow entering the frame. 98 cm along the flume.

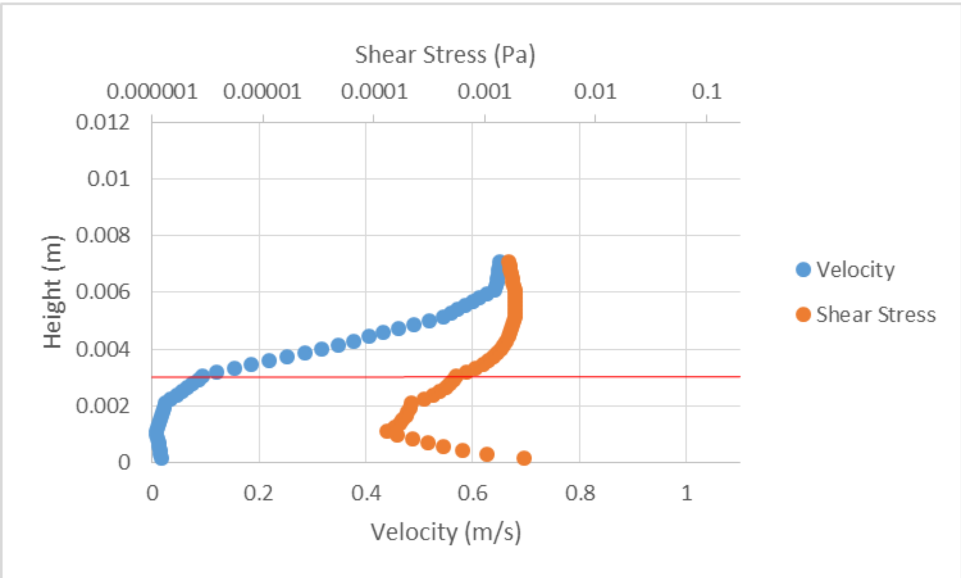

Supplementary Figure C.30 0.586 seconds from flow entering the frame. 100 cm along the flume.

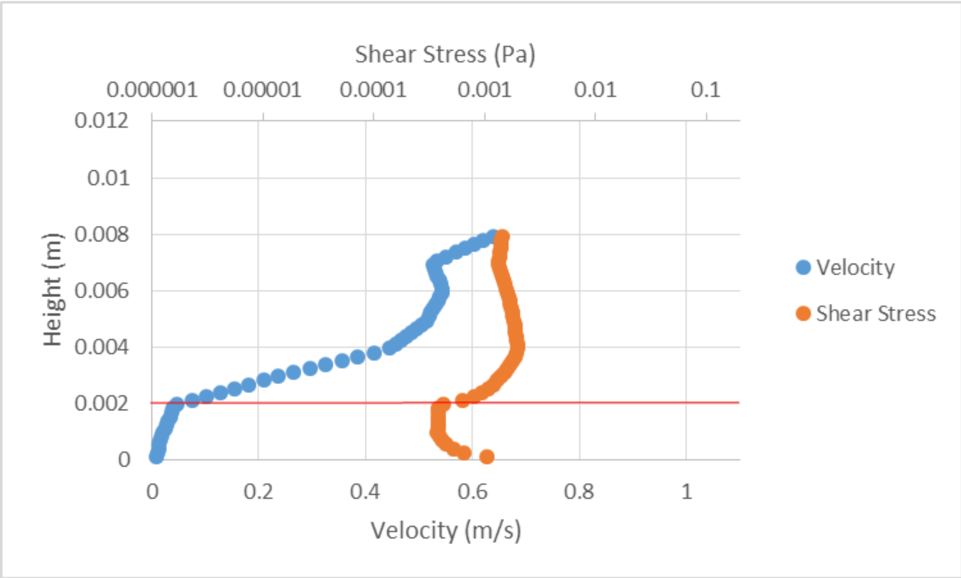

Supplementary Figure C.31 0.586 seconds from flow entering the frame. 102 cm along the flume.

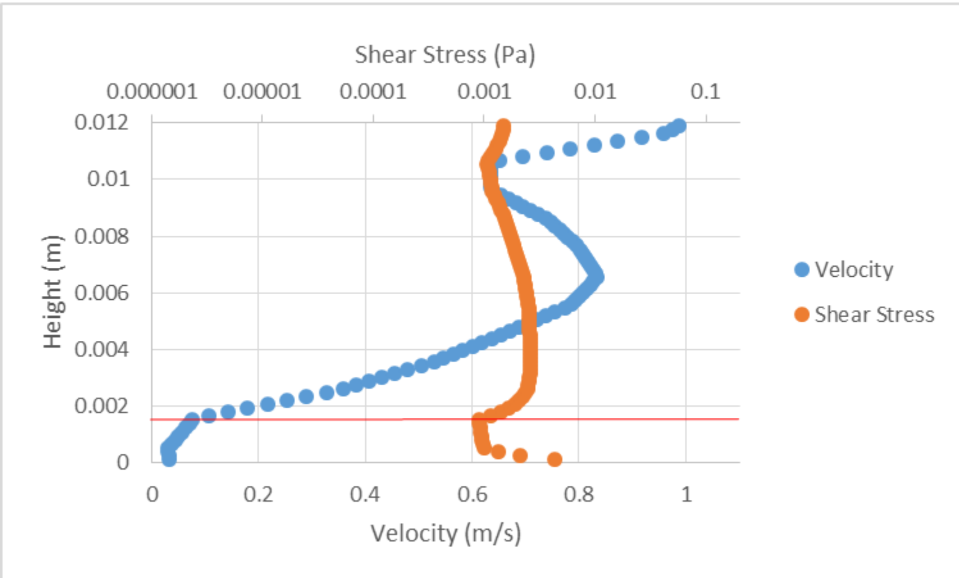

Supplementary Figure C.32 0.418 seconds from flow entering the frame. 94 cm along the flume.

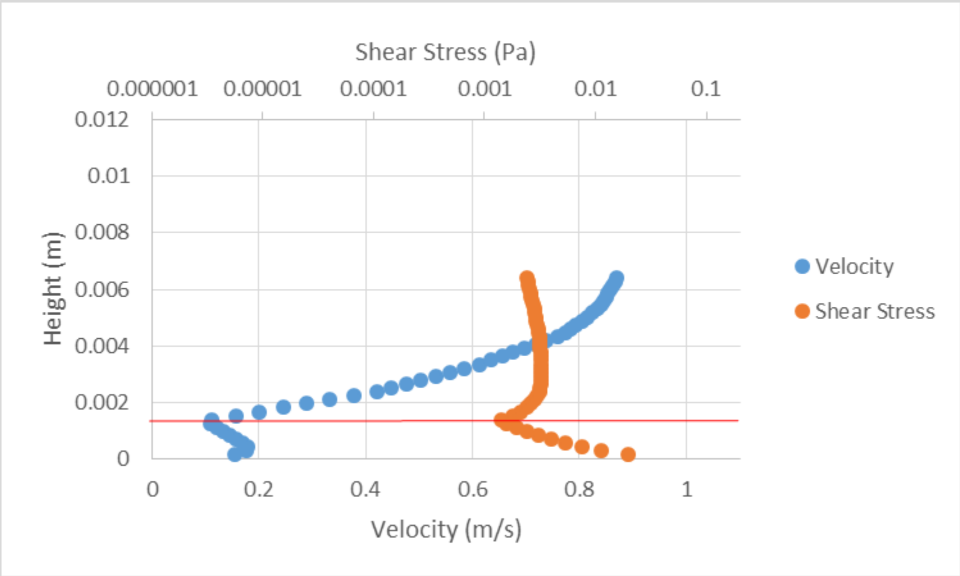

Supplementary Figure C.33 0.418 seconds from flow entering the frame. 96 cm along the flume.

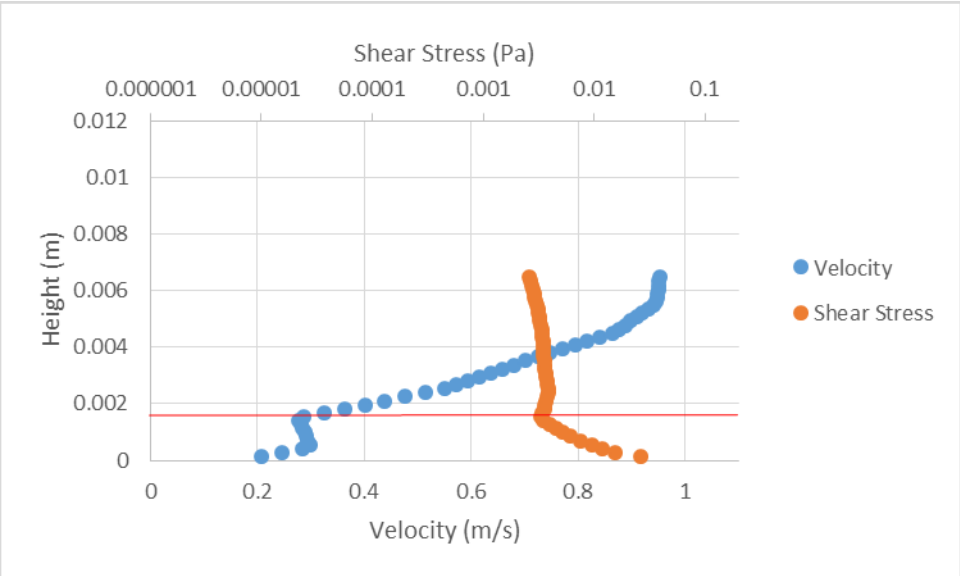

Supplementary Figure C.34 0.418 seconds from flow entering the frame. 98 cm along the flume.

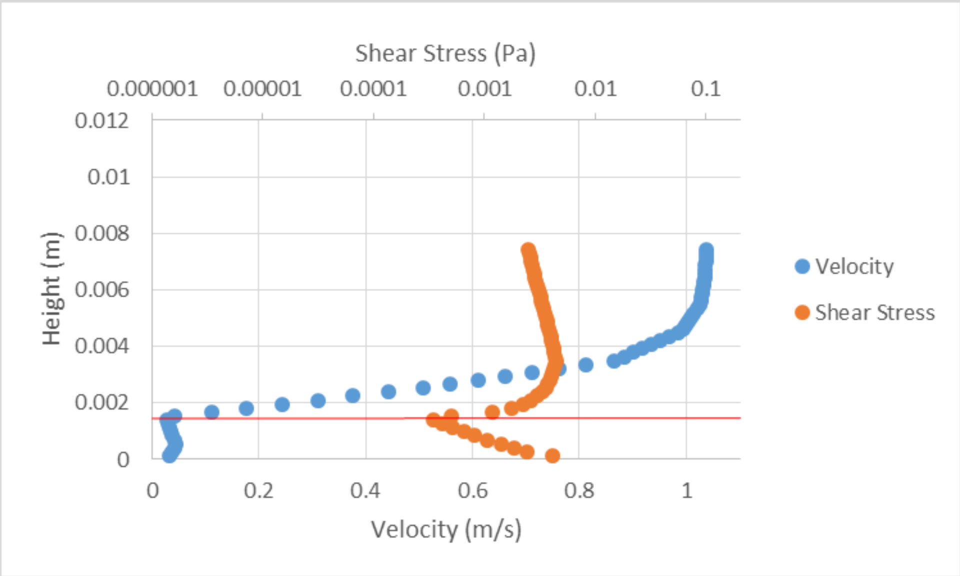

Supplementary Figure C.35 0.418 seconds from flow entering the frame. 100 cm along the flume.

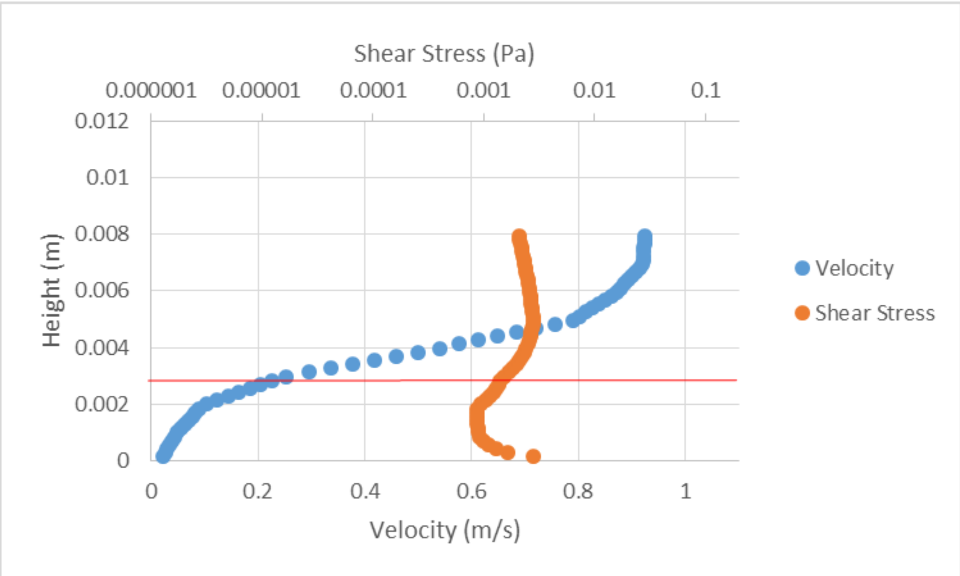

Supplementary Figure C.36 0.418 seconds from flow entering the frame. 102 cm along the flume.

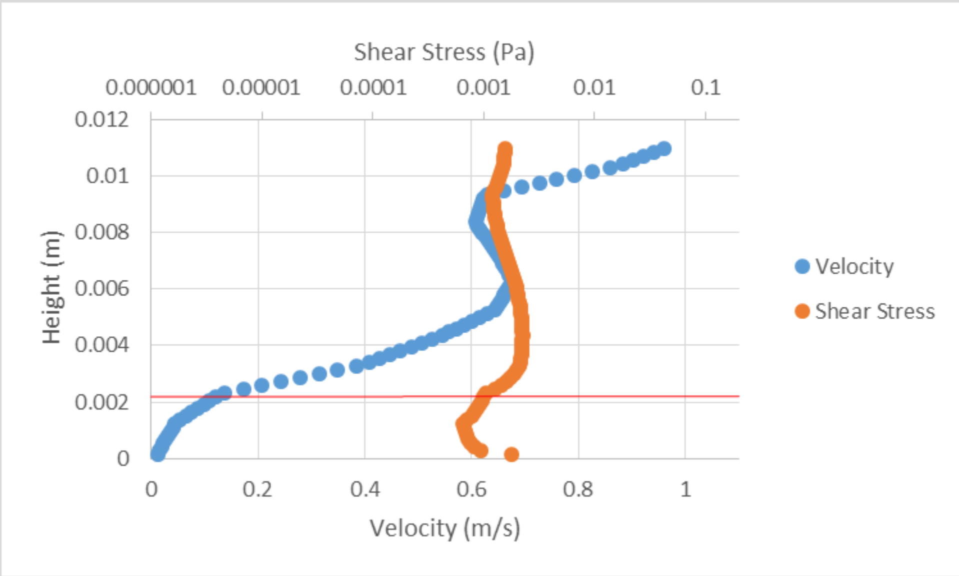

Supplementary Figure C.37 0.461 seconds from flow entering the frame. 94 cm along the flume.

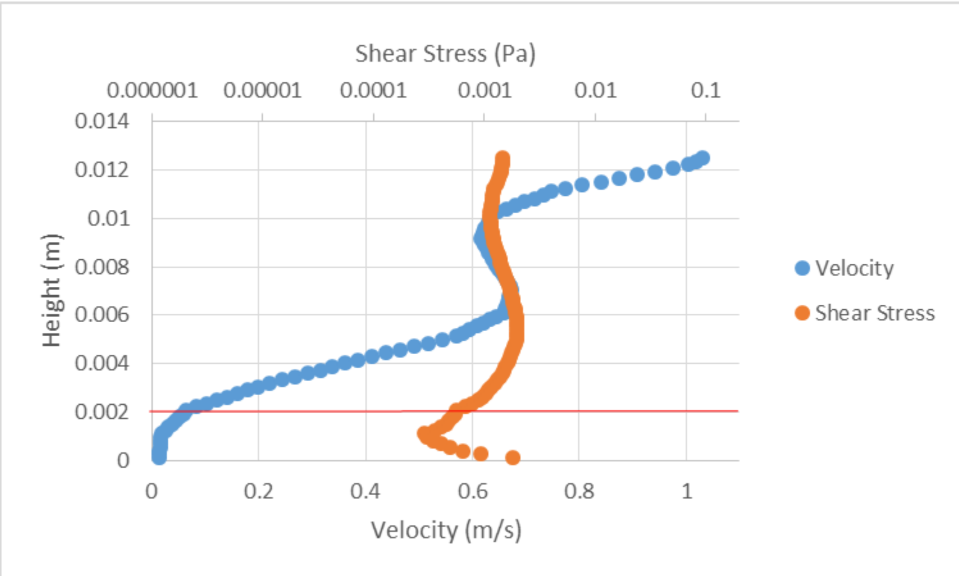

Supplementary Figure C.38 0.461 seconds from flow entering the frame. 96 cm along the flume.

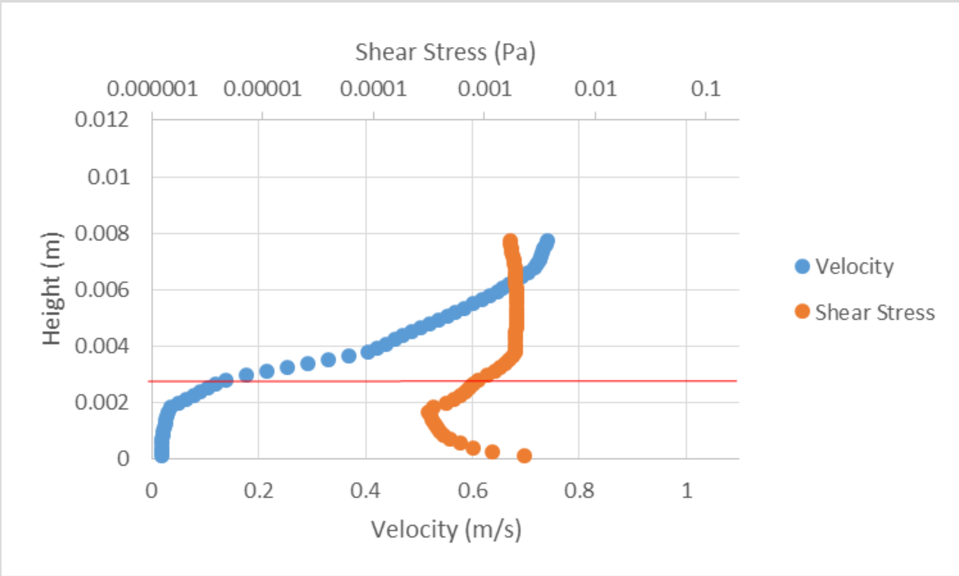

Supplementary Figure C.39 0.461 seconds from flow entering the frame. 98 cm along the flume.

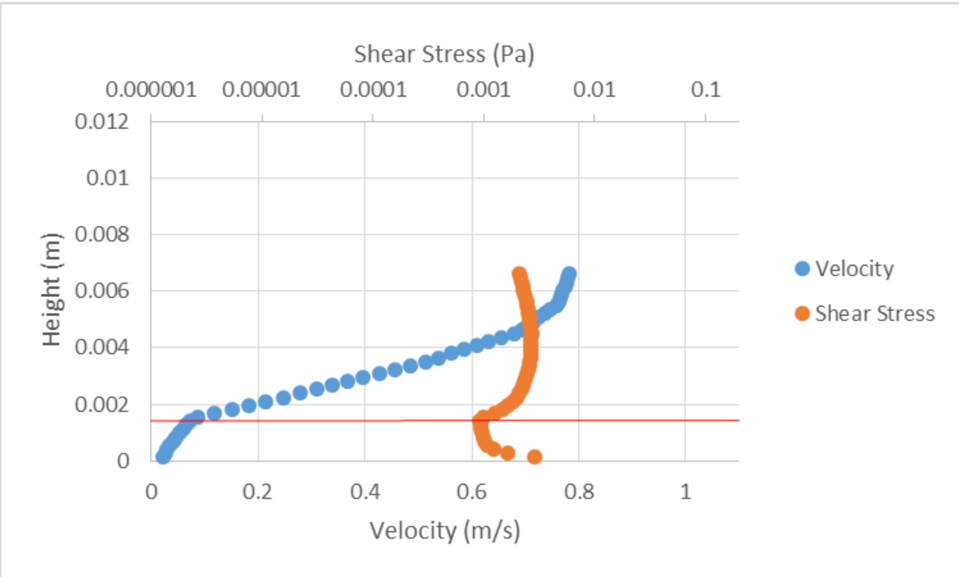

Supplementary Figure C.40 0.461 seconds from flow entering the frame. 100 cm along the flume.

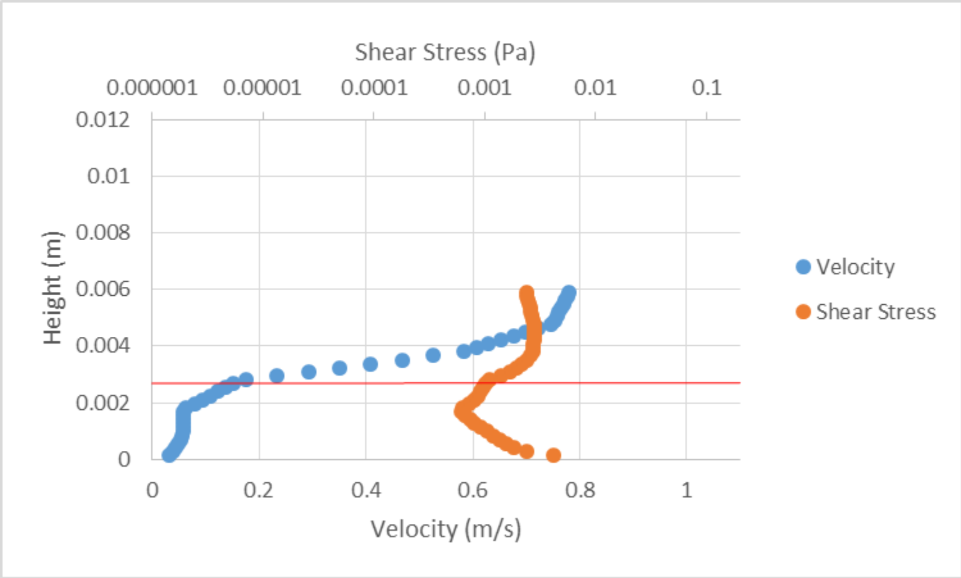

Supplementary Figure C.41 0.461 seconds from flow entering the frame. 102 cm along the flume.

Current depositing shallow bedforms velocity and shear stress profiles

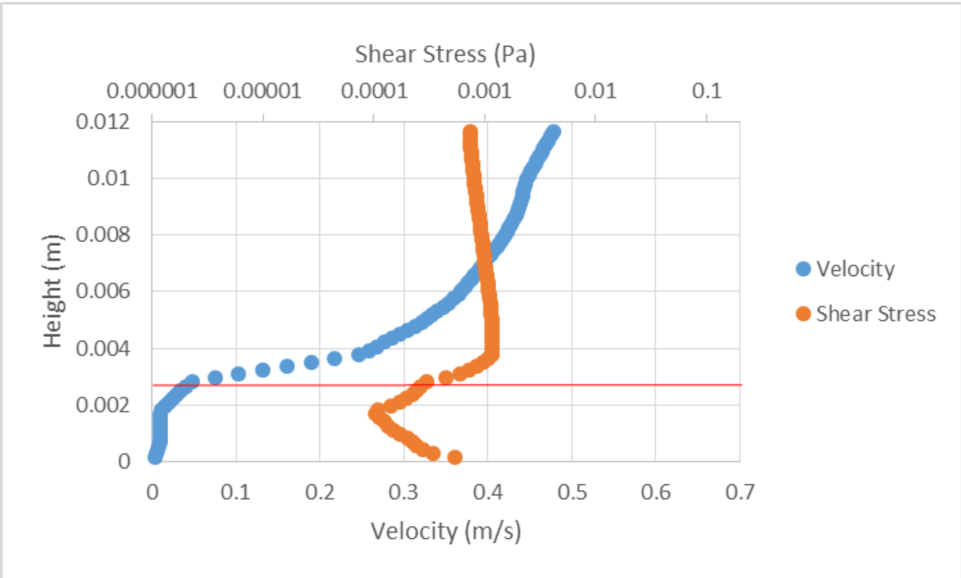

Supplementary Figure C.42 1.24 seconds from flow entering the frame. 98 cm along the flume.

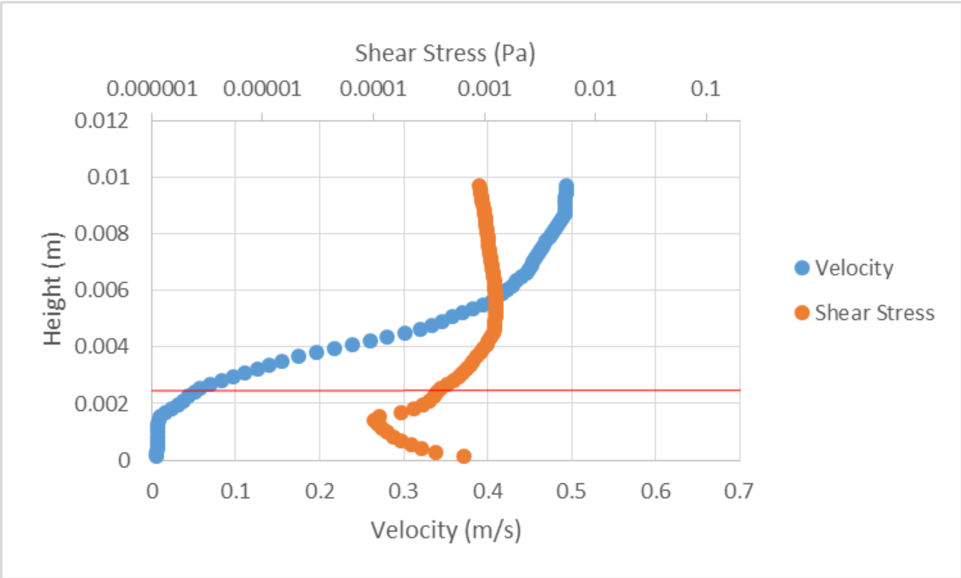

Supplementary Figure C.43 1.24 seconds from flow entering the frame. 100 cm along the flume.

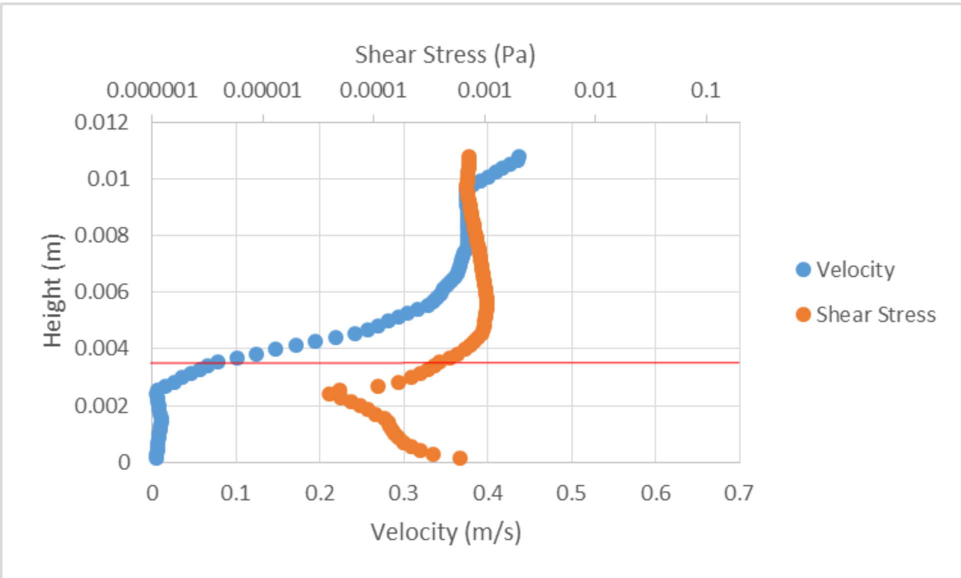

Supplementary Figure C.44 1.24 seconds from flow entering the frame. 102 cm along the flume.

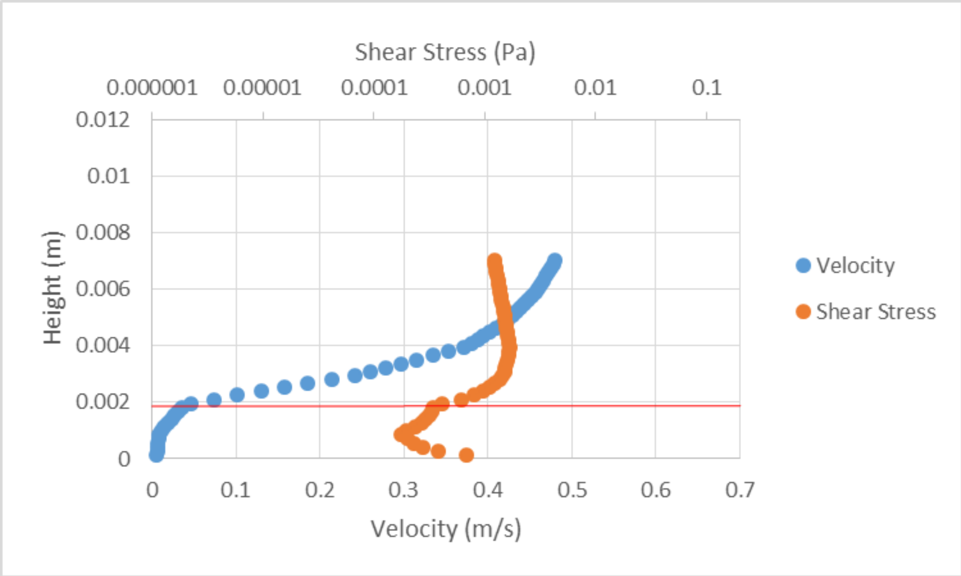

Supplementary Figure C.45 1.18 seconds from flow entering the frame. 98 cm along the flume.

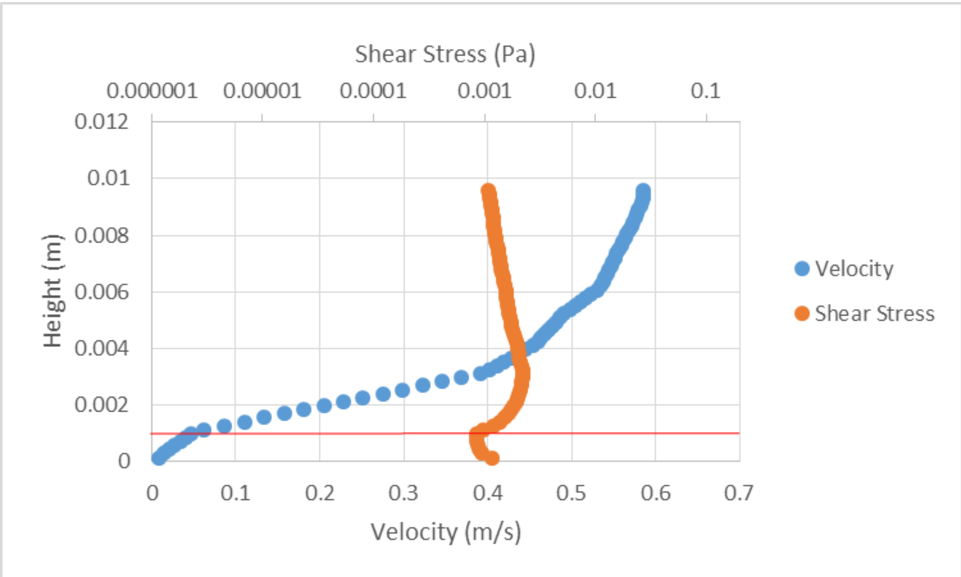

Supplementary Figure C.46 1.18 seconds from flow entering the frame. 100 cm along the flume.

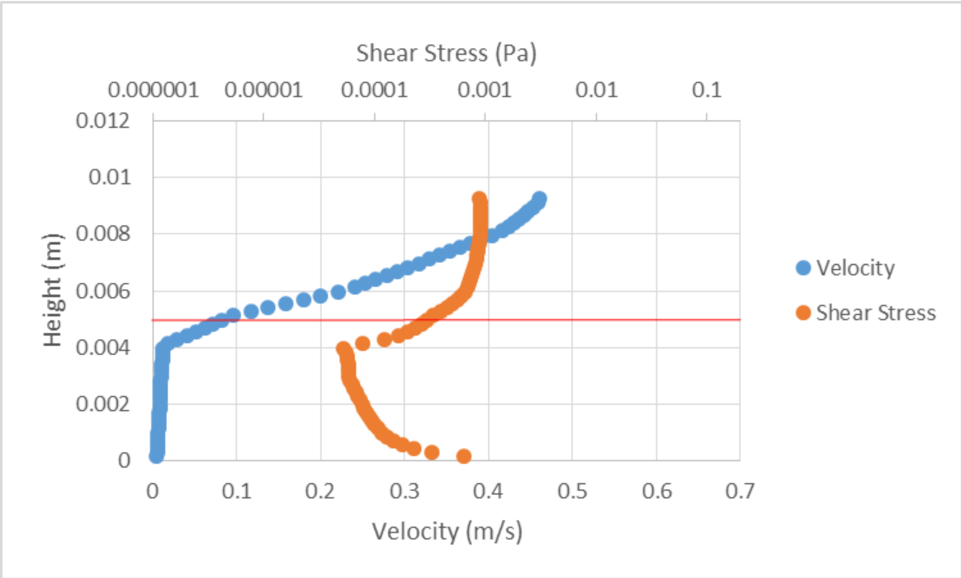

Supplementary Figure C.47 1.18 seconds from flow entering the frame. 102 cm along the flume.

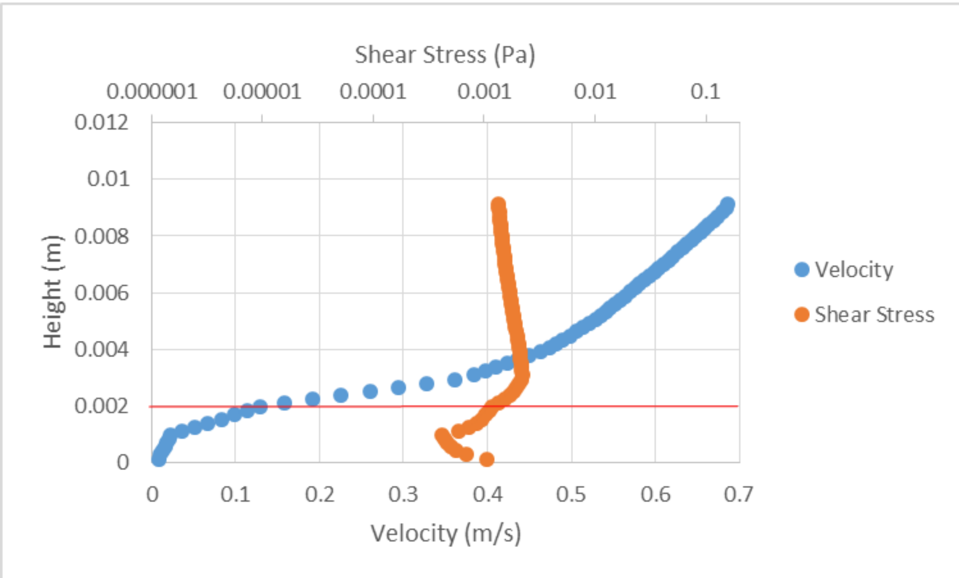

Supplementary Figure C.48 0.699 seconds from flow entering the frame. 100 cm along the flume.

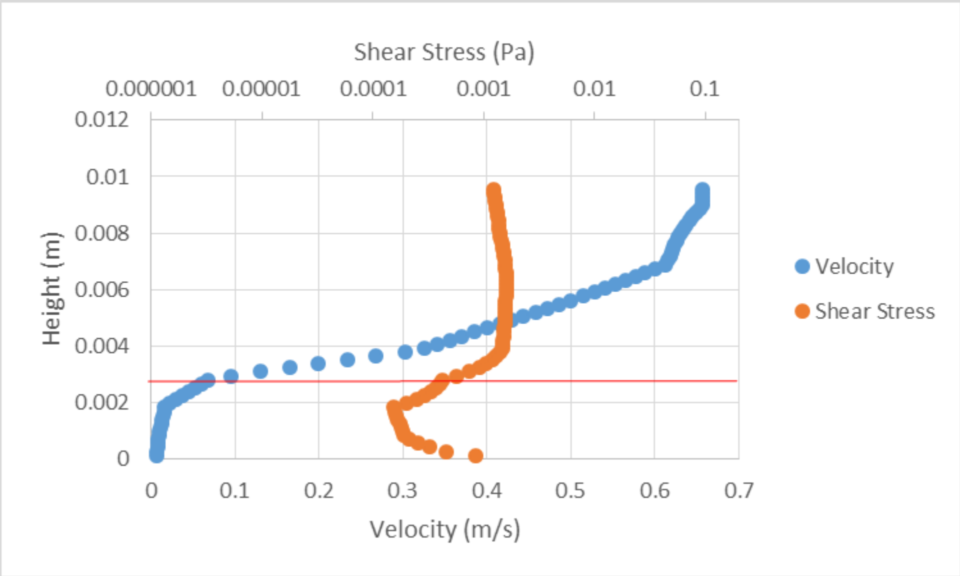

Supplementary Figure C.49 0.699 seconds from flow entering the frame. 102 cm along the flume.

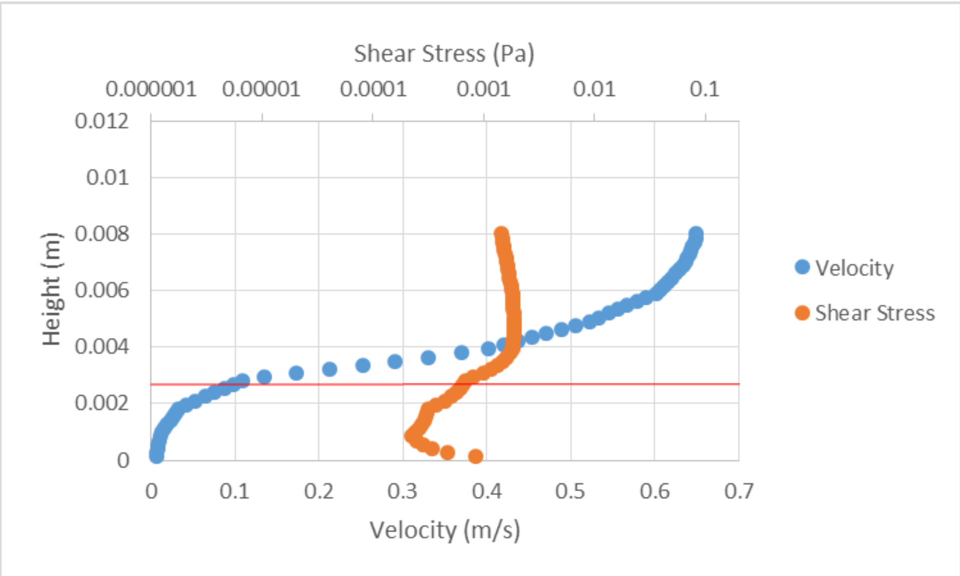

Supplementary Figure C.50 0.93 seconds from flow entering the frame. 98 cm along the flume.

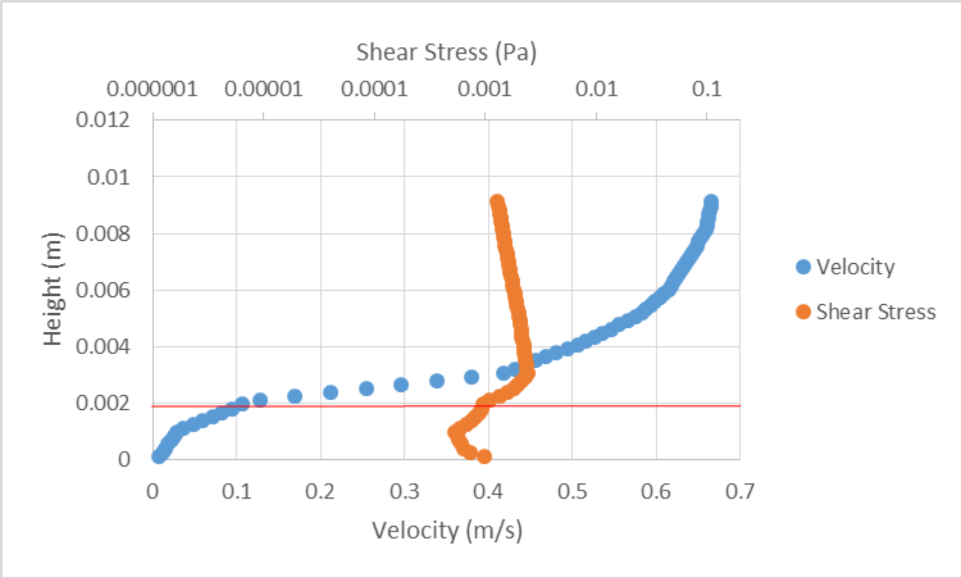

Supplementary Figure C.51 0.93 seconds from flow entering the frame. 100 cm along the flume.

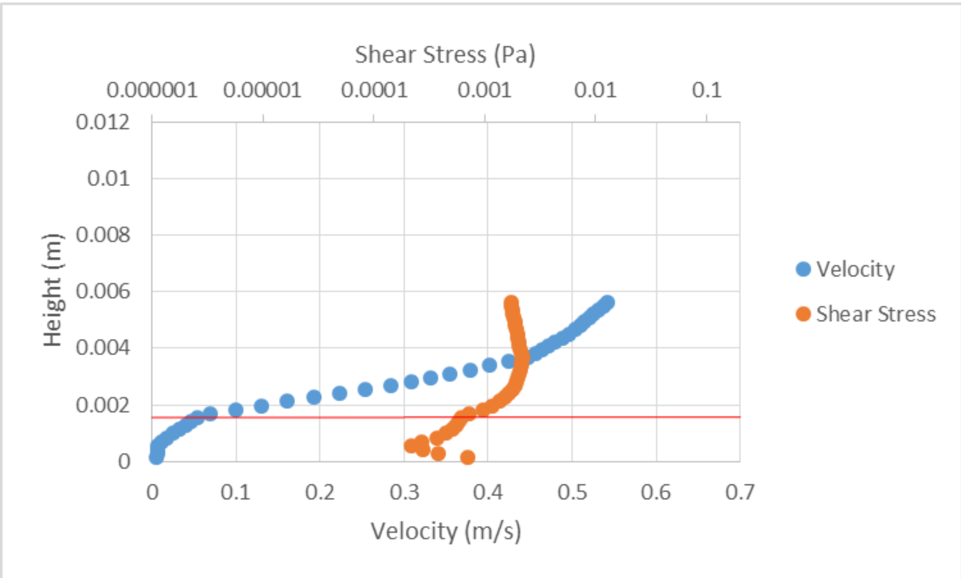

Supplementary Figure C.52 0.93 seconds from flow entering the frame. 102 cm along the flume.

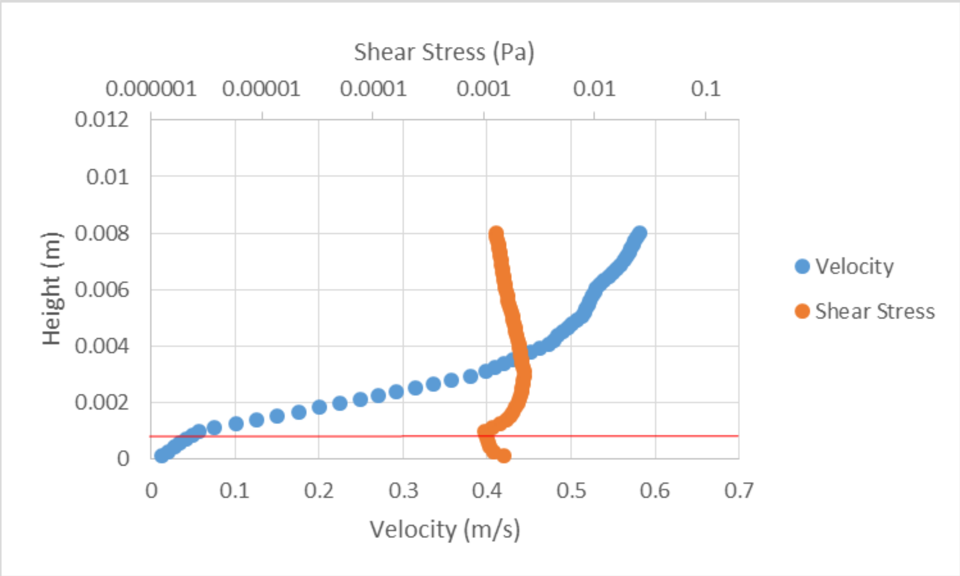

Supplementary Figure C.53 1.06 seconds from flow entering the frame. 98 cm along the flume.

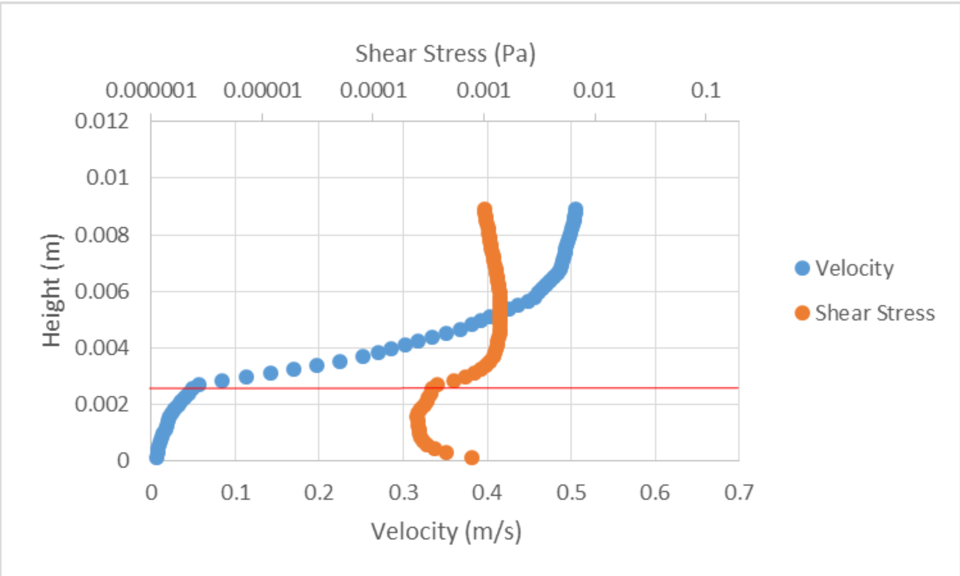

Supplementary Figure C.54 1.06 seconds from flow entering the frame. 100 cm along the flume.

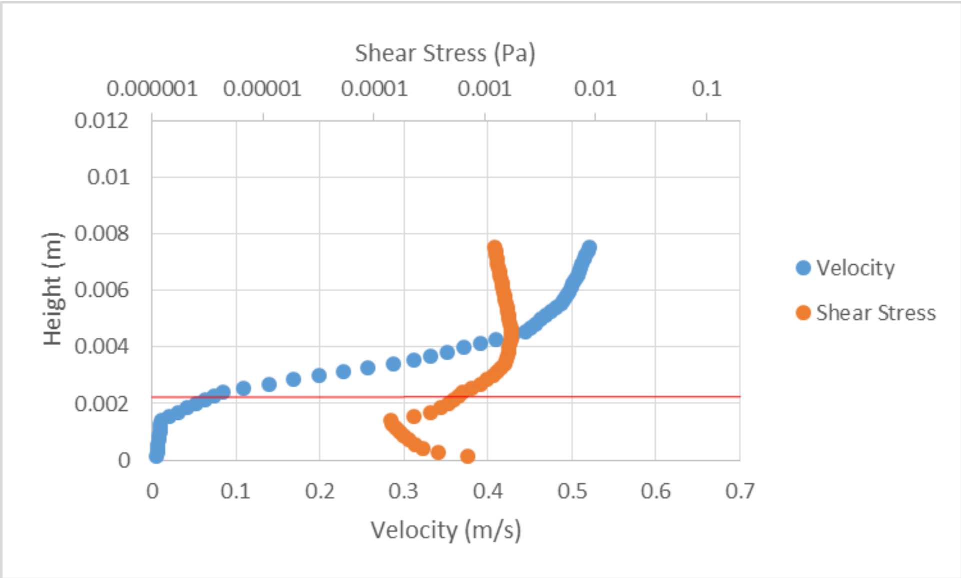

Supplementary Figure C.55 1.06 seconds from flow entering the frame. 102 cm along the flume.

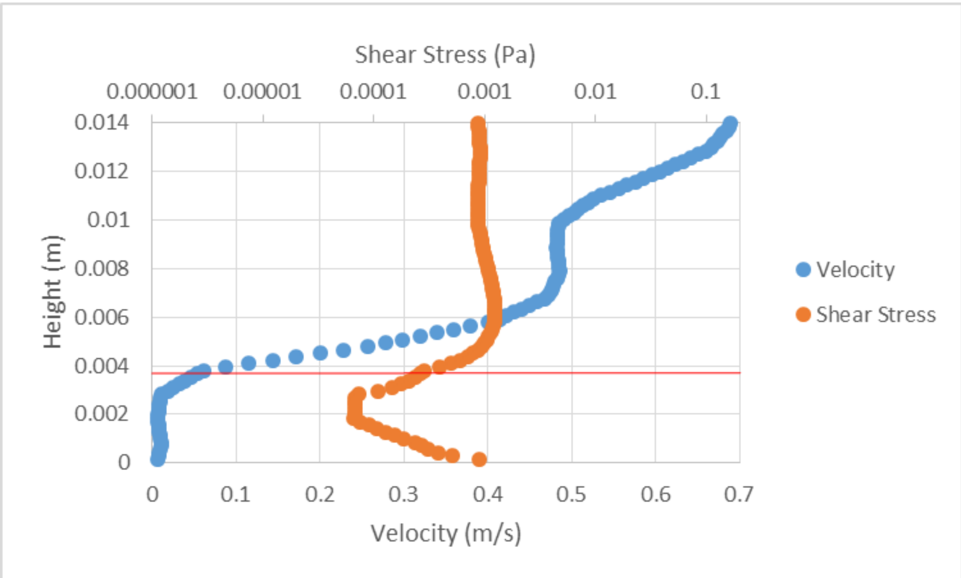

Supplementary Figure C.56 0.824 seconds from flow entering the frame. 98 cm along the flume.

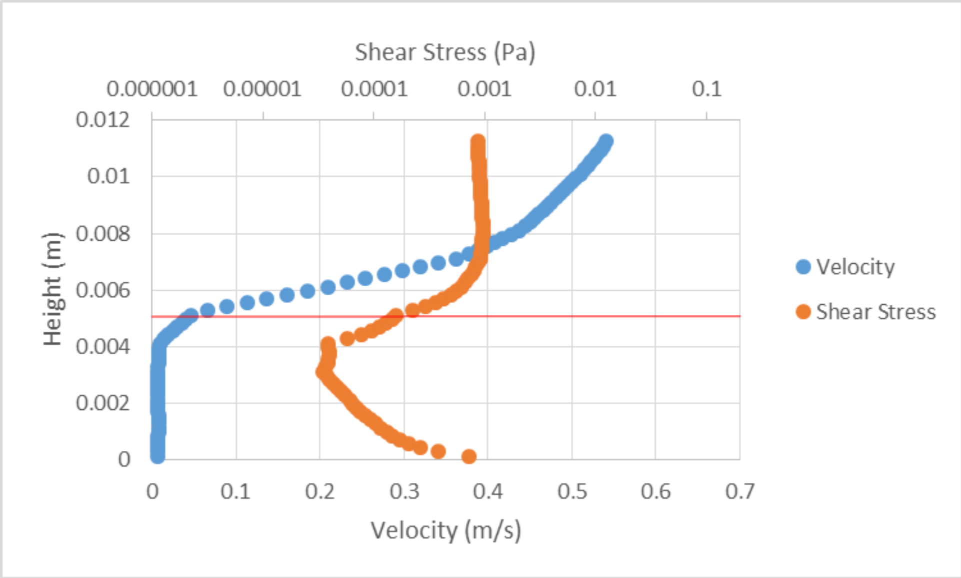

Supplementary Figure C.57 0.824 seconds from flow entering the frame. 100 cm along the flume.

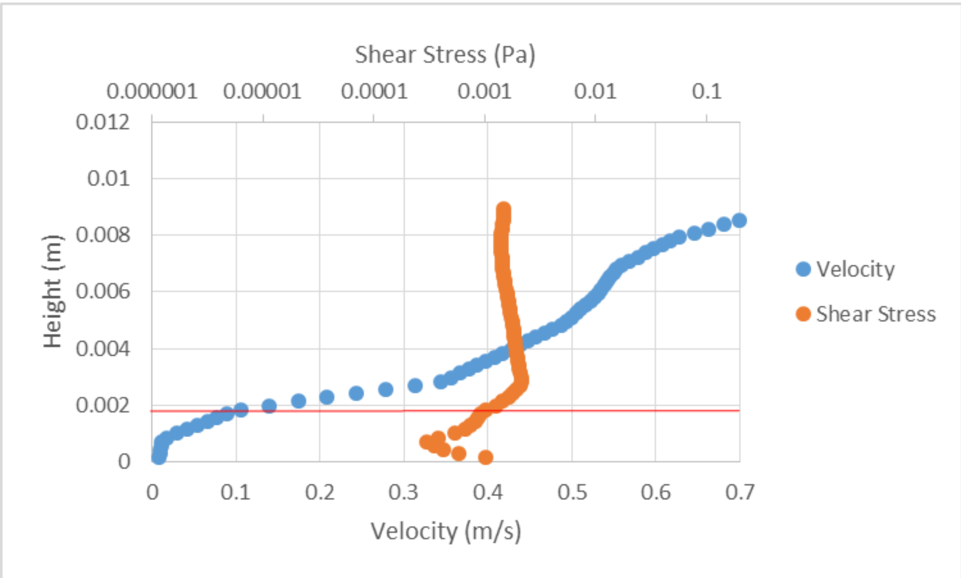

Supplementary Figure C.58 0.824 seconds from flow entering the frame. 102 cm along the flume.

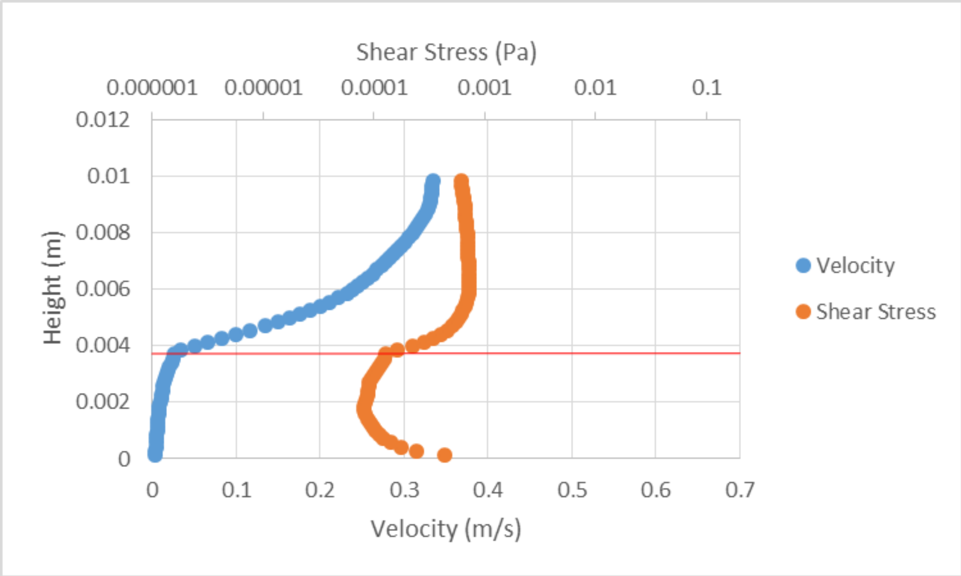

Supplementary Figure C.59 1.49 seconds from flow entering the frame. 98 cm along the flume.

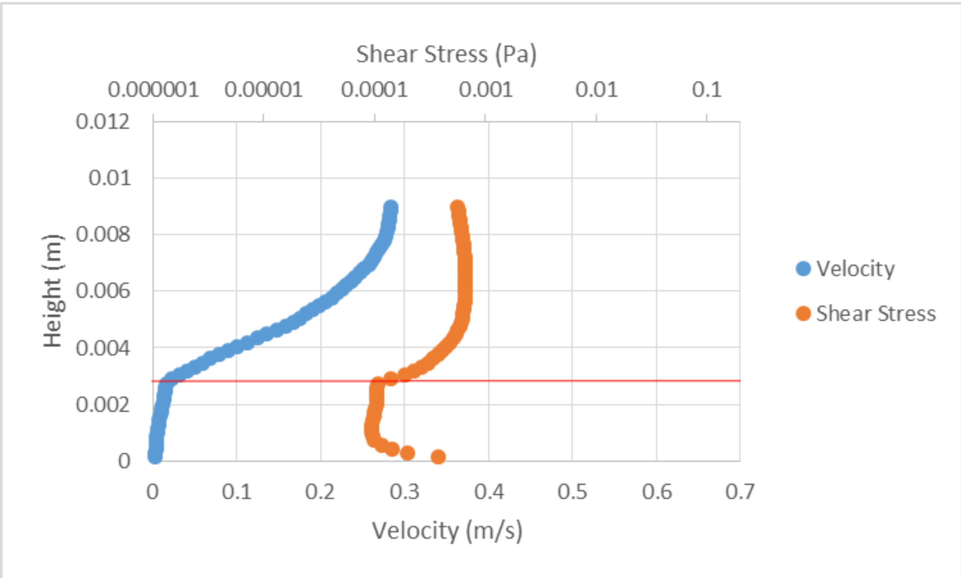

Supplementary Figure C.60 1.49 seconds from flow entering the frame. 100 cm along the flume.

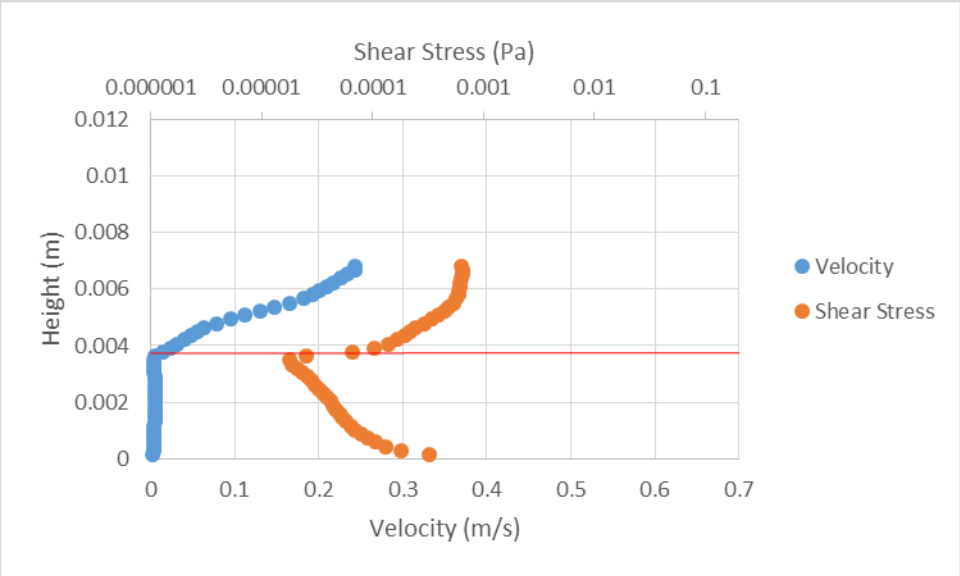

Supplementary Figure C.61 1.49 seconds from flow entering the frame. 102 cm along the flume.

Current depositing steep bedforms velocity and shear stress profiles

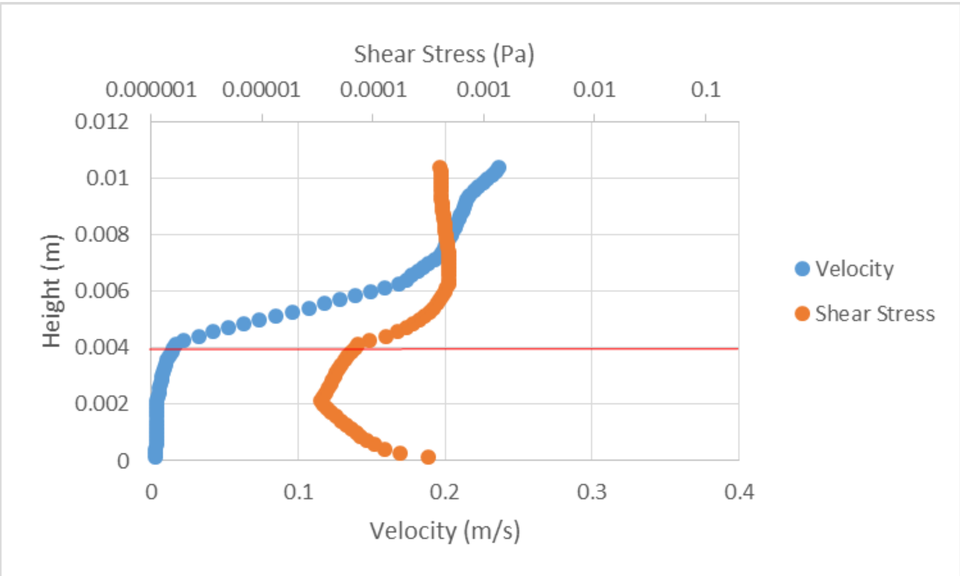

Supplementary Figure C.62 1.68 seconds from flow entering the frame. 96 cm along the flume.

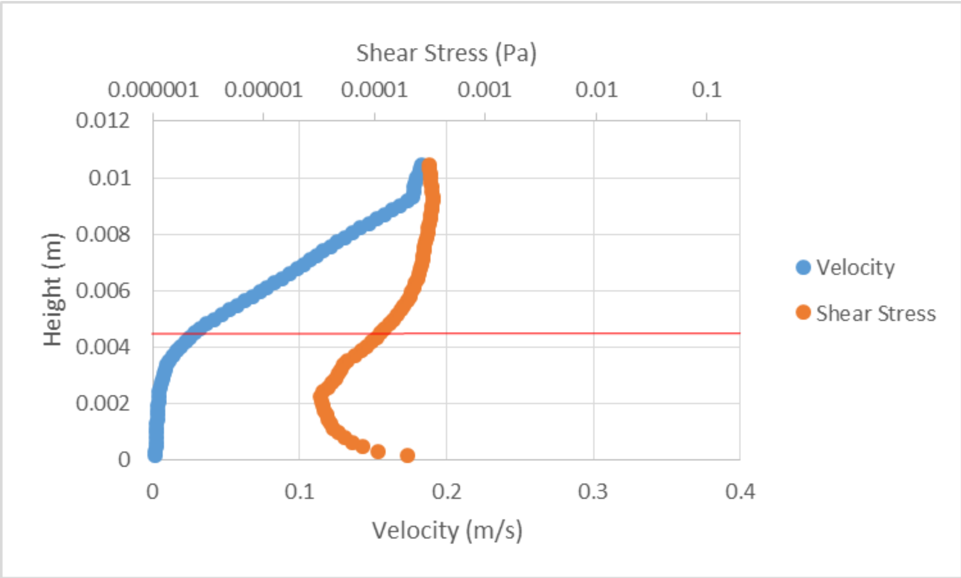

Supplementary Figure C.63 1.68 seconds from flow entering the frame. 98 cm along the flume.

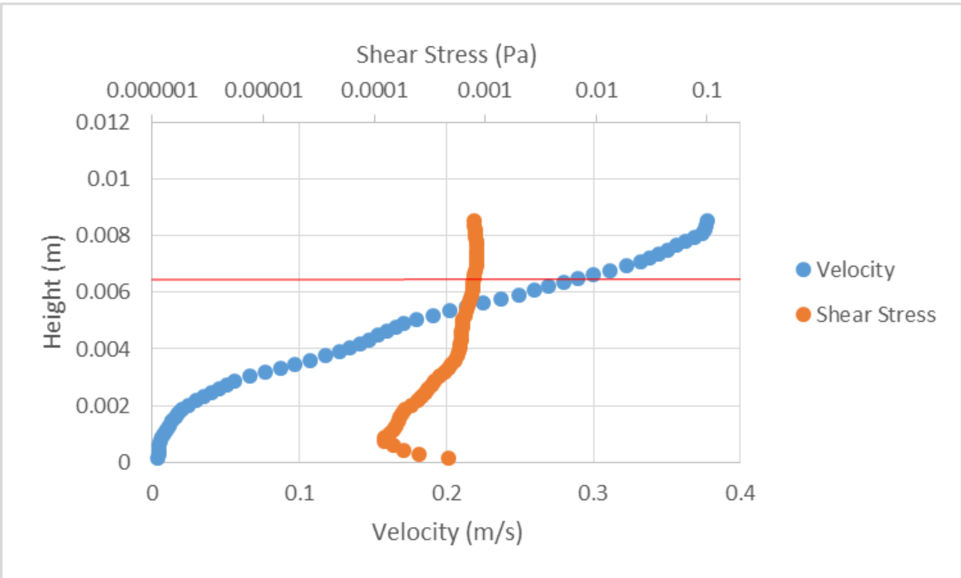

Supplementary Figure C.64 1.64 seconds from flow entering the frame. 96 cm along the flume.

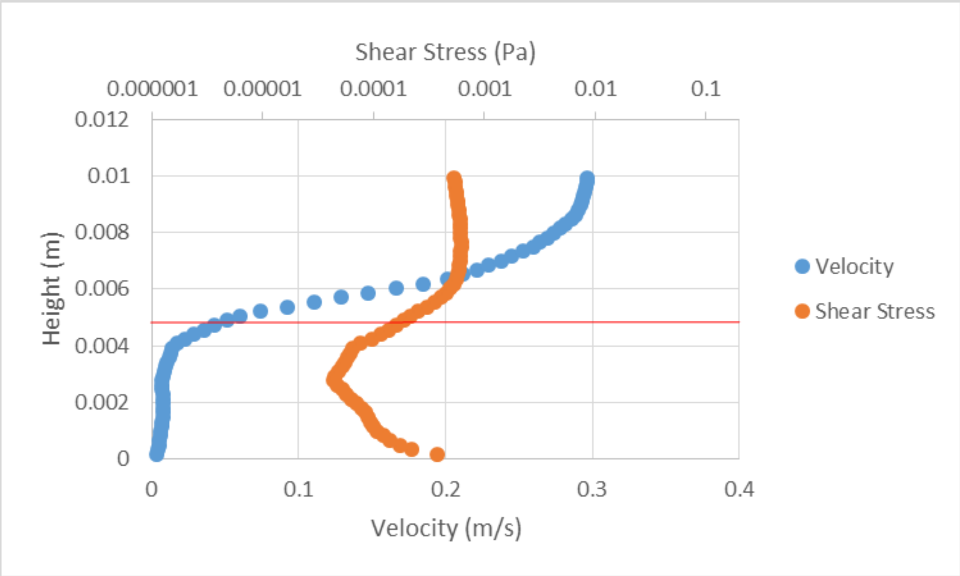

Supplementary Figure C.65 1.64 seconds from flow entering the frame. 98 cm along the flume.

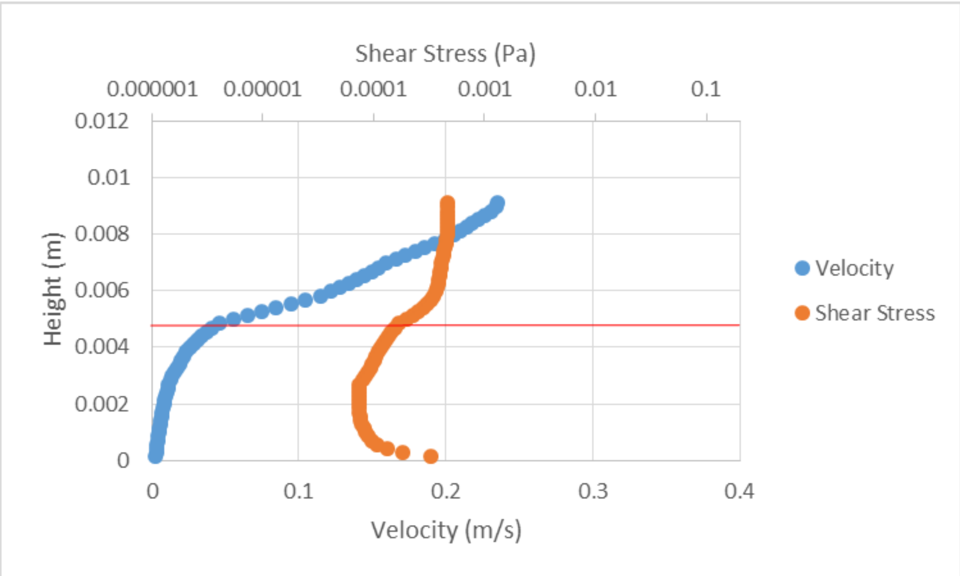

Supplementary Figure C.66 1.71 seconds from flow entering the frame. 96 cm along the flume.

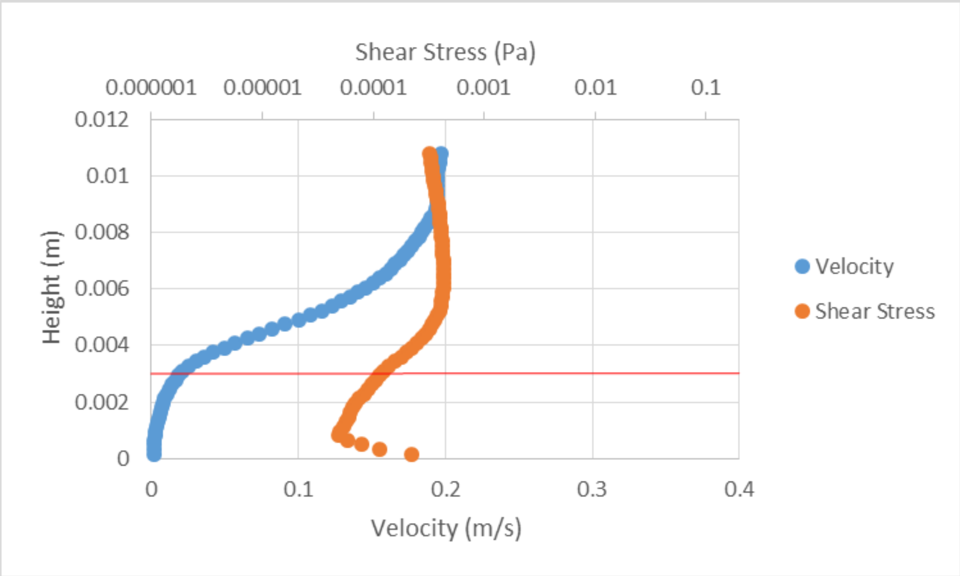

Supplementary Figure C.67 1.71 seconds from flow entering the frame. 98 cm along the flume.

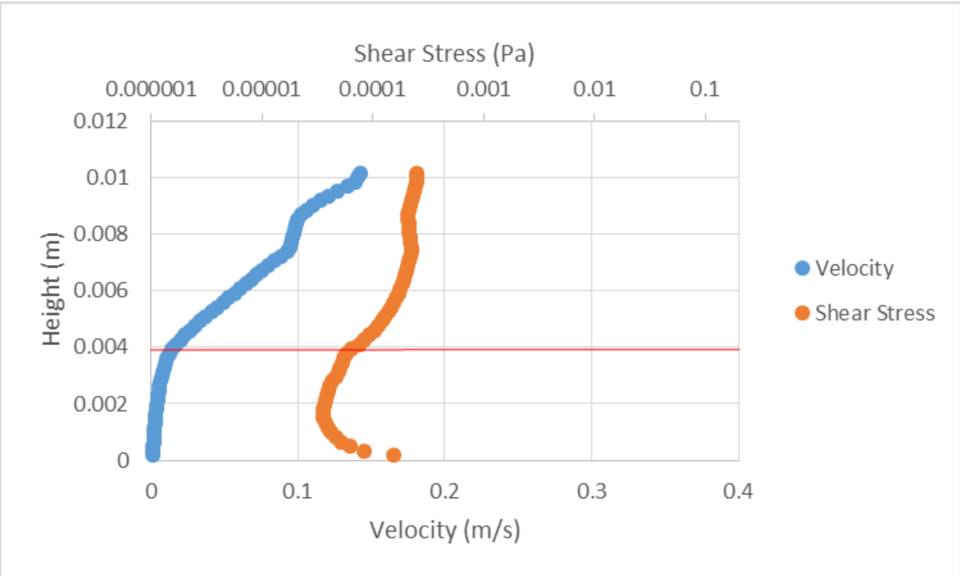

Supplementary Figure C.68 1.77 seconds from flow entering the frame. 96 cm along the flume.

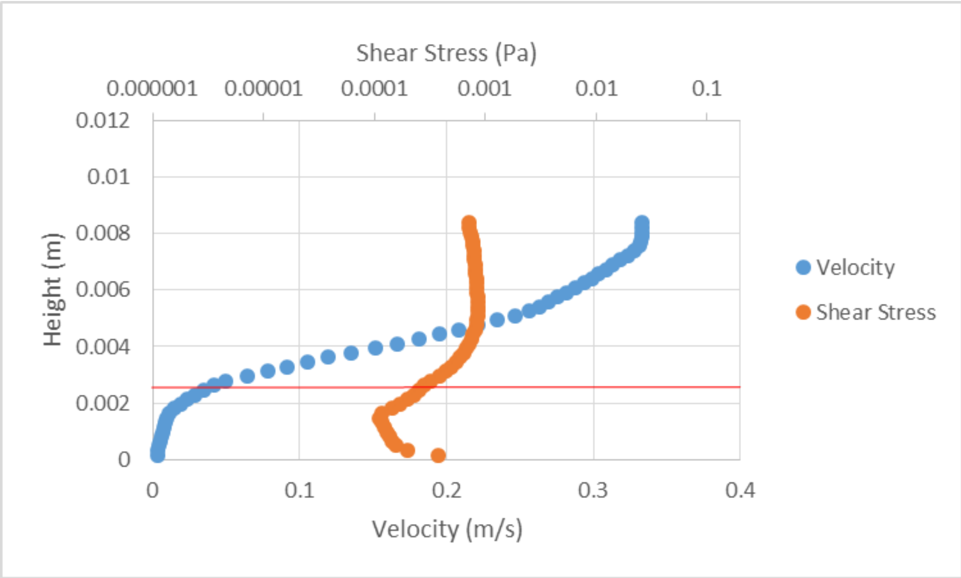

Supplementary Figure C.69 1.62 seconds from flow entering the frame. 98 cm along the flume.

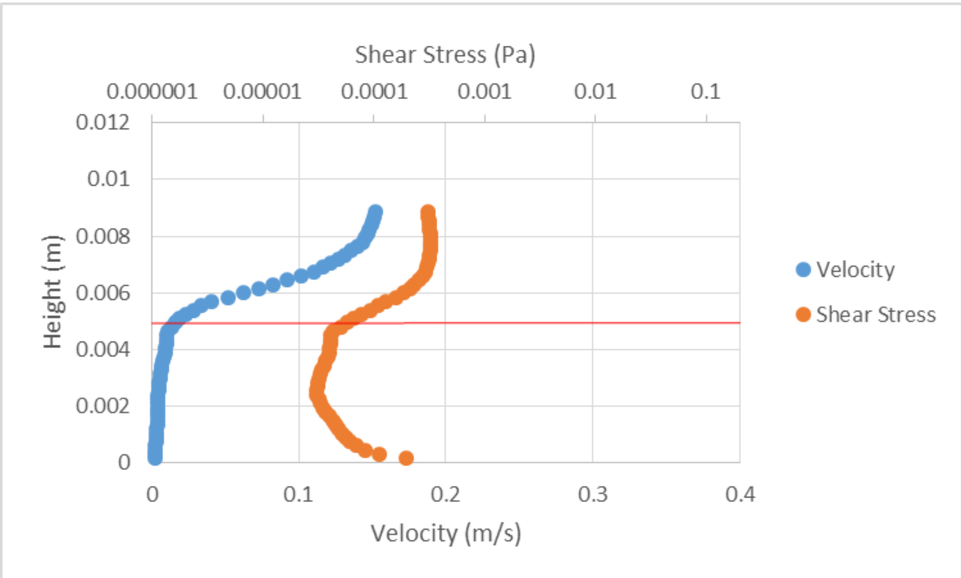

Supplementary Figure C.70 1.62 seconds from flow entering the frame. 100 cm along the flume.

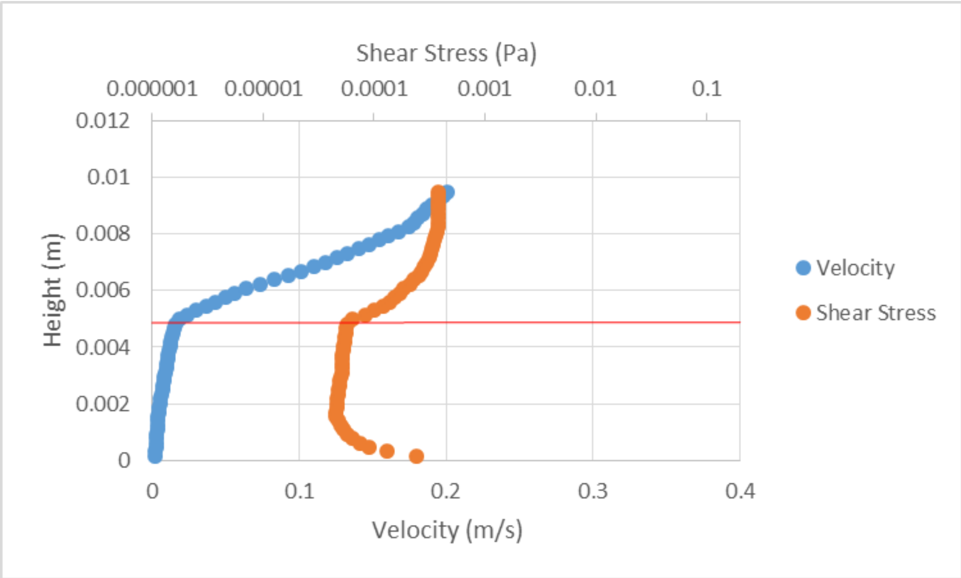

Supplementary Figure C.71 1.74 seconds from flow entering the frame. 96 cm along the flume.

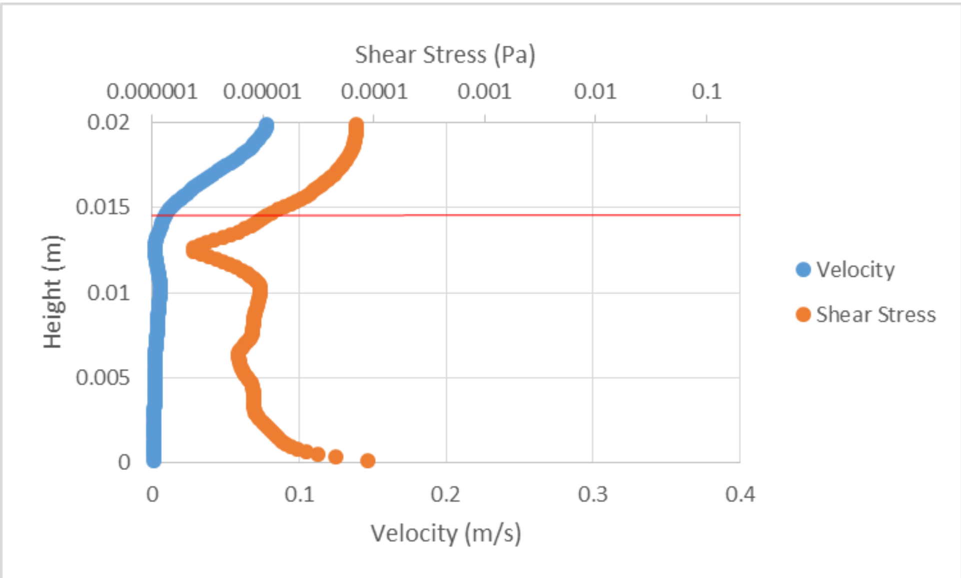

Supplementary Figure C.72 1.74 seconds from flow entering the frame. 96 cm along the flume.

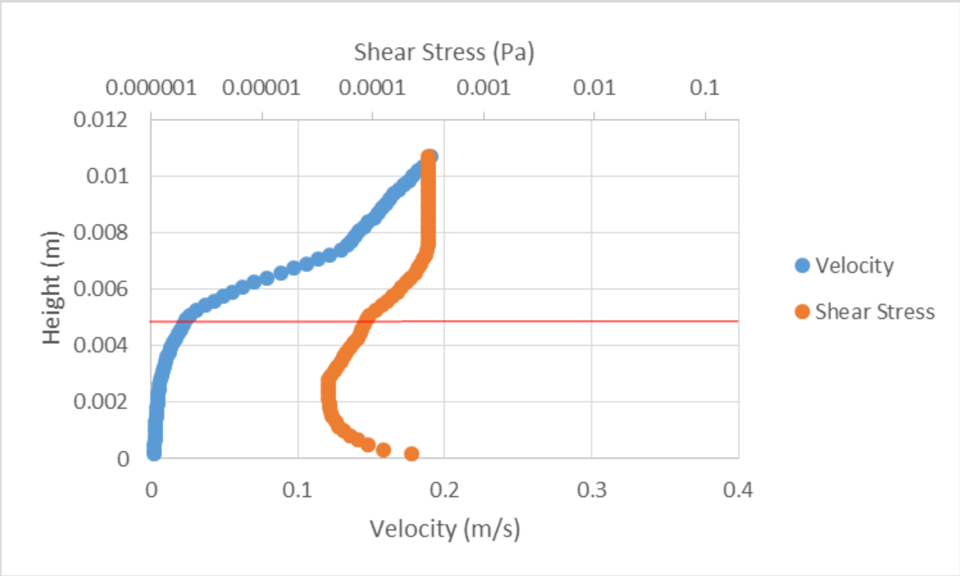

Supplementary Figure C.73 1.76 seconds from flow entering the frame. 96 cm along the flume.

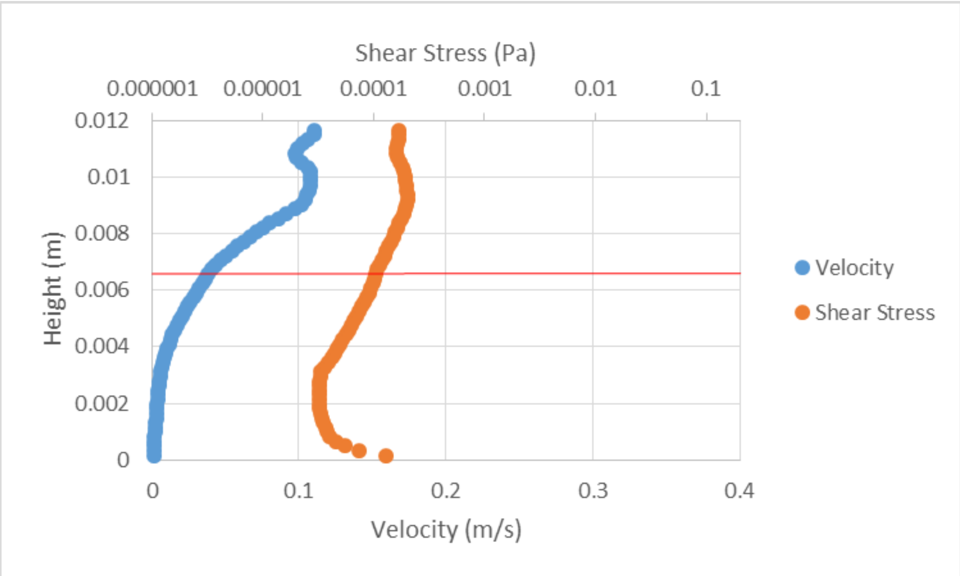

Supplementary Figure C.74 1.79 seconds from flow entering the frame. 96 cm along the flume.

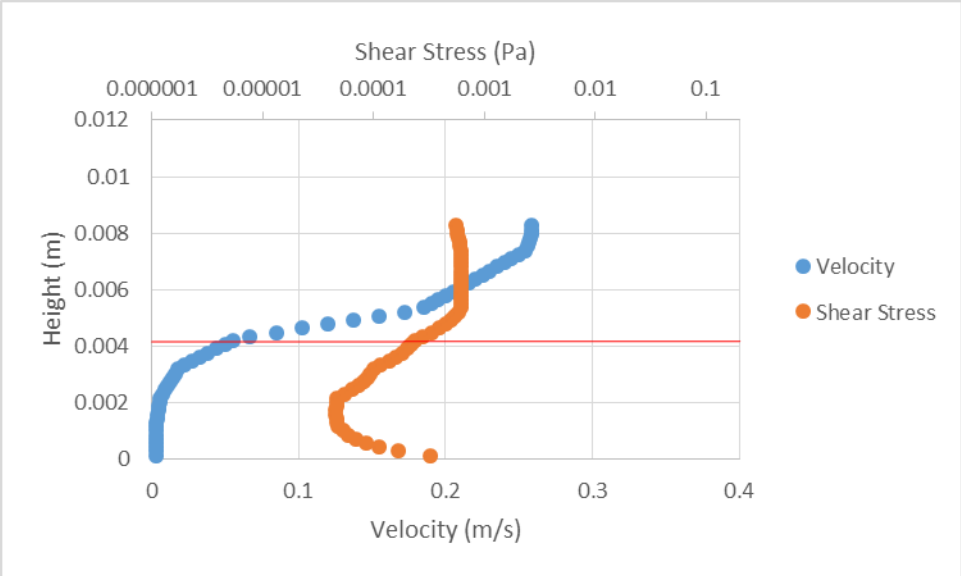

Supplementary Figure C.75 1.66 seconds from flow entering the frame. 96 cm along the flume.

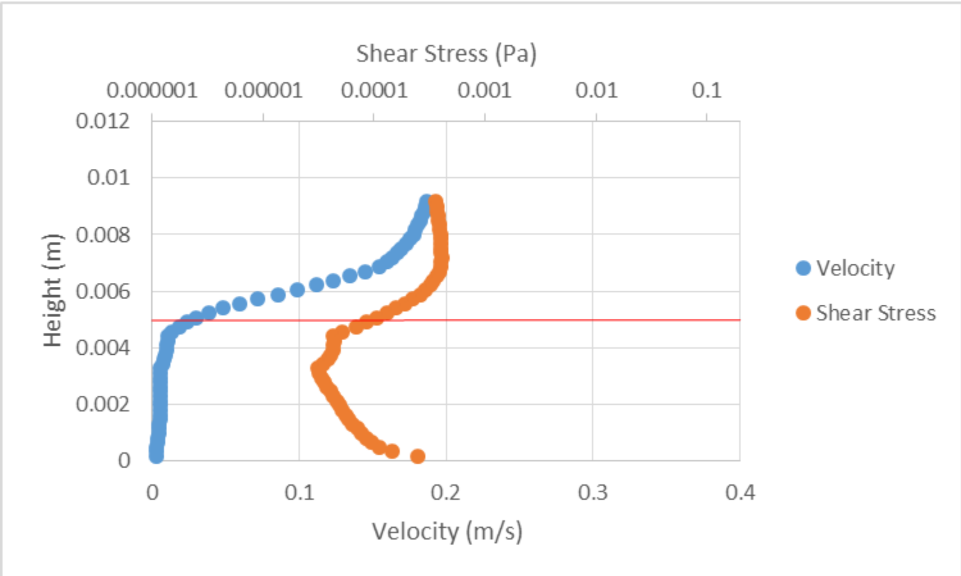

Supplementary Figure C.76 1.66 seconds from flow entering the frame. 98 cm along the flume.

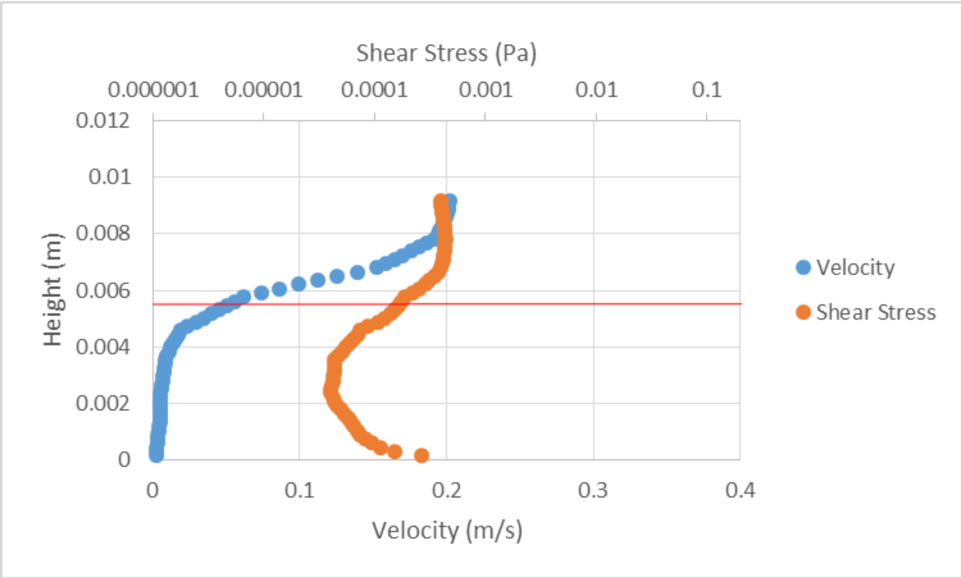

Supplementary Figure C.77 1.69 seconds from flow entering the frame. 96 cm along the flume.

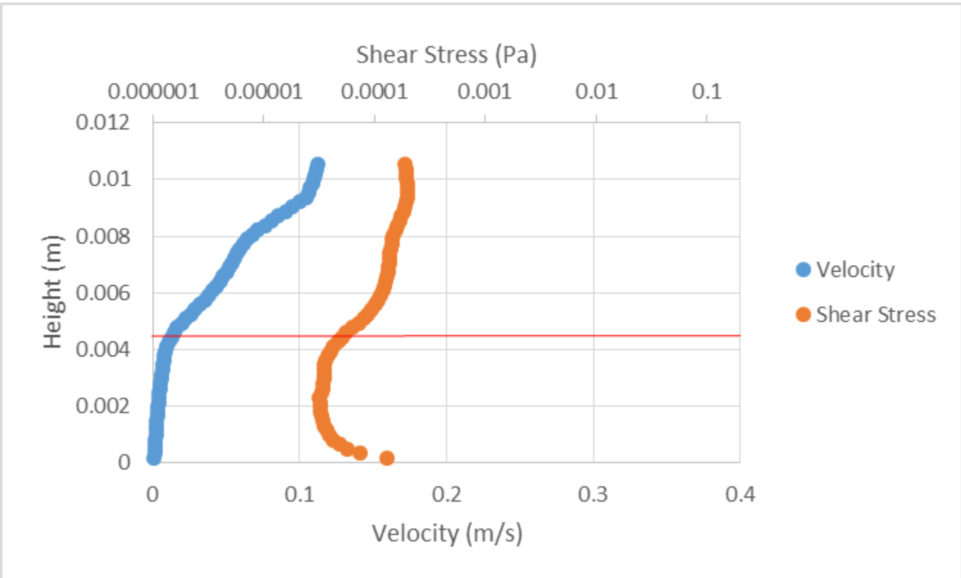

Supplementary Figure C.78 1.69 seconds from flow entering the frame. 98 cm along the flume.

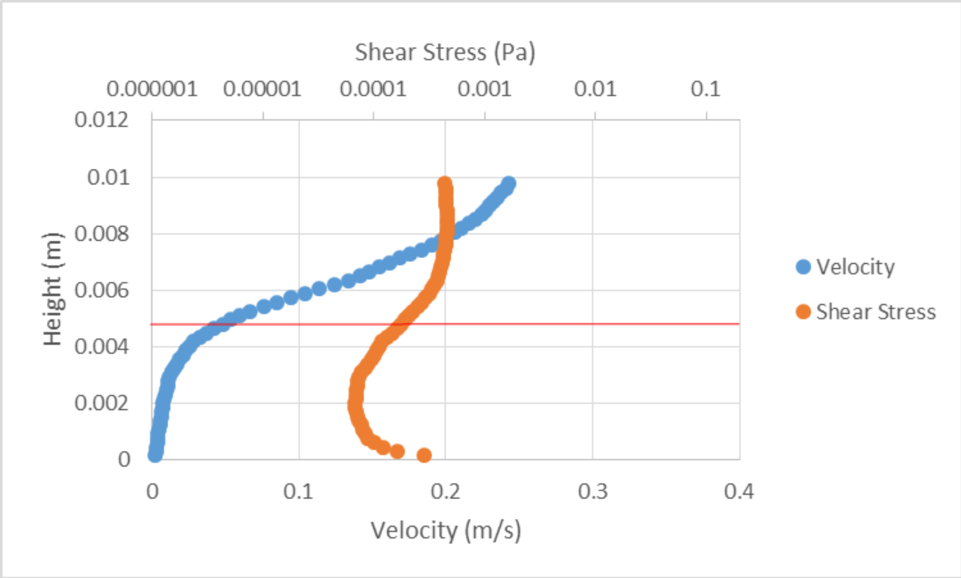

Supplementary Figure C.79 1.72 seconds from flow entering the frame. 96 cm along the flume.

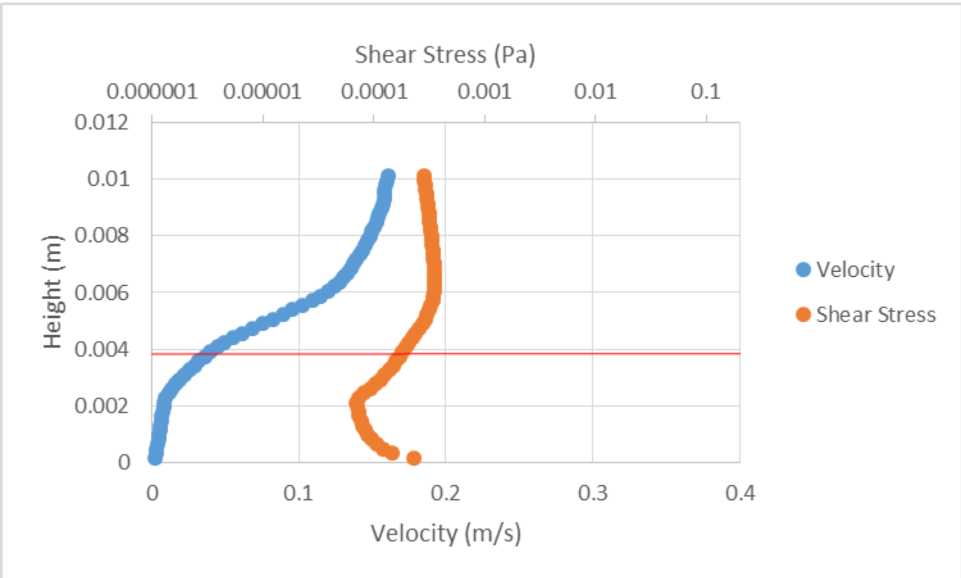

Supplementary Figure C.80 1.72 seconds from flow entering the frame. 98 cm along the flume.

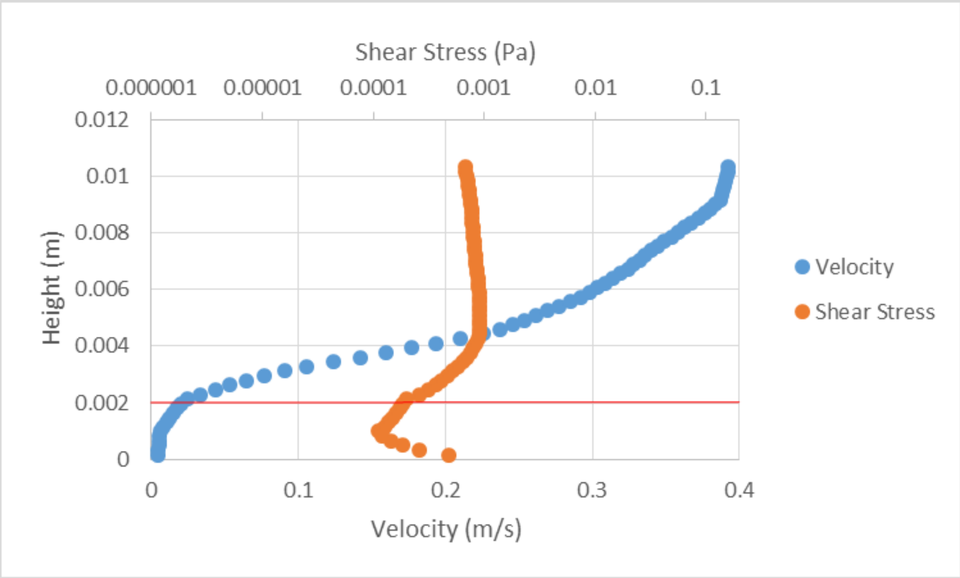

Supplementary Figure C.81 1.63 seconds from flow entering the frame. 98 cm along the flume.

==

Appendix D – Supplementary Material for Chapter 6

==

Supplementary Table D.1 Characteristics of backset bedforms in PDC deposits from the literature. Subscript h describes angles measured from the horizontal, otherwise angles have been measured from a depositional surface. (A) denotes apparent dip, otherwise angles are assumed to be true dip. Particularly in the case of “chute-and-pool” structures lee-side lamina are absent/not reported. Generally, bedform length and thickness are reported as opposed to wavelength and amplitude; where sources include the latter two they are denoted with * and + respectively. Black text denotes values taken from other author’s tables, text or plots. Blue text denotes values measured from other authors’ field photographs. Green text denotes values from this author’s own fieldwork.

Author	Location	Name in source	$Stoss_h$	Lee_h	$Stoss_h$ (A)	Lee_h (A)	Stoss (Range)	Lee (Range)	Stoss	Lee	Stoss (A)	Lee (A)	Length (Range)	Thickness (Range)	Length (m)	Thickness (m)	Aspect Ratio	Dep. Surface (°)	Distance from vent	Data Source	Figure in chapter
		Elongate Dune Bedform (mean)	17.6	24.1											7.4	0.55	0.074		"Proximal"	Table 1, text	
		Transverse DB (mean)	25.2	21.7											5.3	0.61	0.115		"Distal"		
		Lunate DB (mean)	24	22.4											5.2	0.51	0.098				
		Elongate DB	5	25															"Proximal"		
			10	30																	
			10	28																	
			10	26																	
			10	24																	
			10	20																	
			15	28																	
			15	22																	
			20	24																	
			20	15																	
			24	28																	
			26	15																	
			30	25																	
			35	35																	
		Transverse DB	12	24																	
			12	20																	
			14	24																	
			14	18																	
			15	26																	
			16	28																	
			18	28																	
			18	26																	
			18	20																	
			20	25																	
			22	32																	
			22	28																	
			22	20																	
			22	17																	
			22	16																	
			22	15																	
			24	21																	
			24	20																	
			24	18																	
			24	15																	
			24	12																	
			25	30																	
			25	20																	
			25	18																	
			26	30																	
			26	28																	
			26	26																	
			26	22																	
			26	21																	
			26	20																	
			28	34																	
			28	32																	
			28	30																	
			28	28																	
			28	26																	
			28	25																	
			28	24																	
			28	22																	
			28	20																	
			28	18																	
			28	16																	
			28	10																	
			28	1																	
			29	20																	
			30	32																	
			30	26																	
			30	25																	

4430

Author	Location	Name in source	$Stoss_h$	Lee_h	$Stoss_h$ (A)	Lee_h (A)	Stoss (Range)	Lee (Range)	Stoss	Lee	Stoss (A)	Lee (A)	Length (Range)	Thickness (Range)	Length (m)	Thickness (m)	Aspect Ratio	Dep. Surface (°)	Distance from vent	Data Source	Figure in chapter
Douillet et al. 2013	Tungurahua		30	24														10-25	"Distal"	Figure 3c, text	
			30	22																	
			30	20																	
			30	18																	
			30	14																	
			30	8																	
			32	26																	
			32	24																	
			32	22																	
			32	16																	
			32	15																	
			32	14																	
			35	28																	
			35	22																	
			35	18																	
			35	8																	
		Lunate DB	5	30																	
			10	30																	
			10	24																	
			10	22																	
			10	20																	
			12	24																	
			12	22																	
			15	31																	
			15	22																	
			15	20																	
			16	20																	
			16	18																	
			18	24																	
			18	22																	
			18	20																	
			18	18																	
			18	16																	
			18	5																	
			20	21																	
			20	18																	
			20	16																	
			20	10																	
			22	30																	
			22	28																	
			22	25																	
			22	22																	
			22	20																	
			24	32																	
			24	30																	
			24	24																	
			24	18																	
			26	28																	
			26	26																	
			26	24																	
			26	22																	
			26	20																	
			26	15																	
			28	32																	
			28	28																	
			28	26																	
			28	24																	
			28	20																	
			28	19																	
			28	18																	
			28	17																	
			28	16																	
			28	14																	
			29	22																	

4431

Author	Location	Name in source	Stoss$_h$	Lee$_h$	Stoss$_h$ (A)	Lee$_h$ (A)	Stoss (Range)	Lee (Range)	Stoss	Lee	Stoss (A)	Lee (A)	Length (Range)	Thickness (Range)	Length (m)	Thickness (m)	Aspect Ratio	Dep. Surface (°)	Distance from vent	Data Source	Figure in chapter
			30	32																	
			30	26																	
			30	22																	
			30	20																	
			30	12																	
			32	26																	
			32	24																	
			32	22																	
			33	22																	
			34	22																	
			34	20																	
			34	18																	
			35	22																	
			35	20																	
Crowe & Fisher 1973*	Ubehebe	Dunelike Structures	6	12					14	4					1.1	0.05	0.045	-6-20	0.8-1 km	Table 3, text	
			2	17					10	9					1.1	0.06	0.055				
			0	19					8	11					1.4	0.07	0.050				
			6	10					13	3					1.3	0.07	0.054				
			3	11					10	4					1.3	0.07	0.054				
			9	10					14	5					0.7	0.05	0.071				
			10	10					13	7					0.75	0.05	0.067				
			6	12					11	7					0.65	0.04	0.062				
			9	13					10	12					0.55	0.06	0.109				
			4	12					4	12					0.6	0.05	0.083				
			14	9					14	9					0.6	0.06	0.100				
			2	14					7	9					0.7	0.04	0.057				
			3	15					8	10					0.85	0.05	0.059				
				7						13						0.06					
			18	3					12	9						0.06					
			16	11					23	4					1.05	0.08	0.076				
			15	8					22	1					1.3	0.08	0.062				
			8	14					15	7					1.05	0.08	0.076				
			8	7					12	3					1.55	0.08	0.052				
			6	6					10	2					1.1	0.07	0.064				
			8	5					10	3					0.65	0.06	0.092				
		Dunes													1.8	0.15	0.083		0.8 km	Table 2	
															1.8	0.2	0.111				
															1.2	0.1	0.083				
															1.1	0.138	0.125				
															1.8	0.2	0.111				
															1.1	0.075	0.068				
															1.8	0.15	0.083				
															1.2	0.1	0.083				
															1.8	0.125	0.069				
															1.5	0.123	0.082				
															1.2	0.1	0.083				
															1.4	0.125	0.089				
															1.5	0.123	0.082				
															1.5	0.213	0.142				
															2.1	0.238	0.113				
															0.33	0.032	0.097				
															0.3	0.035	0.117				
															0.37	0.043	0.116				
															0.82	0.063	0.077				
															0.54	0.052	0.096				
															1.5	0.155	0.103				
															0.47	0.024	0.051				
Waters & Fisher 1971*	Capelinhos	Thin base-surge beds			84.5														0.7 km	Figure 17	6.4
					53																
	Taal	Dune	9	20.5															2 km	Figure 25	6.3
		Antidunes													11.5	2	0.174		0.75 km	Table 1	
															9	1	0.111		1 km		
															5.5	0.7	0.127		1.5 km		
															4	0.5	0.125		2 km		

Author	Location	Name in source	$Stoss_h$	Lee_h	$Stoss_h$ (A)	Lee_h (A)	Stoss (Range)	Lee (Range)	Stoss	Lee	Stoss (A)	Lee (A)	Length (Range)	Thickness (Range)	Length (m)	Thickness (m)	Aspect Ratio	Dep. Surface (°)	Distance from vent	Data Source	Figure in chapter
Schmincke et al. 1973*	Laacher See	Chute-and-pool structures									49	13							2.8 km	Figure 5	6.5
											51.5	13									
		Chute-and-pool structures			26.5														2.75 km	Figure 3	6.6
					24																
					25																
					30																
					36.5																
		Chute-and-pool structure			25	0													2.75 km	Figure 6	6.7
		Chute-and-pool structures							29.5										2.9 km	Figure 8	6.8
											35										
		Antidune									14	6.5							2.75 km	Figure 10	6.9
		Antidune	24.5	11.5											2.1	0.32	0.152		2.75 km	Figure 11	6.10
		Dunes, Antidunes, Chute and Pool structures													2	0.2	0.100			Figure 15	
															4	0.25	0.063				
															10.8	0.46	0.043				
															17.8	0.5	0.028				
															16.7	0.5	0.030				
															13.7	0.5	0.036				
															10.7	0.5	0.047				
															8.9	0.5	0.056				
															7	0.5	0.071				
															16.8	0.56	0.033				
															14.5	0.6	0.041				
															9.8	0.6	0.061				
															13.6	0.71	0.052				
															10.3	0.71	0.069				
															15.6	0.82	0.053				
															13.8	0.82	0.059				
															10.8	0.8	0.074				
															7.8	0.81	0.104				
															21.4	1	0.047				
															16.6	1	0.060				
															11.7	1	0.085				
															9.6	1	0.104				
															13.6	1.3	0.096				
															15.5	1.5	0.097				
															21.6	1.8	0.083				
															16.7	2	0.120				
Mattson & Alvarez 1973*[+]	Baccano Crater (Roman Volcanic Province)	Antidune			25	16.5												5	Crater Rim	Figure 3, text	6.12
		Symmetrical Dune Form													4.5	0.32	0.071			Table 1	
		Asymmetrical Dune Form													6	0.3	0.050				
		Symmetrical Dune Form													2	0.1	0.050				
		Asymmetrical Dune Form													20	1.25	0.063				
		Symmetrical Dune Form													15	1.5	0.100				
		Symmetrical Dune Form													28	2	0.071				
		Asymmetrical Dune Form													16	1	0.063				
		Asymmetrical Dune Form													5	0.5	0.100				
		Symmetrical Dune Trough													22	2	0.091				
	Martignano Crater (RVP)	Antidune									18.5	7			9	0.5	0.056		2.3 km	Figure 7, text	6.13
											17.5	20			9	0.5	0.056				
	Vico Crater (RVP)	Asymmetrical Dune Forms													2.8	1.15	0.411			Table 1	
															7	0.65	0.093				
	Bolsena Crater (RVP)														6	1.12	0.187				
															3.3	0.2	0.061				
															4.2	1.35	0.321				
											11	8			0.33	0.04	0.121				
											24	8			0.5	0.2	0.400				
											37	4			1.3	0.25	0.192				
											4	10			4	1	0.250				
											8	12			1.5	0.4	0.267				
											15	7			1	0.2	0.200				
											1	17			0.4	0.04	0.100				
											12	11			4	0.9	0.225				
											14	11			2	0.3	0.150				

4433

Author	Location	Name in source	$Stoss_h$	Lee_h	$Stoss_h$ (A)	Lee_h (A)	Stoss (Range)	Lee (Range)	Stoss	Lee	Stoss (A)	Lee (A)	Length (Range)	Thickness (Range)	Length (m)	Thickness (m)	Aspect Ratio	Dep. Surface (°)	Distance from vent	Data Source	Figure in chapter
Giannetti & Luongo 1994*	Roccamonfina	Dune-like Structures									8	8			0.8	0.05	0.063		Within 1 km of 3 source vents	Table 1	
											11	6			0.5	0.04	0.080				
											12	4			1	0.6	0.600				
											11	18			5	0.82	0.164				
											4	20			8	1	0.125				
											5	14			6	0.45	0.075				
											18	21			4	0.4	0.100				
											9	19			3	0.35	0.117				
											7	17			2	0.2	0.100				
											13	10			1.5	0.2	0.133				
											18	4									
											7	12			2	0.3	0.150				
											12	11			5	0.7	0.140				
											15	9			7	1	0.143				
											11	14			7	1	0.143				
											8	14			9	1.5	0.167				
											13	8			8	1	0.125				
											17	4			5	0.3	0.060				
											10	11			0.8	0.08	0.100				
											28	16			1.8	0.2	0.111				
											11	8			2.5	0.28	0.112				
											25	0			4	0.5	0.125				
											4	8			4	0.4	0.100				
											6	12			3	0.2	0.067				
											20	8			1.2	0.14	0.117				
											28	8			3						
											1	6			5	0.7	0.140				
											16	4			0.5	0.1	0.200				
											21	13			5	0.5	0.100				
											14	13			5	1	0.200				
											2	10			3.5	0.25	0.071				
											7	8			6	0.4	0.067				
											39	18			3	1	0.333				
											13	1			10	2	0.200				
											4	0			0.7	0.1	0.143				
											10	8			2	0.3	0.150				
											9	13			5	1	0.200				
											1	14			1	0.1	0.100				
											16	11			2	0.2	0.100				
											2	12			4	0.4	0.100				
											13	12			4	0.6	0.150				
											14	9			4	0.4	0.100				
											10	10			5	0.7	0.140				
											10	14			1	0.15	0.150				
											8	0			0.3	0.15	0.500				
											33	16			0.4	0.16	0.400				
											18	3			0.4	0.15	0.375				
											10	30			0.4	0.1	0.250				
											1	11			1	0.1	0.100				
											5	8			0.3	0.05	0.167				
											13	6			0.5	0.2	0.400				
											12	13			1.8	0.21	0.117				
											23	10			1.4	0.2	0.143				
											5	12			1.2	0.2	0.167				
											12	8			2	0.3	0.150				
											7	13			3	0.15	0.050				
											13	18			1.5	0.3	0.200				
											16	6			1.5	0.3	0.200				
											1	15			5	0.5	0.100				
											17	4									
											18	6			3	0.6	0.200				
											10	24			2.5	0.25	0.100				
											3	10			1.5	0.2	0.133				
											2	13			1.5	0.3	0.200				

4434

Author	Location	Name in source	$Stoss_h$	Lee_h	$Stoss_h$ (A)	Lee_h (A)	Stoss (Range)	Lee (Range)	Stoss	Lee	Stoss (A)	Lee (A)	Length (Range)	Thickness (Range)	Length (m)	Thickness (m)	Aspect Ratio	Dep. Surface (°)	Distance from vent	Data Source	Figure in chapter
											9	18			8	1.5	0.188				
											18	14			3	0.6	0.200				
											8	8			1.5	0.3	0.200				
											28	11			1.5	0.25	0.167				
											31	11			1.5	0.3	0.200				
											8	2			3.5	0.35	0.100				
											12	8									
											40	9			3	0.3	0.100				
											25	16			4	0.8	0.200				
											18	10			2	0.35	0.175				
											8	15			4	1	0.250				
											16	4			4	0.4	0.100				
											8	2			4	0.4	0.100				
											17	3			4	0.8	0.200				
											18	2			2	0.3	0.150				
											3	6			3	0.6	0.200				
											15	4			2	0.25	0.125				
											10	8			1	0.2	0.200				
											17	7			0.5	0.08	0.160				
											13	15			3	0.8	0.267				
											11	4			1.8	0.15	0.083				
											12	3			4.5	1.5	0.333				
											8	5			3	0.4	0.133				
											7	15			1.5	0.4	0.267				
											14	12			4	1	0.250				
											16	12			3	0.65	0.217				
											23	16			4	0.8	0.200				
											11	12			10	0.2	0.020				
											6	17			3	0.25	0.083				
											3	10			2	0.3	0.150				
											7	11			1.2	0.1	0.083				
											10	13			1.2	0.3	0.250				
											7	13			2.5	0.5	0.200				
											2	17			4	0.6	0.150				
											30	4									
											0	20									
											12	6									
											2	15			1	0.2	0.200				
											41	15			0.6	0.06	0.100				
											7	15			0.8	0.2	0.250				
											14	2									
											35	1			1	0.12	0.120				
											20	15			1.6	0.15	0.094				
											3	15			1.2	0.15	0.125				
											10	15			4	1	0.250				
											30	5			1.6	0.4	0.250				
											9	12			2	0.4	0.200				
											0	15			0.7	0.07	0.100				
											2	15			1.3	0.07	0.054				
											10	11			0.5	0.05	0.100				
											19	8			4	1	0.250				
											7	15			0.8	0.2	0.250				
											8	11			1.2	0.25	0.208				
											2	11			3	0.25	0.083				
											9	6			3	0.3	0.100				
											3	14			2	0.25	0.125				
											29	2			2	0.6	0.300				
											11	13			0.8	0.15	0.188				
											19	13			3	0.8	0.267				
											3	11			4	0.3	0.075				
											17	11			1	0.08	0.080				
											12	1			1	0.1	0.100				
											6	10			1	0.3	0.300				
									44												

4435

Author	Location	Name in source	Stoss$_h$	Lee$_h$	Stoss$_h$ (A)	Lee$_h$ (A)	Stoss (Range)	Lee (Range)	Stoss	Lee	Stoss (A)	Lee (A)	Length (Range)	Thickness (Range)	Length (m)	Thickness (m)	Aspect Ratio	Dep. Surface (°)	Distance from vent	Data Source	Figure in chapter
		Chute-and-pool structures							49											Text	
							10-60														
					15.5	15.5														Figure 8	6.24
Gençalioğlu-Kuşcu et al. 2007	Cora Maar	Antidunes			15	17.5												10		Figure 7b	6.31
			9.5	22																	
															5.3	0.14	0.026			Figure 9	
															5.3	0.35	0.066				
															7.7	0.45	0.058				
															7	0.47	0.067				
															15.3	0.6	0.039				
															9.1	0.6	0.066				
															13.8	0.83	0.060				
															12.7	0.9	0.071				
															9.6	0.9	0.094				
					17															Figure 7c	6.32
		Chute-and-pool structure			15	0														Figure 8	6.33
Valentine & Giannetti 1995	Roccamonfina	Surge deposits	20.5	7.5															~7 km	Figure 2	6.25
			11	12.5																	
Giannetti & De Casa 2000	Roccamonfina	Chute-and-pool structures	31																	Figure 8	6.26
					36.5																
Cole 1991*	Sugarloaf Mt.	Regressive sandwave			23	18									1.66	0.45	0.271		0.75 km	Figure 3	6.27
	Roccamonfina	Regressive sandwaves											<1	<0.5						Text	
Brand et al. 2009	Narbona Pass Maar	Chute-and-pool structure			59	0													~1 km	Figure 4a	6.35
Brand & Clarke 2012	Table Rock Complex	Chute-and-pool structure	74.5															<2	~2 km	Figure 6, text	6.36
			90																		
			72																		
			67																		
Cole & Scarpati 1993	Neapolitan Yellow Tuff	Sandwave	45.5																11 km	Figure 5	6.28
		Regressive sandwave	20	16											4.16	1.05	0.252			Figure 7	6.29
Douillet et al. 2018	Tungurahua	Erosive based backset							69											Figure 5a	6.37
									74												
									59.5												
									65.5												
		Stoss-aggrading laminasets	22.5	33																Figure 6c	6.38
			25.5	15																	
			22.5	19																	
Brand et al. 2016	Mt St Helens Proximal Bedded Deposits	Regressive Bedforms					30-68	0-10					2-15	0.5-5				10-28	2.3-3.3 km	Text, Table 2	
		Regressive Bedform	50	10																Figure 4b	6.16
			31	5																	
					33	4.5															
		Regressive Bedform			68															Figure 4c	6.17
					30.5																
		Regressive Bedform	35	11																Figure 5d	6.18
			50.5	11																	
			58	10																	
			50	10																	
					45	17.5															
		Regressive Bedform							21.5	5										Figure 7b	6.19
									30.5	8											
		Regressive Bedform									50									Figure 7d	6.20
											28.5										
											47.5										
		Regressive Bedform	44.5																	Figure 7e	6.21
											21.5										
											34										
Rowley et al. 1985	Mt St Helens PBD	Antidunes					<45	"Gently"					<4	<1				5-30		Text	
		Antidune			30	4														Figure 4	6.15
					43	5															
Bryan et al. 1998	El Abrigo	High-relief bedform									30	30						<2	~28 km	Figure 5e, text	6.23
Fisher & Waters 1970	Ubehebe	Antidune									16.5	24.5							"tens of m"	Plate 3	6.2
Fisher & Waters 1969	Ubehebe	Antidune									14	15								Figure 2	6.1
Petrinovic & Colombo Piñol 2006	Tocomar	Chute-and-pool structure									21.5	0								Figure 5e	6.14
															12.3	0.7	0.057				
															12.3	0.9	0.073				

Author	Location	Name in source	Stoss$_h$	Lee$_h$	Stoss$_h$ (A)	Lee$_h$ (A)	Stoss (Range)	Lee (Range)	Stoss	Lee	Stoss (A)	Lee (A)	Length (Range)	Thickness (Range)	Length (m)	Thickness (m)	Aspect Ratio	Dep. Surface (°)	Distance from vent	Data Source	Figure in chapter
Sigurdsson et al. 1987	El Chichon	Sandwaves													12.7	1.5	0.118		4-6 km	Figure 23	
															30.4	2	0.066				
															19.2	2.1	0.109				
															39.2	3.1	0.079				
															30	2.9	0.097				
															12.5	4.1	0.328				
	Bandelier Tuff														0.2	0.01	0.050				
															0.4	0.01	0.025				
															1	0.02	0.020				
															0.8	0.02	0.025				
															1	0.03	0.030				
															2	0.04	0.020				
															1.6	0.04	0.025				
															1	0.04	0.040				
															2	0.05	0.025				
															1.2	0.05	0.042				
															1	0.05	0.050				
															1.2	0.09	0.075				
															3.5	0.1	0.029				
															2	0.1	0.050				
															1.8	0.1	0.056				
															1.5	0.1	0.067				
															3.5	0.12	0.034				
															3	0.12	0.040				
															1	0.12	0.120				
															3	0.15	0.050				
															6	0.2	0.033				
															1.6	0.2	0.125				
															6	0.25	0.042				
															5	0.3	0.060				
This Study	Pozzolane Rosse	Backset Bedform							41	25								3	22.5 km	Figure 6	
									67	25											
									87	45											
									20	18											
									22	10											
									11	10											
									21	11											
									15	16											
									21	17											
									18	14											
									24	18											
	Mt St Helens PBD										33.5	4						18	2.7 km		6.22
	Laacher See								22	7					6.7	1.1	0.164		2 km		6.11
					27	0													2.4 km		
					32	13													2.1 km		
					16	7															
	Neapolitan Yellow Tuff										21.5	0							11.6 km		6.30
									25	11					2.2	0.4	0.182	10	3.5 km		
									18	12								12	3.4 km		
									18.5	8					2.14	0.25	0.117		8.7 km		
									6	8.5					2.5	0.13	0.052	12.5	11.6 km		
									28	12					1.6	0.26	0.163	8			
	Astroni Crater								22	7.5					0.95	0.2	0.211	<5	1.7 km		6.34
											21	23			1	0.25	0.250				
									30	8					2.4	0.3	0.125	10			
									17	4								-6			
Pollock et al. 2018	Mt St Helens	Recumbent Flame Structures													0.08	0.04	0.500		~5 km	Table 1	
															0.4	0.04	0.100				
															0.5	0.09	0.180				
															0.5	0.1	0.200				
															2.5	0.5	0.200				
															3.4	0.6	0.176				
															3.4	0.5	0.147				
															3.3	0.4	0.121				

4437

Author	Location	Name in source	$Stoss_h$	Lee_h	$Stoss_h$ (A)	Lee_h (A)	Stoss (Range)	Lee (Range)	Stoss	Lee	Stoss (A)	Lee (A)	Length (Range)	Thickness (Range)	Length (m)	Thickness (m)	Aspect Ratio	Dep. Surface (°)	Distance from vent	Data Source	Figure in chapter
															4	0.25	0.063				
															6	0.4	0.067				
															17.9	2	0.112				
Rowley et al. 2011	Lab	Vortical Shear Features													0.013	0.00154	0.118	5		Figure 7	
															0.014	0.0016	0.114				
															0.0166	0.0019	0.114				
															0.018	0.00183	0.102				
															0.0183	0.0021	0.115				
															0.02	0.0023	0.115				
															0.021	0.0025	0.119				
															0.0217	0.00253	0.117				
															0.0234	0.0027	0.115				
															0.0234	0.00286	0.122				
															0.025	0.00288	0.115				
															0.0253	0.0031	0.123				
															0.0263	0.00305	0.116				
															0.0267	0.00322	0.121				
															0.0275	0.0031	0.113				
															0.0293	0.00334	0.114				
															0.0316	0.0038	0.120				
															0.0333	0.00377	0.113				
															0.0356	0.00397	0.112				
															0.0356	0.00361	0.101				
															0.0368	0.00344	0.093				
															0.0377	0.00447	0.119				
															0.072	0.00812	0.113				
															0.0806	0.00908	0.113				
															0.0846	0.00862	0.102				
															0.0834	0.00807	0.097				
															0.089	0.0076	0.085				
															0.0916	0.011	0.120				

==

Appendix E – Experimental Apparatus

==

The experimental flume consists of 0.4 m high Perspex sidewalls (0.01 m thick) along a 3 m long and 0.15 m wide base. The base consists of a porous plate sitting on top of three unconnected chambers constructed from 0.02 m thick PVC, and to which the sidewalls were attached with screws. All seals were grouted with silicone paste. The porous plate is a “Poremet” model sintered wire mesh manufactured by BOPP, with 10 µm diameter pores (30% porosity), and is attached to the PVC chambers by glue. Independently controlled gas fluxes are fed into the base of each chamber from a dried compressed air supply through plastic hoses. The gas flux for each chamber is controlled through a separate valve and is set at the required velocity for the required amount of fluidisation before the particles are released into the flume. Hoses connecting the air supply to the control valves are 10 mm internal diameter, and hoses connecting the control valves to the flume are 6 mm internal diameter. The control valves have a 100 litre per minute capacity. To ensure a homogenous gas flux through the porous plate above a chamber, the chambers were packed with layers of PVC sacking.

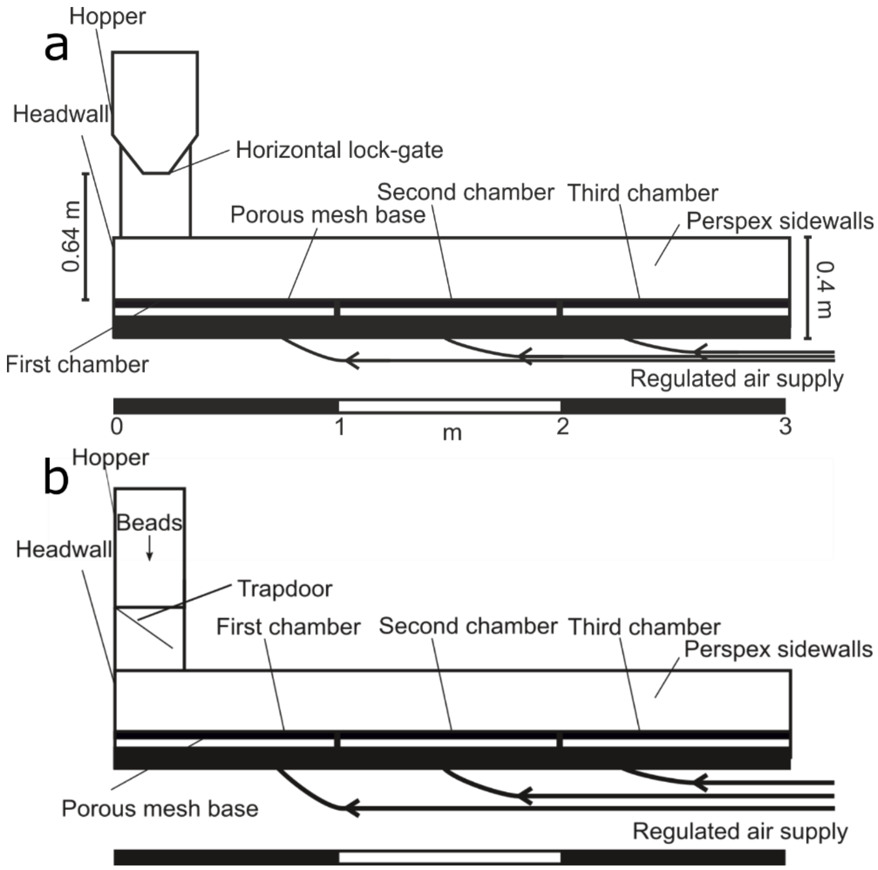

Supplementary Figure E.1 Experimental apparatus used in **a)** Chapter 3, and **b)** Chapter 4 & 5.

Particles were fed into the flume channel in two separate ways, shown in Supplementary Figure E.1. a) a hopper with a horizontal lock gate, and b) a hopper with a trapdoor released by a toggle latch. In the first case drop height was 0.64 m, and in the second 0.6 m. In all experiments presented in this thesis 10 kg of particles were used per experiment.

Experiments were captured using a high-speed video camera, the Optronis CR600X2 with a 50 mm lens, viewed in the associated software (TimeBench 2.6.30), and exported as mp4 and png files for analysis. FPS ranged from 200 in Chapter 3 to 800 in Chapter 5. To reduce strobing in the resulting videos overhead lights were turned off and spotlights used to illuminate the flume instead. To increase visibility of the currents and deposits, the outside of the far sidewall was covered in black paper. The flume was laid on adjustable trestles, which could be lowered incrementally downstream to allow an increased slope angle.

The 45-90 μm particles used in Chapters 3-5 were sodalime spherical blasting media produced by Potters. The coloured particles used in Chapter 4 were dyed black. The 150-250 μm particles used in Chapter 5 were sodalime decobeads (dyed black) produced by SiLi. All beads were spherical with a density of 2500 kg/m^3.